High-resolution, multi-proxy cyclostratigraphic characterization of the early Eocene Green River Formation, Wyoming and Utah, U.S.A

By
Andrew P. Walters

A dissertation submitted in partial fulfilment of
The requirements for the degree of

Doctor of Philosophy
(Geoscience)

at the
UNIVERSITY OF WISCONSIN-MADISON
2020

Date of the final oral examination: 8/13/2020
This dissertation is approved by the following members of the Final Oral Committee:

Stephen R. Meyers, Professor, Geoscience (Co-advisor)
Alan R. Carroll, Professor, Geoscience (Co-advisor)
D. Clay Kelly, Professor, Geoscience
Sara C. Hotchkiss, Professor, Botany

Abstract

Geological records of past periods of unusually warm climate are critical for understanding how the Earth system behaves during greenhouse climates, and thus can be valuable for predicting responses to potential climate warming in the future. The Early Eocene Climatic Optimum (EECO; 53-50 Ma)—Earth's last sustained greenhouse climate—produced the warmest recorded temperatures of the last 66 Ma and represents one of the premier geological examples of greenhouse climate dynamics.

The lacustrine Green River Formation of Wyoming and Utah represents an ideal location from which to examine continental sedimentary system responses during this period of global warmth, boasting a voluminous, detailed, and temporally well-constrained terrestrial section. This dissertation leverages the strength of the Green River Formation archive through the application of X-ray fluorescence (XRF) core scanning methods, in combination with high-precision radioisotopic data and statistical times series analysis, to shed new light on continental sedimentary system responses during the EECO.

In chapter 1, I find evidence that the deposition of ~100 micrometer scale lamina couplets in oil shale from the Parachute Creek Member is primarily driven by alternations in the redox state of paleo-Lake Uinta. Additionally, I identify punctuated intervals in the core record where Si decouples from the silicate input, which I ascribe to a biogenic or authigenic Si source driven by precession-scale changes in lake productivity. In chapter 2, I identify a previously unrecognized shift in the frequency distribution of Milankovitch-band variance in the Wilkins Peak Member, which I attribute to the influence of lake basin morphology on the climate-sediment transfer function. In chapter 3, I constrain the phase of eccentricity in the Wilkins Peak Member XRF data by identifying theoretically-established frequency modulation that is

associated with constructive and destructive interference between the short eccentricity periods. This reveals that minima in short eccentricity are associated with alluvial siliciclastic deposition. I also identify an ~100 ky offset between the radioisotopically-anchored signal of the long eccentricity cycle in the Wilkins Peak Member and the signal of this cycle in five published astronomical solutions for the EECO, which may be related to the reduced accuracy of these solutions beyond 50 Ma. These results provide a new perspective on terrestrial responses to the EECO and the mechanisms by which astronomical signals are encoded in sedimentary strata, while also yielding new constraints for numerical modeling of the solar system.

Acknowledgements

I would like to express my sincere gratitude to my advisors, Stephen R. Meyers and Alan R. Carroll. Through their mentorship, guidance, support, and encouragement, I have grown immensely as a scientist and educator over the last five years.

I would also like to thank D. Clay Kelly, Sara C. Hotchkiss, Bradley S. Singer, and Zhengyu Liu for serving as members of my committee over the course of my dissertation. Their constructive feedback, mentorship, and support was invaluable to the development of my research.

I am also grateful for the help given by collaborators on my research, including Michael Vanden Berg, Tina R. Hill, M. Elliot Smith, and Tim K. Lowenstein. I would also like to thank Shlomo Honig, Elizabeth Klonowski, and Isaac Sageman for their help with core preparation.

I thank the Department of Geoscience for their financial support as both a teaching and research assistant. Funding from the National Science Foundation (NSF-EAR 1151438 and NSF-EAR 1813278), Geological Society of America, and the American Association of Petroleum Geologists (AAPG) also supported my research, fieldwork, and travel.

Thank you to members of the Sed/Strat/Paleo research group for their support and constructive feedback over the years, including (but not limited to) Shanan Peters, Nicholas Sullivan, Ethan Parrish, Shlomo Honig, M'bark Baddouh, Chao Ma, Alexandra Villa, Brittany Hupp, Daniel Segessenman, Benjamin Linzmeier, and Sharon McMullen. I am also truly grateful for the support and friendship of countless members of the Department of Geoscience community.

I am indebted to my fiancée, Jemma Sepich, and my parents, Ann and John Walters, for their encouragement and support, without which I would not be where I am today.

Table of Contents

Introduction

Geological records of past periods of unusually warm climate are critical for understanding how the Earth system behaves during greenhouse climates, and thus can be valuable for predicting responses to potential climate warming in the future. As the last interval of sustained warm climate, the Early Eocene Climatic Optimum (EECO; ~53-50 Ma) represents one of the premier geologic examples from which to study warm climate dynamics (**Figure 1**).

The EECO marks the peak of a ~ 6 million-year secular rise in temperatures, which started in the late Paleocene and ended in the Eocene when temperatures began to decline again (**Figure 1**) (Zachos et al., 2008). This broad ~6 million-year interval of warmth, which culminated in the EECO, is also marked by a series of rapid, abrupt climate warming events called hyperthermals. The Paleocene-Eocene Thermal Maximum (PETM, ~56 Ma) is the first and largest of these Cenozoic hyperthermal events, which proxy records suggest produced warming of approximately 5°C in the deep oceans (Kennett and Stott, 1991; Thomas and Shackleton, 1996; Zachos et al., 2001, 2003, 2008; Tripati and Elderfield, 2005) and about 5-8°C of warming on the continents (Bowen et al., 2001; Fricke and Wing, 2004; Fricke et al., 1998; Koch et al., 2003; Wing et al., 2005). These hyperthermal events continued to occur into the early Eocene, and at least ten of these rapid warming events were thought to have occurred during the EECO (Zachos et al., 2008; Lauretano et al., 2016) (**Figure 1).**

These hyperthermals are hypothesized to result from a massive release of carbon dioxide (Kirtland Turner et al., 2014), although the precise source is debated. One hypothesis calls upon the destabilization of marine methane hydrates (Dickens et al., 1995; Katz et al., 1999; Zachos et al., 2010; Lunt et al., 2011) as a trigger, while others invoke terrestrially derived organic carbon

(Kurtz et al., 2003; DeConto et al., 2012) or aerated marine organic carbon (Higgins and Schrag, 2006; Sexton et al., 2011).

Much of our current understanding of this EECO warm period—including the hypothesized magnitude and timing of the shorter term hyperthermal events—has come from detailed cyclostratigraphic, sedimentological, and geochemical studies of deep marine cores in the South Atlantic (such as Demerara Rise and Walvis Ridge) and Pacific (such as Shatsky Rise) Oceans, and from climate and carbon cycle modeling (e.g. Dickens, 2003; Ridgewell, 2007; Panchuk et al., 2008; Zachos et al., 2008; Zeebe, et al., 2009; Kirtland Turner et al., 2014, Penman et al., 2016). While enormously valuable in understanding the impact of the EECO on the deep oceans, these available deep marine records also include some key limitations that hinder a more detailed understanding of this unique climate period. First, these archives have limited radioisotopic age control, largely due to a lack of ashes within the stratigraphic record for radioisotopic analysis. Additionally, the low sedimentation rates typical of deep marine depositional environments result in a condensed EECO section, on the order of 15 m or less in thickness in the highly-studied ODP Site 1209 and 1262 cores (Westerhold et al., 2018). Finally, the deep marine record of the EECO exhibits punctuated intervals of carbonate dissolution resulting from acidification of the oceans during hyperthermal events, which acts to reduce stratigraphic completeness during these particularly noteworthy events.

Terrestrial records from the EECO are far less well-characterized than those of the deep marine archive, but can serve as a complimentary record in reaching a global understanding of sedimentary system response to the EECO greenhouse climate. Among the terrestrial records available for the EECO, the lacustrine Wilkins Peak and Parachute Creek Members of the Green River Formation in the Greater Green River Basin (Wyoming) and the Uinta Basin (Utah)

(**Figure 2**) represent two of the premier locations from which to study continental sedimentary system responses to this period of global warmth, with a rich terrestrial archive of climate dynamics, tectonics, and geomorphology. In comparison to contemporaneous deep marine records, these Green River Formation units offer superior age control (due to widespread radioisotopically-dated tuff deposits), an expanded EECO stratigraphic section (due to higher sedimentation rates), and a lack of carbonate dissolution horizons (due to an alkaline lake composition, which likely acted as a buffer to increases in atmospheric carbon dioxide).

Leveraging the strengths of these Green River Formation records, this dissertation seeks to improve the characterization of continental sedimentary system responses during the EECO through the application of X-ray fluorescence (XRF) core scanning methods in combination with high-precision radioisotopic data and statistical time series analysis techniques. XRF core scanning provides a non-destructive, high-resolution (0.01 to 1.5 cm), continuous, and rapid record of elemental intensity (in counts) for a broad suite of major and minor elements in a sediment core. While several cyclostratigraphic assessments of the Green River Formation have been published to date (e.g. Fischer and Roberts, 1991; Machlus et al., 2008; Meyers, 2008; Aswasereelert et al., 2013), this project's application of radioisotopically-calibrated XRF core scanner data provides a new level of detail, multi-proxy element breadth, and temporal constraint compared to previous assessments. This provides the opportunity to apply new approaches to evaluate the sedimentary response of the Green River Formation to the EECO greenhouse climate.

The objectives of this dissertation are four-fold: 1) To identify and characterize cyclic sedimentation—including astronomical cycles—in the Green River Formation with a new level of detail and breadth, 2) To explore the interplay between astronomical climate forcing and

regional landscape evolution, 3) To characterize the long-term evolution of the Green River Formation climate-sediment transfer function, which encodes environmental signals into the rock record, and 4) To apply astronomical cycles extracted from the Green River Formation as a means of testing the accuracy of current astronomical solutions for the EECO.

Overview of Chapters

In chapter one, I examine one of the most detailed sedimentary records available for the EECO, the finely laminated oil shale facies of the Parachute Creek Member in the Uinta Basin, Utah. Interest in these laminites has spanned more than a century, but the fine spatial scale of individual laminations (~100 micrometers) had previously thwarted a detailed cyclostratigraphic examination of these facies. Using high-resolution micro-XRF and XRF methods paired with radioisotopic age data, I develop a series of cyclostratigraphic models for this interval, evaluate the paleo-environmental significance of observed sedimentary rhythms, test a range of previously proposed forcing hypotheses, and evaluate potential linkages between high- and low-frequency forcing within the record. I find evidence for a redox-driven mechanism for lamination formation, strong decadal- to centennial-scale variations in carbonate and siliciclastic input, and punctuated millimeter- to centimeter-scale intervals of Si decoupling from the silicate input, which I attribute to precession-driven authigenic or biogenic sources. The results of this chapter were published in the *Journal of Sedimentary Research* in April 2020 (Walters et al., 2020).

In chapter two, I investigate the evolution of the climate-sediment transfer function in the Wilkins Peak Member of the Greater Green River Basin, Wyoming. This transfer function plays a critical role in filtering which signals are preserved in the rock record, but it has received little

attention in deep time lacustrine systems such as the Green River Formation. In this study, I apply spectral analysis to five high-resolution, temporally-calibrated XRF core scanner elemental intensity records, with the aim of characterizing cyclic sedimentation in the Wilkins Peak Member at a previously unattainable level of detail and assessing changes in the expression of cyclic sedimentation. I identify a previously unrecognized shift in the frequency distribution of Milankovitch-band variance, with the lower Wilkins Peak Member showing enhanced obliquity, precession, and sub-Milankovitch scale variance. This transition coincides with the decline in volume and number of bedded evaporite in the depocenter of the WPM. I attribute this altered transfer function to a change in the morphology of the Bridger basin, which directly influenced the preservation of bedded evaporite. The loss of bedded evaporite, combined with obscuration of other primary lithologies by secondary evaporite growth, results in reduced obliquity and precession band power, and enhanced eccentricity band power. I plan to submit this manuscript to *Palaeogeography, Palaeoclimatology, Paleoecology* in summer 2020.

In chapter three, I evaluate the relationship between eccentricity phase and lithofacies in the Wilkins Peak Member. This assessment analyzes interference patterns within the eccentricity signal using two temporally-calibrated XRF core scanner elemental intensity records for the lower and middle Wilkins Peak Member. This assessment provides one of the few available constraints on terrestrial sedimentary system response to astronomical forcing during the EECO, while also facilitating the comparison of the Wilkins Peak Member eccentricity record to published theoretical orbital solutions for the EECO. I find that lake lowstands and accompanying alluvial deposition in the WPM is exclusively associated with minima in short eccentricity, and I develop a WPM lithofacies model based on these findings. Additionally, I observe a ~100 ky offset in the long eccentricity cycle between the WPM astronomical signal

and the La10d, La11, ZB17a, and ZB18a astronomical solutions, which I attribute to the diminished accuracy of the astronomical models starting at ~50 Ma. I plan to submit this manuscript to *Earth and Planetary Science Letters* in fall 2020.

References Cited

Aswasereelert, W., Meyers, S.R., Carroll, A.R., Peters, S.E., Smith, M.E., and Feigl, K.L., 2013, Basin-scale cyclostratigraphy of the Green River Formation, Wyoming: GSA Bulletin, v. 125, p. 216-228.

Bowen, G., Koch, P., Gingerich, P., Norris, R.D., Bains, S., and Corfield, R.M., 2001, Refined isotope stratigraphy across the continental Paleocene-Eocene boundary on Polecat Bench in the northern Bighorn Basin, University of Michigan Papers on Paleontology, 33, 77–83.

DeConto, R.M., Galeotti, S., Pagani, M., Tracy, D., Schaefer, K., Zhang, T., Pollard, D., and Beerling, D.J., 2012, Past extreme warming events linked to massive carbon release from thawing permafrost: Nature, v. 484, p. 87–91.

Dickens, G.R., O'Neil, J.R., Rea, D.K., and Owen, R.M., 1995, Dissociation of oceanic methane hydrate as a cause of the carbon isotope excursion at the end of the Paleocene: Paleoceanography, v. 10, p. 965–971.

Dickens, G.R., 2003, Rethinking the global carbon cycle with a large, dynamic and microbially mediated gas hydrate capacitor: Earth and Planetary Science Letters, v. 213, p. 169–183.

Fischer, A.G., and Roberts, L.T., 1991, Cyclicity in the Green River Formation (lacustrine Eocene) of Wyoming: Journal of Sedimentary Petrology, v. 61, p. 1146-1154.

Fricke, H.C., Clyde, W.C., O'Neil, J.R., and Gingerich, P.D., 1998, Evidence for rapid climate change in North America during the latest Paleocene thermal maximum: oxygen isotope compositions of biogenic phosphate from the Bighorn Basin (Wyoming), Earth and Planetary Science Letters, v. 160, no. 1, 193–208.

Fricke, H.C., and Wing, S.L., 2004, Oxygen isotope and paleobotanical estimates of temperature and δ18O–latitude gradients over North America during the early Eocene, American Journal of Science, v. 304, no. 7, 612–635.

Higgins, J.A., and Schrag, D.P., 2006, Beyond methane: Towards a theory for the Paleocene–Eocene Thermal Maximum: Earth and Planetary Science Letters, v. 245, p. 523–537.

Katz, M.E., Pak, D.K., Dickens, G.R., and Miller, K.G., 1999, The Source and Fate of Massive Carbon Input During the Latest Paleocene Thermal Maximum: Science, v. 286, p. 1531–1533.

Kennett, J.P., and Stott, L.D., 1991, Abrupt deep-sea warming, palaeoceanographic changes and benthic extinctions at the end of the Palaeocene, Nature, v. 353, p. 225–229.

Kirtland Turner, S., Sexton, P.F., Charles, C.D., and Norris, R.D., 2014, Persistence of carbon release events through the peak of early Eocene global warmth: Nature Geoscience, v. 7, p. 748–751.

Koch, P.L., Clyde, W.C., Hepple, R.P., Fogel, M.L., Wing, S.L., and Zachos, J.C., 2003, Carbon and oxygen isotope records from Paleosols spanning the Paleocene-Eocene boundary, Bighorn Basin, Wyoming, Geological Society of America Special Papers, v. 369, p. 49–64.

Kurtz, A.C., Kump, L.R., Arthur, M.A., Zachos, J.C., and Paytan, A., 2003, Early Cenozoic decoupling of the global carbon and sulfur cycles: Paleoceanography, v. 18, p. 1-14.

Jagniecki, E.A., Lowenstein, T.K., Jenkins, D.M., and Demicco, R.V., 2015, Eocene atmospheric CO_2 from the nahcolite proxy: Geology, p. G36886.1.

Lauretano, V., Hilgen, F.J., Zachos, J.C., and Lourens, L.J., 2016, Astronomically tuned age model for the early Eocene carbon isotope events: A new high-resolution $d^{13}C_{benthic}$ record

of ODP Site 1263 between ~ 49 and ~ 54 Ma: Newsletters on Stratigraphy, v. 49, p. 383–400.

Laurin, J., Meyers, S.R., Galeotti, S., and Lanci, L., 2016, Frequency modulation reveals the phasing of orbital eccentricity during Cretaceous Oceanic Anoxic Event II and the Eocene hyperthermals: Earth and Planetary Science Letters, v. 442, p. 143–156.

Lunt, D.J., Ridgwell, A., Sluijs, A., Zachos, J., Hunter, S., and Haywood, A., 2011, A model for orbital pacing of methane hydrate destabilization during the Palaeogene: Nature Geoscience, v. 4, p. 775–778.

Machlus, M.L, Olsen, P.E., Christie-Blick, N., Hemming, S.R., 2008, Spectral analysis of the lower Eocene Wilkins Peak Member, Green River Formation, Wyoming: Support for Milankovitch cyclicity: Earth and Planetary Science Letters, v. 268, p. 64-75.

Meyers, S.R, 2008, Resolving Milankovitchian controversies: the Triassic Latemar Limestone and the Eocene Green River Formation: Geology, v. 36, p. 319-322.

Panchuk, K., Ridgwell, A., and Kump, L.R., 2008, Sedimentary response to Paleocene-Eocene Thermal Maximum carbon release: A model-data comparison: Geology, v. 36, p. 315.

Penman, D.E. et al., 2016, An abyssal carbonate compensation depth overshoot in the aftermath of the Palaeocene–Eocene Thermal Maximum: Nature Geoscience, v. 9, p. 575–580.

Ridgwell, A., 2007, Interpreting transient carbonate compensation depth changes by marine sediment core modeling: Paleoceanography, v. 22, PA4102.

Sexton, P.F., Norris, R.D., Wilson, P.A., Pälike, H., Westerhold, T., Röhl, U., Bolton, C.T., and Gibbs, S., 2011, Eocene global warming events driven by ventilation of oceanic dissolved organic carbon: Nature, v. 471, p. 349–352.

Smith, M.E., Carroll, A.R., and Singer, B.S., 2008, Synoptic reconstruction of a major ancient lake system: Eocene Green River Formation, western United States: Geological Society of America Bulletin, v. 120, p. 54–84.

Thomas, E., and Shackleton, N.J., 1996, The Paleocene-Eocene benthic foraminiferal extinction and stable isotope anomalies, Geological Society, London, Special Publications, v. 101, p. 401–441.

Tripati, A., and Elderfield, H., 2005, Deep-Sea Temperature and Circulation Changes at the Paleocene-Eocene Thermal Maximum, Science, v. 308, p. 1894-1898.

Walters, A.P., Meyers, S.R., Carroll, A.R., Hill, T.R., and Vanden Berg, M.D., 2020, Lacustrine cyclicity in the early Eocene Green River Formation, Uinta Basin, Utah: Evidence from X-ray fluorescence core scanning: Journal of Sedimentary Research, v. 90, p. 429–447.

Westerhold, T., Röhl, U., Donner, B., and Zachos, J.C., 2018, Global Extent of Early Eocene Hyperthermal Events: A New Pacific Benthic Foraminiferal Isotope Record from Shatsky Rise (ODP Site 1209): Paleoceanography and Paleoclimatology, v. 33, p. 626–642.

Wing, S.L., Harrington, G.J., Smith, F.A., Bloch, J.I., Boyer, D.M., and Freeman, K.H., 2005, Transient floral change and rapid global warming at the Paleocene-Eocene boundary, Science, v. 310, p. 993–996.

Zachos, J.C., Pagani, M., Sloan, L., Thomas, E., Billups, K., 2001, Trends, Rhythms, and Aberrations in Global Climate 65 Ma to Present, Science, v. 292, p.686-693.

Zachos, J.C., Wara, M.W., Bohaty, S., Delaney, M.L., Petrizzo, M.R., Brill, A., Bralower, T.J., and Premoli-Silva, I., 2003, A Transient Rise in Tropical Sea Surface Temperature During the Paleocene-Eocene Thermal Maximum, Science, v. 302, p. 1551-1554.

Zachos, J.C., Dickens, G.R., and Zeebe, R.E., 2008, An early Cenozoic perspective on greenhouse warming and carbon-cycle dynamics: Nature, v. 451, p. 279–283.

Zachos, J.C., McCarren, H., Murphy, B., Röhl, U., and Westerhold, T., 2010, Tempo and scale of late Paleocene and early Eocene carbon isotope cycles: Implications for the origin of hyperthermals: Earth and Planetary Science Letters, v. 299, p. 242–249.

Zeebe, R.E., Zachos, J.C., and Dickens, G.R., 2009, Carbon dioxide forcing alone insufficient to explain Palaeocene–Eocene Thermal Maximum warming: Nature Geoscience, v. 2, p. 576–580.

Zeebe, R.E., 2012, LOSCAR: Long-term Ocean-atmosphere-Sediment Carbon cycle Reservoir Model v2.0.4: Geoscientific Model Development, v. 5, p. 149–166.

Figures

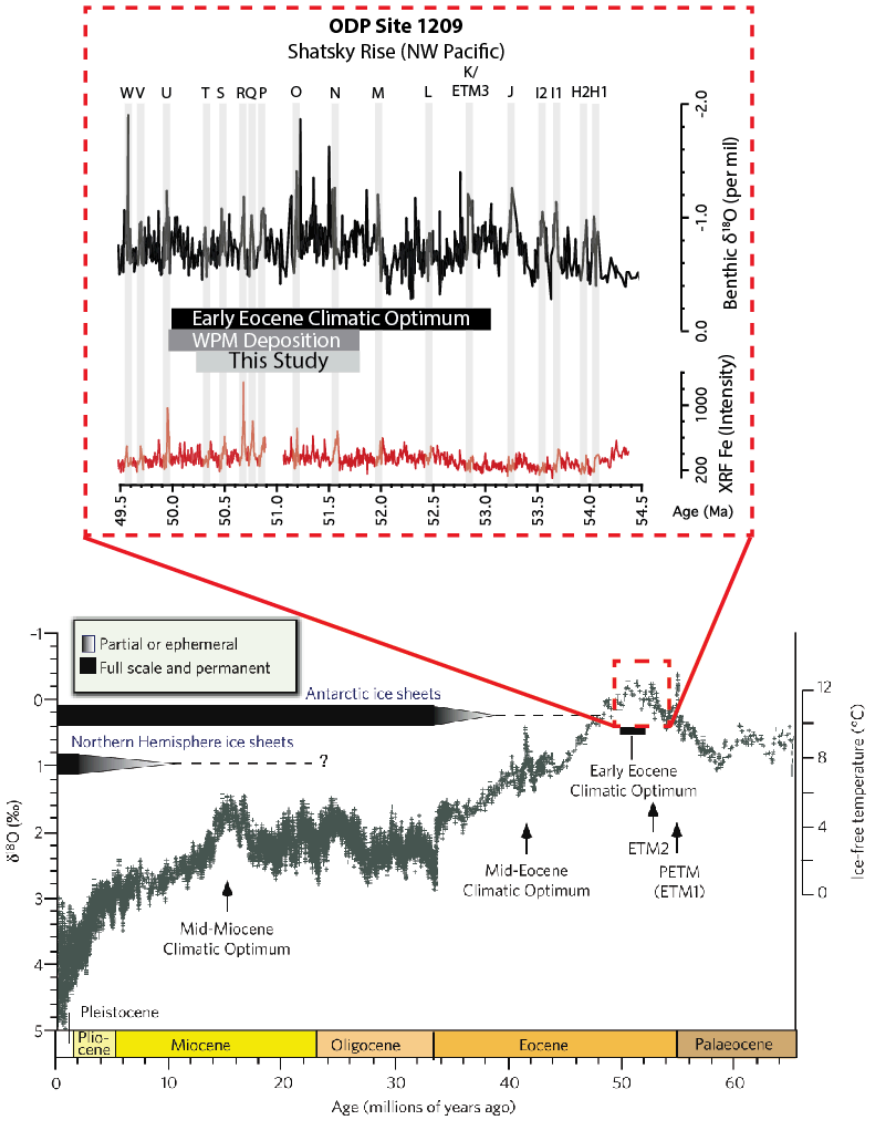

Figure 1: Climate context of the Early Eocene Climatic Optimum (EECO). Lowermost plot shows inferred deep marine paleo-temperature using the oxygen isotope record of Zachos et al. (2008). The upper inset shows an EECO oxygen isotope and Fe intensity record from ODP Site 1209 (Shatsky Rise), with hypothesized hyperthermal events highlighted in light grey. Vertical bars represent the duration of the EECO, overall WPM deposition, and the WPM interval covered in this study. Modified from Zachos et al. (2008) and Westerhold et al. (2018).

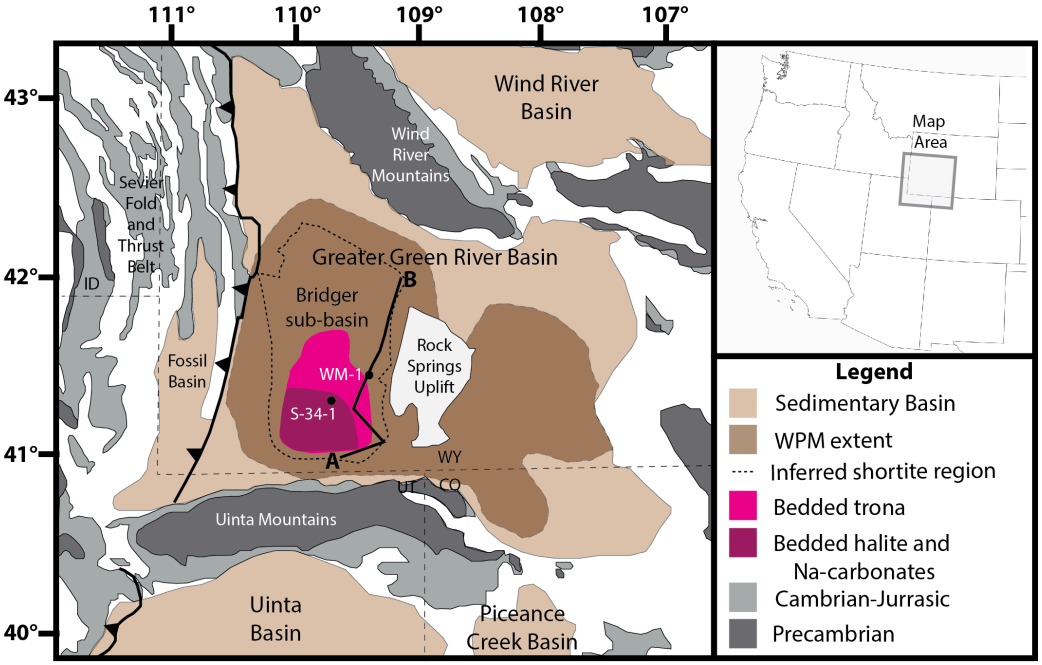

Figure 2: Location map for the Green River Formation, Wyoming, Utah, and Colorado. Modified from Smith et al. (2008) and Jagniecki et al. (2015).

Chapter 1

Lacustrine cyclicity in the Early Eocene Green River Formation, Uinta Basin, Utah: Evidence from X-ray fluorescence core scanning

Andrew P. Walters[1], Stephen R. Meyers[1], Alan R. Carroll[1],

Tina R. Hill[2], Michael D. Vanden Berg[3]

[1]Department of Geoscience, University of Wisconsin-Madison, 1215 W. Dayton St., Madison, Wisconsin 53706

[2]Bruker Nano, Inc., 5465 E. Cheryl Pky., Madison, Wisconsin 53711

[3]Utah Geological Survey, 1594 W. North Temple, Suite 3110, Salt Lake City, Utah 84114

Walters, A.P., Meyers, S.R., Carroll, A.R., Hill, T.R., and Vanden Berg, M.D., 2020, Lacustrine cyclicity in the early Eocene Green River Formation, Uinta Basin, Utah: Evidence from X-ray fluorescence core scanning: *Journal of Sedimentary Research*, v. 90, p. 429–447.

Abstract

The Green River Formation preserves an extraordinary archive of terrestrial paleoclimate during the Early Eocene Climatic Optimum (EECO; ~ 53-50 Ma), expressing multiple scales of sedimentary cyclicity previously interpreted to reflect annual to Milankovitch-scale forcing. Here we utilize X-ray fluorescence (XRF) core scanning and micro X-ray fluorescence (micro-XRF) scanning in combination with radioisotopic age data to evaluate a rock core record of laminated oil shale and carbonate mudstone from Utah's Uinta Basin, with the parallel objectives of elucidating the paleo-environmental significance of the sedimentary rhythms, testing a range of forcing hypotheses, and evaluating potential linkages between high- and low-frequency forcing. This new assessment reveals that the ~ 100-μm-scale laminae—the most fundamental rhythm of the Green River Formation—are most strongly expressed by variations in abundance of iron and sulfur. We propose that these variations reflect changes in redox state, consistent with annual stratification of the lake. In contrast to previous studies, no support was found for ENSO or sunspot cycles. However, millimeter- to centimeter-scale rhythms—temporally constrained to the decadal to centennial scale—are strongly expressed as alternations in the abundance of silicate- versus carbonate-associated elements (e.g., Al and Si vs. Ca), suggesting changes in precipitation and sediment delivery to the paleo-lake. Variations also occur at the meter scale, defining an approximate 4 m cycle interpreted to reflect precession. We also identify punctuated intervals, associated principally with one phase of the proposed precession cycle, where Si disconnects from the silicate input. We propose an alternative authigenic or biogenic Si source for these intervals, which reflects periods of enhanced productivity. This result reveals how long-term astronomical forcings can influence short-term processes, yielding insight into decadal- to millennial-scale terrestrial climate change in the Eocene greenhouse earth.

Introduction

Annual sedimentary laminae, commonly known as varves, are regularly observed in Holocene lake deposits, where their mode of formation can often be directly examined in the context of ongoing sedimentary processes (Glenn and Kelts 1991). Composed of alternating laminations of varying composition and color, varves can be useful in reconstructing detailed lacustrine chronologies. Fine-scale (< 1 mm) laminae are also observed in many ancient lake deposits, but an annual origin is often more difficult to demonstrate conclusively. The early Eocene Green River Formation (**Figures 1, 2**) contains some of the best-known pre-Quaternary lacustrine laminites, which typically consist of light-colored carbonate-rich layers that alternate with dark-colored organic-rich layers at the 100-200 micrometer scale (**Figure 3**) (Bradley 1929; Washburn et al. 2015).

These Green River Formation laminites (**Figure 3**) offer a potentially invaluable archive of the Early Eocene greenhouse climate, which reached the peak of Cenozoic warmth at the Early Eocene Climatic Optimum (EECO; ~ 53-50 Ma) (Zachos et al. 2001; Zachos et al. 2008; Smith et al. 2008). The oil shale of the Green River Formation has been a subject of keen interest for nearly a century, and has been interpreted to reflect a range of temporal variability spanning annual, subdecadal (2-8 year), quasidecadal (8-18 year), and longer (20-2400 ky) timescales (Sayles 1922; Bradley 1929; Fischer and Roberts 1991; Ripepe et al. 1991; Cole 1998; Machlus et al. 2008; Meyers 2008; Aswasereelert et al. 2013). Based on an assumed annual origin for laminae, these variations have previously been attributed to the El Niño Southern Oscillation (ENSO), sunspot cycles, and Milankovitch-band astronomical perturbations (Bradley 1929; Crowley et al. 1986; Ripepe et al. 1991). However, many aspects of these laminae—including whether they are truly annual—remain unknown, largely due to the small

spatial scale of the individual laminae. Key questions include lamination composition, lateral continuity, and connections to physical, chemical, and biologic limnologic processes occurring in the paleo-lake.

This study aims to improve this understanding through a sub-millimeter-scale stratigraphic assessment of the elemental and compositional variability of the Green River Formation laminated oil shale and carbonate mudstone facies. Objectives include elucidating the paleo-environmental significance of its sedimentary rhythms, testing the previously hypothesized range of climatic forcing hypotheses, and evaluating potential linkages between short-term (annual to millennial) and long-term (Milankovitch) depositional cyclicity.

Geologic Setting

The Green River Formation accumulated over approximately 12 million years in the Early Eocene (~ 54-43 Ma) in a network of mid-latitude, mid-continental, intermittently saline and alkaline lakes (Sheliga 1980; Remy 1992; Smith et al. 2008). Green River Formation strata were mainly deposited in four depositional basins, the Uinta Basin (northeast Utah), the Greater Green River Basin (southwest Wyoming), the Fossil Basin (southwest Wyoming), and the Piceance Basin (northwest Colorado) (**Figure 1**). Structural formation of these basins started in the Late Cretaceous when the Laramide Orogeny began to produce a series of basement-cored anticlinal uplifts in the region east of the Cordilleran fold and thrust belt (Dickinson et al. 1988; Cashion 1995; Rhodes et al. 2002; Smith et al. 2008). Flat slab subduction of the Farallon plate under the North American plate is thought to have been the driver of this deformation (Coney and Reynolds 1977; Dickinson and Snyder 1978; Smith et al. 2014). Each Green River Formation depositional basin has a different morphology and depositional character; for

example, the Piceance Basin is smaller and deeper than the Uinta Basin, while the Greater Green River Basin is shallower and broader (Rosenberg et al. 2015).

This study focuses on the Uinta Basin, which is confined by the Uinta Mountains in the north, the San Rafael Swell in the southwest, the Uncompahgre Uplift to the southeast, and the Douglas Creek Arch to the east (**Figure 1**) (Abbott 1957; Johnson, R.C., 1984; Johnson 1985; Johnson and Brownfield 2015). For periods of the region's history, lake water levels in the Uinta Basin and the adjoining Piceance Basin overtopped the Douglas Creek Arch to form a unified and connected water body termed Lake Uinta (Surdam and Stanley 1980; Smith et al. 2008; Davis et al. 2008; Davis et al. 2009; Tanavssu-Milkeviciene and Sarg 2012; Johnson et al. 2018).

In each Green River Formation depositional basin, a diverse assemblage of lithofacies resulted from highly variable depositional environments (Smith and Carroll 2015). In the Uinta Basin, the Green River Formation has been divided stratigraphically into lower, middle, and upper members (**Figure 2**) (Weiss et al. 1990; Witkind 1995; Morgan et al. 2003; Rosenberg et al. 2015). The lower member is composed of the lacustrine carbonate Uteland Butte Member, overlain by the fluviodeltaic tongues of the Wasatch Formation and Colton Formation (also called the Castle Peak Member), and capped by the lacustrine carbonates of the Long Point Bed and Carbonate Marker Unit (**Figure 2**) (Abbott 1957; Ryder et al. 1976; Weiss et al. 1990; Morgan et al. 2003; Birgenheier and Vanden Berg 2011; Rosenberg et al. 2015; Johnson et al. 2019). The middle and upper members of the Green River Formation are composed of the Douglas Creek Member and the overlying Parachute Creek Member (**Figure 2**) (Rosenberg et al. 2015). The Douglas Creek Member is principally fluvial deltaic with minor intervals of carbonate, while the Parachute Creek Member is predominantly lacustrine carbonate (Birgenheier and Vanden Berg 2011; Rosenberg et al. 2015).

Due to the considerable variation in the organic richness of Parachute Creek Member carbonate mudstone, this unit is subdivided into alternating organic-rich (R) and organic-lean (L) zones (**Figure 2**) (Donnell and Blair 1970; Cashion and Donnell 1972; Birgenheier and Vanden Berg 2011). The "Upper R-6" zone, the focus of this study (**Figure 2**), was deposited in an expanded, moderately saline lake (Vanden Berg and Birgenheier 2017) under balanced-fill conditions (cf. Carroll and Bohacs, 1999), in which input of sediment and water were approximately equivalent to potential basin accommodation (Smith et al. 2008; Birgenheier and Vanden Berg 2011). The overlying "Mahogany zone" (R-7), one of the most organic-rich intervals of the Parachute Creek Member, marks the maximum depth and expansion of the lake and serves as the boundary between the middle and upper Green River Formation members (Johnson 1985; Birgenheier and Vanden Berg 2011; Tanavsuu-Milkeviciene and Sarg 2012; Johnson and Brownfield 2015).

Methods

Skyline 16 Core

The Utah Geological Survey and the University of Utah drilled the 10-cm-diameter Skyline 16 core in 2010, sampling ~ 300 m of lacustrine and deltaic facies preserved near the present eastward limit of Uinta Basin lacustrine strata (**Figures 1, 2**) (Vanden Berg and Birgenheier 2011; Vanden Berg and Birgenheier 2016). The core extends from the R-8 interval at the top of the Parachute Creek Member, downward to the top of the underlying Douglas Creek Member (**Figure 2**). Down-hole well log data, including gamma-ray logs, were also collected from the Skyline 16 borehole. The present study focuses on a 9.2 m section of thinly laminated

oil shale and carbonate mudstone facies in the organic-rich "Upper R-6" zone in the Parachute Creek Member of the Green River Formation, spanning 170.6-179.8 m core depth (**Figure 2**).

XRF Scanning

A third-generation Avaatech X-ray fluorescence (XRF) core scanner at the University of Wisconsin-Madison was used to measure elemental intensities at two down-core resolutions. Core samples were placed slab face up in the scanner, cleaned of debris, leveled, described, and covered in SPEX 3525 Ultralene foil. A continuous down-core measurement path was chosen for each individual core segment to target representative facies and, when possible, avoid any irregularities in the core. A continuous 5-millimeter-resolution (5 mm x 5 mm window size) scan captured millimeter- to- meter-scale variations in elemental intensity across the 9.2 m study section of the core. For a 202.6 mm sub-section of this 9.2 m interval (171.47-171.67 m depth; **Figure 4**), a second high-resolution scan was completed at a continuous 100 micrometer resolution (0.1 mm x 2 mm window size). This scan aimed to resolve elemental intensity variations at the lamina to near-lamina scale.

To measure a wide range of elements using the XRF core scanner, instrument settings were optimized into two down-core scans per individual core section for both the 5 mm and 100 μm resolution assessments. For 5-mm-resolution evaluations, an acceleration voltage of 10 kV (1200 μA source current, no filter, 20 second measurement time) was used to optimally measure elements in the range of Mg-Fe, while an acceleration voltage of 30 kV (1600 μA source current, thin palladium filter, 20 second measurement time) was used to measure elements Cu-U. For 100-μm -resolution XRF measurements, a 10 kV acceleration voltage (2000 μA source current, no filter, 90 second measurement time) was used to optimally measure Mg-Fe, while a 30 kV acceleration voltage (2000 μA source current, thin palladium filter, 90 second measurement

time) was used to evaluate Cu-U. X-ray fluorescence spectra were deconvolved to provide the intensities for various elements using a customized deconvolution model in the WinAxil (v. 4.5.2) X-ray analysis software.

Standard samples were analyzed between each scan run of an individual core section (SARM-4) and before and after the complete analysis of each individual core section (JGb-1, JR-1) to evaluate instrument stability (Supplement A1). For each core section measured, replicate measurements were also taken to quantify instrument variation and evaluate reproducibility for each element (Supplement A2-5). Through examining mean coefficients of variation, standard deviation of the coefficient of variation, and cross plots of elemental intensities for all replicate measurements, we identified sixteen elements (Mg, Al, Si, S, K, Ca, Ti, Mn, Fe, Cu, Zn, Rb, Sr, Zr, Mo, Pb) at the 5 mm resolution and seven elements (Al, Si, S, K, Ca, Fe, Sr) at the 100 μm resolution that displayed superior reproducibility (Supplement A2-5).

Inductively coupled plasma mass spectrometry (ICP-MS) and inductively coupled plasma atomic emission spectroscopy (ICP-AES) analyses were used to provide a means of calibrating Avaatech XRF core scanner elemental intensities to elemental weight percent or parts per million values. For 36 XRF analysis sites, samples were drilled to match the 5 mm down-core resolution using a tungsten carbide cutter affixed to a rotary tool, yielding approximately 1 gram of powder from near the surface of the core. For 5 of the 36 sites, sufficient powder was collected to analyze a duplicate sample using ICP-MS and ICP-AES. At SGS Mineral Services, these samples were prepared using a sodium peroxide fusion technique and measured using ICP-MS and ICP-AES, yielding weight percent or parts per million values for 56 elements. Since weight percent or ppm of S could not be evaluated using these techniques, data for S are presented as elemental intensity. Using these 36 calibration points and 5 duplicate measurements, 5-mm-

resolution XRF data were calibrated to measured ICP-MS weight percent or parts per million values using a linear regression calibration (**Table** 1, Supplement A6). Using the "downscaling approach" of Ma et al. (2014), the 100 μm resolution data were calibrated to weight percent by averaging the 100 μm resolution XRF core scanner results into 5 mm bins that match the location and resolution of the 5 mm ICP calibrated-XRF data. These two measurements were cross-plotted against each other and linearly regressed to produce an ICP-XRF calibration at the 100 μm scale (Ma et al. 2014) (**Table 2**, Supplement A7).

Micro X-ray fluorescence (micro-XRF) scanning, an elemental-analysis technique that relies on the same principles as XRF core scanning, was also applied to the Skyline 16 core using a Bruker M4 Tornado. This instrument uses polycapillary X-ray focusing optics to create a focal spot of less than 20 μm in diameter, producing a much smaller excitation spot than that of the Avaatech XRF core scanner. The use of high-brilliance focusing X-ray optics, which create a more intense irradiation of the focal spot, produces sufficient fluorescence intensity from sample areas for enhanced trace-element analysis and better resolution of small features.

For this study, a Bruker M4 micro-XRF generated a 25-μm -resolution elemental record for 186.85 mm of the 202.6 mm sub-section of the Skyline 16 study interval (**Figure 5**). While the Avaatech XRF core scanner is limited to a resolution of 100 μm, the micro-XRF can measure spot sizes as small as 20 μm, better ensuring that elemental variability at the lamina to sub-lamina scale will be resolved. This instrument measured elemental intensities (in counts) for 20 elements (Na, Mg, Al, Si, S, Cl, K, Ca, Ti, V, Cr, Mn, Fe, Zn, Rb, Sr, Y, Zr, Rh, Ba) under vacuum using two 30 mm^2 detectors and a Rh X-ray source at an acceleration voltage of 50 kV (600 μA source current, 10 ms/pixel, 8 μm step size).

Grayscale Image Analysis

Grayscale, a type of data that numerically quantifies the light intensity of pixels in an image, was collected for the Skyline 16 core interval. This enabled the comparison of visual lamination, mainly defined by differences in facies brightness, and elemental composition. Intensity values for grayscale measurements range between 0 (Black) and 255 (White). For the 202.6 mm sub-section of the core evaluated with XRF core scanning and micro-XRF, a high-resolution image of the slabbed side of the core was collected using an Epson V500 photo scanner at 3200 dots per inch resolution. Using the National Institute of Health's ImageJ software, grayscale data were collected down the core along the micro-XRF and XRF measurement transects. These transects of grayscale data were then optimally aligned with the high-resolution micro-XRF and XRF data using a sliding correlation algorithm ("slideCor" function in Astrochron; Meyers 2014). This correlation was completed with identified pyrite layers both included and excluded (**Table 3**, Supplement A8, Supplement A9).

Constant-Net-Accumulation-Rate Model

Time-series records were developed from micro-XRF and XRF data using a constant-net-accumulation-rate methodology, which uniformly applies one of three radioisotopically constrained net annual accumulation rates (minimum, nominal, or maximum) across the 202.6 mm study section. This approach makes no assumptions about changes in lamina thickness. Net annual accumulation rates were calibrated using Ar-Ar ages for two volcanic tuff beds that overlie and underlie the study interval. The Skyline Tuff (49.58 ± 0.28 Ma (2σ); Smith and Carroll 2015), located 91 m below the base of the study interval, was sampled directly from the Skyline 16 core and dated by laser fusion of sanidine (**Figure 2**). The Wavy Tuff (48.67 ± 0.23 Ma (2σ); Smith et al. 2008; Smith et al. 2010), sampled for Ar-Ar analysis from an outcrop 98 km west of the Skyline 16 core location and dated using incremental heating of biotite, was

correlated to 52 m above the top of the study interval (**Figure 2**). Using these Ar-Ar ages and their associated 2σ analytical uncertainties, we calculated the minimum, nominal, and maximum net annual accumulation rates for this interval to be 119.8 μm/year, 167.6 μm/year, and 278.4 μm/year, respectively (**Table 4**). Studies of modern large lakes show that sedimentation rates can vary widely, ranging from 10 to 1000 μm/year (Johnson, T.C., 1984), but our calculated values are well within the range of net annual accumulation rates previously modeled for the Green River Formation based on established Ar-Ar ages (Smith et al. 2003; Smith et al. 2008).

Time-Series Analysis

Using Astrochron (Meyers 2014), a computational package for astrochronologic analysis available for the R statistical computing software (R Core Team 2014), a range of statistical and spectral analysis techniques were applied to the XRF and micro-XRF data. The multi-taper method (MTM), a Fourier technique that uses a specified series of prolate tapers for spectral estimation (Thomson 1982), was used to provide insight into oscillatory variability within a time series record using the "mtm" function in Astrochron (Meyers 2014). To test for a cyclic signal within the noise of the stratigraphic record, the LOWSPEC (locally weighted regression spectral background estimation) technique was applied via the "lowspec" function in Astrochron (Meyers 2012; Meyers 2014). Additionally, evolutive harmonic analysis (EHA), a method which applies MTM to a moving window, was applied using the "eha" function in Astrochron to identify cyclic variability and evaluate potential changes in sedimentation rate (Meyers et al. 2001; Meyers 2014).

Results

Lamina-Scale Results

High-resolution XRF and micro-XRF scanning of the Skyline 16 core permitted analysis of elemental intensities at a previously unattainable resolution for these oil shale and carbonate mudstone facies (Supplement A10). In the 186.85 mm interval of the Skyline 16 core evaluated in high resolution by micro-XRF, several fine-scale elemental trends emerged. Ca, Fe, K, S, and Si all show millimeter-scale variability in elemental composition, while Ca, K, and Si also show distinct centimeter-scale variations in composition (**Figure 5**). Millimeter-scale pyrite beds produce the peak elemental intensity values in both Fe and S; however, when looking at other intervals of the micro-XRF record, sub-millimeter-scale variations appear to drive changes in elemental intensity (**Figure 5**).

Cross-correlating grayscale with elemental composition, we found that Fe, Mg, and S have the strongest correlation with grayscale in both 25 μm micro-XRF and 100 μm XRF data (**Table 3**). Higher Fe counts correlate to lighter color laminae (correlation coefficient = 0.431), while higher S counts correlate to darker color laminae (correlation coefficient = -0.371). Like Fe, Mg (correlation coefficient = 0.496) was also found to have a strong association with lighter-colored micro-facies, perhaps indicating the presence of Fe- and Mg-rich carbonates in the lighter intervals. Likewise, the association of S with darker-colored intervals appears related to the content of enhanced pyrite and organic matter in these intervals. Other key elements, including Si, Ca, and K, had weaker correlations with grayscale (**Table 3**). With the removal of pyrite-rich lamina from the record, identified through paired high-magnitude peaks in Fe and S elemental intensities, the strength of the correlation of Fe and S to grayscale improved slightly (**Table 3**). Apart from Mg, the correlation of other elements to grayscale remained comparatively weak (**Table 3**).

Moving window cross-correlation ("mwCor" function in Astrochron; Meyers 2014) was applied to pairs of micro-XRF records for the entire interval, providing a higher-resolution view of the interrelationship of elements than is possible in a single correlation coefficient (Sageman and Hollander 1999). Use of this technique to compare K and Si, two elements that usually covary, showed punctuated intervals of positive correlation and anti-correlation between the two elements at the millimeter to centimeter scale using a 5 mm moving window (**Figure 5**). MTM analysis of this K-Si cross correlation record also identifies millimeter- to centimeter-scale cyclicity, with strong variance present at frequencies between 0 and 0.3 cycles/mm (period: > 3.3 mm/cycle) (Supplement A11). Adjusting the window size of the moving window cross correlation within the range of 3-10 mm consistently shows variance present in the MTM results at millimeter- to centimeter-scale periodicities (Supplement A11).

Following application of minimum (120 μm/year), nominal (168 μm/year), and maximum (278 μm/year) net annual accumulation rates to the micro-XRF record using a "constant net accumulation rate" model (Supplement A12), MTM and LOWSPEC were used to evaluate cyclic variability in these time-series records. Across the range of time models, MTM results for Si show variance that is concentrated above interdecadal (> 15 year) periodicities, with the strongest variance concentrated in the multidecadal (20-100 years), centennial (100-1000 years), and millennial (> 1000 years) bands (**Figure 6**). Integrating power across these spectra showed that frequencies between 0 and 0.09 cycles/year (period: ≥ 11 years) account for 30-80% of spectral power for the range of temporal models for Si, with much of the power at higher frequencies located in the background (Supplement A13). Taner bandpass filtering of the time-series record was used to visualize this variability and to show the influence of

multidecadal- to millennial-scale variability on the Si signal (**Figure 7**). Spatially, this variability is expressed as millimeter- to centimeter-scale oscillations in the oil shale.

MTM spectra for S, K, Ca, and Fe time models show comparable results, with variance similarly concentrated in the multidecadal to millennial periodicities (Supplement A14). MTM analyses of Si, S, K, Ca, and Fe time models which were pre-whitened using a LOESS curve display similar interdecadal to millennial variance (Supplement A15), as do LOWSPEC analyses of the Si, S, K, Ca, and Fe time models (Supplement A16). Looking at the higher frequencies, MTM analysis of the range of Si, S, K, Ca, and Fe time models shows low variance within decadal to annual periodicities (approximately 0.1 cycles/year to 1 cycle/year), where ENSO, sunspot, and annual-varve cyclicity are expected to be expressed (Supplement A17). While some frequencies in the quasidecadal to annual range may be statistically significant, none have strong concentrations of spectral power.

Meter-Scale Results

In the 9.2 m core study interval, light- and dark-colored facies alternate at the meter scale (**Figure 4**). Grayscale analysis of core images confirms that darker, more organic-rich facies predominate in this interval, with an average grayscale value of 81 on a scale of 0 (Black) to 255 (White). Comparisons of facies color to elemental composition shows an association for several elements; darker-colored facies are generally accompanied by higher K, S, and Si composition, while lighter-colored intervals are typically associated with higher Ca composition (**Figure 4**). The association of higher K and Si content with darker-colored facies is consistent with the findings of Robb and Smith (1974), who identified a direct relationship between organic volume and silicate-mineral content in Green River Formation oil shales in Colorado.

In this study interval, composed principally of the oil shale and carbonate mudstone facies, Si and Ca are the two most abundant elemental components. Given that the mineralogy of these facies in the Green River Formation most commonly contains calcite, dolomite, quartz, alkali feldspar, plagioclase, and illite and other clay minerals, we expect Ca composition to generally reflect carbonate mineral content and K and Si to principally reflect silicate-mineral content (Bradley and Eugster 1969; Hosterman and Dyni 1972; Picard and High 1972; Robb and Smith 1974; Dyni 1976). Looking at the interrelationship of different elements in the 5 mm resolution XRF data, we find that Si positively correlates with K (0.484), while Ca negatively correlates with both Si (-0.814) and K (-0.578) (**Table 5**). This anti-phased relationship reflects meter-scale cyclicity between darker, more silicate-rich and lighter, more carbonate-rich facies (**Figure 4**). Washburn et al. (2015) also identified this anti-phased relationship between carbonate and silicate plus organic matter in their Transmission Fourier transform infrared spectroscopy assessment of oil shale samples from the Parachute Creek Member in the Piceance Basin.

In the 5 mm XRF data, K and Ca demonstrate the most coherent multi-meter scale cyclicity. For these two elements, an approximate 4-5 m cycle is visually apparent in the XRF record (**Figure 4**). MTM and LOWSPEC analysis of the K record confirms this visually inferred cyclicity, identifying an ~ 4.4 m cycle (frequency: 0.229 cycle/m) and 2 m cycle (frequency: 0.480 cycle/m) (**Figure 8,** Supplement A18), while EHA analysis for K shows strong concentrations of power and amplitude at these periodicities across the study interval (**Figure 9**). For Ca, MTM and LOWSPEC analysis identified an ~ 5.1 m (frequency: 0.196 cycle/m) and an ~ 2.13 m (frequency: 0.469 cycle/m) cycle (**Figure 8**, Supplement A18). EHA analysis of Ca

shows strong concentrations of power and amplitude in this range, with the strongest and most consistent signal in the uppermost 5 meters of the study section (**Figure 9**).

While Si generally mirrors K, Si also shows more dynamic swings in elemental composition and more apparent influence of higher-frequency cycles. MTM and LOWSPEC analysis indicates the presence of an ~ 7 m (frequency: 0.142 cycle/m) cycle and a range of sub-1 m (frequency: > 1 cycle/m) cycles (**Figure 8**, Supplement A18). This 7 m cycle in Si is anti-phased with the 5.1 m cycle identified in the Ca record (**Figure 4**), a result which is consistent with the negative Pearson correlation coefficient calculated for Si and Ca (**Table 5**). EHA analysis of this Si record shows strong power and amplitude at the frequencies associated with those periods for much of the study section (**Figure 9**).

MTM and LOWSPEC analysis of S indicates the presence of a 1 m (frequency: 1.02 cycle/m) cycle (**Figure 8**, Supplement A18). Maxima of this oscillation appear to correspond to periods of high silicate input and darker color (**Figure 4**). Based on XRF results, S is associated with both organic material and in iron sulfides. EHA analysis for S shows inconsistent concentrations of power and amplitude at the frequencies associated with these cycles, with the strongest signals observed in intervals of the study section showing the highest S intensity (**Figure 9**).

MTM analyses of Si, S, K, and Ca records that were pre-whitened using a LOESS curve display similar results to the untreated data (Supplement A19). EHA plots of gamma-ray-log data (Supplement A20) indicate the presence of peaks in power and amplitude at frequencies similar to those cycles identified in the XRF data through the entire "Upper R-6" interval of the Parachute Creek Member in the Skyline 16 core. MTM and LOWSPEC analysis identified spectral peaks at periods of 15.63 m (frequency: 0.064 cycle/m), and 3.88 m (frequency: 0.258

cycle/m) in the gamma-ray-log data. The shorter of these two cycles is consistent with the 4 m to 5 m cycle identified in the XRF data for Ca and K.

Moving-window cross-correlation of pairs of elemental records was used to identify intervals of positive correlation and anti-correlation ("mwCor" function; Meyers 2014). While the moving-window cross-correlation results for most pairs of elements were consistent with their overall correlation coefficient, Si and K showed punctuated intervals of anti-correlation in the moving-window cross correlation despite an overall positive Pearson correlation coefficient (0.48) (**Figure 10**, **Table 5**). These zones of Si and K anti-correlation include the section of core studied at high resolution using micro-XRF and XRF, where we observed this anti-correlation at the millimeter and centimeter scale (**Figure 5**, Supplement A21), but also encompass other parts of the core (**Figure 10**). Comparing the moving-window cross-correlation coefficient to the XRF record for K, we observe that anti-correlation events are largely associated with the low-weight-percent phase of the ~ 4 m oscillation in K (**Figure 10**). MTM analysis of these K-Si moving-window cross-correlation results calculated using a range of window sizes (50 mm to 0.5 m) supports this observation, identifying an ~ 4.8 m cyclicity and strong variance concentrated at low frequencies (Supplement A21).

Discussion

Spectral analysis of XRF and micro-XRF data reveals multiple scales of cyclicity expressed in various proxy elements, suggesting that different earth system processes are exerting a control on cyclicity at disparate time scales (**Figure 11**). Meter-scale cycles are interpreted to reflect the impact of precession-scale change on the flux of allogenic (siliciclastic) vs. autogenic (carbonate) sediment. Centimeter- to millimeter-scale cycles are inferred to be

related to decoupling of biogenic silica from the silicate flux and appear to be related to the phase of precession. Sub-millimeter laminae are interpreted to mainly record seasonal change in redox state.

Precessional to Sub-Precessional Modulation of Carbonate vs. Siliciclastic Sedimentation

In the XRF data, we observed oscillations in elemental composition at the multi-meter scale for K, Ca, Si, and S (**Figures 4, 8**), which we infer to be related to alternations in carbonate versus silicate fluxes into Early Eocene Lake Uinta. Of the cycles identified through spectral analysis, a 4-5 m cycle in both K and Ca is particularly well defined (**Figures 4, 8**). Radioisotopically constrained estimates of net annual accumulation rates place the nominal net annual accumulation rate at 168 μm/year, suggesting that each of these ~ 4 m cycles represent approximately 23,000 years. Based on lamina counting (Bradley 1929) and on analysis of well-log and Fischer-assay data (Cole 1998; Machlus et al. 2008; Meyers 2008; Machlus et al. 2015), Green River Formation cycles in the Parachute Creek Member of Colorado and Wilkins Peak Member of Wyoming on the order of 3-5 m have been linked to 21-23 ky precessional periods. In the "Upper R-6" interval of the Parachute Creek Member studied here, we propose that precession paced a two-component, anti-phased oscillation between autogenic (carbonate dominated) and allogenic (silicate dominated) facies, as reflected in the relative abundances of K and Ca. These facies alternations could result from the influence of precession on the hydrologic system and on productivity, which governed precipitation, sediment, and biological-matter input into the paleo-lake.

Given a nominal 168 μm/year net accumulation rate, the 1 m cyclicity observed in S and the 2 m cyclicity observed in K and Ca may represent sub-precessional cyclicity on the order of 6 ky and 12 ky, respectively. The scale of S cyclicity appears to correspond to the ~ 1 m and ~ 2

m scale dark to light color alternations visible in this core section, most easily observed in the grayscale data (**Figure 4**). Sub-precessional depositional cycles have previously been noted in the Wilkins Peak Member of the Green River Formation in Wyoming (Pietras et al. 2003; Machlus et al. 2008), but the mechanism for their formation remains unclear. Pietras et al. (2003) suggested that this sub-Milankovitch cyclicity may be related to either depositional system auto-cyclicity connected to regional tectonic and geomorphic controls on drainage network stability or nonlinear climate responses to astronomical forcing. Machlus et al. (2008) declined to attribute the identified sub-Milankovitch cyclicity to a particular source, citing ambiguities in their temporal model which do not permit precise characterization of these cycles.

In the case of S, commonly interpreted to be a redox-sensitive element (e.g., Sageman and Lyons, 2003; Sluijs et al. 2008), this sub-precessional cyclicity likely reflects changes in lake-bottom oxygenation. The enrichment of organic matter and pyrite in the S rich intervals of the core likewise suggests lake-bottom anoxia and reducing conditions, which enhanced organic-matter preservation and allowed the formation of pyrite. Additionally, the observation that these S-rich intervals are often coincident with intervals of enhanced Si and K input suggests a silicate-redox connection in the paleo-lake (**Figure 4**). Explanations for this association include an increase in nutrient flux from rivers during times of increased silicate input, a reduction in the production of carbonates leading to diminished organic-matter dilution, or an enhancement of organic-matter preservation as the result of ectogenic meromixis, in which the addition of freshwater to the surface waters of the lake acts to strengthen stratification (e.g., Horsfield et al. 1994).

Multi-Decadal to Millennial Decoupling of Siliciclastic vs. Biogenic Silica Input

While XRF data showed that Si and K typically co-vary with changing silicate mineral content (**Table 5**), application of a moving-window cross correlation (window size: 0.1 m) to these two elements identified intervals of clear centimeter-scale anti-correlation in the 9.2 m study section (**Figure 10**). These intervals of anti-correlation are clustered principally in the low K phase of the 4 m oscillation observed in K (**Figure 10**). Based on micro-XRF results of this study, this decoupling of Si from other elements associated with siliciclastic influx occurs all the way down to the millimeter to centimeter scale, which temporally equates to multidecadal to millennial cyclicity based on our time-series models (**Figures 6, 7**).

This decoupling may reflect input from one of several Si sources. One source of this additional Si could be ash or volcaniclastic material, but this is unlikely given that the "Upper R-6" zone in the Skyline 16 core is sparsely populated with tephra (Vanden Berg and Birgenheier 2016). Additionally, detailed examination of the study interval and comparison with XRF spectra for individual measurements across these decoupling events suggest that they generally are not related to tuffs or reworked volcanic detritus.

Biological productivity is a second potential source of non-detrital Si in lake systems. In the fossil record of the Green River Formation, however, there is a dearth of preserved siliceous remains. Diatoms, the most common siliceous lacustrine organisms in many modern and ancient lakes, have not yet been identified in the Green River Formation, and previous studies suggest that these organisms may not have proliferated in lakes in western North America until later in the Eocene (Lohman and Andrews 1968; Krebs 1994, Bradbury and Krebs 1995; Mustoe 2005; Wolfe et al. 2006). A biological source of non-detrital Si cannot be definitively ruled out, however. Laboratory experiments and studies of Pleistocene and Holocene saline lakes show that diatom preservation may be reduced in alkaline, saline lake waters (Barker et al. 1994; Ryves et

al., 2006; Flower and Ryves 2009; Riemer et al. 2009; North et al. 2018). It is therefore possible that the non-detrital silica we observe could represent the recrystallization of silica from dissolved diatoms.

An authigenic source of Si, however, may also account for non-detrital Si. While silica is more soluble at high pH (Knauss and Wolery, 1988; Dove and Rimstidt, 1994; Crundwell, 2014), a lower-pH environment may allow dissolved silica to recrystallize. In Lake Uinta, pore space near the sediment-water interface could be more restricted, permitting less alkaline conditions than the main body of the lake. Organic-matter decomposition could provide a mechanism for lowering the pH in the pore space of the sediment, thus providing more favorable conditions for the precipitation of authigenic silica. If organic-matter decomposition is driving the changes in pore-water chemistry that periodically enhance authigenic Si deposition, we infer that this signal principally reflects productivity levels in the lake.

The close association of millimeter- to centimeter-scale Si decoupling events with the silicate-poor, carbonate-rich phase of the ~ 4 m proposed precession cycle (**Figure 10**) suggests that precessional forcing influenced the timing and expression of these shorter-term cycles. Stimulation of short-lived episodes of enhanced productivity in Lake Uinta through precessional forcing is one mechanism that could generate the authigenic or biogenic silica that appears to drive these decoupling events.

Annual Redox Fluctuation

Spectral analysis of the temporally calibrated records of Ca, K, and Si show high concentrations of power at frequencies of less than 0.07 cycle/year (Period: ≥ 14 years) (**Figures 6,7**), suggesting that carbonate and silicate deposition evolved with a multidecadal- to precessional-scale cyclicity (**Figures. 6, 7, 8**). In contrast, low concentrations of spectral power

are observed at frequencies greater than 0.07 cycles/year (periods: ≤ 14 years) (**Figure 6**). Therefore, our results in the "Upper R-6" zone of the Parachute Creek Member do not support previous studies that interpreted a strong ENSO and sunspot forcing of Green River Formation laminites.

Additionally, despite the apparent lamina-scale variations in Fe and S intensity, no strong concentration of variance was observed at an annual periodicity in MTM and LOWSPEC results across the range of Fe and S time models (Supplements A16, A17). There are several plausible explanations for the absence of an annual signal in the spectral results. First, it is possible that variable sedimentation rates in the study section are not fully captured in the constant-sedimentation-rate modeling methodology. This mismatch, which preferentially influences the high frequencies, could cause the variance associated with an annual signal to be smeared across a broad range of frequencies rather than concentrated in a narrow band of frequencies. Alternatively, it is possible that the formation of these laminae is not strictly annual, and is instead connected to irregular earth-systems processes acting on subannual to interannual timescales. Additionally, it is possible that at least some of these laminae have no connection to climate if they represent the distal deposits of turbidites, which can form thin couplets that look like varves (Ludlam 1969; Johnson et al. 2018). No obvious graded bedding or turbidite-related sedimentary structures appear in the "Upper R-6" zone study interval, and the expanded lake intervals of the Green River Formation, such as the Mahogany zone, appear to contain fewer visible sediment gravity flows (Johnson et al. 2018). However, this does not preclude the presence of finer turbidite deposits in these laminated oil shales (Johnson et al. 2018).

To provide a possible climatic mechanism for the formation of these fine-scale laminae, we propose a depositional model which calls upon changes in lake stratification as a driver for

cyclic anoxia of Lake Uinta's bottom waters. For much of the deposition of the Parachute Creek Member, Lake Uinta was likely salinity stratified, with a more dense, saline monimolimnion underlying a fresher epilimnion (Smith and Lee, 1982; Johnson et al. 2018). A lack of freshwater fish and mollusk fossils in the "Upper R-6" zone strengthens the evidence that the lake waters were saline in composition during its deposition (Vanden Berg and Birgenheier 2016). Variations in this salinity could serve as a mechanism for changes in the strength of stratification in the lake. We envision that these lamina couplets were produced on subannual to interannual timescales, with their formation strongly driven by processes of evaporation and water input acting on the lake. These combined evaporation and water-input factors influenced the strength of stratification, the positioning of the chemocline in the water column, and the depth and extent of the lake (**Figure 12**). These processes have a strong seasonal influence, but irregular variations in evaporation and water input in a season due to natural variations in climate could potentially generate subseasonal to interannual lamina.

In the summer, Lake Uinta would have generally experienced stronger evaporative processes and reduced water input into the lake basin from its catchment area, leading to a shallowing and shrinking of the lake. The increased overall salinity of the lake resulting from this downsizing would have acted to weaken salinity stratification, allowing the depth of Lake Uinta's chemocline to rise in response to enhanced mixing (**Figure 12**). With more of the lake bottom's area falling below the chemocline during this seasonal configuration, organic-rich sediments were more likely to be preserved due to the reduced amount of oxygen present below the chemocline. Therefore, we infer that the darker, more organic- and S-enriched lamina were formed under these conditions.

During the winter season, evaporation processes were likely weaker due to cooler temperatures, and Early Eocene regional coupled climate models suggest enhanced precipitation input to the Green River Formation basins from Pacific storms (Sewall and Sloan 2006). While some mixing would have occurred, the addition of this fresh water input into the surface waters of the saline lake would have strengthened lake stratification, increasing the density contrast between the now fresher epilimnion and the underlying monimolimnion. This stronger density gradient would have acted to reduce lake overturning and deepen the chemocline of the lake (**Figure 12**). During these winter months, we infer that the lighter-colored, more carbonate- and iron-rich laminae were formed in these more oxygenated, less saline waters through precipitation as Ca-, Mg-, and Fe-rich riverine input mixed with alkaline lake waters. The low permeability of the carbonate muds that make up these laminated oil shales and carbonate mudstone facies may have been one factor that aided in the continued preservation of the underlying more organic-rich lamina.

It is important to note that the model we propose is based on our analysis of the "Upper R-6" zone, which was deposited as Lake Uinta was reaching its maximum extent in the Early Eocene. This model may have utility in understanding Green River Formation laminites which formed under similar paleo-environmental conditions; however, caution must be exercised when applying this model to deposits from more restricted periods of Lake Uinta, when marginal shelves were more prominent due to lower lake levels and sediment gravity flows and other mass-transport processes exerted a stronger influence on deposition (Johnson et al. 2018).

Conclusions

In this study, the application of XRF and micro-XRF techniques, in combination with available radioisotopic ages, provides the opportunity to evaluate an interval of the well-studied Green River Formation oil shale with a new level of detail. This fresh perspective permits the testing of long-proposed forcing hypotheses, of the paleo-environmental significance of sedimentary rhythms, and of potential linkages between high- and low-frequency forcing.

At the finest scale, laminae in the "Upper R-6" zone of the Parachute Creek Member are most strongly associated with changes in lake redox state, reflecting variations in Fe and S that are consistent with annual stratification of the lake and changes in the depth of the lake chemocline. In contrast, variations in deposition of silicate and carbonate appear to be dominated by interdecadal to millennial rhythms, suggesting changes in precipitation and sediment delivery to the paleo-lake (**Figure 11**). While no strong support was found for ENSO or sunspot-scale cyclicity in this "Upper R-6" zone record, new evidence for a redox-driven origin for laminae provides key insights into the seasonal dynamics of this paleo-lake during the EECO greenhouse climate.

Additionally, punctuated intervals of non-detrital Si deposition with an interdecadal to millennial rhythmicity were identified in micro-XRF and XRF data (**Figure 11**). Based on the lack of evidence for a direct biogenic, volcanogenic, or siliciclastic source, this non-detrital Si is thought to be authigenic in origin and connected to changes in pore-water chemistry resulting from organic-matter decomposition. This decomposition followed conditions of enhanced productivity in the early Eocene paleo-lake.

We observed, at the meter scale, an antithetic relationship between carbonate and silicate components of the Skyline 16 core, alternating at a scale consistent with the astronomical cycle of precession (**Figures 4, 11**). Intervals of non-detrital Si deposition, such as the one identified

in our high-resolution scan, appear to most strongly align with one phase of this proposed precession beat (**Figures 10, 11**), illustrating how a long-term astronomical cycle manifested in the form of much shorter interdecadal to millennial scale cyclicity.

Acknowledgements

We thank M.E. Smith, B.S. Singer, D.C. Kelly, and Z. Liu for their discussions over the course of this project. This paper benefited from helpful feedback from L.A. Hinnov, R.C. Johnson, B.B. Bowen, and J.B. Southard. Additionally, we would like to thank the Utah Geological Survey and the University of Utah's Institute for Clean and Secure Energy for access to the Skyline 16 core. This study received financial support from the National Science Foundation Faculty Early Career Development Program (NSF-EAR 1151438), the National Science Foundation Integrated Earth Systems Program (NSF-EAR 1813278), the Geological Society of America Graduate Student Research Grant program, BP America Inc., and the Department of Geoscience at the University of Wisconsin-Madison.

References Cited

Abbott, W., 1957, Tertiary of the Uinta Basin: Guidebook to the geology of the Uinta Basin: Intermountain Association of Petroleum Geologists, Eighth Annual Field Conference, p. 102–109.

Aswasereelert, W., Meyers, S.R., Carroll, A.R., Peters, S.E., Smith, M.E., and Feigl, K.L., 2013, Basin-scale cyclostratigraphy of the Green River Formation, Wyoming: Geological Society of America Bulletin, v. 125, p. 216-228.

Barker, P., Fontes, J.C., and Gasse, F., 1994, Experimental dissolution of diatom silica in concentrated salt solutions and implications for paleoenvironmental reconstruction: Limnology and Oceanography, v. 39, p. 99–110.

Birgenheier, L.P., and Vanden Berg, M.D., 2011, Core-based integrated sedimentologic, stratigraphic, and geochemical analysis of the oil shale bearing Green River Formation, Uinta Basin, Utah: Topical Report submitted to the U.S. Department of Energy, Natural Energy Laboratory, DE-FE0001243.

Birgenheier, L.P., Vanden Berg, M.D., Plink-Björklund, P., Gall, R.D., Rosencrans, E., Rosenberg, M.J., Toms, L.C., and Morris, J., 2019, Climate impact on fluvial-lake system evolution, Eocene Green River Formation, Uinta Basin, Utah, USA: Geological Society of America Bulletin, v. 132, p. 562-587.

Bradbury, J.P., and Krebs, W.N., 1995, Fossil Continental Diatoms: Paleolimnology, Evolution, and Biochronology, *in* Blome, C.D. et al., Siliceous Microfossils: The Paleontological Society, Short Courses in Paleontology, v. 8, p. 119–138.

Bradley, W.H., 1929, The Varves and Climate of the Green River Epoch: U.S. Geological Survey, Professional Paper 496A, 110 p.

Bradley, W.H., and Eugster, H.P.,1969, Geochemistry and paleolimnology of the trona deposits and associated authigenic minerals of the Green River Formation of Wyoming: U.S. Geological Survey, Professional Paper 496-B, 71 p.

Carroll, A.R., and Bohacs, K.M., 1999, Stratigraphic classification of ancient lakes: Balancing tectonic and climatic controls: Geology, v. 27, p. 99–102.

Cashion, W.B., 1995, Stratigraphy of the Green River Formation, eastern Uinta Basin, Utah and Colorado, *in* Averett, M.R., ed., The Green River Formation in Piceance Creek and eastern Uinta Basins: Grand Junction Geological Society, 1995 Field Trip Guidebook, p. 15–21.

Cashion, W.B., and Donnell, J.R., 1972, Chart showing correlation of selected key units in the organic-rich sequence of the Green River Formation, Piceance Creek basin, Colorado, and Uinta Basin, Utah: U.S. Geological Survey, Oil and Gas Investigation Chart Report 65.

Cole, R., 1998, Possible Milankovitch cycles in the Lower Parachute Creek Member of the Green River Formation (Eocene), North-Central Piceance Creek Basin, Colorado: An analysis, *in* Pitman, J., and Carroll, A., eds., Modern and Ancient Lake Systems: Utah Geological Association, Guidebook 26, p. 233-259.

Coney, P.J., and Reynolds, S.J., 1977, Cordilleran Benioff zones: Nature, v. 270, p. 403.

Crowley, K.D., Duchon, C.E., and Rhi, J., 1986, Climate record in varved sediments of the Eocene Green River Formation: Journal of Geophysical Research, v. 91, p. 8637-8647.

Crundwell, F.K., 2014, The mechanism of dissolution of minerals in acidic and alkaline solutions: Part II Application of a new theory to silicates, aluminosilicates and quartz: Hydrometallurgy, v. 149, p. 265–275.

Davis, S.J., Wiegand, B.A., Carroll, A.R., and Chamberlain, C.P., 2008, The effect of drainage reorganization on paleoaltimetry studies: An example from the Paleogene Laramide foreland: Earth and Planetary Science Letters, v. 275, p. 258–268.

Davis, S.J., Mulch, A., Carroll, A.R., Horton, T.W., and Chamberlain, C.P., 2009, Paleogene landscape evolution of the central North American Cordillera: Developing topography and hydrology in the Laramide foreland: Geological Society of America, Bulletin, v. 121, p. 100–116.

Dickinson, W.R., and Snyder, W.S., 1978, Plate tectonics of the Laramide orogeny, *in* Matthews, V., III, ed., Laramide folding associated with basement block faulting in the western United States: Geological Society of America, Memoir 151, p. 355–366.

Dickinson, W.R., Klute, M.A., Hayes, M.J., Janecke, S.U., Lundin, E.R., McKittrick, M.A., and Olivares, M.D., 1988, Paleogeographic and paleotectonic setting of Laramide sedimentary basins in the central Rocky Mountain region: Geological Society of America, Bulletin, v. 100, p. 1023–1039.

Donnell, J.R., and Blair, R.W.J., 1970, Resource appraisal of three rich oil-shale zones in the Green River Formation, Piceance Creek Basin, Colorado: Colorado. School of Mines Quarterly, v. 65, no. 4, p. 73-87.

Dove, P.M., and Rimstidt, J.D., 1994, Silica-water interactions, *in* Heaney, P.J., ed., Silica: Physical Behavior, Geochemistry and Materials Applications: Mineralogical Society of America, Reviews in Mineralogy, v. 29, 606 p.

Dyni, J.R., 1976, Trioctahedral Smectite in the Green River Formation, Duchesne County, Utah: U.S. Geological Survey, Professional Paper 967, 14 p.

Fischer, A.G., and Roberts, L.T., 1991, Cyclicity in the Green River Formation (lacustrine Eocene) of Wyoming: Journal of Sedimentary Petrology, v. 61, p. 1146-1154.

Flower, R.J., and Ryves, D.B., 2009, Diatom preservation: differential preservation of sedimentary diatoms in two saline lakes: Acta Botanica Croatica, v. 68, p. 381–399.

Glenn, C.R., and Kelts, K., 1991, Sedimentary rhythms in lake deposits, *in* Einsele, G., Ricken, W., and Seilacher, A., eds., Cycles and Events in Stratigraphy: New York, Springer-Verlag, p. 188-221.

Horsfield, B., Curry, D.J., Bohacs, K., Littke, R., Rullkötter, J., Shenk, H.J., Radke, M., Schaefer, R.G., Carroll., A.R., Isaksen, G., and Witte, E.G., 1994, Organic geochemistry of freshwater and alkaline lacustrine sediments in the Green River Formation of the Washakie Basin, Wyoming, USA: Organic Geochemistry, v. 22, p. 415–440.

Hosterman, J.W., and Dyni, J.R., 1972, Clay mineralogy of the Green River Formation, Piceance Creek Basin-A preliminary study: U.S. Geological Survey, Research 1972, Professional. Paper 800-D, p. D159-D163.

Johnson, R.C., 1984, New Names for Units in the Lower Part of the Green River Formation, Piceance Creek Basin, Colorado: U.S. Geological Survey, Bulletin, v. 1529, 26 p.

Johnson, R.C., 1985, Early Cenozoic History of the Uinta and Piceance Creek Basins, Utah and Colorado, with Special Reference to the Development of Eocene Lake Uinta, *in* Flores, R.M, and Kaplan, S.S., eds., Cenozoic Paleogeography of Western United States: SEPM, Rocky Mountain Section, Denver, p. 247–276.

Johnson, R.C., and Brownfield, M.E., 2015, Development, evolution, and destruction of the saline mineral area of Eocene Lake Uinta, Piceance Basin, western Colorado: U.S. Geological Survey, Scientific Investigations Report, Numbered Series 2013–5176, 87 p.

Johnson, R.C., Birdwell, J.E., and Mercier, T., 2018, Controls on organic matter distributions in Eocene Lake Uinta, Utah and Colorado: The Mountain Geologist, v. 55, p. 177–216.

Johnson, R.C., Birdwell, J.E., Brownfield, M.E., Mercier, T.J., and Hansley, P.L., 2019, Connections between Eocene Lakes Uinta and Gosiute with emphasis on the infilling stage of Lake Uinta in Piceance Basin: The Mountain Geologist, v. 56, p. 143–183.

Johnson, T.C., 1984, Sedimentation in Large Lakes: Annual Review of Earth and Planetary Sciences, v. 12, p. 179-204.

Knauss, K.G., and Wolery, T.J., 1988, The dissolution kinetics of quartz as a function of pH and time at 70°C: Geochimica et Cosmochimica Acta, v. 52, p. 43–53

Krebs, W., 1994, The biochronology of freshwater planktonic diatom communities in western North America, *in* Kociolek, J.P., ed., Proceedings of the 11th International Diatom Symposium: California Academy of Sciences, San Francisco, p. 485–499.

Lohman, K.E., and Andrews, G.W., 1968, Late Eocene Nonmarine Diatoms from the Beaver Divide Area Fremont County, Wyoming: U.S. Geological Survey, Professional Paper 593E, 38 p.

Ludlam, S.D., 1969, Fayetteville Green Lake, New York. 3. the Laminated Sediments: Limnology and Oceanography, v. 14, p. 848–857.

Ma, C., Meyers, S.R., Sageman, B.B., Singer, B.S., and Jicha, B.R., 2014, Testing the astronomical time scale for oceanic anoxic event 2, and its extension into Cenomanian strata of the Western Interior Basin (USA): Geological Society of America, Bulletin, v. 126, p. 974–989.

Machlus, M.L, Olsen, P.E., Christie-Blick, N., and Hemming, S.R., 2008, Spectral analysis of the lower Eocene Wilkins Peak Member, Green River Formation, Wyoming: Support for Milankovitch cyclicity: Earth and Planetary Science Letters, v. 268, p. 64-75.

Machlus, M.L., Ramezani, J., Bowring, S.A., Hemming, S.R., Tsukui, K., and Clyde, W.C., 2015, A strategy for cross-calibrating U–Pb chronology and astrochronology of sedimentary sequences: An example from the Green River Formation, Wyoming, USA: Earth and Planetary Science Letters, v. 413, p. 70–78.

Meyers, S.R, 2008, Resolving Milankovitchian controversies: the Triassic Latemar Limestone and the Eocene Green River Formation: Geology, v. 36, p. 319-322.

Meyers, S.R., 2012, Seeing red in cyclic stratigraphy: Spectral noise estimation for astrochronology: Paleoceanography, v. 27, no. PA3228.

Meyers, S.R., 2014, Astrochron: An R Package for Astrochronology. https://cran.r-project.org/package=astrochron

Meyers, S.R., Sageman, B.B., and Hinnov, L.A., 2001, Integrated quantitative stratigraphy of the Cenomanian-Turonian Bridge Creek Limestone Member using evolutive harmonic analysis and stratigraphic modeling: Journal of Sedimentary Research, v. 71, p. 628–644.

Morgan, C.D., Chidsey, T.C., Jr., McClure, K.P., Bereskin, S.R., and Deo, M.D., 2003, Reservoir Characterization of the Lower Green River Formation, Uinta Basin, Utah: Utah Geological Survey, Open File Report 411, 142 p.

Mustoe, G.E., 2005, Diatomaceous origin of siliceous shale in Eocene lake beds of central British Columbia: Canadian Journal of Earth Sciences, v. 42, p. 231-241.

North, S.M., Stockhecke, M., Tomonaga, Y., and Mackay, A.W., 2018, Analysis of a fragmentary diatom record from Lake Van (Turkey) reveals substantial lake-level variability during previous interglacials MIS7 and MIS5e: Journal of Paleolimnology, v. 59, p. 119–133.

Picard, M.D. and High, L.R., 1972, Paleoenvironmental reconstructions in an area of rapid facies change, Parachute Creek Member of Green River Formation (Eocene), Uinta Basin, Utah, Geological Society of America, Bulletin, v. 83, no. 9, p. 2689–2708.

Pietras, J.T., Carroll, A.R., Singer, B.S., and Smith, M.E., 2003, 10 k.y. depositional cyclicity in the early Eocene: Stratigraphic and $^{40}Ar/^{39}Ar$ evidence from the lacustrine Green River Formation: Geology, v. 31, p. 593-596.

R Core Team, 2014, R: A language and environment for statistical computing: R Foundation for Statistical Computing, Vienna, Austria.

Reimer, A., Landmann, G., and Kempe, S., 2009, Lake Van, Eastern Anatolia, Hydrochemistry and History: Aquatic Geochemistry, v. 15, p. 195–222.

Remy, R.R., 1992, Stratigraphy of the Eocene part of the Green River Formation in the south-central part of the Uinta Basin, Utah: U.S. Geological Survey, Bulletin Report 1787BB.

Rhodes, M.K., Carroll, A.R., Pietras, J.T., Beard, B.L., and Johnson, C.M., 2002, Strontium isotope record of paleohydrology and continental weathering, Eocene Green River Formation, Wyoming: Geology, v. 30, p. 167–170.

Ripepe, M., Roberts, L.T., and Fischer, A.G., 1991, ENSO and sunspot cycles in varved Eocene oil shales from image analysis: Journal of Sedimentary Petrology, v. 61, p. 1155-1163.

Robb, W.A., and Smith, J.W., 1974, Mineral profile of the oil shales in Colorado Core Hole No. 1, Piceance Creek Basin, Colorado, *in* Murray, D. K., ed., Guidebook to the Energy Resources of the Piceance Creek Basin Colorado: Rocky Mountain Association of Geologists Twenty-Fifth Field Conference Guidebook, p. 91-100.

Rosenberg, M.J., Birgenheier, L., and Vanden Berg, M.D., 2015, Facies, Stratigraphic Architecture, and Lake Evolution of the Oil Shale Bearing Green River Formation, Eastern Uinta Basin, Utah, *in* Smith, M., and Carroll, A., eds., Stratigraphy and Paleolimnology of the Green River Formation, Western USA: Syntheses in Limnogeology, vol. 1: Springer, Dordrecht, p. 211–249.

Ryder, R.T., Fouch, T.D., and Elison, J.H., 1976, Early Tertiary sedimentation in the western Uinta Basin, Utah: Geological Society of America, Bulletin, v. 87, p. 496–512.

Ryves, D.B., Battarbee, R.W., Juggins, S., Fritz, S.C., and Anderson, N.J., 2006, Physical and chemical predictors of diatom dissolution in freshwater and saline lake sediments in North America and West Greenland: Limnology and Oceanography, v. 51, p. 1355–1368.

Sageman, B.B., and Hollander, D.J., 1999, Integration of paleoecological and geochemical proxies: a holistic approach to the study of past global change, *in* Johnson, C.J., and Barrera, E., eds., The Evolution of Cretaceous Ocean/Climate Systems: Geological Society of America, Special Paper 332, p. 365-384.

Sageman, B.B., and Lyons, T.W., 2003, Geochemistry of Fine-grained Sediments and Sedimentary Rocks, *in* Holland, H.D., and Turekian, K.K., eds., Treatise on Geochemistry: Oxford, Pergamon, p. 115–158.

Sayles, R.W., 1922, The dilemma of the paleoclimatologists: American Journal of Science, Series 5, v. 3, p. 458.

Sewall, J.O., and Sloan, L.C., 2006, Come a little bit closer: A high-resolution climate study of the early Paleogene Laramide foreland: Geology, v. 34, no. 2, p. 81–84.

Sheliga, C.M., 1980, Sedimentation of the Eocene Green River Formation in Sevier and Sanpete Counties, Utah [M.S. Thesis]: Columbus, The Ohio State University, 166 p.

Sluijs, A., Röhl, U., Schouten, S., Brumsack, H.-J., Sangiorgi, F., Damasté, J.S.S., and Brinkhuis, H., 2008, Arctic late Paleocene–early Eocene paleoenvironments with special emphasis on the Paleocene-Eocene thermal maximum (Lomonosov Ridge, Integrated Ocean Drilling Program Expedition 302): Paleoceanography, v. 23, PA1S11.

Smith, J.W., and Lee, K.K., 1982, Geochemistry and physical paleolimnology of Piceance Creek basin oil shales, *in* Gary, J.H., ed., 15th Oil Shale Symposium Proceedings: Colorado School of Mines Press, v. 15, p. 101–114.

Smith, M.E., Singer, B.S., and Carroll, A.R., 2003, $^{40}Ar/^{39}Ar$ geochronology of the Eocene Green River Formation, Wyoming: Geological Society of America, Bulletin, v. 115, p. 549–565.

Smith, M.E., Carroll, A.R., and Singer, B.S., 2008, Synoptic reconstruction of a major ancient lake system: Eocene Green River Formation, western United States: Geological Society of America, Bulletin, v. 120, p. 54-84.

Smith, M.E., Chamberlain, K.R., Singer, B.S., and Carroll, A.R., 2010, Eocene clocks agree: Coeval $^{40}Ar/^{39}Ar$, U-Pb, and astronomical ages from the Green River Formation, Geology, v. 38, no. 6, p. 527–530.

Smith, M.E., Carroll, A.R., Jicha, B.R., Cassel, E.J., and Scott, J.J., 2014, Paleogeographic record of Eocene Farallon slab rollback beneath western North America: Geology, v. 42, p. 1039–1042.

Smith, M.E., and Carroll, A.R., 2015, Introduction to the Green River Formation, *in* Smith, M., and Carroll, A., eds., Stratigraphy and Paleolimnology of the Green River Formation, Western USA: Syntheses in Limnogeology, vol. 1: Springer, Dordrecht, p. 1-12.

Surdam, R.C., and Stanley, K.O., 1980, Effects of changes in drainage-basin boundaries on sedimentation in Eocene Lakes Gosiute and Uinta of Wyoming, Utah, and Colorado: Geology, v. 8, p. 135–139.

Tänavsuu-Milkeviciene, K., and Sarg, J.F., 2012, Evolution of an organic-rich lake basin-stratigraphy, climate and tectonics: Piceance Creek basin, Eocene Green River Formation: Evolution of an organic-rich lake: Sedimentology, v. 59, p. 1735–1768.

Thomson, D.J., 1982, Spectrum estimation and harmonic analysis: Institute of Electrical and Electronics Engineers, Proceedings, v. 70, p. 1055–1096.

Vanden Berg, M.D., and Birgenheier, L.P., 2011. Not All Rich Zones Are Created Equal: Geologic Characterization Results Of Green River Formation Core Descriptions From Utah's Uinta Basin, Including The Newly Drilled Skyline 16 Core: 31st Oil Shale Symposium, Golden, CO, Oct. 17-19.

Vanden Berg, M.D., and Birgenheier, L.P., 2016, Evaluation of the Upper Green River Formation's Oil Shale Resource in the Uinta Basin, *in* Spinti, J.P, ed., Utah Oil Shale: Science, Technology, and Policy Perspectives: CRC Press, New York, p. 59-82.

Vanden Berg, M.D., and Birgenheier, L.P., 2017, An examination of the hypersaline phases of Eocene Lake Uinta, upper Green River Formation, Uinta Basin, Utah: Journal of Paleolimnology, v. 58, p. 353–371.

Washburn, K.E., Birdwell, J.E., Foster, M., Gutierrez, F., 2015, Detailed description of oil shale organic and mineralogical heterogeneity via Fourier transform infrared microscopy, Energy & Fuels, v. 29, p. 4264-4271.

Weiss, M.P., Witkind, I.J., and Cashion, W.B., 1990, Geologic map of the Price 30′ x 60′ quadrangle, Carbon, Duchesne, Uintah, Utah, and Wasatch Counties, Utah: U.S. Geological Survey, Miscellaneous Investigations Series, Map I-1981.

Witkind, I.J., 1995, Geologic map of the Price 1 degree by 2 degrees Quadrangle, Utah: U.S. Geological Miscellaneous Investigations Series, Map I-2462.

Wolfe, A.P., Edlund, M.B., Sweet, A.R., and Creighton, S.D., 2006, A first account of organelle preservation in Eocene nonmarine diatoms: Observations and paleobiological implications: Palaios, v. 21, p. 298-304.

Zachos, J.C., Pagani, M., Sloan, L., Thomas, E., and Billups, K., 2001, Trends, Rhythms, and Aberrations in Global Climate 65 Ma to Present: Science, v. 292, p. 686-693.

Zachos, J.C., Dickens, G.R., and Zeebe, R.E., 2008, An early Cenozoic perspective on greenhouse warming and carbon-cycle dynamics: Nature, v. 451, p. 279-283.

Figures and Tables

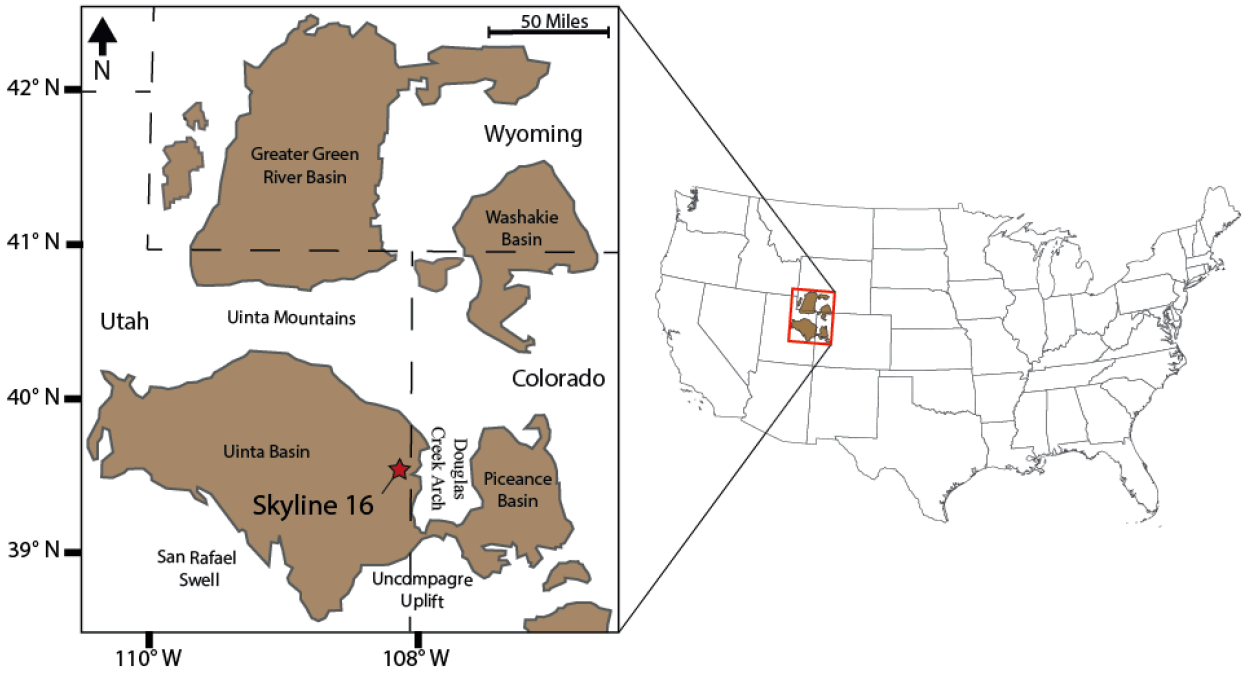

Figure 1: Location map of the Green River Formation of Wyoming, Utah, and Colorado. The brown shading represents areas where the Green River Formation is present in outcrop or in the subsurface. The location of the Skyline 16 core is marked by a red star (39° 52' 14.329" N, 109° 6' 44.212" W). Figure modified from Birgenheier and Vanden Berg (2011).

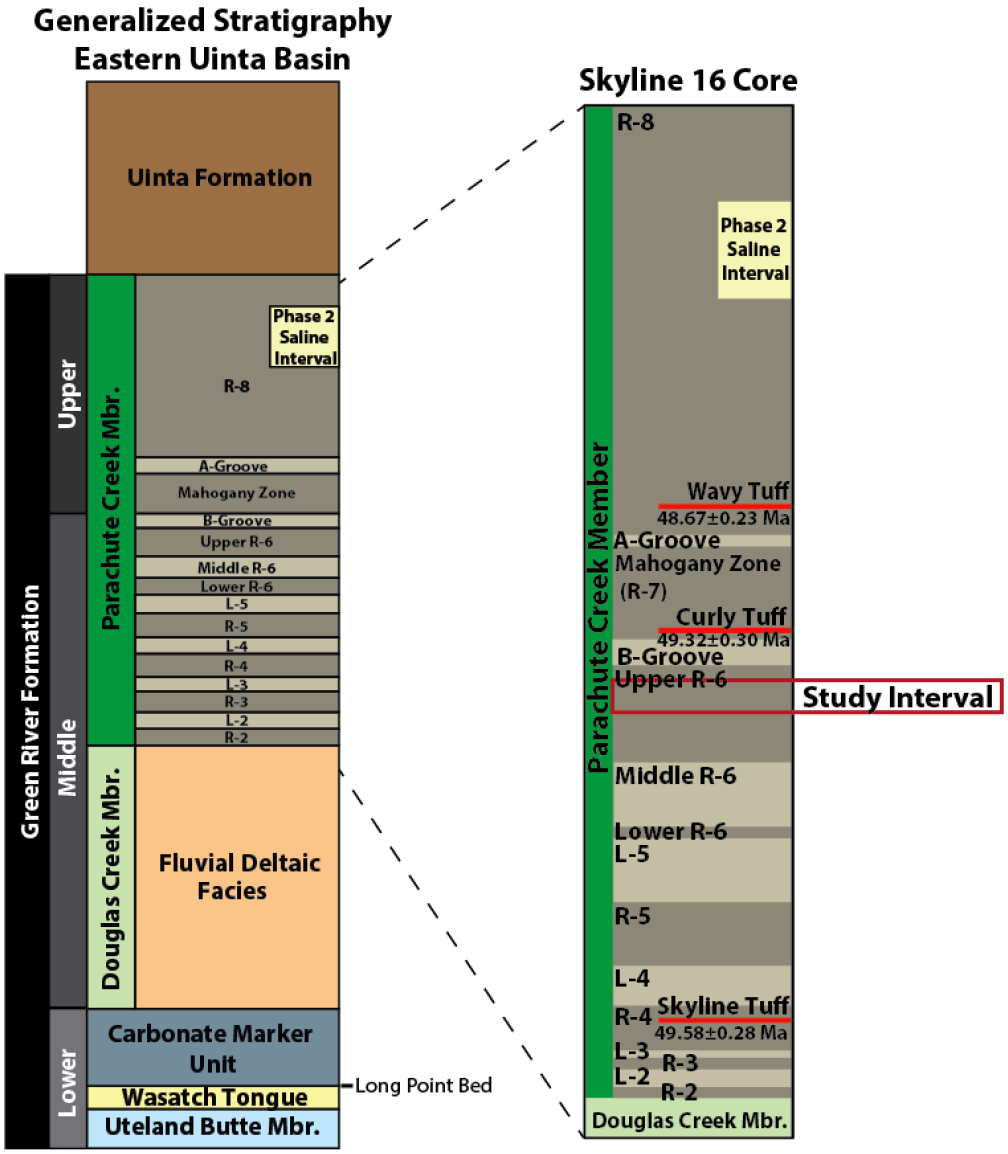

Figure 2: The stratigraphy of the Skyline 16 core in the context of the generalized stratigraphy for the Green River Formation in the eastern Uinta Basin. The study interval, marked within a red box, lies in the "Upper R-6" zone of the Parachute Creek Member of the Green River Formation at 170.6-179.8 m (560-590 ft) core depth. Modified from Vanden Berg and Birgenheier (2016), Vanden Berg and Birgenheier (2017), Johnson et al. (2018), and Birgenheier et al. (2019).

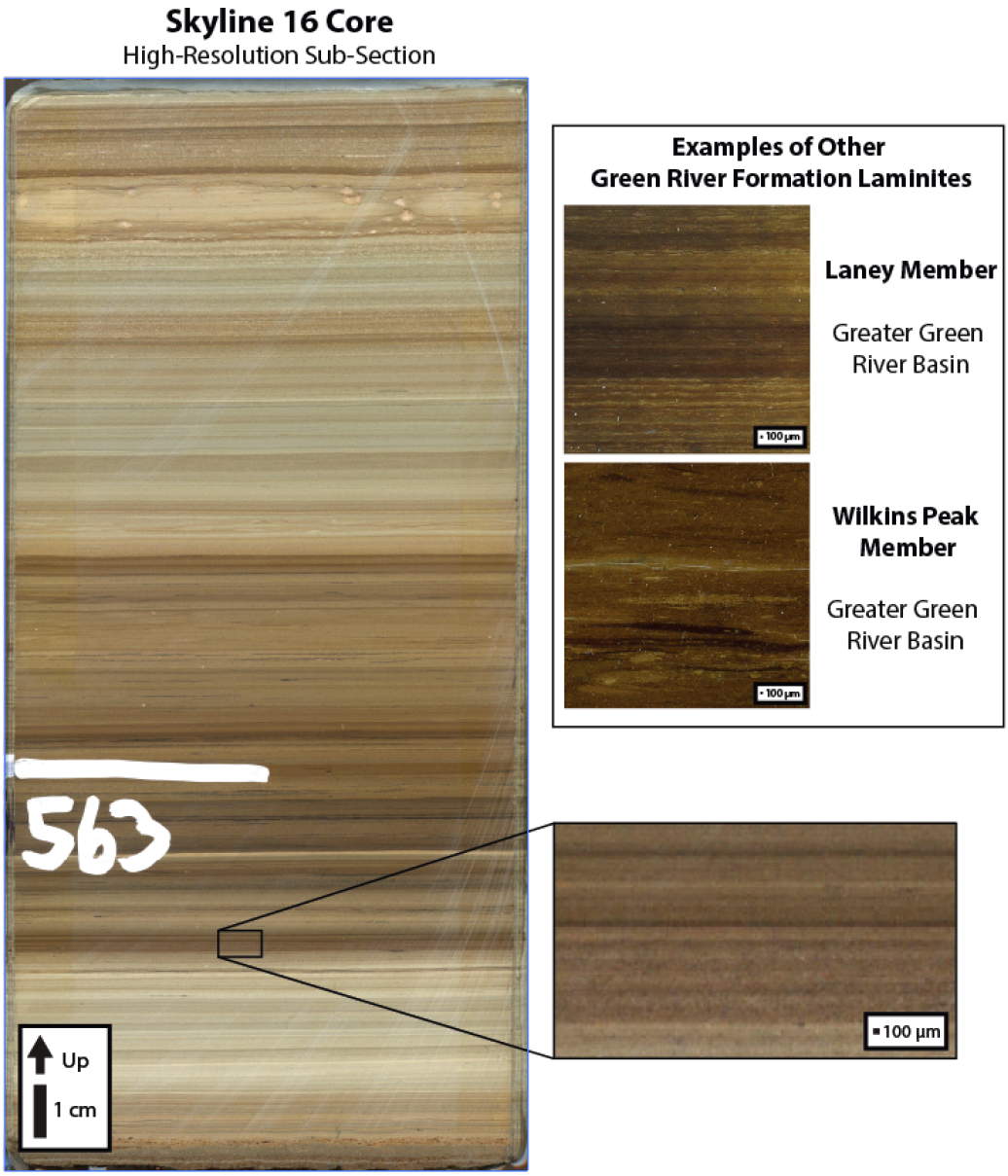

Figure 3: Laminated mudstone in the "Upper R-6" zone of the Parachute Creek Member of the Green River Formation captured in the Skyline 16 core. This interval was studied using the 100 micrometer capabilities of the Avaatech XRF core scanner and the 25 micrometer resolution capabilities of the Bruker M4 micro-XRF. Included for comparison are examples of laminites from the Laney Member (Arco Washakie Basin 1 Drill Core: Section 17 T14N R99W) and Wilkins Peak Members (Breathing Gulch Site: 41° 48.50′ N, 109° 17.64′ W) of the Green River Formation in Greater Green River Basin of Wyoming.

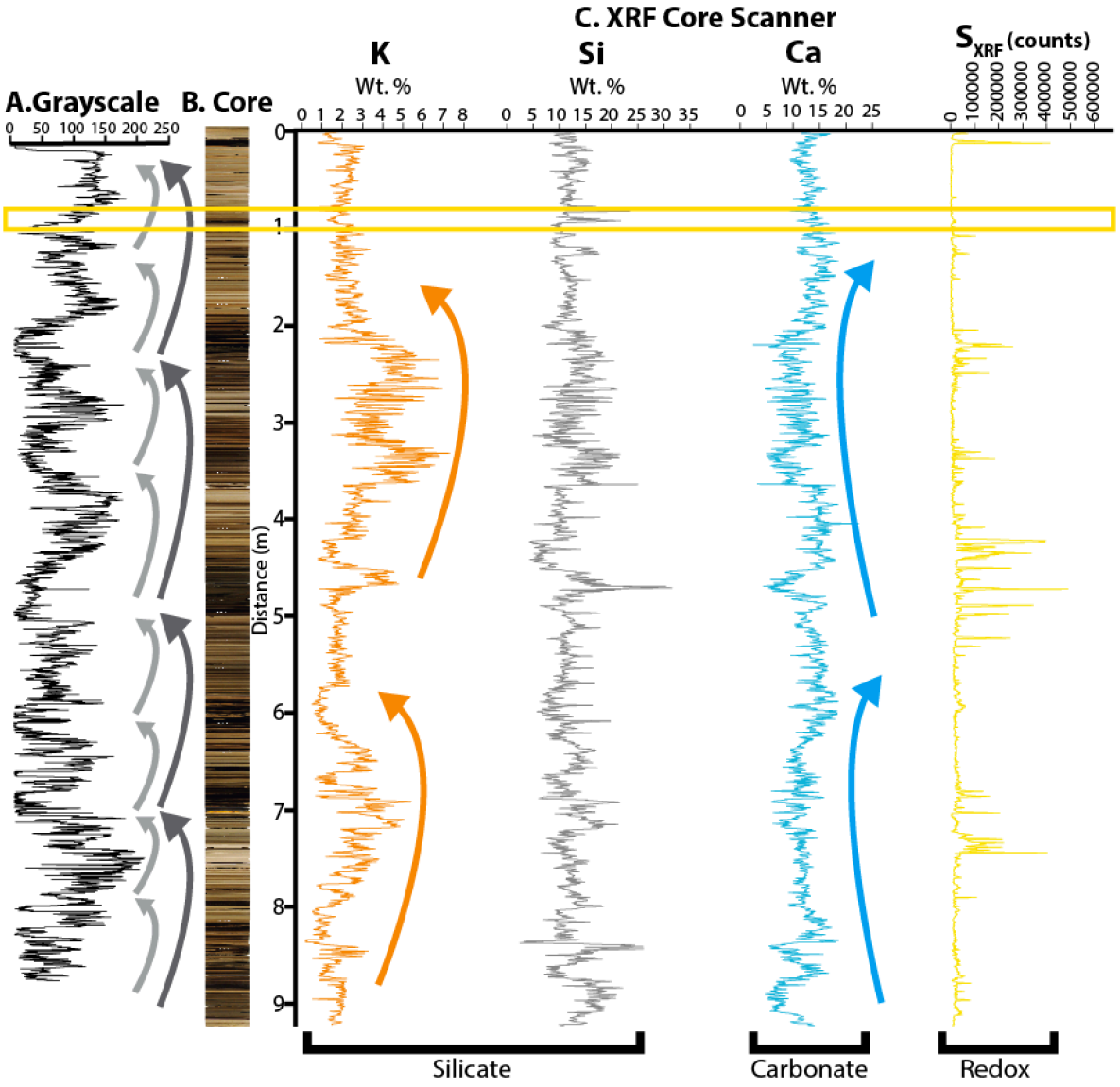

Figure 4: 5 mm Avaatech XRF core scanner data from the 170.6-179.8 m (560-590 ft) interval of the Skyline 16 core showing A) Grayscale values for the study interval, B) an image of the core interval, and C) selected silicate (K, Si), carbonate (Ca), and redox (S) proxy elements measured using the XRF core scanner. K, Si, and Ca elemental intensities have been converted to wt. % values through calibration with ICP-MS measurements. Arrows represent inferred cyclicity in the 5 mm core record, with the light gray arrows representing the ~ 1 m cycles in grayscale, the dark gray arrows representing the ~ 2 m cycles in grayscale, the orange arrows representing the ~ 4 m cycles in K and blue arrows representing the ~ 5 m cycles in Ca. The 202.6 mm interval studied at higher resolution is outlined in the yellow box.

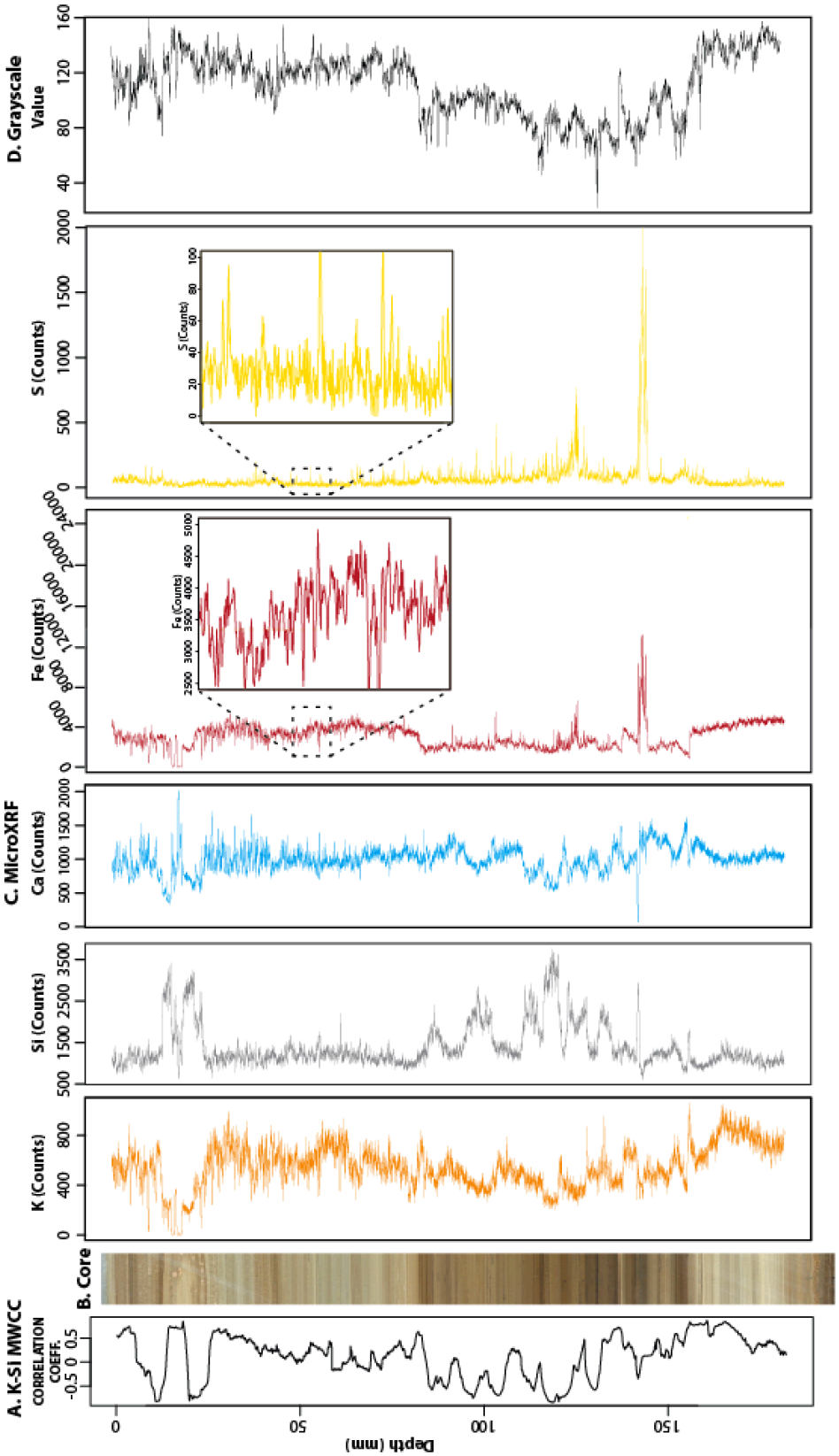

Figure 5: Micro-XRF results for the 202.6 mm sub-section of the study interval, showing A) the K-Si moving-window cross correlation (window size: 5 mm), B) an image of the study section, C) the micro-XRF results for K, Si, Ca, Fe, and S, and D) grayscale.

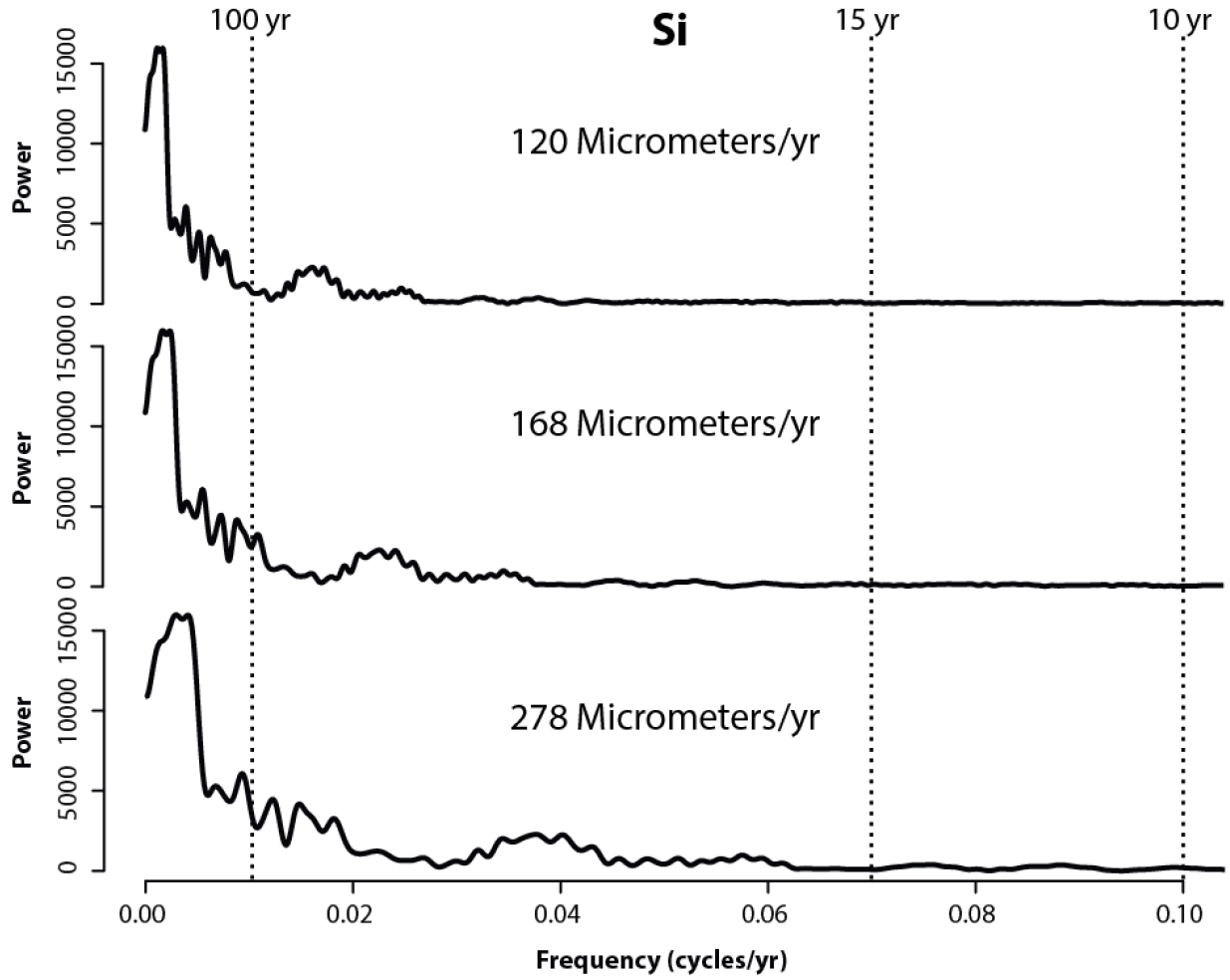

Figure 6: MTM results (3-2π DPSS tapers) for Si time models based on application of a constant minimum (120 μm/year), nominal (168 μm/year rate), and maximum (278 μm/year rate) net accumulation rate. Dashed vertical lines highlight approximate 100 year, 15 year, and 10 year periodicities based on the nominal 168 μm/year net accumulation rate.

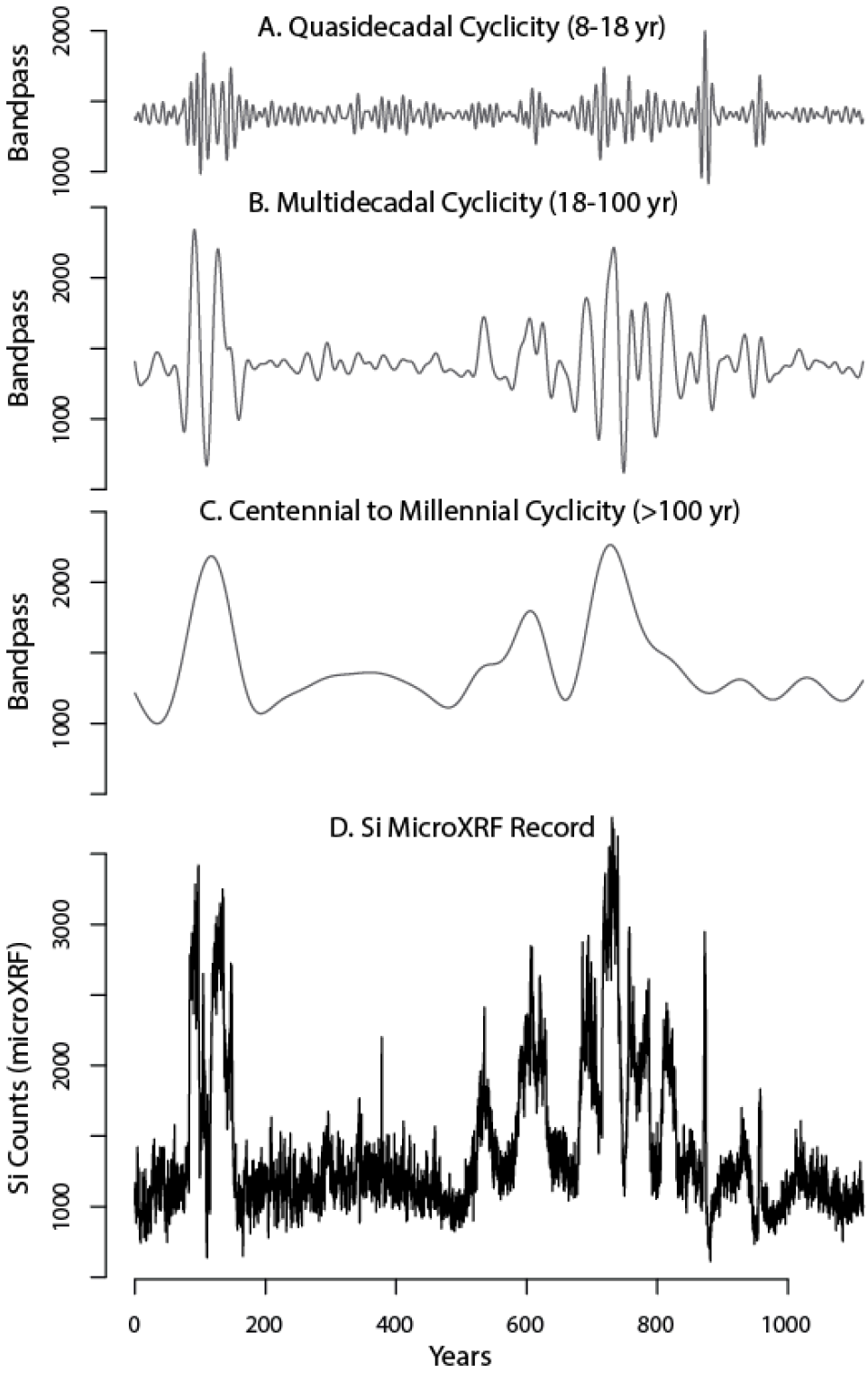

Figure 7: Taner bandpass filter of Si record of the constant sedimentation rate model using the nominal case (168 μm/year) net accumulation rate for time scale construction, showing (a) quasidecadal variability (8-18 years), (b) multidecadal variability (18-100 years), (c) centennial-to millennial-scale variability (> 100 years), and (d) micro-XRF results for Si for comparison.

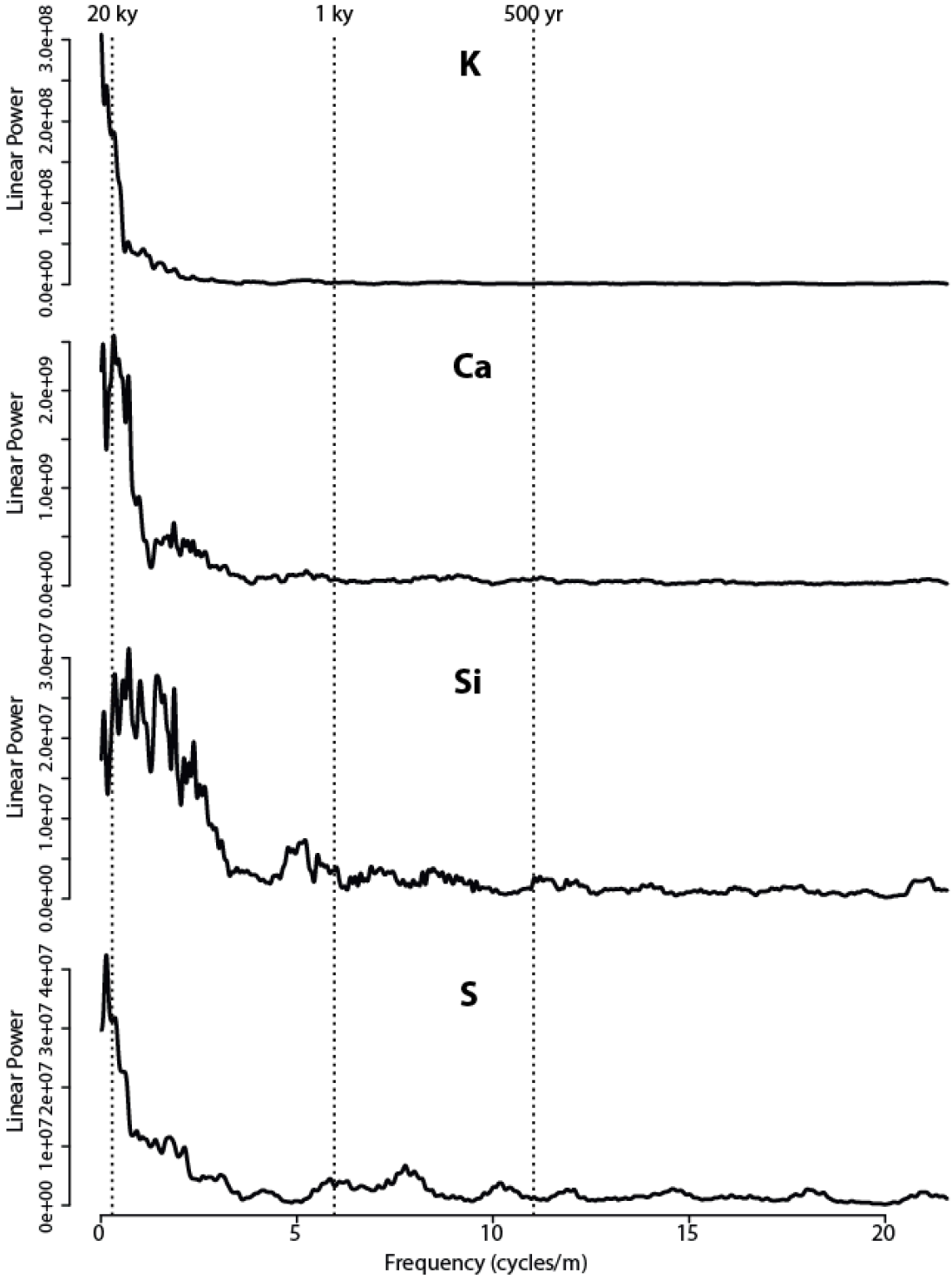

Figure 8: MTM power-spectra results (3-2π DPSS tapers) from 5 mm XRF core scanner data for K, Ca, Si, and S. Dashed vertical lines represent approximate 20 ky, 1 ky, and 500 year periodicities based on a 168 μm/year net accumulation rate.

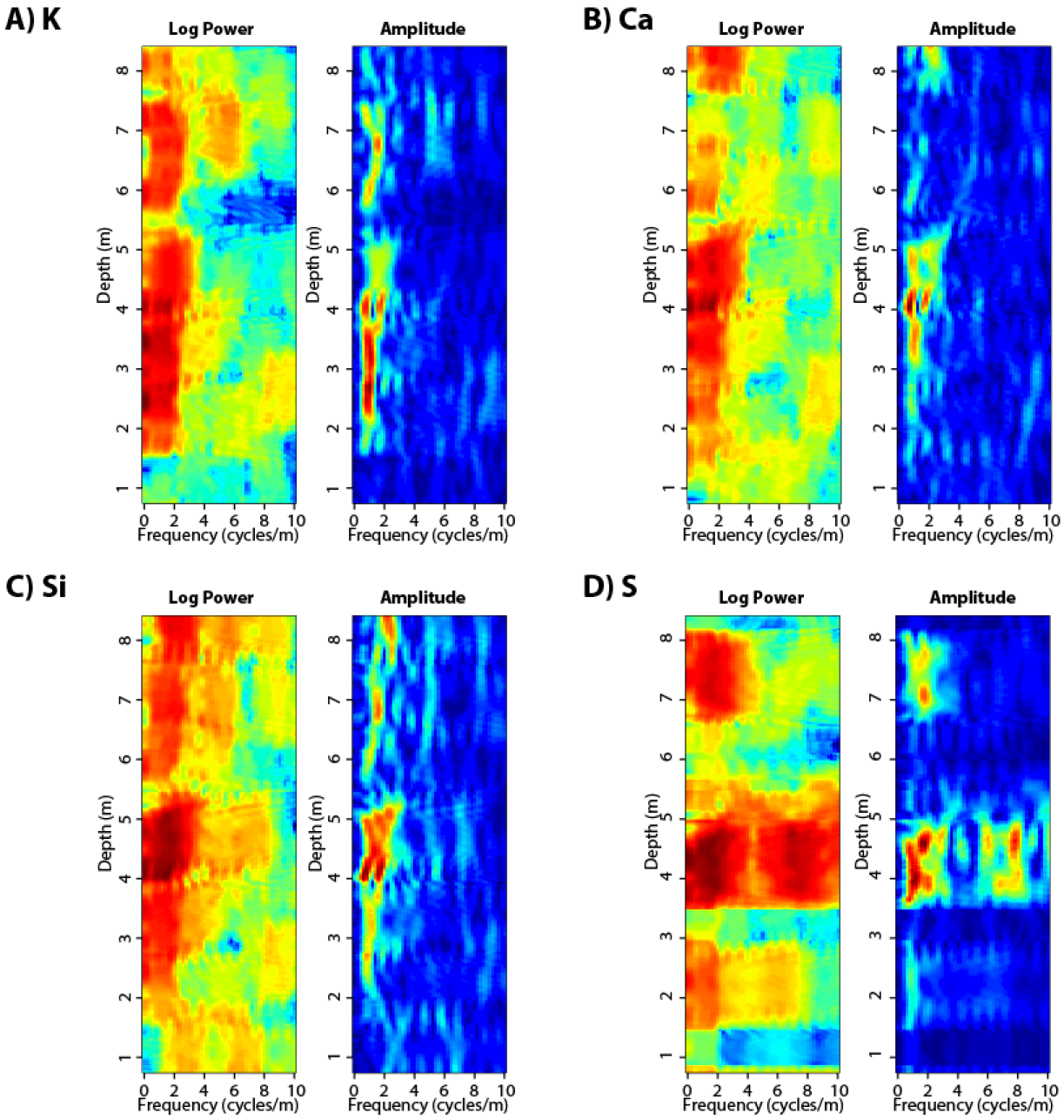

Figure 9: EHA plots (3-2π DPSS tapers; window size: 1.5 m) showing log power and amplitude for the 5 mm resolution XRF core scanner record of A) K, B) Ca, C) Si, and D) S.

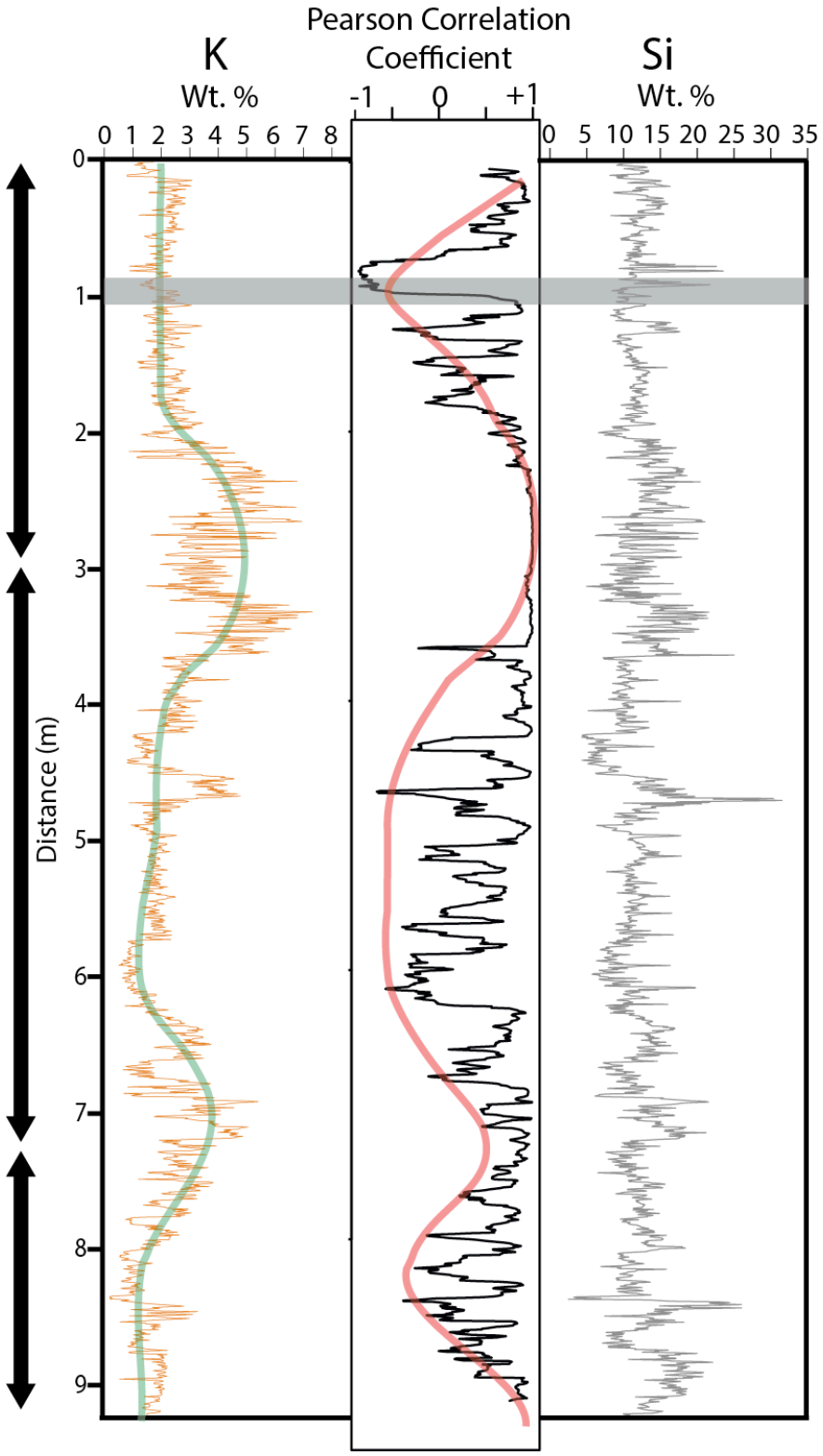

Figure 10: Moving-window cross correlation (window size: 0.1 m) of 5 mm resolution XRF core scanner data for K and Si showing the proposed precession beat in K (green line) and the approximate cycle of Si anti-correlation events from the silicate signal (red line). The gray shaded box highlights the interval selected for higher-resolution XRF and micro-XRF analysis.

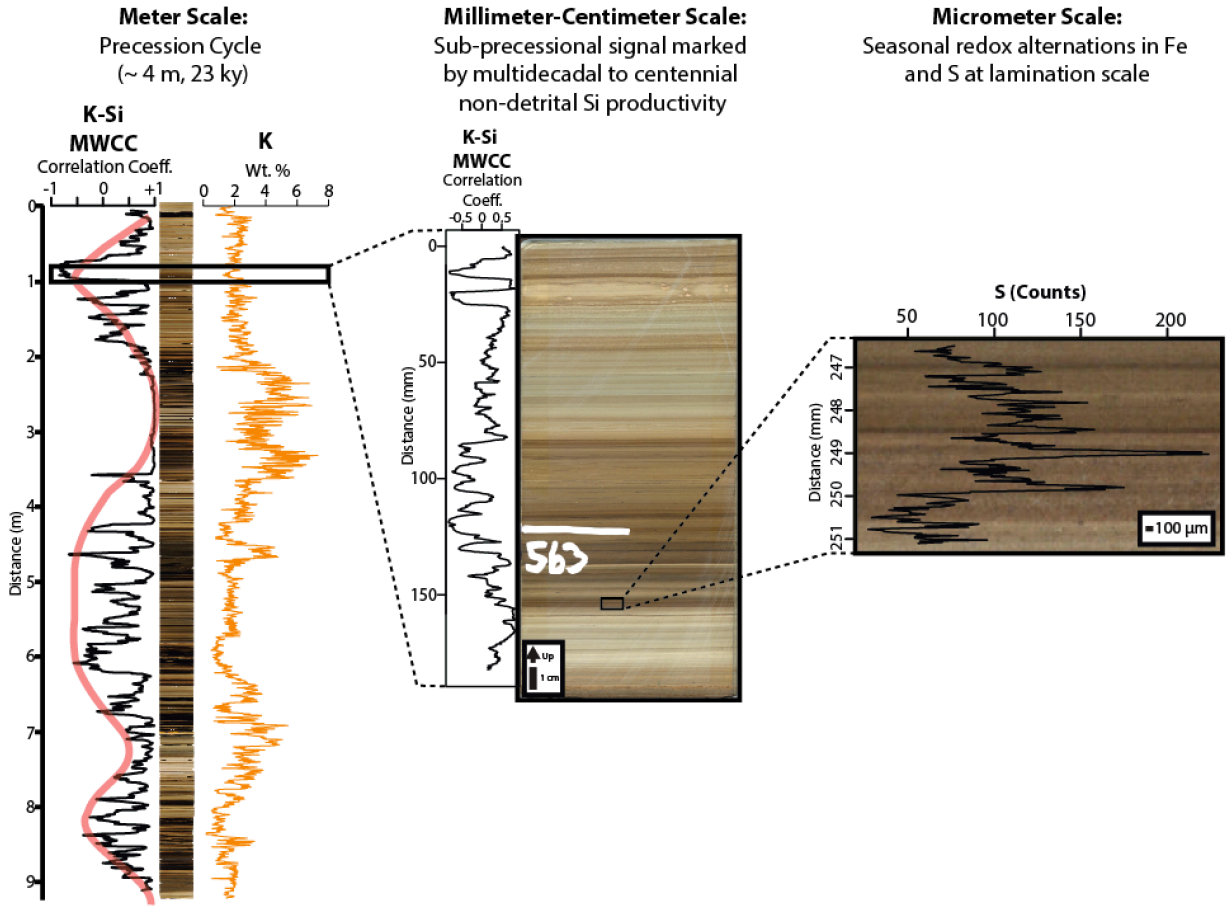

Figure 11: Synthesis of cyclicity from the meter scale to the micrometer scale in the "Upper R-6" study interval of the Parachute Creek Member, Green River Formation in the Skyline 16 core.

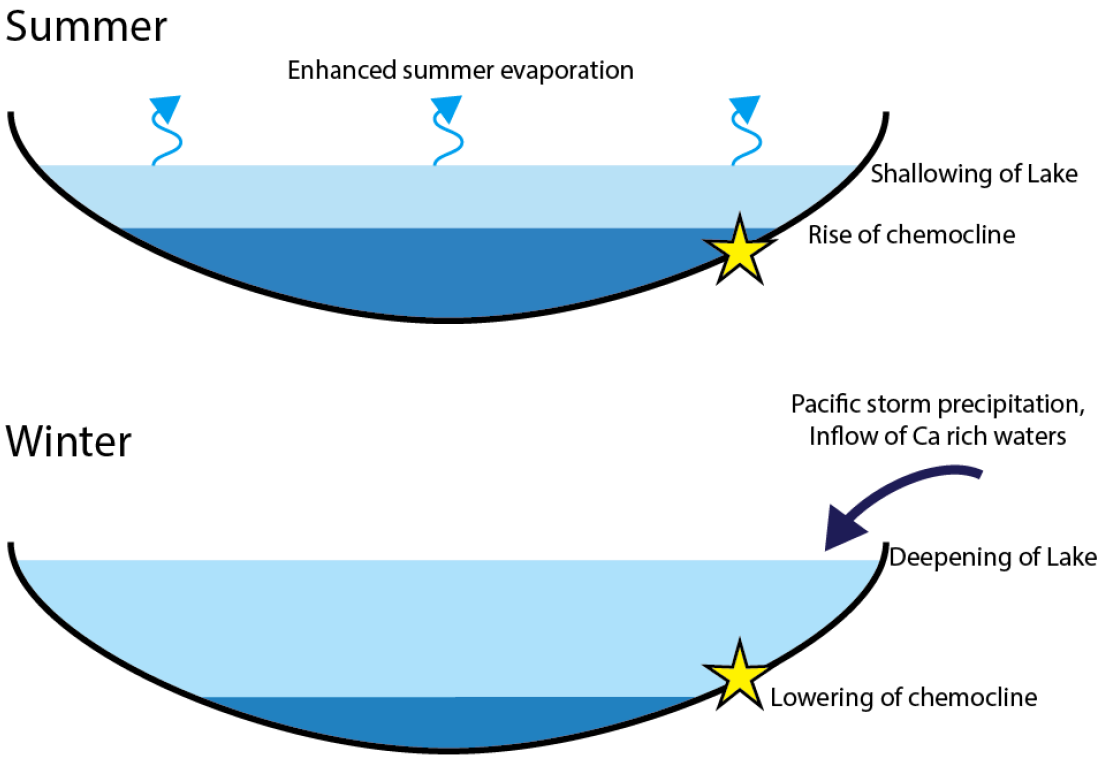

Figure 12: Depositional model for the formation of laminae based on results from the "Upper R-6" study interval. The location of the Skyline 16 core is marked by a yellow star.

Table 1. Results for ICP elemental calibration of XRF core scanner data at 5 mm resolution

Proxy	Calibration Equation	R^2 Value	Samples
Al	$y = 0.0002(x) + 0.767$	0.78139	38
Si	$y = 7*10^{-5}(x) + 1.5234$	0.79192	38
K	$y = 2*10^{-5}(x) + 0.2022$	0.94409	38
Ca	$y = 1*10^{-5}(x) + 2.0271$	0.80238	38
Fe	$y = 1*10^{-5}(x) + 0.2643$	0.5616	38
Sr	$y = 0.0061(x) + 150.87$	0.8619	38

Table 2. Results for ICP elemental calibration of XRF core scanner data at 100 micrometer resolution.

Proxy	Calibration Equation	R^2 Value	Samples
Al	$y = 0.001(x) + 1.3373$	0.6882	37
Si	$y = 0.0005(x) + 1.1549$	0.97111	37
K	$y = 0.0001(x) + 0.3464$	0.99302	37
Ca	$y = 6*10^{-05}(x) + 2.5665$	0.99341	37
Fe	$y = 5*10^{-05}(x) + 0.2698$	0.99729	37
Sr	$y = 0.0223(x) + 127.28$	0.95534	37

Table 3. Correlation results between 100 micrometer XRF core scanner data or 25 micrometer micro-XRF data and grayscale data. Pearson correlation coefficients were calculated for both the raw data and following removal of pyrite layers in the interval of study.

	MicroXRF (25 µm) Correlation to grayscale	**MicroXRF (25 µm)** Correlation to grayscale (Pyrite layers removed)	**Avaatech (100 µm)** Correlation to grayscale	**Avaatech (100 µm)** Correlation to grayscale (Pyrite layers removed)
Na	0.020	0.020		
Mg	0.496	0.480		
Al	0.014	0.001	-0.210	-0.249
Si	-0.319	-0.335	-0.279	-0.281
S	-0.371	-0.599	-0.557	-0.811
Cl	-0.085	-0.092		
K	0.326	0.314	0.431	0.418
Ca	0.010	0.026	0.120	0.144
Ti	0.066	0.047		
V	0.076	0.068		
Cr	0.055	0.050		
Mn	0.206	0.185		
Fe	0.431	0.605	0.664	0.715
Zn	-0.002	-0.011		
Rb	0.029	0.018		
Sr	0.115	0.106	0.287	0.292
Y	0.014	0.013		
Zr	0.005	0.004		
Rh	-0.047	-0.055		
Ba	-0.265	-0.262		

Table 4. Criteria for the three testable time series models.

	Minimum Case	Nominal Case	Maximum Case
Constant Net Accumulation Rate Model	120 micrometers/yr	168 micrometers/yr	278 micrometers/yr

Table 5. Correlations between elemental intensities in the 5-mm-resolution XRF data.

	Mg	Al	Si	P	S	Cl	K	Ca	Ti	V	Cr	Mn	Fe	Cu	Zn	Br	Rb	Sr	Y	Zr	Mo	Pb	U
Mg	1.00	-0.26	-0.31	-0.21	-0.28	-0.07	0.00	0.17	-0.19	0.11	0.18	0.05	0.02	-0.35	-0.28	-0.02	-0.05	0.15	-0.12	-0.09	-0.33	-0.32	-0.08
Al	-0.26	1.00	0.81	0.08	-0.18	0.02	0.68	-0.84	0.69	0.47	-0.37	0.15	0.46	0.58	0.76	0.03	0.77	-0.76	0.46	0.28	0.21	0.18	-0.10
Si	-0.31	0.81	1.00	0.04	-0.18	0.12	0.48	-0.81	0.60	0.42	-0.38	0.16	0.33	0.43	0.61	0.04	0.64	-0.71	0.35	0.41	0.09	0.13	-0.06
P	-0.21	0.08	0.04	1.00	-0.12	-0.17	0.18	-0.02	0.04	0.04	0.06	-0.08	-0.02	0.11	0.10	-0.09	-0.03	0.24	0.18	0.07	0.09	0.00	0.06
S	-0.28	-0.18	-0.18	-0.12	1.00	-0.28	-0.11	-0.06	-0.06	-0.07	-0.24	0.43	0.10	0.05	-0.03	0.23	-0.09	-0.03	-0.02	0.00	0.14	0.27	0.02
Cl	-0.07	0.02	0.12	-0.17	-0.28	1.00	-0.01	0.04	-0.05	-0.06	0.00	-0.26	-0.17	-0.10	-0.06	0.18	-0.02	-0.01	-0.13	0.01	-0.09	-0.13	-0.02
K	0.00	0.68	0.48	0.18	-0.11	-0.01	1.00	-0.58	0.52	0.26	-0.21	0.11	0.22	0.34	0.51	0.01	0.72	-0.53	0.38	0.13	0.09	-0.08	-0.14
Ca	0.17	-0.84	-0.81	-0.02	-0.06	0.04	-0.58	1.00	-0.70	-0.62	0.44	-0.39	-0.59	-0.63	-0.74	-0.14	-0.76	0.79	-0.49	-0.36	-0.24	-0.30	0.06
Ti	-0.19	0.69	0.60	0.04	-0.06	-0.05	0.52	-0.70	1.00	0.68	-0.28	0.27	0.37	0.61	0.69	0.02	0.77	-0.56	0.54	0.51	0.15	0.19	-0.01
V	0.11	0.47	0.42	0.04	-0.07	-0.06	0.26	-0.62	0.68	1.00	-0.40	0.34	0.52	0.46	0.46	0.09	0.53	-0.40	0.44	0.40	0.09	0.20	0.00
Cr	0.18	-0.37	-0.38	0.06	-0.24	0.00	-0.21	0.44	-0.28	-0.40	1.00	-0.32	-0.24	-0.27	-0.32	-0.16	-0.25	0.37	-0.17	-0.21	-0.11	-0.09	0.02
Mn	0.05	0.15	0.16	-0.08	0.43	-0.26	0.11	-0.39	0.27	0.34	-0.32	1.00	0.31	0.21	0.27	0.10	0.21	-0.32	0.32	0.24	-0.01	0.12	-0.01
Fe	0.02	0.46	0.33	-0.02	0.10	-0.17	0.22	-0.59	0.37	0.52	-0.24	0.31	1.00	0.45	0.41	0.13	0.41	-0.52	0.27	-0.02	0.20	0.41	-0.05
Cu	-0.35	0.58	0.43	0.11	0.05	-0.10	0.34	-0.63	0.61	0.46	-0.27	0.21	0.45	1.00	0.73	-0.01	0.56	-0.46	0.46	0.14	0.53	0.43	0.01
Zn	-0.28	0.76	0.61	0.10	-0.03	-0.06	0.51	-0.74	0.69	0.46	-0.32	0.27	0.41	0.73	1.00	0.01	0.68	-0.59	0.50	0.30	0.30	0.27	-0.05
Br	-0.02	0.03	0.04	-0.09	0.23	0.18	0.01	-0.14	0.02	0.09	-0.16	0.10	0.13	-0.01	0.01	1.00	-0.01	-0.08	-0.01	0.06	0.02	0.25	0.03
Rb	-0.05	0.77	0.64	-0.03	-0.09	-0.02	0.72	-0.76	0.77	0.53	-0.25	0.21	0.41	0.56	0.68	-0.01	1.00	-0.66	0.52	0.40	0.14	0.10	-0.12
Sr	0.15	-0.76	-0.71	0.24	-0.03	-0.01	-0.53	0.79	-0.56	-0.40	0.37	-0.32	-0.52	-0.46	-0.59	-0.08	-0.66	1.00	-0.36	-0.13	-0.11	-0.20	0.13
Y	-0.12	0.46	0.35	0.18	-0.02	-0.13	0.38	-0.49	0.54	0.44	-0.17	0.32	0.27	0.46	0.50	-0.01	0.52	-0.36	1.00	0.41	0.18	0.17	0.04
Zr	-0.09	0.28	0.41	0.07	0.00	0.01	0.13	-0.36	0.51	0.40	-0.21	0.24	-0.02	0.14	0.30	0.06	0.40	-0.13	0.41	1.00	-0.07	0.06	0.03
Mo	-0.33	0.21	0.09	0.09	0.14	-0.09	0.09	-0.24	0.15	0.09	-0.11	-0.01	0.20	0.53	0.30	0.02	0.14	-0.11	0.18	-0.07	1.00	0.48	0.05
Pb	-0.32	0.18	0.13	0.00	0.27	-0.13	-0.08	-0.30	0.19	0.20	-0.09	0.12	0.41	0.43	0.27	0.25	0.10	-0.20	0.17	0.06	0.48	1.00	0.12
U	-0.08	-0.10	-0.06	0.06	0.02	-0.02	-0.14	0.06	-0.01	0.00	0.02	-0.01	-0.05	0.01	-0.05	0.03	-0.12	0.13	0.04	0.03	0.05	0.12	1.00

Chapter 2

Influence of Lake Basin Morphology on Climate-Sediment Transfer Functions: Early Eocene Wilkins Peak Member, Green River Formation, Wyoming

In preparation for submission to

Palaeogeography, Palaeoclimatology, Paleoecology

Abstract

Lacustrine strata are among the most detailed and integrative of terrestrial paleoclimate archives. It has long been recognized, however, that not all lake systems are equally sensitive to climate forcing due to differences in the processes by which climate signals are transferred into their sedimentary records. This sedimentary transfer function, which describes the process by which an environmental signal is encrypted into the geologic record through climate, deposition, burial, and diagenesis processes, plays a critical role in filtering which signals are preserved, but has received little attention in deep time lacustrine systems. We use high-resolution X-ray fluorescence (XRF) core scanning of the Wilkins Peak Member (WPM) to characterize the evolution of the sedimentary transfer function in this ancient lacustrine record.

Our analysis identifies a previously unrecognized shift in the frequency distribution of Milankovitch-band variance in temporally-calibrated Si, S, K, Ca, and Fe between the lower and upper WPM. Spectral analysis of the lower-WPM shows power and amplitude concentrated in frequencies associated with short eccentricity (Period: ~100 ky), obliquity (Period: ~40 ky), precession (Period: ~20 ky), and sub-Milankovitch (Period: <18 ky) cyclicity. In the upper WPM, power and amplitude are concentrated in frequencies associated with long and short eccentricity, with reduced power at higher frequencies. This transition coincides with a dramatic decline in the number and volume of bedded evaporite.

We attribute this altered transfer function to a change in the morphology of the Bridger basin, which directly influenced the preservation of bedded evaporite. Initially, a structural foredeep near the southern basin margin accommodated a relatively deep, meromictic lake with a well-defined thermocline. The high degree of lithologic contrast afforded by evaporite beds in alternation with carbonate mudstone and siliciclastic mudstone, siltstone, and sandstone results

in enhanced spectral power at higher frequencies (obliquity, precession, sub-precession). As the depocenter became broader and flatter, however, the lake evolved to be shallower and holomictic. Shallow lake waters resulted in the dissolution and recycling of bedded evaporite and the preferential growth of displacive phases beneath the sediment-water interface. The loss of bedded evaporite, combined with obscuration of other primary lithologies by secondary evaporite growth, results in reduced obliquity- and precession-band power and enhanced eccentricity-band power.

Introduction

Lacustrine deposits are among the most valuable archives of terrestrial sedimentary deposition. With sedimentation rates as much as two orders of magnitude faster than in the deep marine environment (Johnson 1984; Cohen 2003), lakes can offer a detailed and integrative perspective on regional continental change, expressing variations in regional climate, tectonics, landscape evolution, ecology, and magmatism through changes in physical, chemical, and biological processes within the lake and its associated drainage network (Surdam and Stanley, 1980; Johnson, 1984; Pietras et al., 2003a; 2003b; Smith et al., 2008; Smith et al., 2014a; 2014b; Scott et al., 2015). When looking back further than the Quaternary, these integrative deposits are critical for understanding the environmental influences acting on lakes and their associated drainage networks, particularly during periods of major climatic, tectonic, or biologic change.

It has long been recognized, however, that not all lake systems are equally sensitive, with some lake basins amplifying environmental signals within their depositional records and others muting them (Cohen, 2003). This variable sensitivity to environmental forcing may be thought of as differences in the sedimentary 'transfer function,' a term describing the process by which

an environmental signal is encrypted into the geologic record through climate, deposition, burial, and diagenesis processes (Meyers 2017; Meyers 2019). While this sedimentary transfer function plays a critical role in filtering how environmental signals are preserved in the sedimentary record, little attention has been paid to characterizing the influence sedimentary transfer functions in paleo-lakes deposited in deep time, the geologic records of which are key evidence in understanding past continental change.

The Wilkins Peak Member (WPM) of the Green River Formation in Wyoming (**Figure 1**) represents one of the premier lacustrine records for the early Eocene, and makes a compelling deep-time locale to study the long-term evolution of the depositional transfer function. Not only does it have a thick, temporally well-constrained, and highly-studied foreland basin record of lacustrine and alluvial deposition during the Early Eocene Climatic Optimum (EECO; 52-50 Ma; Zachos et al., 2001, 2008; Smith et al., 2008) greenhouse climate, but it also shows a distinct lithofacies change mid-way through its deposition (**Figures 2, 3**). This is suggestive of a change in the depositional expression of the paleo-lake which deposited it and potentially represents a shift in the depositional transfer function. Additionally, the WPM has a long history of cyclostratigraphic study, including the interpretation of a range of Milankovitch- and sub-Milankovitch-scale cyclicity in its strata (Bradley, 1929; Fischer and Roberts, 1991; Machlus et al., 2008; Meyers, 2008; Aswasereelert et al., 2013).

This study aims to evaluate the evolution of the Wilkins Peak Member transfer function through the application of high-resolution, multi-proxy elemental characterization via X-ray fluorescence (XRF) scanning, in combination with radioisotopic dating and spectral analysis methods. Using this approach, we seek to characterize cyclic sedimentation within the Wilkins Peak Member of the Green River Formation at a previously unattainable level of detail, assess

changes in the expression of cyclic sedimentation, and evaluate potential transfer-function linkages to climate, tectonics, and landscape evolution.

Geologic Setting

The Green River Formation was deposited in a series of mid-latitude, Laramide foreland basins during the early to middle Eocene (~ 54-43 Ma; Sheliga, 1980; Remy 1992; Smith et al. 2008) (**Figures 1, 2**). Sedimentary deposition within this regional lacustrine system was centered around four primary basins: the Greater Green River Basin (southwestern Wyoming), the Fossil Basin (southwestern Wyoming), the Uinta Basin (northeastern Utah), and the Piceance Creek Basin (northwestern Colorado). Laramide Orogeny deformation, thought to be connected to the flat slab subduction of the Farallon plate under North America (Coney and Reynolds 1977; Dickinson and Snyder 1978; Smith et al. 2014a), produced a series of basement-cored anticlinal uplifts and structural basins in the Laramide foreland east of the Sevier fold and thrust belt during the late Cretaceous to the early Eocene (Dickinson et al. 1988; Cashion 1995; Rhodes et al. 2002; Smith et al. 2008).

This study focuses on the Bridger sub-basin, which makes up the western portion of the Greater Green River Basin. This sub-basin is bounded in the south by the Uinta Mountains, in the west by the Sevier fold and thrust belt, in the east by the Rock Springs Uplift, and in the north by the Wind River Mountains (**Figure 1**). Broad and low in relief in comparison to the other Green River Formation basins, the Bridger sub-basin contains a thick sequence of strata deposited by the paleo-Lake Gosiute lacustrine system and its associated alluvial deposits. Over its lifetime, paleo-Lake Gosiute experienced major shifts in chemistry and hydrologic balance, producing a diverse assemblage of sedimentary facies resulting from environmental changes

such as lake depth, lake water chemistry, and lake paleo-ecology (Smith et al., 2008; Smith and Carroll, 2015).

Broadly, the Green River Formation in the Bridger sub-basin is divided into three primary depositional members: the Tipton Member, the Wilkins Peak Member, and the Laney Member (**Figure 2**). The Tipton Member, the lowermost member of the Green River Formation in the Bridger sub-basin (**Figure 2**), ranges from 25.5 m to 51.5 m thick and records several alternations between overfilled and balance-filled lake conditions (Carroll and Bohacs, 1999). It is principally divided into two sub-units, the Scheggs Bed and the Rife Bed (Roehler, 1991; Graf et al., 2015).

This study primarily evaluates the Wilkins Peak Member, the middle member of the Green River Formation in the Bridger sub-basin. During deposition of the Wilkins Peak Member, the lake exhibited underfilled, evaporative conditions, leading to widespread alkaline and saline conditions within the lake (Carroll and Bohacs, 1999). Deposition of this unit is also coincident with the Early Eocene Climatic Optimum (EECO; ~ 53-50 Ma), the acme of the early Cenozoic greenhouse climate interval (Zachos et al. 2001, 2008; Smith et al., 2008). Shallow lake levels, combined with the broad, low-relief morphology of the basin, appear to have made this unit particularly sensitive to climatic forcing—including hypothesized astronomical cycles—during this unusually warm period (Fischer and Ripepe, 1991; Machlus, 2008; Meyers 2008; Aswassereelert et al., 2013).

Within the Wilkins Peak Member, which ranges from 200-325 m thick in the depocenter of the Bridger sub-basin, lithofacies can be broadly grouped into lacustrine carbonate, lacustrine bedded evaporite, and alluvial siliciclastic deposits (**Figure 2**). Alluvial facies are principally green mudstone and siltstone at the basin center, with fine- to medium-grain sandstone also

present toward the basin margins. These alluvial facies are interpreted to be deposited during intervals of low lake level, during which low-gradient alluvial plains grade into the basin (Smith and Carroll, 2015). Within the Wilkins Peak Member, nine of these alluvial units have been identified and correlated at the basin scale (Culbertson, 1961). Each of these key alluvial beds has been given a letter designation (A-bed through I-bed) by Culbertson (1961), starting at the base of the Wilkins Peak Member.

Lacustrine carbonate facies are primarily organic carbon-poor carbonate marlstones, with some intervals of organic-rich oil shales that are interpreted to reflect punctuated deepening and expansion of paleo-Lake Gosiute. Lacustrine evaporite mineral beds, principally composed of trona, halite, and shortite, are present in the lower Wilkins Peak Member, principally below the C-bed in the region of the Bridger sub-basin depocenter (**Figure 2**). Above the C-bed, bedded evaporite units are not as voluminous or numerous, and their concentration is shifted closer to the geographic center of the Bridger sub-basin (Wiig et al., 1995). Evaporite mineralization above the C-bed is primarily expressed as displacive crystals of shortite within carbonate marl facies. Within the Wilkins Peak Member, twenty-five evaporite beds have been identified, correlated within the basin, and assigned numerical designations (Trona Bed 1-25) (Wiig et al., 1995).

The Laney Member, which is not examined in this study, lies above the Wilkins Peak Member in the Bridger sub-basin, and represents the uppermost member of the WPM (**Figure 2**). This member records Lake Gosiute's shift from an evaporitic, underfilled lake during Wilkins Peak Member deposition to a balance-fill and, eventually, overfilled lake (Roehler, 1973; Rhodes et al., 2007; Smith et al., 2008; Rhodes and Carroll, 2015).

Methods

Solvay S-34-1 Core

This study is based on the Solvay S-34-1 core, which was drilled in 2016 and recovered approximately 642 m of 63.5 mm diameter core from the Green River Formation and the overlying Bridger Formation (**Figure 3**). This core is positioned in the south-central Bridger sub-basin (41°24'51.23"N; 109°41'48.30"W), close to the basin depocenter during deposition of the early Wilkins Peak Member (**Figure 2**).

This study examines the lowermost 257.29 m of core (estimated recovery: 97%), which includes an 11.78-m interval of the upper Tipton member, a 238.22-m section of the overlying lower and middle Wilkins Peak Member, and a 7.29-m interval of deltaic sandstone and oil shale thought to be associated with the Desertion Point Tongue of the Wasatch Formation (Sullivan, 1980) (**Figures 3, 4**). This interval of the Solvay S-34-1 core was split, imaged, and logged at the LacCore facility at the University of Minnesota-Twin Cities.

Within the Wilkins Peak Member section preserved in the core, dominant lithologies include carbon-poor carbonate marl, oil shale, green siltstone, green mudstone, and bedded evaporite, with minor intervals of volcanic tuff and very fine- to medium-grained sandstone. This interval of core includes 17 bedded evaporite units (TB1-7 and 9-18) and the A- through H-bed sequence of named alluvial beds (Culbertson, 1961) (**Figure 3**).

XRF Core Scanning

Data Collection

X-ray fluorescence (XRF) core scanning was completed at the University of Wisconsin-Madison using a third-generation Avaatech X-ray fluorescence core scanner. Prior to scanning, split core samples were prepared slab face up in the scanner and cleaned of debris, leveled to horizontal, described, and covered in SPEX 3525 Ultralene foil. For each individual core

section, a continuous down-core measurement path was selected to avoid anomalous intervals of core, which may include cracks, surface irregularities, or sedimentary clasts.

XRF core scanning was completed at a continuous 5-mm resolution (5 mm x 5 mm window size) to capture millimeter- to meter-scale variations in elemental intensity across the 257.29 m of core. To optimally measure a wide range of elements within the core, two different scans were completed at this resolution using different instrument settings. To measure Mg through Rh, an acceleration voltage of 10 kV (1200 uA source current, no filter, 20-second measurement time) was used. For elements Cu through U, an acceleration voltage of 30 kV (1600 uA source current, thin palladium filter, 20-second measurement time) was used. Deconvolution of X-ray fluorescence spectra was completed using a customized deconvolution model in the WinAxil (v. 4.5.2) X-ray analysis software.

We instituted a comprehensive approach to evaluate data quality and reproducibility. Standard samples were analyzed between each scan run of an individual core section (SARM-4) and before and after the complete analysis of each individual core section (JGb-1, JR-1) to evaluate instrument stability (Supplement B1). For each core section measured, sample replicate measurements were also taken at every fifth measurement at each of the two instrument settings to quantify instrument variation and evaluate reproducibility for each element (Supplement B2, B3). Through examination of mean coefficient of variation, standard deviation of the coefficient of variation, and cross plots of elemental intensities for all replicate measurements, we identify twenty elements (Mg, Al, Si, P, S, Cl, K, Ca, Ti, V, Mn, Fe, Cu, Zn, Br, Rb, Sr, Zr, Mo, Pb) with superior quality (Supplement B4).

Data Correction for Instrument Drift

Over the fourteen-month course of XRF scanning, long-term instrumental drift was observed in the XRF count values for standard samples (Supplement B1). In additional, the replacement of the instrument's X-ray source while the project was in progress manifested as a stepwise shift in the XRF count values for the standard measurements. To account for these artifacts and minimize the impact on subsequent data analysis and interpretations, we implemented data corrections on an element-by-element basis. The correction approach used a two-step process. For each element, one standard sample of the three measured standards (SARM-4, JGb-1, JR-1) was identified as the basis for drift correction; the specific standard was selected based on its sensitivity to a given element, with the standard that registers the highest count values selected for that element's correction. For Al, S, Ti, and Cr, the JGb-1 standard was used. For Si, P, Cl, K, Ca, Mn, and Fe, the JR-1 standard was used. For Cu, Zn, Br, Rb, Sr, Zr, Mo, and Pb, the SARM-4 standard was used.

For the first correction step, a manual correction is applied to individual outlier standard measurement values to reduce the influence of these measurements on the following data corrections. If a standard measurement result for a given element registers 5% greater or fewer counts than standard measurements taken before or after it, an outlier correction coefficient is calculated by dividing this outlier value by an average of the 5 points either before or after it. This outlier correction coefficient is then used to adjust the XRF data associated with that standard measurement on an element by element basis. For the 10 kV elements, 3 points out of 490 standard measurements were deemed as outliers and corrected. For the 30 kV elements, 2 points out of 490 standard measurements were found to be outliers and corrected.

Following outlier removal, the primary drift correction step was completed for all standard measurements. Standard values for each element were input into the R statistical

computing program, and the "noLow" function within the Astrochron package (Meyers, 2014) for R was used to calculate a LOWESS fit to the fourteen-month standard measurement data series for each element. This fit uses a locally weighted regression, allowing the long-term trend to be identified for each element within the standard measurement data series. Instrumental drift was removed from the standard measurement data series through application of a drift-correction coefficient; this parameter was calculated by dividing the observed LOWESS fit by a reference measurement (in this case, the LOWESS fit value from the first core section measured). Using this drift-correction coefficient, XRF core scanner data for each core section associated with a standard measurement was corrected on an element-by-element basis through multiplication by its corresponding drift-correction coefficient.

Following these two data correction steps, the XRF datasets for each individual core piece were combined into a composite section for the lower 257.29 m of the S-34-1 core. Through comparison of core images, core description, and XRF core scanner results, the top and base of each core piece were identified. Cracks and gaps in the core were noted and the data were either deleted or blanked to preserve the depth associated with this measurement. This step reduced the number of spurious or poor-quality data points within the data set due to gaps or cracks in the core. One missing ~3 m core box and several intervals of alluvial mudstone and siltstone with an uneven core surface were unable to be measured. In both cases, the missing depth associated with these areas was preserved as blank intervals. The depth covered by the missing box was estimated using the top, bottom, and preserved core length of the surrounding boxes. For select core intervals not able to be XRF scanned due to an irregular surface, approximate depth measurements from core pieces were used to estimate interval length and preserve spatial relationships.

Depth-Time Conversion

Spectral analysis was completed in the spatial domain to provide a point of comparison to past cyclostratigraphic studies of the WPM (e.g. Machlus et al., 2008; Meyers 2008) and to examine the XRF data without the influence of a time model. Additionally, spectral analysis was also completed in the time domain. Time-depth conversion was modeled using two different approaches. The first approach, which we designate the "tuff calibration" (TC) model, uses the published weighted mean U-Pb ages of Machlus et al. (2015) for the Firehole, Second, and Grey tuffs (**Table 1**) along with the depths of their midpoints in the S-34-1 core (**Figure 3**) to calibrate the data in time. Using these time-depth control points, the 'tune' function within the 'Astrochron' package for R (Meyers, 2014) was applied to create a piecewise linear time-depth model for the XRF dataset. This approach makes minimal assumptions and uses three control points with low temporal and stratigraphic uncertainty to derive the time-depth calibration. However, extrapolation is required to temporally-calibrate the XRF record at the top and bottom of the core that is not spanned by radioisotopically dated tuffs.

The second method, designated the "time-equivalent surface" (TES) model, follows the approach used by Aswasereelert et al. (2013) to assign modeled ages to 51 time-equivalent surfaces within the Wilkins Peak Member. These time-equivalent surfaces are primarily widely correlatable tuffs, oil shale beds, and alluvial beds present within the Wilkins Peak Member. A second-order polynomial equation was fit to the weighted mean U-Pb ages of Machlus et al. (2015) for the Firehole, Second, Grey, Main, Layered, and Sixth tuffs and the cumulative depths associated with these tuffs in the White Mountain 1 core, a location north east of the Solvay S-34-1 core (**Figure 1**) where each of these time-equivalent surfaces are present (Aswasereelert et al., 2013). Within the Solvay S-34-1 core, 30 time-equivalent surfaces in the lower, middle, and

upper WPM were identified (**Figure 3**), and their depths in the S-34-1 core were used to calculate a modeled age using the second-order polynomial time-depth model developed from the six U-Pb dated tuffs (**Table 2**). The WM-1 core was used for the polynomial fit because each of the WPM time-equivalent surfaces is physically present and unambiguous in this core, unlike in the S-34-1 core (Aswasereelert et al., 2013).

The advantage of the TES method compared to the TC model is addition of extra time-depth control points, resulting in more frequent sedimentation rate adjustments. Unresolved sedimentation rate changes have the potential to cause "peak splitting" within power spectra by smearing the high frequency variance across a range of frequencies (Meyers et al., 2001; Aswasereelert et al., 2013) and can lead to the creation of artifact "cycles" that look like harmonics of the fundamental cycle (Schiffelbein and Dorman, 1986; Aswasereelert et al., 2013). By applying two independent time-depth modeling approaches, our intention is to model a range of reasonable time-depth calibrations rather than rely on one set of sedimentation-rate assumptions as the basis of our analysis.

Time Series Analysis

Spectral analysis in both depth and time domains was conducted using Astrochron (Meyers, 2014), a package designed for astrochronologic analysis using the open-source R statistical program. For both depth and time domain, a range of statistical and spectral analysis techniques were applied to evaluate this high-resolution, multi-proxy XRF data.

Multi-Taper Method (MTM) spectral analysis (Thomson, 1982) was applied to the XRF dataset in both the spatial and temporal domains to provide information on oscillatory variability within our data series. This power spectra technique, which uses a specified series of prolate tapers for spectral estimation (Thomson, 1982), was applied to the linearly interpolated records

of XRF-measured elements using the "mtm" function in Astrochron (Meyers, 2014). This method is widely used to in the paleoclimate field to evaluate cyclic influences in sedimentation, in part because it is well suited to evaluating spectra containing a mix of periodic signals, quasi-periodic signals, and stochastic noise (Meyers et al., 2008). Additionally, Evolutive Harmonic Analysis (EHA), a method which applies MTM to a moving window, was applied using the 'eha' function in Astrochron to identify cyclic variability and evaluate potential changes in sedimentation rate (Meyers et al. 2001; Meyers, 2014). This analysis is particularly useful for visualizing stratigraphic changes in power, amplitude, and frequency associated with a given cycle in sedimentation. Across the entire core record, correlation of pairs of elements within the XRF record was completed using Pearson correlation. Moving window cross-correlation was also applied to pairs of elements within the XRF record via the "mwCor" function in Astrochron (Meyers, 2014) to get a more detailed perspective on the interrelation of elements across facies than what is possible using a single correlation coefficient for the entire record (Sageman and Hollander, 1999). This permits the examination of correlation coefficients between different element pairs across different lithofacies at sub-bed-scale resolution.

Results

Lithofacies Identification and Composition

High-resolution, multi-proxy XRF core scanning of the Solvay S-34-1 core provides information on variations in elemental intensity (in counts) at a resolution and continuity that was not previously attainable for the WPM. Several groupings of closely associated elements emerge. Al, Si, K, Ti, Cu, Zn, and Rb have a strong and consistent positive inter-correlation in their Pearson correlation coefficients (Table 3), and are inferred to be siliciclastic proxy

elements. Mg, Ca, Cr, and Sr have a strong positive inter-correlation, and are inferred to be carbonate proxy elements (**Table 3**). S and Pb have positive correlation, and are inferred to be redox proxy elements. Additionally, Cl and Br are positively correlated, and are inferred to be evaporite proxies (**Table 3**). Finally, Fe appears to act as both a siliciclastic and a redox proxy, showing positive correlations with elements from both proxy groups.

Comparing the XRF elemental record for six key proxy elements (Si, S, Ca, K, Fe, and Br) to the stratigraphy of the Green River Formation within the S-34-1 core, the main member boundaries and inter-Wilkins Peak Member lithologic variations are identifiable (**Figure 4**). Near the base of the core section (631 m depth), the upper Tipton Member meets the lower Wilkins Peak Member. Moving across this boundary into the WPM, we observe a major and abrupt decrease in counts for carbonate and silicate proxy elements, particularly Si, K, Ca, and Fe. These changes in elemental counts correspond to a lithology change from predominantly oil shale facies in the upper Tipton Member to predominantly bedded evaporite and organic-poor carbonate marlstone in the lowermost Wilkins Peak Member.

Within the Wilkins Peak Member in the S-34-1 core (392.78-631 m core depth), elemental variations associated with alternations in lacustrine and alluvial lithofacies are also observed. Alluvial beds, including the A- through H-bed, were identified as 1.5 m to 16 m thick intervals of green mudstone, green siltstone, and fine-grained sandstone, and are associated with increases in Al, Si, K, Ti, Cu, Zn, and Rb **(Figures 3, 4**), consistent with their inferred silicate proxy element designation. Within these alluvial beds, consistently low counts were measured for inferred carbonate proxy elements, such as Ca (**Figure 4**). Moving-window cross-correlation analysis of the Si and Ca elemental records shows generally negative correlation coefficient for

the A- and B-beds, but generally positive correlation coefficients for the overlying C- through G-beds (**Figure 5**).

Carbonate marlstone, the dominant lacustrine lithofacies of the middle and upper Wilkins Peak Member in the S-34-1 core, are characterized by high, but variable, counts in carbonate (Ca) and siliciclastic (Si, K) proxy elements (**Figures 3, 4**). Previous assessments of Green River Formation carbonate marl and oil shale mineralogy found that they commonly contain calcite, dolomite, quartz, alkali feldspar, plagioclase, and illite and other clay minerals (Bradley and Eugster 1969; Hosterman and Dyni 1972; Picard and High 1972; Robb and Smith 1974; Dyni 1976; Mason, 1987), a mineralogy that is consistent with our XRF results for these facies. Moving-window cross-correlation analysis of Si and Ca show a largely negative Pearson correlation coefficient in the carbonate mudstone facies, suggesting a generally antithetic relationship between carbonate and silicate inputs (**Figure 5**). Similar alternations in inferred carbonate and siliciclastic content have been observed in carbonate marls and oil shales in other basins of the Green River Formation, such as the Parachute Creek Member of the Uinta Basin of Utah (Walters et al., 2020)

Bedded evaporite, the third major lithofacies group, range from 0.25 m to 8 m in thickness and are concentrated in the lower Wilkins Peak Member, located between the base of the Wilkins Peak Member and the base of the C-bed (**Figure 3**). These beds, designated as "TB" (trona beds) in **Figure 4** are associated with an abrupt decrease in elemental counts for most proxy elements, including Si, S, K, Ca, and Fe. This can be attributed to the trona- and halite-rich composition of these beds, which are dominantly composed of H, C, O, Na, and Cl, of which only the latter is possible to measure on the Avaatech XRF core scanner. Br is also present in small amounts, primarily within halite (Higley, 1983). Due to this reduction in counts in both

silicate and carbonate proxy elements, moving-window cross-correlation analysis of Si and Ca show the two elements positively correlated within the evaporite.

Above the H-bed interval of the Solvay core and near the top of the study section, we observe a major lithofacies shift from the lacustrine and alluvial facies of the Wilkins Peak Member to approximately deltaic sandstone and oil shale. We attribute these 8.29 m of fluvial-lacustrine facies to the Desertion Point Tongue of the Wasatch Formation (Sullivan, 1980). Moving into this sandstone- and oil shale-dominated interval, carbonate proxy element (Ca) counts decrease, while siliciclastic (Si, K, Fe) and redox (S) element counts increase (**Figure 4**).

Spectral Analysis in the Depth Domain

As the most pristine elemental intensity records for the carbonate, siliciclastic, and redox element proxy groups within the S-34-1 core, Si, S, Ca, K, and Fe were selected as the basis for spectral analysis. In the depth domain, MTM spectra for each of these elements show variance that is principally concentrated in the low frequencies, with at least 75 percent of power expressed between 0-0.5 cycles/m (Period: 2 m) (**Figure 6**).

The MTM spectra for K (**Figure 6**) shows primary peaks in power at approximately 0.1 cycle/m (Period: 10 m) and 0.2 cycle/m (Period: 5 m), with smaller peaks at approximately 0.3 cycle/m (Period: 3.3 m), and 0.4 cycle/m (Period: 2.5 m). MTM results for Si and Fe (**Figure 6**) show a stronger influence of the low frequencies than K, with a large peak in power at around 0.01 cycle/m (Period: 100 m) in addition to the 0.1 cycle/m (Period: 10 m), 0.2 cycle/m (Period: 5 m), and 0.3 cycle/m (Period: 3.3 m) peaks also observed in K. MTM results for Ca (**Figure 6**) also show a strong low-frequency influence, with large peaks in power around 0.015 cycle/m (Period: 67 m) and 0.05 cycle/m (Period: 20 m), with smaller peaks in power around 0.1 cycle/m (Period: 10 m), 0.2 cycle/m (Period: 5 m), 0.3 cycle/m (Period: 3.3 m), and 0.4 cycle/m (Period:

2.5 m). MTM analysis of S (**Figure 6**) shows strong power in the 0.01-0.1 cycle/m frequency band (Period: 10-100 m), with additional peaks in power from 0.1-0.6 cycle/m (Period: 1.6-10 m).

Based on published sedimentation rate estimates for the Wilkins Peak Member (e.g. Smith et al, 2003, 2008; Meyers 2008), the observed variability at 0-0.1 cycles/m, 0.2 cycles/m, and 0.3 cycles/m are potential candidates for the astronomical forcing of eccentricity (~100 ky and ~ 400 ky), obliquity (~ 40 ky), and precession (~ 20 ky). However, this depth domain assessment makes no corrections for changes in sedimentation rate, which can lead to the smearing of variance associated with a given cycle across a broader range of frequencies (Meyers et al. 2001).

Evolutive Harmonic Analysis (EHA) was also used to visualize the spectral results. For Si, K, and Fe, EHA plots show the strongest power and amplitude from 510-631 m, with comparatively weak power and amplitude in the section of the Wilkins Peak Member above this interval (**Figure 7**). Additionally, Si, K, and Fe show strong power and amplitude over a much broader range of frequencies (approximately 0-0.5 cycles/m) than is found above this interval, where the strongest power and amplitude are found in the low amplitudes from 0-0.1 cycles/m (**Figure 7**). Conversely, EHA analysis of Ca shows the strongest power and amplitude in the interval from 392-510 m in the S-34-1 core, where power and amplitude are weaker in K and Si (**Figure 7**). The strongest power and amplitude are observed in the low frequencies (0-0.1 cycles/m) but higher-frequency variability is also observed in the Ca record (**Figure 7**). The EHA plot for S shows strong amplitude and power at the base and top of the section across a wide range of frequencies, which corresponds to the most S-rich zones.

This distinct boundary observed in the EHA results for Si, Ca, K, and Fe in the S-34-1 core corresponds to a basin-wide lithofacies shift in the Wilkins Peak Member within the Bridger sub-basin (**Figures 2, 3**). Below this transition point, which is located at the top of the C-bed, sedimentation is dominated by alternations in carbonate marls, bedded evaporites, with occasional alluvial siliciclastic facies. Above this transition point, however, the bedded evaporites are no longer present and deposition primarily alternates between the lacustrine carbonate marls and alluvial mudstones and siltstones (**Figures 2, 3**). Ca shows an enhanced elemental intensity response within the upper Wilkins Peak Member, above the last occurrence of the evaporite beds in the S-34-1 core primarily because this interval prominently features alternations in carbonate content. Si and K, on the other hand, show increased variance in the lower Wilkins Peak Member where bedded evaporites are present, since these intervals produce the largest swings in elemental intensity within the S-34-1 core record. This observed shift in patterns of cyclic sedimentation across a range of elements led us to divide the S-34-1 core XRF record into two datasets at this 510-m boundary for independent spectral analysis: a lower record exhibiting the bedded evaporite-rich lower Wilkins Peak Member and the upper record encompassing the lacustrine carbonate marls and alluvial siliciclastics of the upper Wilkins Peak Member.

In the upper WPM, MTM spectra for Si, Ca, Fe, and S are dominated by large peaks in power between 0.0-0.1 cycle/m (Period: 0-10 m), with comparatively little cyclic influence from higher frequencies (**Figure 8**). Only K shows substantial concentrations of variance within 0.2-0.6 cycles/m within this upper interval, but the magnitude of these peaks is still smaller than those within the 0.0-0.1 cycle/m (Period: >10 m) frequency band (**Figure 8**). Compared to results for the upper WPM, MTM results for Si, Ca, K, S, and Fe in the lower WPM show

enhanced high frequency variability, particularly within Si, S, K, Ca, and Fe (**Figure 8**). Within this lower interval, Si, K, and Fe, show peaks around 0.1 cycle/m (Period: 10 m), 0.2 cycle/m (Period: 5 m), and 0.27 cycle/m (Period: 3.7 m) (**Figure 8**). Additionally, spectra for lower WPM Si and Fe records show peaks in power between 0.0-0.1 cycle/m, with these peak magnitudes either at a similar scale to those observed in the upper WPM interval (Si) or greater than those observed in the upper WPM interval (Fe) (**Figure 8**). Compared to the upper WPM, the MTM spectra for Ca in the lower WPM show reduced power in the 0.0-0.1 cycle/m frequency band, with peaks of enhanced power around 0.1 cycle/m (Period: 10 m) and 0.35 cycle/m (Period: 2.85 m) (**Figure 8**). Similarly, the MTM spectra for S in the lower WPM shows a muted power peak in the 0.0-0.1 cycle/m frequency band and an enhanced peak in the 0.3-0.4 cycle/m frequency band compared to the upper WPM (**Figure 8**).

Spectral Analysis in the Time Domain

In addition to analysis in the depth domain, we analyzed the XRF data calibrated to the time domain through the application of the two independent time-depth models. These two models used varying numbers of depth-time control points to provide corrections to the sedimentation rate curve applied to the Solvay core XRF record, without the need to explicitly tune the elemental records to any proposed astronomical cycle (**Figure 9**).

Across the core record, both models showed broadly consistent net accumulation rates, (**Figure 9**). The TC method models net accumulation rates ranging from 132-174 micrometers/year for the lower and middle WPM (Median: 153 micrometers/yr) (**Figure 9**). The time-equivalent surface method, which utilizes 27 additional time control points, generated annual net accumulation rates on the order of 38-1300 micrometers/yr (Median: 160.5

micrometers/yr) for the lower and upper Wilkins Peak Member, with the highest net accumulation rates associated with alluvial bed deposition (**Figure 9**).

Within the EHA plots for the TC- and TES-calibrated Si, Ca, K, and Fe records, a clear transition in the frequency distribution of power and amplitude is present at approximately 51.06 Ma (**Figures 10, 11**). This boundary coincides with the top of the C-Bed, which also corresponds to the 510-m transition observed EHA power and amplitude transition in the depth domain analysis (**Figures 7, 10, 11**). Below this 51.06 Ma transition, in the lower Wilkins Peak Member where bedded evaporites are present, EHA plots of TC- and TES-calibrated Si and K records show strong, continuous peaks in power and amplitude across a broad range of frequencies (**Figures 10, 11**). Above this 51.06 Ma transition, the strongest power and amplitude in TC- and TES-calibrated Si and K is concentrated predominantly in the low frequencies (<0.11 cycles/ky; Period: >90 ky) (**Figures 10, 11**). EHA results for Ca calibrated using the TC and TES time models show strong, continuous amplitudes in the low frequencies above 51.06 Ma, a response opposite of Si and K (**Figures 10, 11**). This strong upper-WPM response in Ca corresponds with the alternating deposition of lacustrine carbonate marls and alluvial siliciclastic mudstone, siltstone, and sandstone present in the middle and upper Wilkins Peak Member (**Figures 10, 11**). Additionally, within the EHA plots for Si, Ca, K, and Fe temporally calibrated using both models, amplitude and frequency modulation of the low frequency (<0.012 cycle/ky) signal with a ~400 ky recurrence at frequencies associated with short eccentricity scale is also visible (**Figures 10, 11**). This is particularly well expressed in TES-calibrated Ca and Fe (**Figure 11**).

Although they apply different temporal control points to the dataset, MTM spectra of TC- and TES-calibrated Si, K, Ca, Fe and S show broad similarities (**Figures 12, 13**). In both

models, MTM spectra for Si, S, Ca, K, and Fe, variance is principally concentrated between 0.0-0.02 cycles/ky (Period: >50ky) (**Figure 12, 13**). MTM spectra for Si, S, Ca, and Fe temporally calibrated using both approaches show large peaks in power at frequencies of less than 0.003 cycles/ky (Period: >333 ky)., while S, Ca, and Fe also show a strong ~0.01 cycle/ky (Period: ~100 ky) power peak (**Figures 12, 13**). Additionally, MTM spectra for TC- and TES-calibrated Si and K also show a prominent power peak at ~0.02 cycles/ky (Period: 50 ky) and ~0.05 cycles/ky (Period: 20 ky) (**Figure 12, 13**). MTM spectra for TC-calibrated Si, K, Ca, Fe, and S show a moderate peak in power around 0.025 cycles/ky (Period: 40 ky) (**Figure 12**), while TES-calibrated Si, K, Ca, Fe, and S show a similar peak at approximately 0.03 cycles/ky (Period: 33 ky) (**Figure 13**).

When splitting the dataset into the lower WPM and upper WPM across the observed 51.06 Ma power and amplitude transition in the EHA results, the power spectral results for these two intervals appear markedly different (**Figures 14, 15**). Within the TC- and TES-calibrated records for the upper Wilkins Peak Member, variance in Si, Ca, K, Fe, and S is generally concentrated in frequencies less than 0.011 cycles/ky (Period: >90 ky) (**Figures 14, 15**). Within that frequency range, TC- and TES-calibrated upper-WPM Si, S, Ca, K, and Fe records show a strong power peak between 0.0-0.004 cycles/ky (Period:> 250 ky) and Ca, K, and Fe, show a prominent 0.01 cycle/ky (Period: 100 ky) power peak (**Figures 14, 15**). Within the upper WPM TC- and TEC-calibrated Si, S, K, and Fe spectral results, power peaks at frequencies greater than 0.01 cycle/m (Period: <100 ky) are muted compared to the low frequencies (**Figures 14, 15**).

Within the TC- and TES-calibrated records for the lower Wilkins Peak Member, the largest peaks in power for Si, Ca, K, Fe, and S are shifted to higher frequencies (**Figures 14, 15**). In Si, S, K, and Fe, these peaks are higher in magnitude than those observed at the corresponding

frequencies in the upper-Wilkins Peak Member spectra (**Figures 14, 15**). Only the TC- and TES-calibrated Ca record shows larger peaks in power in the upper WPM than the lower WPM. MTM spectra of TC- and TES-calibrated Si and K show little power concentrated at frequencies lower than 0.007 cycle/ ky (Period:143 ky), unlike what is observed in the upper WPM (**Figures 14, 15**). Within those Si and K records, the major peaks in power are observed around 0.010-0.02 cycle/ky (Period: 50-100 ky), 0.025 cycle/ky (Period: 40 ky), 0.039-0.043 cycle/ky (Period: 23-25ky), and 0.052 cycles/ky (Period: 19.2 ky) (**Figures 14, 15**). MTM spectra of TC- and TES-calibrated S and Ca show power peaks at approximately 0.025 cycle/ky (Period: 40 ky), 0.035-0.043 cycle/ky (Period: 23-28ky), and 0.051 cycles/ky (Period: 19.6 ky), but they display additional strong low-frequency (< 0.01 cycles/ky; >100 ky) and high-frequency (>0.06 cycles/ky; <16.7 ky) variability (**Figures 14, 15**).

Discussion

Spectral analysis of XRF data continuously spanning the Wilkins Peak Member reveals an observable shift in the frequency distribution of power and amplitude within power spectra between the lower and upper Wilkins Peak Member. These results are discussed within the context of previous cyclostratigraphic assessments of the Wilkins Peak member, a potential transfer function shift, and a possible climatic or tectonic trigger for this transfer function shift.

Cyclostratigraphic Characterization

Due to its resolution, continuity, and range of elements measured, this XRF dataset provided an opportunity for a cyclostratigraphic characterization of the WPM at a breadth and level of detail not previously possible. Previous cyclostratigraphic analyses of the WPM, principally based on Fischer-assay oil yield data, found evidence for astronomical forcing

(Fischer and Roberts, 1991; Machlus et al., 2008; Meyers, 2008; Aswasereelert et al., 2013) and short-eccentricity pacing of alluvial bed deposition within the WPM (Aswasereelert et al., 2013). However, these assessments were somewhat limited by the Fischer assay data, which provide no direct proxy information for rocks that lack significant organic matter content (Aswasereelert et al., 2013). Evaporite and alluvial facies are two such facies which may contain low organic matter—yielding similar response in Fischer assay— concealing valuable information on basin response to astronomical forcing.

Spectral analysis results from the WPM XRF data were consistent with the findings of previous cyclostratigraphic assessments but allowed us to better characterize facies. TC- and TES-calibrated Si, K, Ca, Fe, and S each show variance distributed at low frequencies at a temporal scale consistent with long eccentricity (400 ky) in their MTM spectra (**Figures 12, 13**). Si, K, Ca, S, and Fe also show power concentrated around a period of 100 ky, consistent with short-eccentricity forcing. The MTM records of TC- and TES-calibrated Fe and Ca are dominated by low-frequency (Period: >100 ky) cyclicity (**Figures 12, 13**); given the association of Ca with lacustrine carbonate facies and Fe with alluvial facies as well as the identified short-eccentricity pacing of alluvial bed deposition in the WPM, it is consistent that variability at the scale of short and long eccentricity appears to be a major driver of Ca and Fe variance.

In addition to peaks in power at the low frequencies, MTM spectra of TC- and TES-calibrated Si, K, and S also show power peaks of similar magnitude in the higher frequencies (**Figures 12, 13**). In particular, TC- and TES-calibrated Si, K, and S show a broad range of peaks between 0.02-0.025 cycles/ky (Period: 40-50 ky) which may represent an obliquity forcing of siliciclastic and redox systems (**Figure 12, 13**). Similarly, Meyers (2008) observed 40.32-ky and 52.52-ky periodicities in their analysis of Fischer assay oil yield data from the WPM, which

they attributed to the 52.10-ky and 39.9-ky obliquity cycles. Additionally, TC- and TES-calibrated Si, S, and K show a series of peaks around 0.03 cycles/ky (Period: 33 ky), 0.04 cycles/ky (Period: 25 ky) and 0.05 cycles/ky (Period: 20 ky), the latter two of which may record precessional forcing of the siliciclastic and redox systems. Meyers (2008) and Machlus et al. (2008) see a similar range of variability in their MTM power spectra of the WPM Fischer assay record, with Meyers (2008) attributing the observed 18.73-ky and 22.52-ky variability to the 18.8-ky and 22.6-ky precession cycles.

Temporally calibrated Si, S, and K also show power peaks at sub-precessional periodicities (<18 ky), particularly with results calibrated using the TES approach (**Figures 12, 13**) consistent with the identification of a range of sub-Milankovitch cycles by Pietras et al. (2003a). This variance was attributed to a series of lake-expansion cycles within the WPM of approximate 10 ky duration, with each typically capped by an organic-rich mudstone in the basin center locations (Pietras et al., 2003a). Given that S is most closely associated with organic material and sulfide minerals in the S-34-1 core, it is unsurprising that this element appears to be particularly sensitive to these lake depth-driven changes in organic matter content. Pietras et al. (2003a) hypothesized that these cycles resulted from either drainage network autocyclicity or a feedback of orbital forcing, climate, and tectonics.

Overall, this multi-proxy cyclostratigraphic assessment shows significant divergence in the signals recorded within different proxy elements within the same rock record, with some elements (Ca, Fe) dominated by low-frequency forcing and others (K, S) more sensitive to high-frequency forcing. The datasets used in previous cyclostratigraphic assessments of the WPM did not provide the elemental breadth to be able to evaluate the relative cyclic influence of carbonate, siliciclastic, and redox proxy elements. Based on our analysis, carbonate proxy elements, such

as Ca, are dominated by eccentricity-scale variability, with no higher-frequency power peaks showing comparable magnitude (**Figures 12, 13**). Similarly, Fe shows this strong low-frequency influence due to its strong association with alluvial facies (**Figures 12, 13**). Redox proxies such as S, on the other hand, appear to be sensitive to lake-level changes that are operating at periodicities below that of astronomical forcing, resulting in strong power peaks at the high frequencies (**Figures 12, 13**). Siliciclastic proxies such as Si and K appear to record both high- and low-frequency forcing in the WPM, possibly because the siliciclastic depositional system is more sensitive to these shorter timescale forcings than the carbonate depositional system is.

Identification of a mid-WPM Transfer Function Transition

Additionally, the continuous, high resolution, multi-proxy nature of this XRF dataset allows us to identify and characterize a notable mid-WPM change in the frequency distribution of power and amplitude coinciding with the termination of bedded evaporite deposition in the WPM record of the Solvay S-34-1 core. MTM spectra and EHA plots of temporally calibrated Si, K, Ca, and Fe records from the lower WPM show strong power and amplitude across a range of frequencies, particularly in the frequency bands associated with short eccentricity, obliquity, and precession, and sub-precession cycles (**Figures 11, 14, 15**). By contrast, MTM spectra and EHA plots of temporally calibrated Si, K, Ca, and Fe from the upper WPM show dominant low-frequency forcing in the frequencies associated with long and short eccentricity, with comparatively little power concentrated in the frequencies associated with obliquity and precession (**Figure 11, 14, 15**). Additionally, the maximum power of the obliquity and precession scale peaks in Si, K, Ca, and Fe from the lower WPM was greater than the corresponding peaks in the upper WPM (**Figures 14, 15**). This transition in the frequency distribution of power and amplitude is particularly apparent in the EHA plots for temporally

calibrated Si, K, and Ca and corresponds to the last bedded evaporite deposition in the WPM record within the Solvay S-34-1 core.

Overall, this analysis suggests that the lower WPM is more sensitive to higher-frequency obliquity, precession, and sub-Milankovitch-scale variability than the upper WPM. Given the sedimentation-rate corrections made in each of the two time-depth calibration models based on high-precision radioisotopic ages from tuffs found at known depths in the S-34-1 core, we do not anticipate that uncorrected sedimentation rate changes are generating such a major shift in the frequency distribution of power and amplitude between the lower and upper WPM. Astrochronologic analyses of coeval deep marine records do not suggest any abrupt changes in astronomical forcing around 51.06 Ma (Westerhold et al., 2009, 2018). Instead, we posit that this mid-WPM shift in variance distribution is predominantly an expression of a change in the depositional transfer function within the WPM rock record. In this case, an environmental shift in the paleo-Lake Gosiute system around the deposition of the C-Bed led to the discontinuation of bedded evaporite deposition, a facies that appears associated with a greater sensitivity to obliquity, precession, and sub-Milankovitch scale cyclicity.

Mechanisms for Changing the WPM Transfer Function

We hypothesize that this proposed shift in the expression of the sedimentary transfer function—which encrypts climate signals into the rock record—could plausibly result from a dominantly climatic or tectonic driver, which produced an environmental change in the lake that acted to disrupt the formation and/or long-term preservation of bedded evaporites above this mid-WPM transition. Studies of modern bedded evaporite deposits, such as those of the Dead Sea, suggest that deep, stratified, perennial lakes are highly conducive to bedded evaporite precipitation and preservation and that their formation typically occurs below wave base and a

thermocline (Kiro et al., 2015; Sirota et al., 2016; Sirota et al., 2017; Demicco and Lowenstein, 2020). This is largely because bedded evaporites are highly sensitive to temperature, salinity, and mixing processes, which can act to dissolve previously deposited bedded evaporites (Kiro et al., 2015; Sirota et al., 2016; Sirota et al., 2017; Demicco and Lowenstein, 2020). The close association of bedded trona and halite with organic-rich oil shale facies in the S-34-1 core supports a deep, stratified lake as a depositional environment for these bedded evaporite facies in the Wilkins Peak Member.

A shift in the climate system during the EECO greenhouse climate could certainly result in changes to the hydrologic balance of the lake basin, the temperature of the lake, and the strength of evaporative processes, each of which would impact evaporite deposition and preservation. For example, a climate system driven increase in water input into the lake basin could act to freshen the lake, reduce the lakes chemocline, and induce lake mixing, all of which would be unfavorable to the formation of bedded evaporites. Similarly, a tectonically driven change in lake basin bathymetry could change the depth and extent of the lake in a way that either enhances or minimizes the effects of evaporation, warming, and mixing within the lake.

Measurement of oxygen isotope ratios from carbonates spanning the WPM show little change from the lower WPM to the upper WPM (Norris et al., 1996; Carroll, personal communication). These results provide no conclusive evidence for climate-driven enhancement of evaporation or precipitation processes. $^{87}Sr/^{86}Sr$ ratios (Doebbert et al., 2014) also show minimal variation across the WPM, suggesting no fundamental changes in hydrologic sourcing during deposition of the WPM. Furthermore, WPM lithofacies show no major long-term shifts across the transfer function transition beyond the termination of bedded evaporite deposition. Alternations between lacustrine carbonate and alluvial siliciclastic facies start in the lower WPM

and continue similarly in the upper WPM even after the disappearance of bedded evaporites (**Figure 4**), suggesting some amount of continuity in depositional environment between the lower and upper WPM.

Given the lack of clear isotopic and sedimentological evidence in favor of a climatic driver, we suggest that structural changes occurring along the Uinta Mountain uplift were the dominant influence on this mid-WPM transfer function transition. Cross sections of the Wilkins Peak Member in Bridger sub-basin show a visible shift in the basin depocenter from a small, focused trough in the south-central region of the basin during the deposition of the lower WPM to a broad, northward focused depocenter during the deposition of the upper WPM (**Figure 2**) (Roehler 1993; Smith et al., 2015). Based on mapping done by Roehler (1993), this basin-wide mid-WPM depocenter shift coincides with the discontinuation of thrust movement along the Sparks Ranch fault, located in the northeastern boundary of the Uinta Mountains at the margin of the south-central Greater Green River Basin.

We envision that this tectonic change could have a large effect on evaporite deposition within Lake Gosiute during deposition of the WPM, contributing to the observed change the paleo-lake's depositional transfer function (**Figure 16**). During deposition of the lower WPM—prior to the deposition of the C-bed—the continued active movement of the Sparks Ranch thrust provided accommodation in the south-central Bridger sub-basin, near the location of the S-34-1 core (**Figure 1**). This allowed a narrow, deep, perennial, meromictic lake to form around this depocenter during deposition of much of the lower WPM (**Figure 16**). Due to the lake's depth, a thermocline and chemocline could be maintained, permitting bedded evaporite formation and preservation below wave base due to the denser, colder, more saline monimolimnion of the lake (**Figure 16**). Outside of the basin depocenter and above the level of the lake's thermocline and

chemocline, the bedded evaporites were not able to be preserved due to less optimal temperature, salinity, and/or mixing conditions, resulting in individual displacive mineral crystals in these regions rather than discrete evaporite mineral beds.

As movement along the Sparks Ranch thrust began to halt around the time of C-bed deposition, midway through the WPM, the continued generation of accommodation in the south-central Bridger sub-basin waned and the depocenter began to infill and shift northward, away from the location of the S-34-1 core (**Figure 16**). This produced a broader, shallower, more expansive Lake Gosiute during deposition of the upper WPM. This additional surface area and reduced water depth likely led to holomictic lake conditions due to enhanced wind-driven mixing, preventing the formation of a thermocline or chemocline. Seasonal warming of the lake waters likely led to increased lake water temperatures, which enhanced evaporite dissolution. As a result, the depositional environment at the location of the S-34-1 core, previously situated in an environment well-suited to bedded evaporite deposition, is now located in an environment that is poorly suited to the production and preservation of bedded evaporites (**Figure 16**), leading to their omission from the upper-WPM rock record in the S-34-1 core. Instead, evaporites were deposited as early diagenetic displacive crystals, which were less susceptible to dissolution by the warm waters of the lake than bedded evaporites but failed to record a similar signature of cyclic variability.

These results not only highlight the complexity of transfer functions, which integrate the effects of a broad suite of climate, depositional, burial, and diagenetic processes, but also emphasize the influence of changes in any of those processes on the environmental signals recorded in lake sediments. In the case of the Wilkins Peak Member—one of the best available continental records for the Early Eocene Climatic Optimum greenhouse—a subtle change in

basin morphology resulted in to a dramatic shift in the character of cyclic environmental signals that were preserved in the rock. Further study of sedimentary transfer functions, including lateral changes in their expression, may have utility in locating and translating particularly rich paleoclimate records within a study area.

Conclusions

The application of XRF analysis of the Wilkins Peak Member of the Green River Formation provides one of the most detailed multi-element assessments of an ancient lake system, with the goal of characterizing cyclic sedimentation within the Wilkins Peak Member of the Green River Formation at a previously unattainable level of detail, assessing changes in the expression of cyclic sedimentation, and evaluating potential sedimentary transfer-function linkages to changes in climate, tectonics, and landscape evolution.

Overall, our spectral results from the S-34-1 core for key XRF proxy elements show results that are consistent with previous cyclostratigraphic assessments of the WPM, indicating eccentricity, obliquity, precession, and sub-precession-scale cyclicity. More importantly, however, our analysis of this XRF dataset highlights a previously unrecognized shift in the frequency distribution of variance between the lower WPM and the upper WPM, which coincides with the decline of bedded evaporite deposition at approximately 51.06 Ma.

We attribute this shift to a change in the transfer function, which encodes environmental signals into the preserved WPM rock record. While a climatic cause for this change in the transfer function cannot be definitively ruled out, we propose that a structural change to the Bridger sub-basin resulting from the mid-WPM deactivation of a Uinta Mountain thrust fault sufficiently influenced the depth and extent of paleo-Lake Gosiute in a way that transitioned it

from a deep, meromictic lake that was able to deposit bedded evaporites in its depocenter to a shallow, broad, holomictic lake that was too warm and intermixed to permit the preservation of bedded evaporites. As a result, the transfer function of the lower WPM could encrypt environmental signals present in bedded evaporite deposits, while the transfer function of the upper WPM could not. While it has been noted in modern and recent lake systems that not all are depositional records are equally sensitive to recording environmental signals, this paper provides among the first characterizations of this observation within a single ancient lake system.

Acknowledgements

We thank Matteo Paperini and Solvay Chemicals, Inc. for the use of the Solvay S-34-1 core. Elizabeth Klonowski, Shlomo Honig, and Isaac Sageman assisted with the preparation, imaging, and logging of the core. We would also like to thank Mike Smith and Tim Lowenstein for their discussion of this project. This study received financial support from the National Science Foundation Integrated Earth Systems Program (NSF-EAR 1813278) the National Science Foundation Early Career Development Program (NSF-EAR 1151438), the Geological Society of America Graduate Research Grant program, the American Association of Petroleum Geologists Foundation Grants-in-aid program, and the Department of Geoscience at the University of Wisconsin-Madison.

References Cited

Aswasereelert, W., Meyers, S.R., Carroll, A.R., Peters, S.E., Smith, M.E., and Feigl, K.L., 2013, Basin-scale cyclostratigraphy of the Green River Formation, Wyoming: GSA Bulletin, v. 125, p. 216-228.

Bradley, W.H., 1929, The varves and climate of the Green River epoch: U.S. Geological Survey, Professional Paper Report 158-E, p. 87-110.

Bradley, W.H., and Eugster, H.P.,1969, Geochemistry and paleolimnology of the trona deposits and associated authigenic minerals of the Green River Formation of Wyoming: U.S. Geological Survey Professional Paper 496-B.

Carroll, A.R., and Bohacs, K.M., 1999, Stratigraphic classification of ancient lakes: Balancing tectonic and climatic controls: Geology, v. 27, p. 99–102.

Carroll, A.R., 2017, Xenoconformities and the stratigraphic record of paleoenvironmental change: Geology, v. 45, p. 639–642.

Cashion, W.B., 1995, Stratigraphy of the Green River Formation, eastern Uinta Basin, Utah and Colorado, *in* Averett, M.R., ed., The Green River Formation in Piceance Creek and eastern Uinta Basins: Grand Junction Geological Society 1995 Field Trip Guidebook, p. 15–21.

Cohen, A.S., 2003, Paleolimnology: the history and evolution of lake systems: Oxford, New York: Oxford University Press, 500 p.

Coney, P.J., and Reynolds, S.J., 1977, Cordilleran Benioff zones: Nature, v. 270, p. 403.

Culbertson, W.C., 1961, Stratigraphy of the Wilkins Peak member of the Green River Formation, Firehole Basin Quadrangle, Wyoming, Article 348: U. S. Geological Survey Professional Paper, p. D170–D173.

Demicco, R.V., and Lowenstein, T.K. When “evaporites” are not formed by evaporation: The role of temperature and pCO2 on saline deposits of the Eocene Green River Formation, Colorado, USA: GSA Bulletin, v. 132, p. 1365-1380.

Dickinson, W.R., and Snyder, W.S., 1978, Plate tectonics of the Laramide orogeny: Geological Society of America Memoirs, Geological Society of America, v. 151, p. 355–366.

Dickinson, W.R., Klute, M.A., Hayes, M.J., Janecke, S.U., Lundin, E.R., McKittrick, M.A., and Olivares, M.D., 1988, Paleogeographic and paleotectonic setting of Laramide sedimentary basins in the central Rocky Mountain region: GSA Bulletin, v. 100, p. 1023–1039.

Dyni, J.R., 1976, Trioctahedral smectite in the Green River Formation, Duchesne County, Utah: U.S. Geological Survey Professional Paper, no. 967, 14 p.

Fischer, A.G., and Roberts, L.T., 1991, Cyclicity in the Green River Formation (lacustrine Eocene) of Wyoming: Journal of Sedimentary Petrology, v. 61, p. 1146-1154.

Graf, J.W., Carroll, A.R., and Smith, M.E., 2015, Lacustrine Sedimentology, Stratigraphy, and Stable Isotope Geochemistry of the Tipton Member of the Green River Formation, *in* Smith, M., and Carroll, A., eds., Stratigraphy and Paleolimnology of the Green River Formation, Western USA: Syntheses in Limnogeology, vol. 1: Springer, Dordrecht, p. 1-12.

Higley, D.K., 1983, Distribution of bromine in bedded halite in the Green River Formation, southwestern Wyoming: U.S. Geological Survey, Open-File Report USGS Numbered Series 83–726.

Hosterman, J.W., and Dyni, J.R., 1972, Clay mineralogy of the Green River Formation, Piceance Creek Basin-A preliminary study, in Geological Survey research 1972: U.S. Geol. Survey Prof. Paper 800-D, p. D159-D163.

Johnson, T.C., 1984, Sedimentation in Large Lakes: Annual Review of Earth and Planetary Sciences, v. 12, p. 179-204.

Kiro, Y., Goldstein, S.L., Lazar, B., and Stein, M., 2016, Environmental implications of salt facies in the Dead Sea: GSA Bulletin, v. 128, p. 824–841.

Machlus, M.L, Olsen, P.E., Christie-Blick, N., Hemming, S.R., 2008, Spectral analysis of the lower Eocene Wilkins Peak Member, Green River Formation, Wyoming: Support for Milankovitch cyclicity: Earth and Planetary Science Letters, v. 268, p. 64-75.

Machlus, M.L., Ramezani, J., Bowring, S.A., Hemming, S.R., Tsukui, K., and Clyde, W.C., 2015, A strategy for cross-calibrating U–Pb chronology and astrochronology of sedimentary sequences: An example from the Green River Formation, Wyoming, USA: Earth and Planetary Science Letters, v. 413, p. 70–78.

Mason, G.M., 1987, Mineralogic aspects of stratigraphy and geochemisty of the Green River Formation, Wyoming [PhD Thesis]: Laramie, The University of Wyoming, 377 p.

Meyers, S.R, 2008, Resolving Milankovitchian controversies: the Triassic Latemar Limestone and the Eocene Green River Formation: Geology, v. 36, p. 319-322.

Meyers, S.R., 2014, Astrochron: An R Package for Astrochronology. https://cran.r-project.org/package=astrochron

Meyers, S.R., 2017, Cracking the palaeoclimate code: Nature, v. 546, p. 219–220.

Meyers, S.R., 2019, Cyclostratigraphy and the problem of astrochronologic testing: Earth-Science Reviews, v. 190, p. 190–223.

Meyers, S.R., Sageman, B.B., and Hinnov, L.A., 2001, Integrated quantitative stratigraphy of the Cenomanian-Turonian Bridge Creek Limestone Member using evolutive harmonic analysis and stratigraphic modeling: Journal of Sedimentary Research, v. 71, p. 628–644.

Picard, M.D. and High, L.R., 1972, Paleoenvironmental Reconstructions in an Area of Rapid Facies Change, Parachute Creek Member of Green River Formation (Eocene), Uinta Basin, Utah, GSA Bulletin*, v* 83, no. 9, p. 2689–2708.

Pietras, J.T., Carroll, A.R., Singer, B.S., and Smith, M.E., 2003a, 10 k.y. depositional cyclicity in the early Eocene: Stratigraphic and 40Ar/39Ar evidence from the lacustrine Green River Formation: Geology, v. 31, p. 593-596.

Pietras, J.T., Carroll, A.R., and Rhodes, M.K., 2003b, Lake basin response to tectonic drainage diversion: Eocene Green River Formation, Wyoming: Journal of Paleolimnology, v. 30, p. 115–125.

R Core Team, 2014, R: A language and environment for statistical computing: R Foundation for Statistical Computing, Vienna, Austria.

Remy, R.R., 1992, Stratigraphy of the Eocene part of the Green River Formation in the south-central part of the Uinta Basin, Utah: Bulletin Report 1787BB.

Rhodes, M.K., Carroll, A.R., Pietras, J.T., Beard, B.L., and Johnson, C.M., 2002, Strontium isotope record of paleohydrology and continental weathering, Eocene Green River Formation, Wyoming: Geology, v. 30, p. 167–170.

Rhodes, M.K., Malone, D.H., Carroll, A.R., and Smith, E.M., 2007, Sudden Desiccation of Lake Gosiute at ~49 Ma: A Downstream Record of Heart Mountain Faulting?: The Mountain Geologist, v. 44, p. 1–10.

Rhodes, M.K., and Carroll, A.R., 2015, Lake Type Transition from Balanced-Fill to Overfilled: Laney Member, Green River Formation, Washakie Basin, Wyoming, *in* Smith, M., and Carroll, A., eds., Stratigraphy and Paleolimnology of the Green River Formation, Western USA: Syntheses in Limnogeology, vol. 1: Springer, Dordrecht, p. 103-126

Robb, W.A., and Smith, J.W., 1974, Mineral profile of the oil shales in Colorado Core Hole No. 1, Piceance Creek Basin, Colorado: in D. Keith Murray, ed., Guidebook to the Energy Resources of the Piceance Creek Basin Colorado: Rocky Mountain Association of Geologists Twenty-Fifth Field Conference Guidebook, p. 91-100.

Roehler, H.W., 1973, Stratigraphic divisions and geological history of the Laney member of the Green River Formation in the Washakie Basin in southwestern Wyoming: US Geological Survey, Bulletin, v. 1372-E.

Roehler, H.W., 1991, Revised stratigraphic nomenclature for the Wasatch and Green River formations of Eocene age, Wyoming, Utah, and Colorado: US Geological Survey, Professional Paper, v. 1506-B.

Roehler, H.W., 1993, Eocene climates, depositional environments, and geography, greater Green River basin, Wyoming, Utah, and Colorado: US Geological Survey, Professional Paper Report 1506-F.

Sageman, B.B., and Hollander, D.J., 1999, Integration of paleoecological and geochemical proxies: a holistic approach to the study of past global change. In: Johnson, C.J., and Barrera, E., eds., The Evolution of Cretaceous Ocean/Climate Systems. Geological Society of America, Special Paper 332, p. 365-384.

Schiffelbein, P., and Dorman, L., 1986, Spectral effects of time-depth nonlinearities in deep sea sediment records: A demodulation technique for realigning time and depth scales: Journal of Geophysical Research: Solid Earth, v. 91, p. 3821–3835.

Scott, J.J., and Smith, M.E., 2015, Trace Fossils of the Eocene Green River Lake Basins, Wyoming, Utah, and Colorado, *in* Smith, M., and Carroll, A., eds., Stratigraphy and

Paleolimnology of the Green River Formation, Western USA: Syntheses in Limnogeology, vol 1.: Springer, Dordrecht, p. 313-350.

Sheliga, C.M., 1980, Sedimentation of the Eocene Green River Formation in Sevier and Sanpete Counties, Utah [M.S. Thesis]: Columbus, The Ohio State University, 166 p.

Sirota, I., Arnon, A., and Lensky, N.G., 2016, Seasonal variations of halite saturation in the Dead Sea: Water Resources Research, v. 52, p. 7151–7162.

Sirota, I., Enzel, Y., and Lensky, N.G., 2017, Temperature seasonality control on modern halite layers in the Dead Sea: In situ observations: GSA Bulletin, v. 129, p. 1181–1194.

Smith, M.E., Singer, B.S., and Carroll, A.R., 2003, 40Ar/39Ar geochronology of the Eocene Green River Formation, Wyoming: GSA Bulletin, v. 115, p. 549–565.

Smith, M.E., Carroll, A.R., and Singer, B.S., 2008, Synoptic reconstruction of a major ancient lake system: Eocene Green River Formation, western United States: Geological Society of America Bulletin, v. 120, p. 54-84.

Smith, M.E., Chamberlain, K.R., Singer, B.S., and Carroll, A.R., 2010, Eocene clocks agree: Coeval $^{40}Ar/^{39}Ar$, U-Pb, and astronomical ages from the Green River Formation, Geology, v. 38, no. 6, p. 527–530.

Smith, M.E., Carroll, A.R., Jicha, B.R., Cassel, E.J., and Scott, J.J., 2014a, Paleogeographic record of Eocene Farallon slab rollback beneath western North America: Geology, v. 42, p. 1039–1042.

Smith, M.E., Carroll, A.R., Scott, J.J., and Singer, B.S., 2014b, Early Eocene carbon isotope excursions and landscape destabilization at eccentricity minima: Green River Formation of Wyoming: Earth and Planetary Science Letters, v. 403, p. 393–406.

Smith, M.E., and Carroll, A.R., 2015, Introduction to the Green River Formation, *in* Smith, M., and Carroll, A., eds., Stratigraphy and Paleolimnology of the Green River Formation, Western USA: Syntheses in Limnogeology, vol 1.: Springer, Dordrecht, p. 1-12.

Sullivan, R., 1980, A stratigraphic evaluation of the Eocene rocks of southwestern Wyoming: Reports of Investigations, The Geological Survey of Wyoming, No. 20, p. 1-50.

Surdam, R.C., and Stanley, K.O., 1980, Effects of changes in drainage-basin boundaries on sedimentation in Eocene Lakes Gosiute and Uinta of Wyoming, Utah, and Colorado: Geology, v. 8, p. 135–139.

Thomson, D.J., 1982, Spectrum estimation and harmonic analysis: Proceedings of the IEEE, v.70, p. 1055–1096.

Walters, A.P., Meyers, S.R., Carroll, A.R., Hill, T.R., and Vanden Berg, M.D., 2020, Lacustrine cyclicity in the early Eocene Green River Formation, Uinta Basin, Utah: Evidence from X-ray fluorescence core scanning: Journal of Sedimentary Research, v. 90, p. 429–447

Westerhold, T., and Röhl, U., 2009, High resolution cyclostratigraphy of the early Eocene–new insights into the origin of the Cenozoic cooling trend: Climate of the Past, v. 5, p. 309–327.

Westerhold, T., Röhl, U., Donner, B., and Zachos, J.C., 2018, Global Extent of Early Eocene Hyperthermal Events: A New Pacific Benthic Foraminiferal Isotope Record From Shatsky Rise (ODP Site 1209): Paleoceanography and Paleoclimatology, v. 33, p. 626–642.

Wiig, S.V., Grundy, W.D., and Dyni, J.R., 1995, Trona resources in the Green River basin, southwest Wyoming: U.S. Geological Survey, Open-File Report USGS Numbered Series 95–476.

Zachos, J.C., 2001, Trends, Rhythms, and Aberrations in Global Climate 65 Ma to Present: Science, v. 292, p. 686-693.

Zachos, J.C., Dickens, G.R., and Zeebe, R.E., 2008, An early Cenozoic perspective on greenhouse warming and carbon-cycle dynamics: Nature, v. 451, p. 279–283.

Figures and Tables

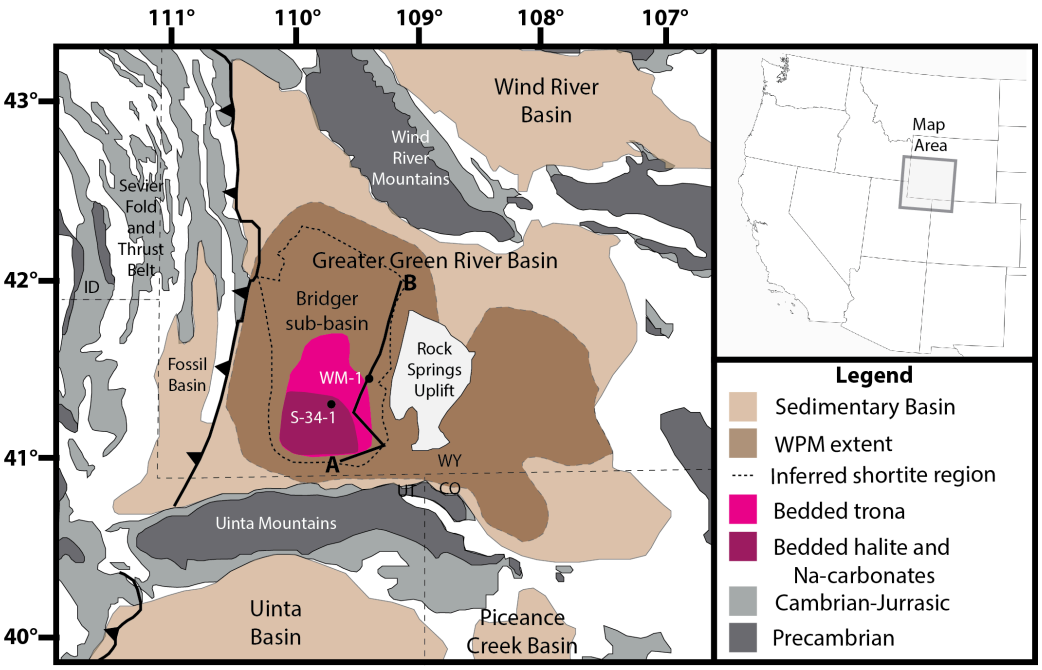

Figure 1: Location map for the Greater Green River Basin, Green River Formation. Modified from Smith et al. (2008) and Jagniecki et al. (2015)

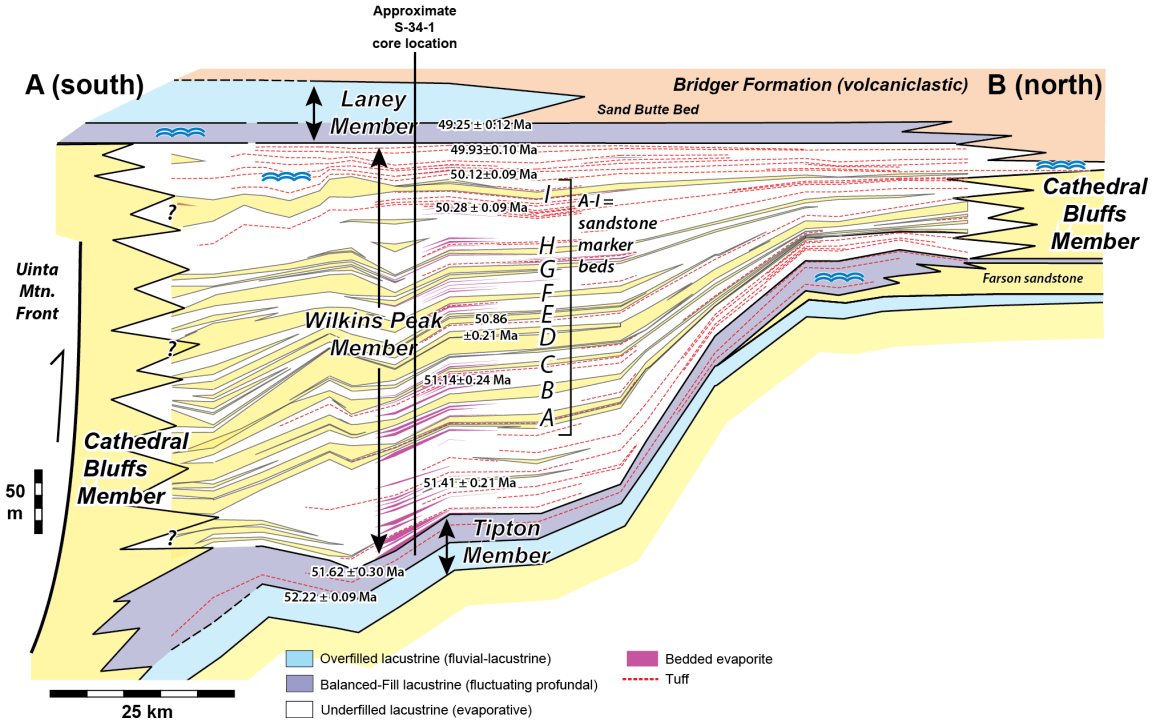

Figure 2: Cross section of the Bridger sub-basin, Greater Green River Basin across the A to B transect shown in Figure 1. Modified from Smith et al. (2015).

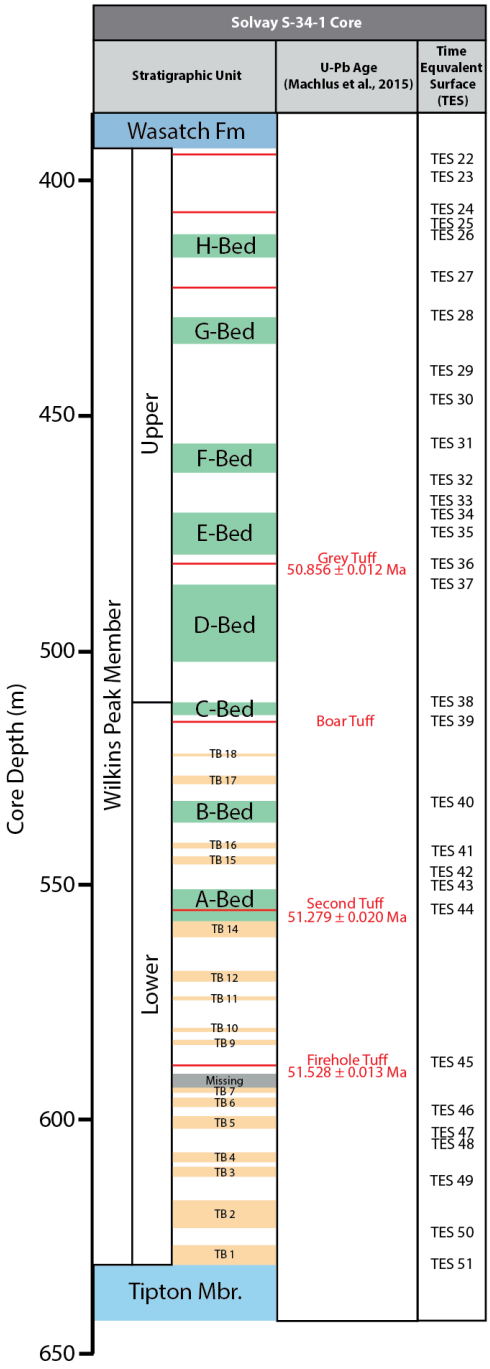

Figure 3: Generalized stratigraphy of the Solvay S-34-1 core, with the locations of the main radioscopically dated tuffs (red) and time-equivalent surface locations. Within the Wilkins Peak Member, green shading represents alluvial facies, orange shading represents bedded evaporite facies (TB=Trona Beds), and white represents lacustrine carbonate facies. U-Pb ages are from Machlus et al. (2015) and the uncertainties shown are analytical uncertainties (2 sigma).

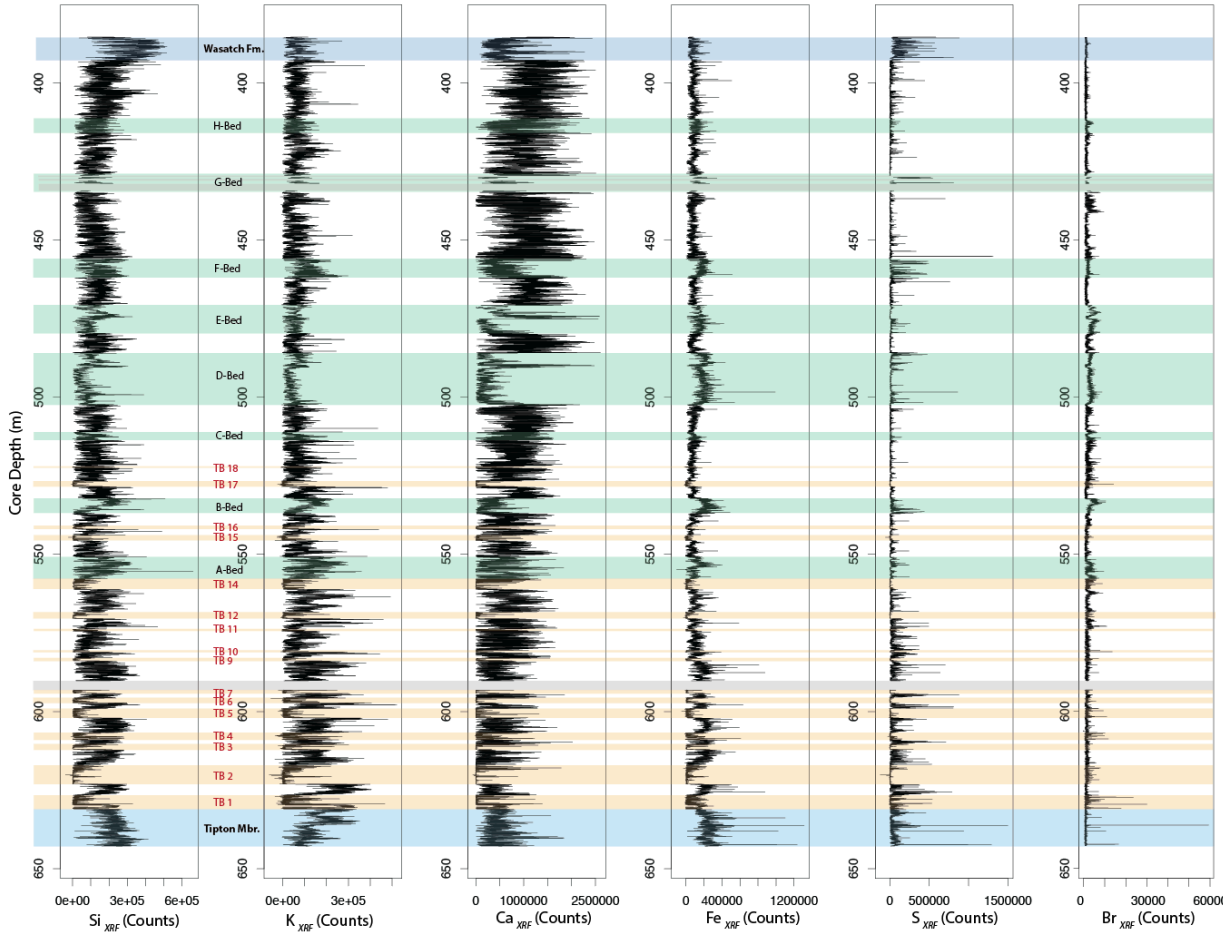

Figure 4: XRF core scanner results (in counts) for Si, K, Ca, Fe, S, and Br. Within the Wilkins Peak Member, green shading represents alluvial facies, orange shading represents bedded evaporite facies (TB=Trona Bed), and white represents lacustrine carbonate facies.

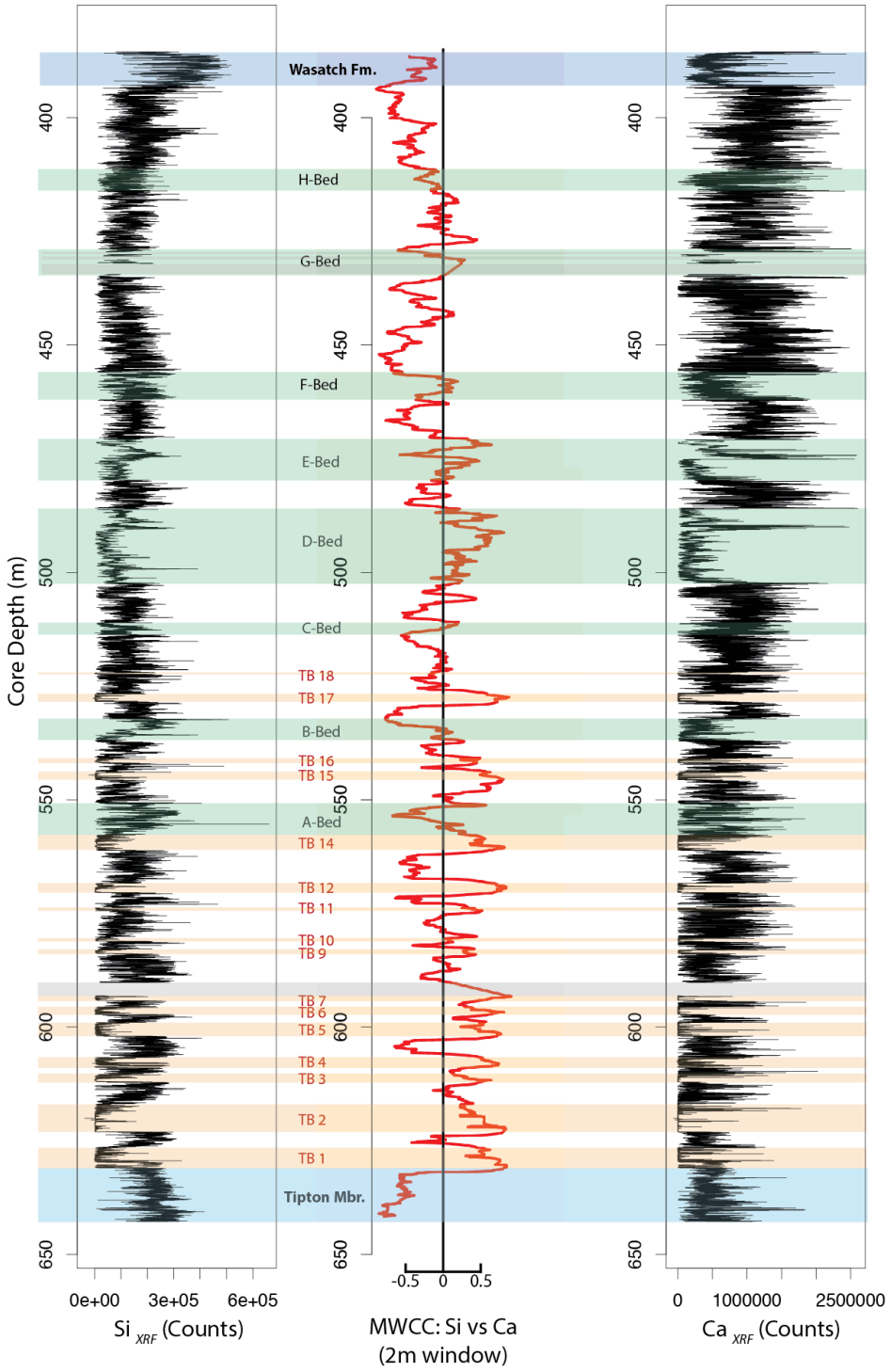

Figure 5: Moving window cross correlation (MWCC) of the Ca and Si XRF data. The MWCC correlation coefficient is represented by the red line. Within the Wilkins Peak Member, green shading represents alluvial facies, orange shading represents bedded evaporite facies, and white represents carbonate marl facies.

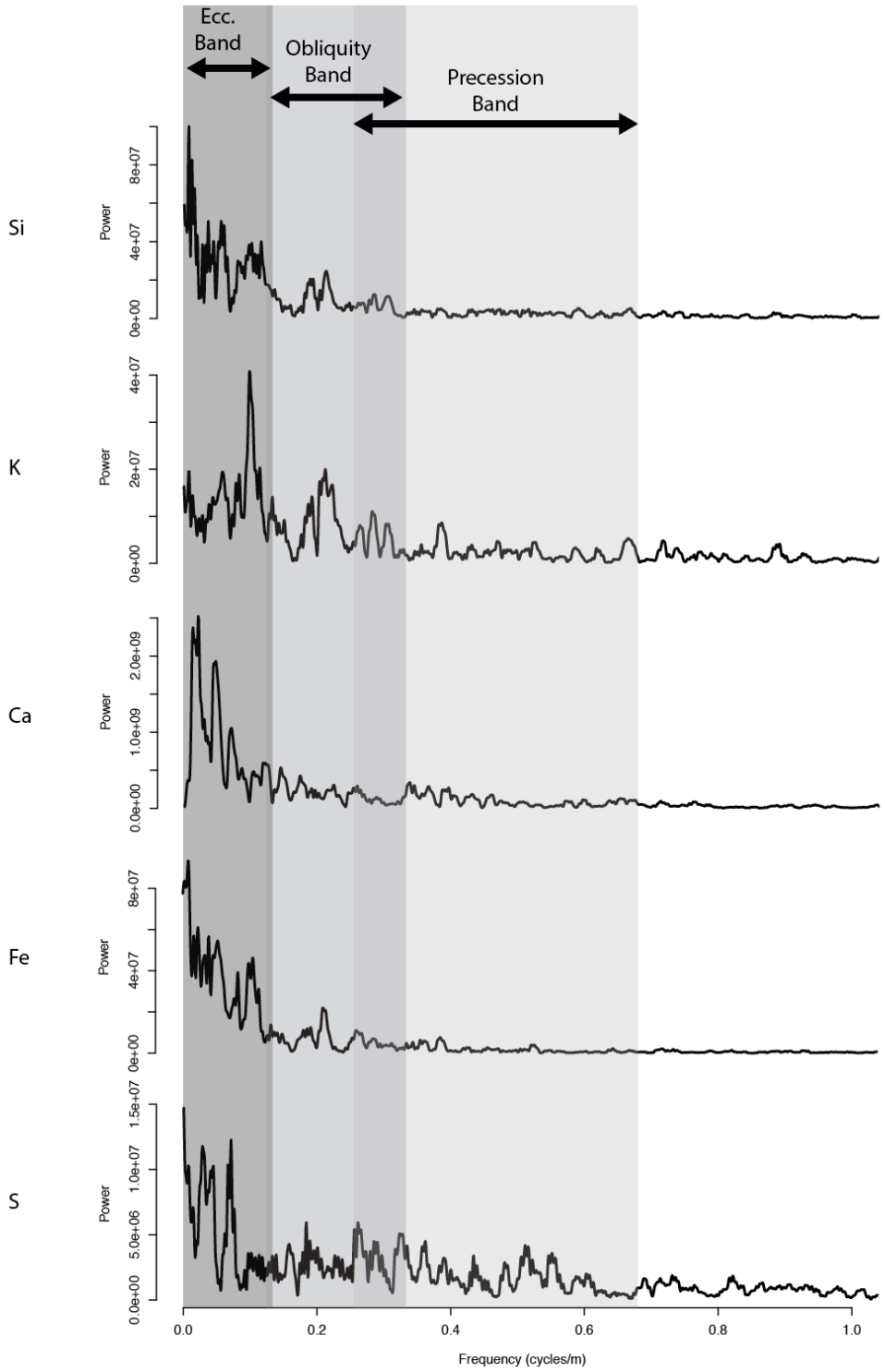

Figure 6: MTM power spectra (3-2 DPSS tapers) for drift corrected Si, K, Ca, Fe, and S elemental records in the depth domain. Grey bars and black arrows denote estimated eccentricity, obliquity, and precession frequency band given annual net accumulation rates of 75 to 200 micrometers/yr.

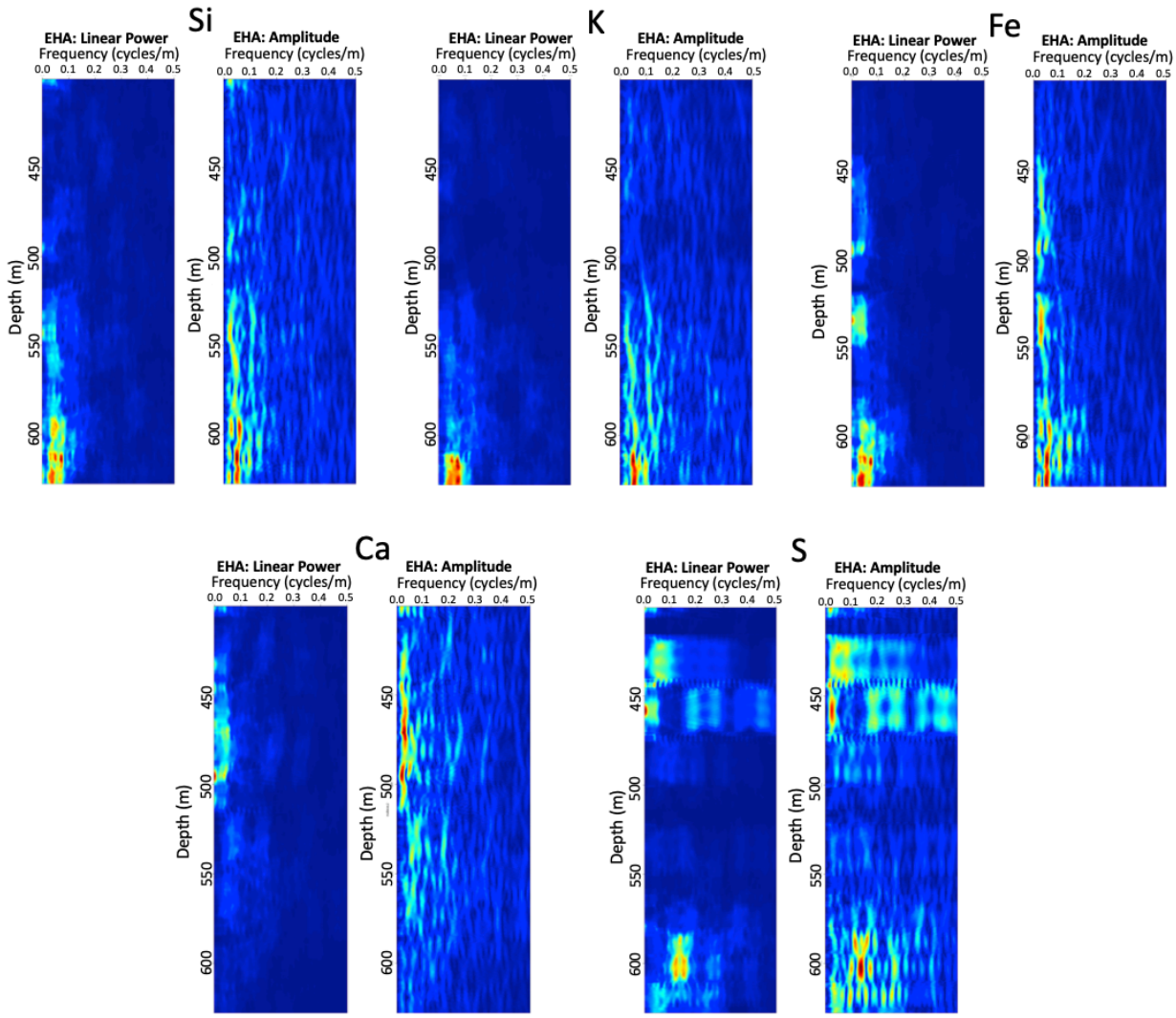

Figure 7: EHA (3-2 DPSS tapers, 30 m window) plots for drift-corrected Si, K, Ca, Fe, and S elemental records in the depth domain.

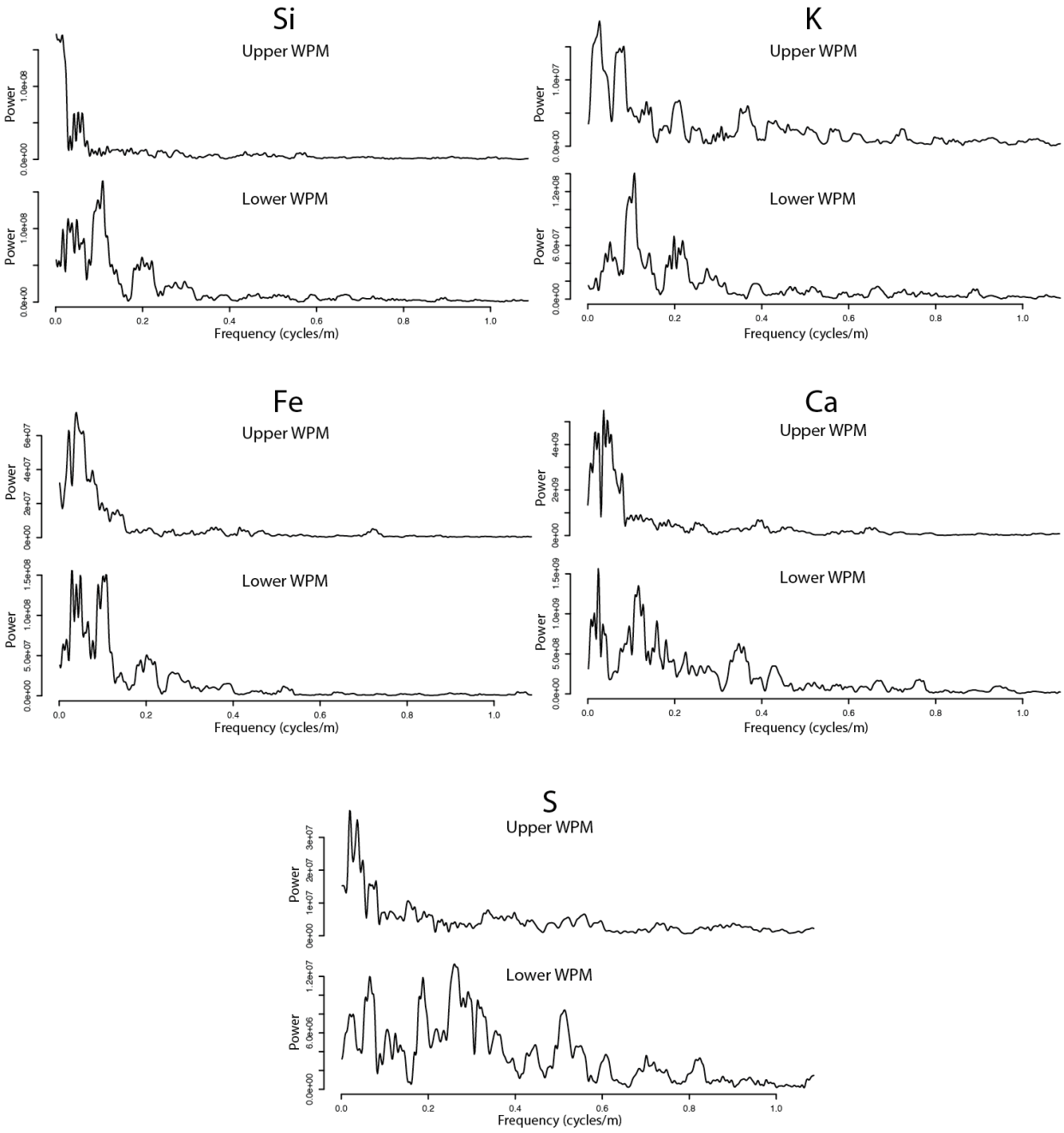

Figure 8: MTM power spectra (3-2 DPSS tapers) for drift-corrected Si, K, Ca, Fe, and S elemental records in the depth domain completed on the upper WPM and lower WPM intervals.

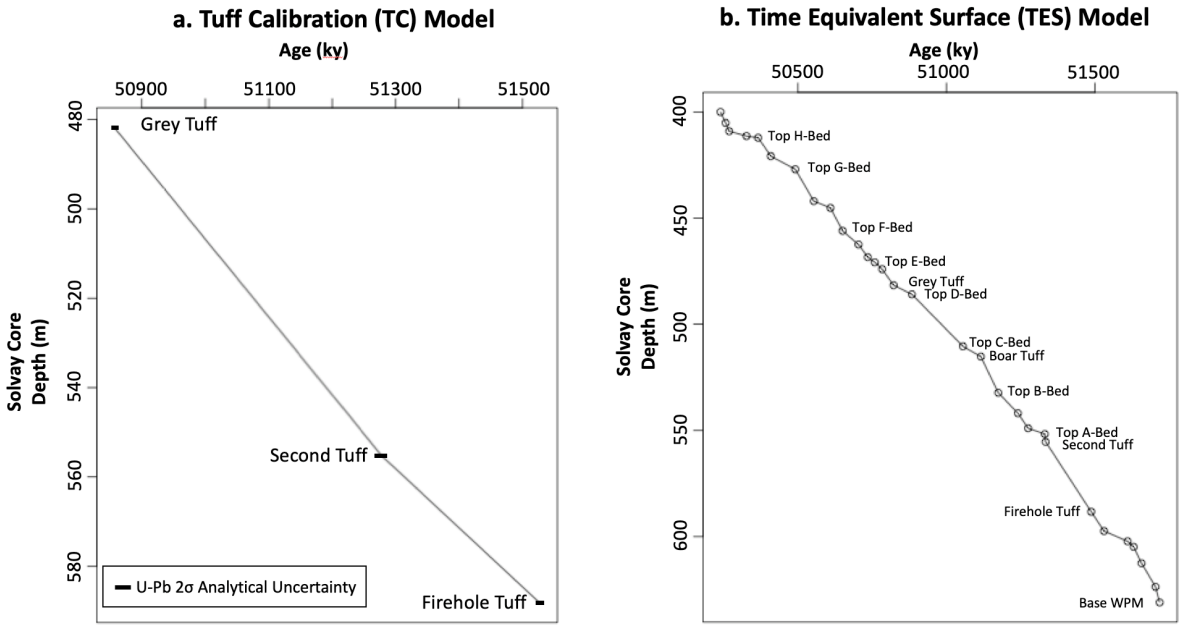

Figure 9: Time-depth models used in the a) tuff calibration model, and b) time-equivalent surface (TES) models. Radioisotopic ages from Machlus et al. (2015).

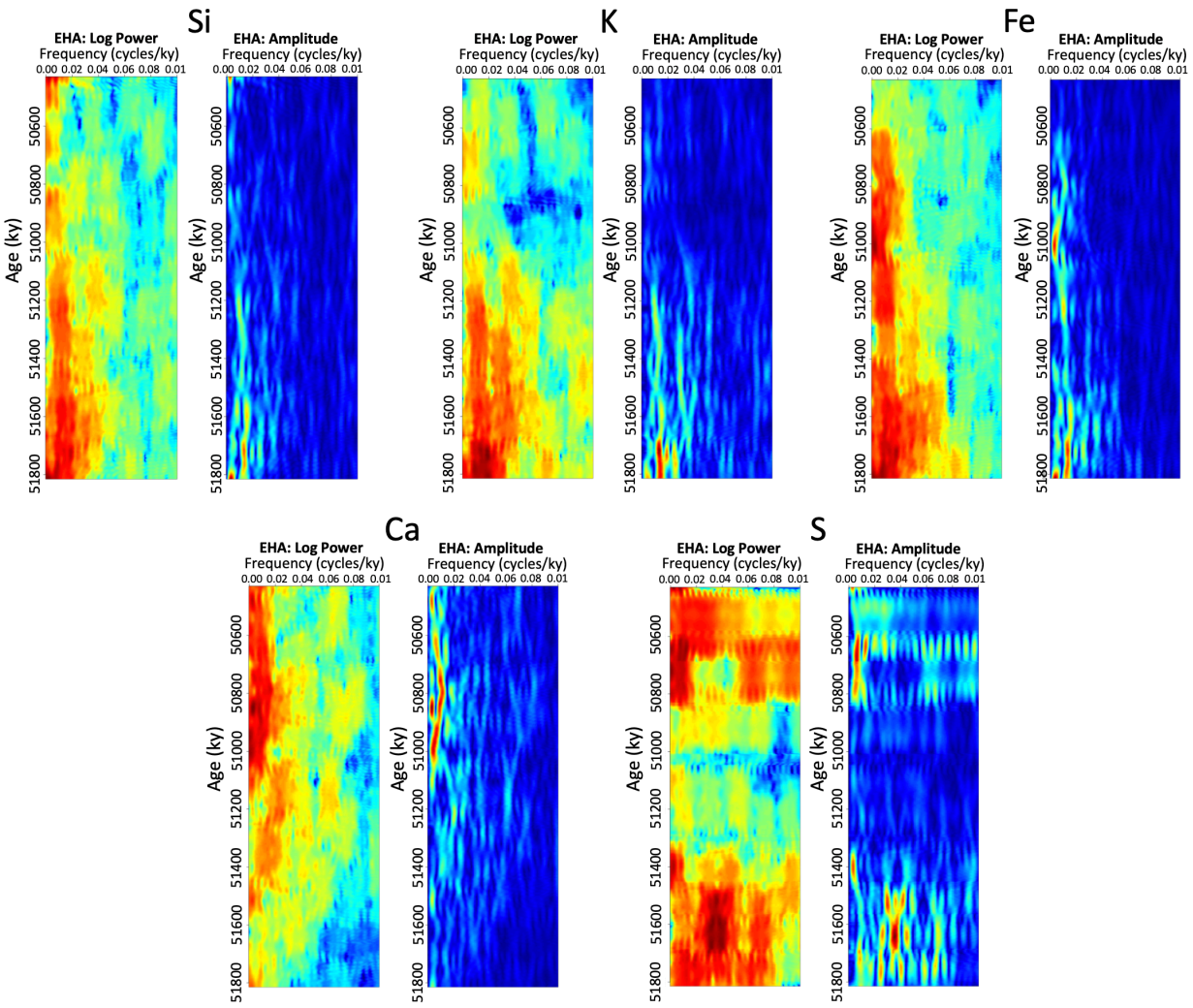

Figure 10: EHA (3-2 DPSS tapers, 250 ky window) plots for drift-corrected Si, K, Ca, Fe, and S elemental records temporally calibrated using the tuff calibration (TC) method.

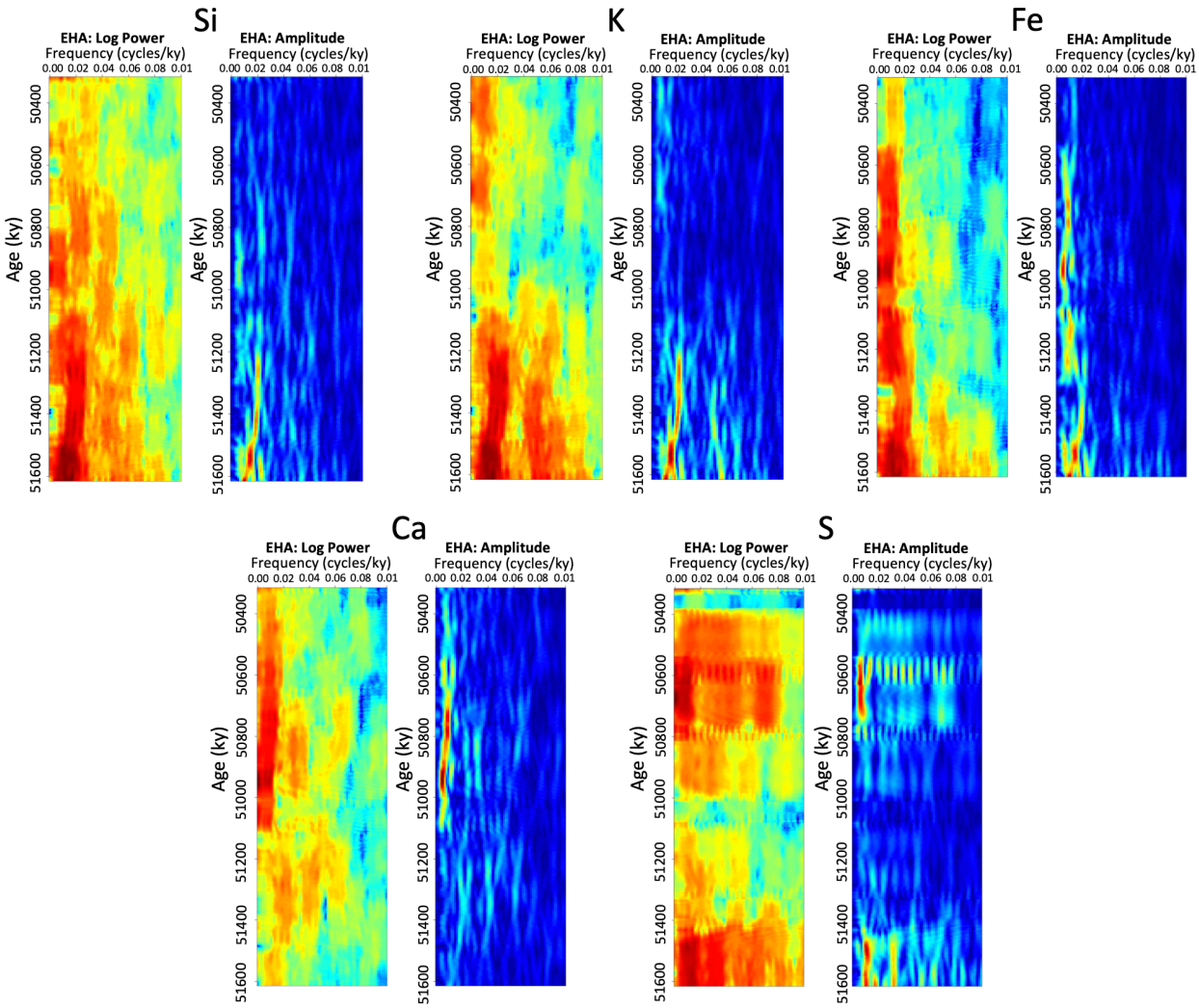

Figure 11: EHA (3-2 DPSS tapers, 250 ky window) plots for drift-corrected Si, K, Ca, Fe, and S elemental records temporally calibrated using the time-equivalent surface (TES) method.

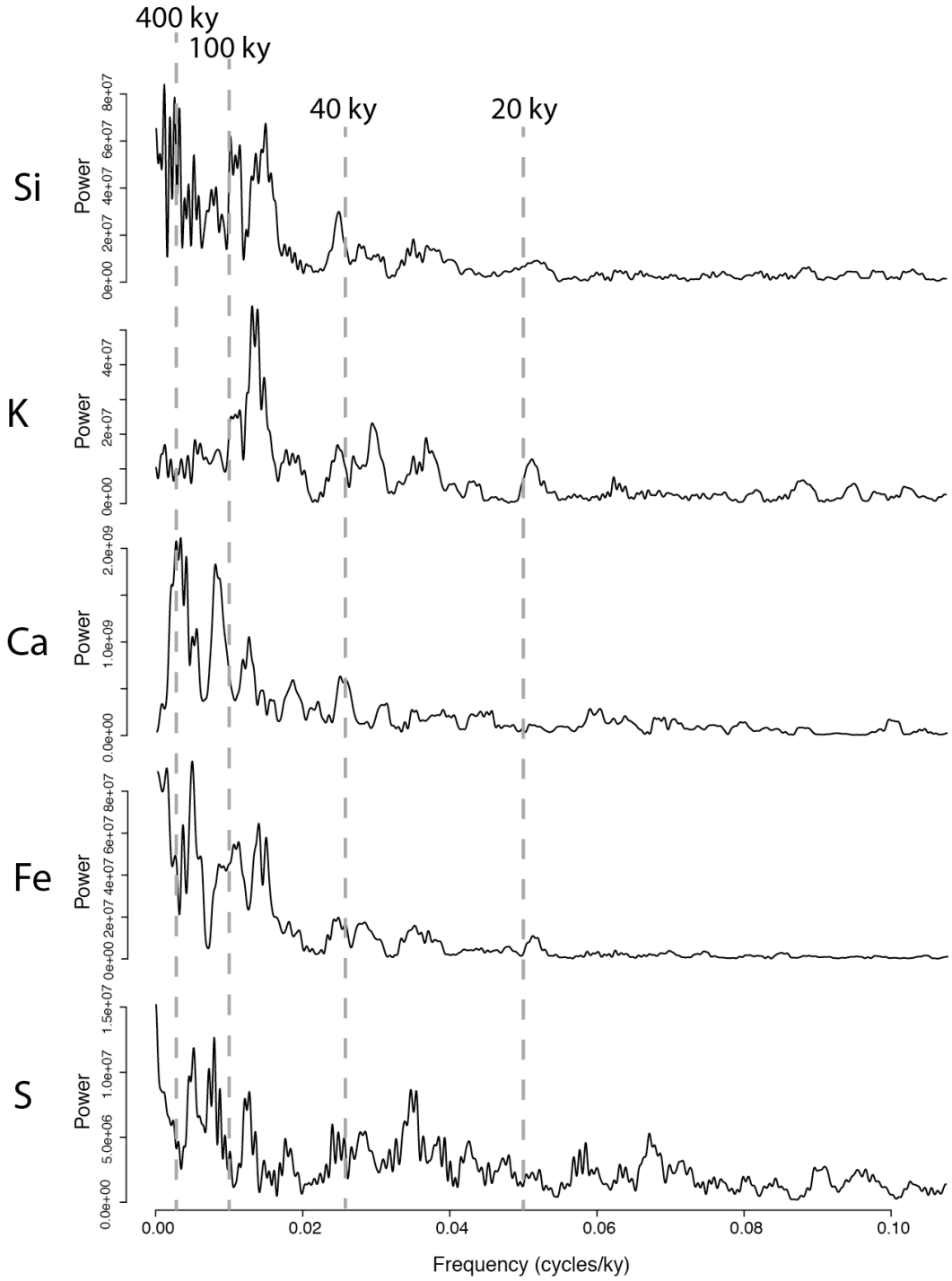

Figure 12: MTM power spectra (3-2 DPSS tapers) for drift-corrected, temporally calibrated (TC method) Si, K, Ca, Fe, and S elemental records. Dotted grey lines represent labeled periodicities within the power spectral plots.

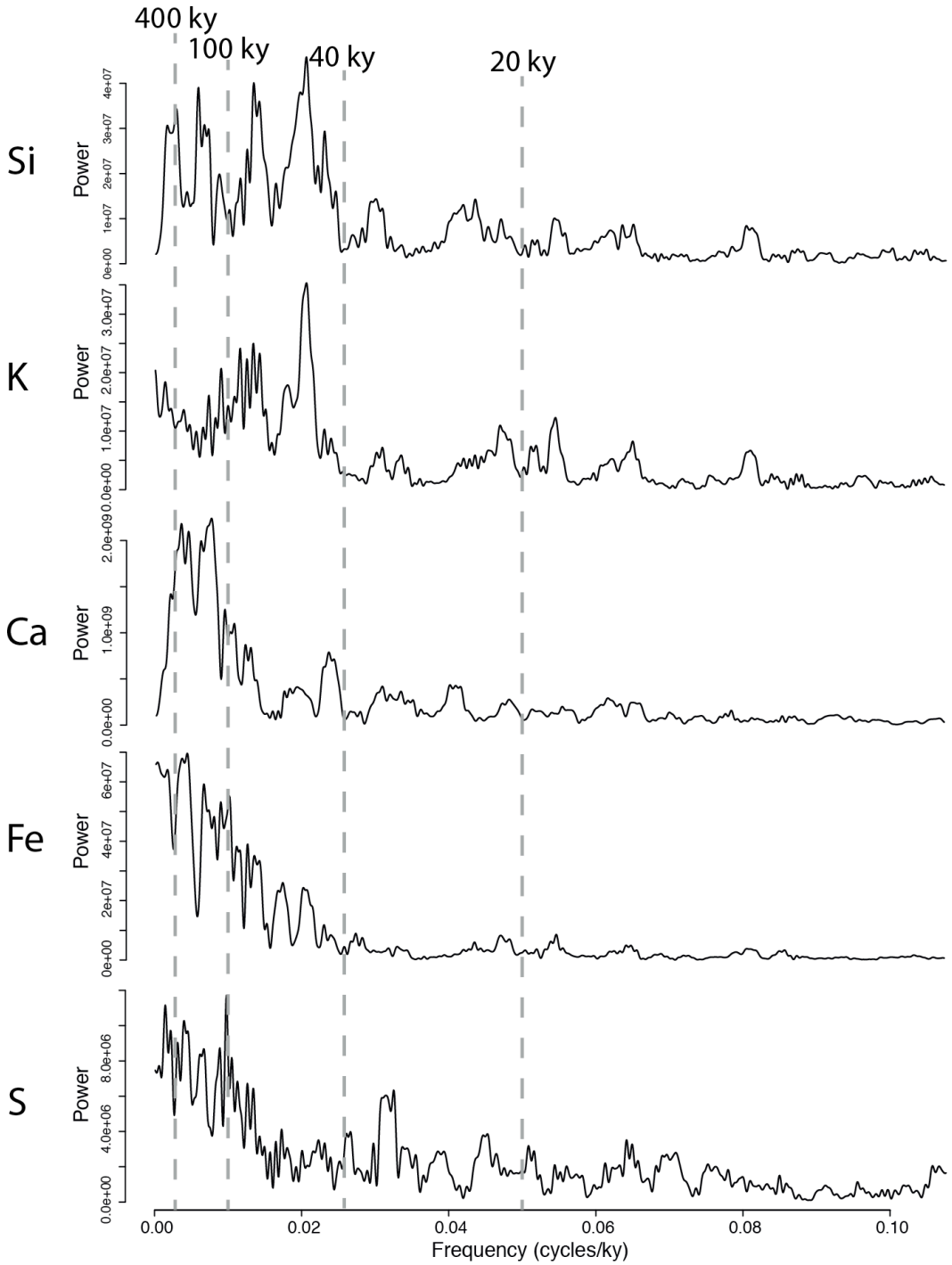

Figure 13: MTM power spectra (3-2 DPSS tapers) for drift-corrected, temporally calibrated (TES method) Si, K, Ca, Fe, and S elemental records. Dotted grey lines represent labeled periodicities within the power spectral plots.

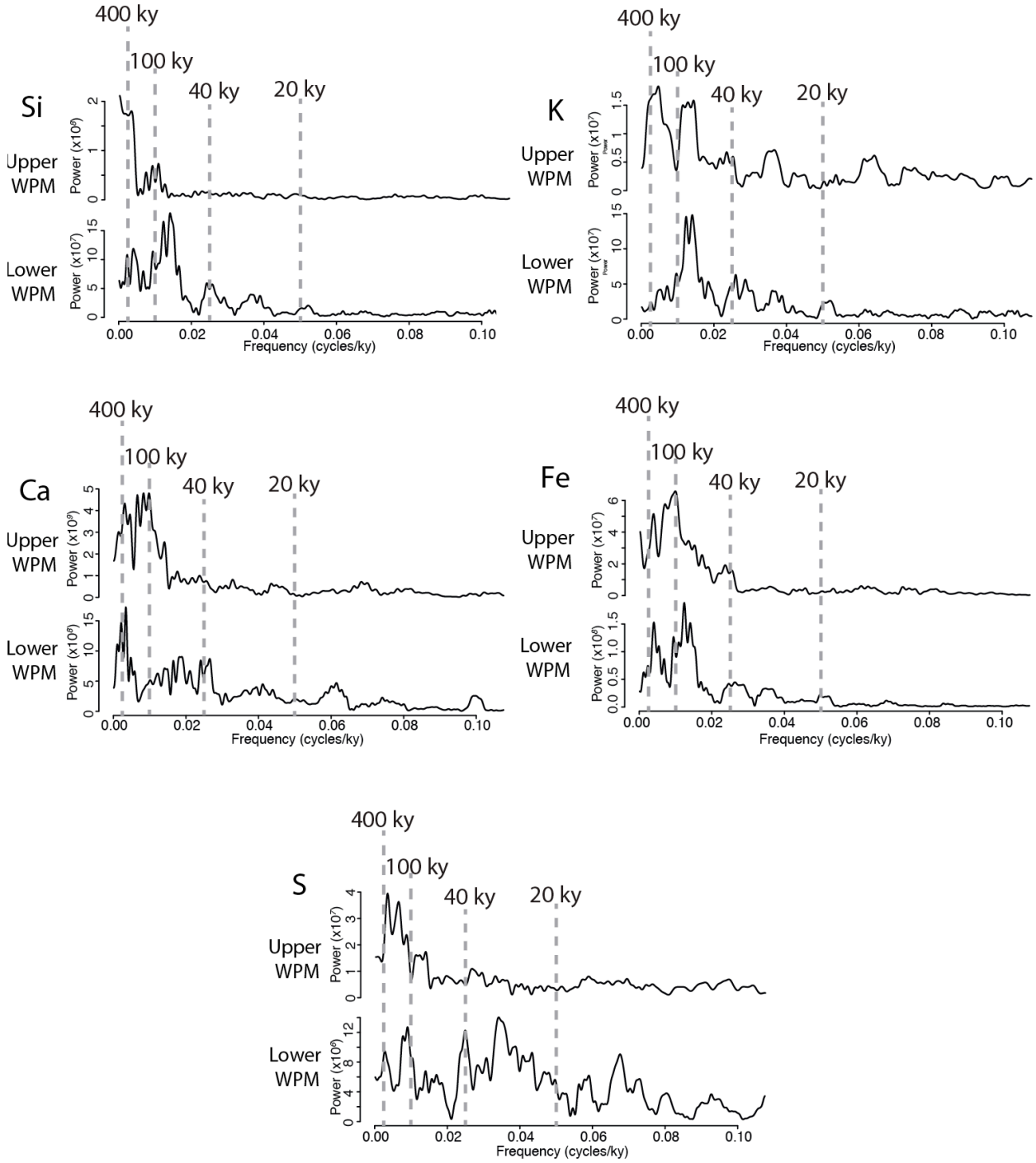

Figure 14: MTM power spectra (3-2 DPSS tapers) for drift-corrected, temporally calibrated (tuff calibration model) Si, K, Ca, Fe, and S elemental records in the depth domain completed on the upper WPM and lower WPM intervals.

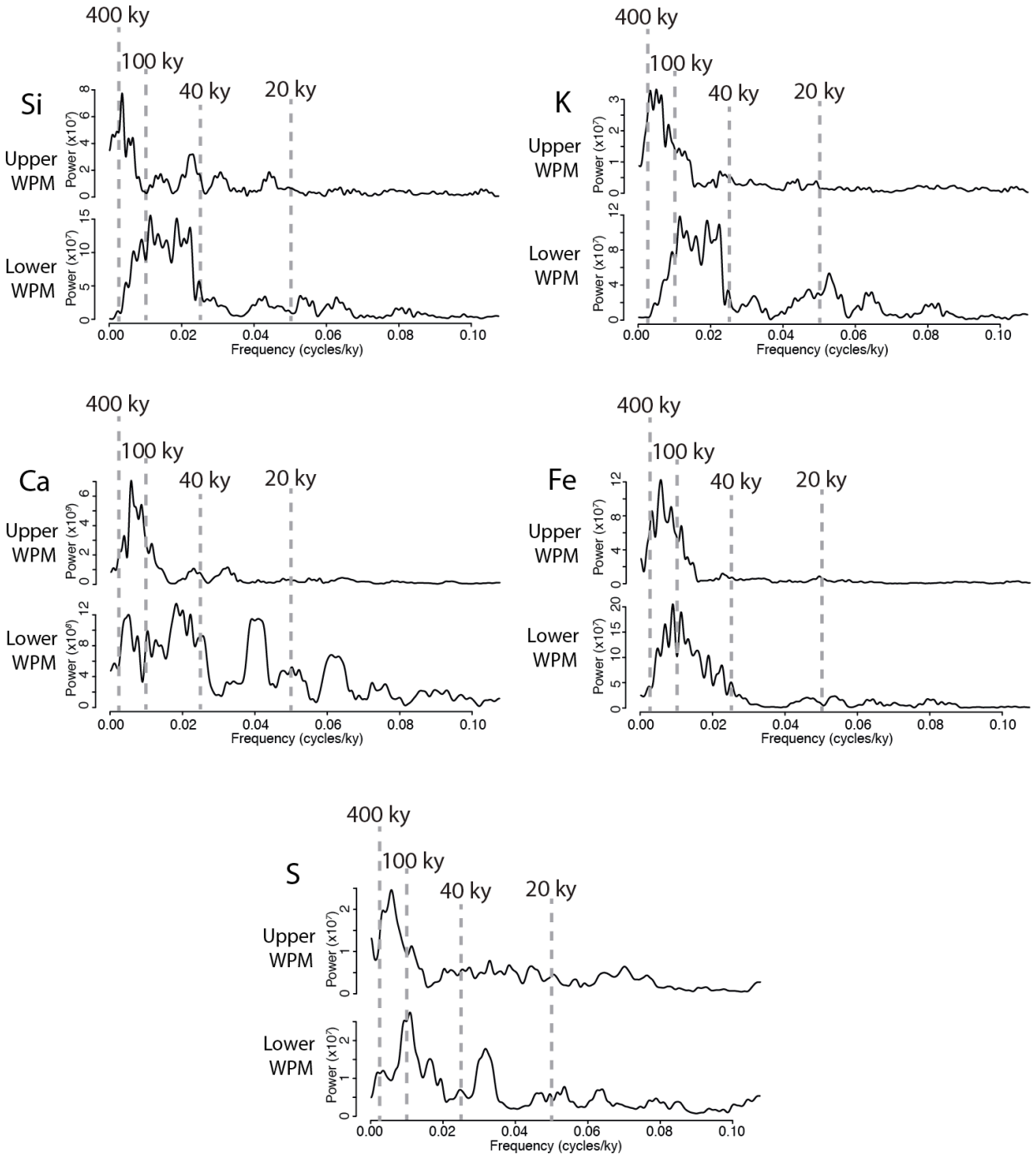

Figure 15: MTM power spectra (3-2 DPSS tapers) for drift-corrected, temporally calibrated (time-equivalent surface model) Si, K, Ca, Fe, and S elemental records in the depth domain completed on the upper WPM and lower WPM intervals.

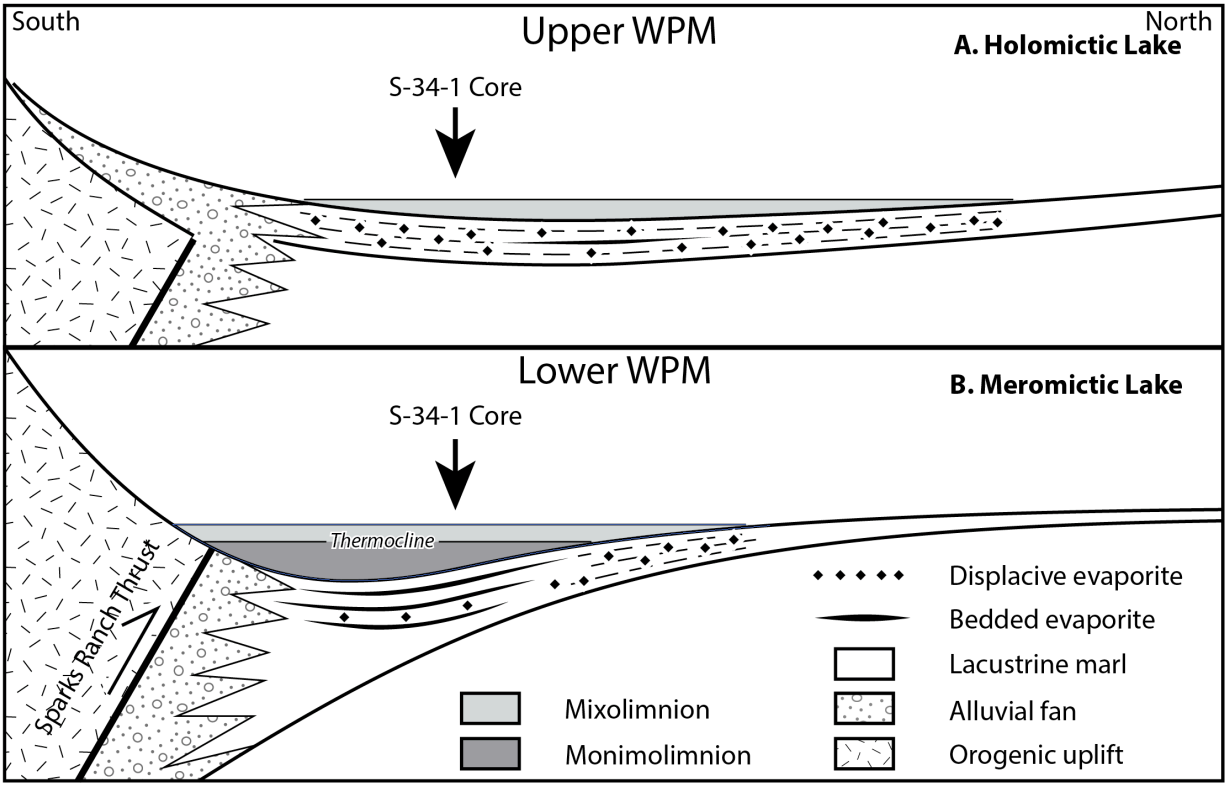

Figure 16: Schematic model for a tectonic-driven change in the depositional transfer function between the lower WPM (lower panel) and upper WPM (upper panel).

Table 1: Weighted mean U-Pb ages from Machlus et al. (2015) used in the tuff calibration model. U-Pb uncertainties are total uncertainties (2 sigma).

Tuff	Age (Ma)	Total Uncertainty (Ma)
Grey	50.856	0.060
Second	51.279	0.064
Firehole	51.528	0.061

Table 2: Modeled ages for the 30 time-equivalent surfaces identified in the S-34-1 core. These surfaces were calculated using the approach of Aswasereelert et al. (2013) and the weighted mean U-Pb ages of Machlus et al. (2015).

TES #	Modeled Age (Ma)	Surface Name
22	50.239	
23	50.256	
24	50.268	
25	50.327	
26	50.366	Top of H-Bed
27	50.409	
28	50.491	Top of G-Bed
29	50.554	
30	50.610	
31	50.650	Top of F-Bed
32	50.704	
33	50.735	
34	50.759	Top of E-Bed
35	50.784	
36	50.822	Grey Tuff
37	50.884	Top of D-Bed
38	51.056	Top of C-Bed
39	51.116	Boar/C-Bed Tuff
40	51.175	Top of B-Bed
41	51.241	
42	51.275	
43	51.331	Top of A-Bed
44	51.334	Second Tuff
45	51.488	Firehole Tuff
46	51.531	
47	51.610	
48	51.631	
49	51.657	
50	51.704	
51	51.718	Base of WPM

Table 3: Pearson correlation coefficients for pairs of XRF elemental records for the S-34-1 core study interval.

Element	Mg	Al	Si	P	S	Cl	K	Ca	Ti	V	Cr	Mn	Fe	Rh	Cu	Zn	Br	Rb	Sr	Y	Zr	Mo	Pb
Mg	1.00	0.10	0.26	0.03	-0.15	-0.25	0.14	0.34	0.02	-0.12	0.17	0.31	0.05	0.02	0.04	-0.06	-0.18	-0.05	0.33	-0.30	-0.09	0.06	-0.03
Al	0.10	1.00	0.74	-0.04	0.15	-0.22	0.84	-0.14	0.71	-0.18	0.15	0.04	0.65	-0.04	0.65	0.62	-0.09	0.65	-0.19	-0.05	0.10	0.17	0.28
Si	0.26	0.74	1.00	-0.26	0.14	-0.29	0.62	0.12	0.47	-0.31	0.24	0.13	0.43	-0.03	0.40	0.48	-0.14	0.44	-0.01	-0.22	0.20	0.05	0.19
P	0.03	-0.04	-0.26	1.00	-0.10	0.06	0.03	-0.16	0.02	0.08	-0.03	0.08	0.06	-0.04	0.02	-0.07	0.10	0.00	0.02	0.09	-0.03	0.12	-0.02
S	-0.15	0.15	0.14	-0.10	1.00	0.05	0.17	-0.14	0.17	-0.08	0.04	-0.07	0.32	-0.06	0.13	0.19	0.06	0.19	-0.15	0.00	0.11	0.15	0.30
Cl	-0.25	-0.22	-0.29	0.06	0.05	1.00	-0.17	-0.30	-0.04	0.10	-0.15	0.07	0.17	-0.25	-0.02	0.26	0.50	0.35	-0.14	0.10	0.11	-0.13	0.01
K	0.14	0.84	0.62	0.03	0.17	-0.17	1.00	-0.12	0.58	-0.21	0.19	0.06	0.55	-0.07	0.57	0.56	-0.06	0.62	-0.12	-0.16	0.04	0.20	0.21
Ca	0.34	-0.14	0.12	-0.16	-0.14	-0.30	-0.12	1.00	-0.23	-0.30	0.41	0.19	-0.21	-0.06	-0.22	-0.25	-0.33	-0.36	0.85	-0.28	-0.03	-0.08	-0.11
Ti	0.02	0.71	0.47	0.02	0.17	-0.04	0.58	-0.23	1.00	-0.12	0.08	0.06	0.67	-0.03	0.57	0.62	0.05	0.67	-0.23	0.05	0.15	0.13	0.24
V	-0.12	-0.18	-0.31	0.08	-0.08	0.10	-0.21	-0.30	-0.12	1.00	-0.30	-0.14	-0.15	0.11	-0.08	-0.15	0.08	-0.12	-0.27	0.23	-0.07	0.00	-0.04
Cr	0.17	0.15	0.24	-0.03	0.04	-0.15	0.19	0.41	0.08	-0.30	1.00	0.07	0.15	-0.11	0.06	0.08	-0.10	0.06	0.40	-0.26	0.04	0.05	0.04
Mn	0.31	0.04	0.13	0.08	-0.07	0.07	0.06	0.19	0.06	-0.14	0.07	1.00	0.17	-0.08	0.02	0.06	0.07	0.07	0.24	-0.17	0.00	-0.04	-0.02
Fe	0.05	0.65	0.43	0.06	0.32	0.17	0.55	-0.21	0.67	-0.15	0.15	0.17	1.00	-0.12	0.55	0.66	0.21	0.75	-0.18	-0.02	0.11	0.14	0.34
Rh	0.02	-0.04	-0.03	-0.04	-0.06	-0.25	-0.07	-0.06	-0.03	0.11	-0.11	-0.08	-0.12	1.00	-0.03	-0.12	-0.13	-0.15	-0.10	0.08	-0.05	-0.02	-0.03
Cu	0.04	0.65	0.40	0.02	0.13	-0.02	0.57	-0.22	0.57	-0.08	0.06	0.02	0.55	-0.03	1.00	0.59	-0.07	0.57	-0.18	-0.03	0.06	0.17	0.34
Zn	-0.06	0.62	0.48	-0.07	0.19	0.26	0.56	-0.25	0.62	-0.15	0.08	0.06	0.66	-0.12	0.59	1.00	0.15	0.83	-0.27	-0.02	0.15	0.05	0.22
Br	-0.18	-0.09	-0.14	0.10	0.06	0.50	-0.06	-0.33	0.05	0.08	-0.10	0.07	0.21	-0.13	-0.07	0.15	1.00	0.30	-0.22	0.09	0.06	-0.04	0.18
Rb	-0.05	0.65	0.44	0.00	0.19	0.35	0.62	-0.36	0.67	-0.12	0.06	0.07	0.75	-0.15	0.57	0.83	0.30	1.00	-0.32	-0.03	0.15	0.10	0.21
Sr	0.33	-0.19	-0.01	0.02	-0.15	-0.14	-0.12	0.85	-0.23	-0.27	0.40	0.24	-0.18	-0.10	-0.18	-0.27	-0.22	-0.32	1.00	-0.30	-0.01	-0.04	-0.11
Y	-0.30	-0.05	-0.22	0.09	0.00	0.10	-0.16	-0.28	0.05	0.23	-0.26	-0.17	-0.02	0.08	-0.03	-0.02	0.09	-0.03	-0.30	1.00	0.11	-0.03	0.02
Zr	-0.09	0.10	0.20	-0.03	0.11	0.11	0.04	-0.03	0.15	-0.07	0.04	0.00	0.11	-0.05	0.06	0.15	0.06	0.15	-0.01	0.11	1.00	-0.01	0.05
Mo	0.06	0.17	0.05	0.12	0.15	-0.13	0.20	-0.08	0.13	0.00	0.05	-0.04	0.14	-0.02	0.17	0.05	-0.04	0.10	-0.04	-0.03	-0.01	1.00	0.11
Pb	-0.03	0.28	0.19	-0.02	0.30	0.01	0.21	-0.11	0.24	-0.04	0.04	-0.02	0.34	-0.03	0.34	0.22	0.18	0.21	-0.11	0.02	0.05	0.11	1.00

Chapter 3

A frequency modulation-based assessment of eccentricity phase in the Wilkins Peak Member, Green River Formation: Implications for astronomical influence on the terrestrial depositional system during the Early Eocene Climatic Optimum

In preparation for submission to

Earth and Planetary Science Letters

Abstract

The Early Eocene Climatic Optimum (EECO; 53-50 Ma), Earth's last sustained greenhouse climate, produced the warmest recorded temperatures of the last 66 Ma. While the deep marine response during this warm climate period is well-characterized, terrestrial responses to EECO climatic change are far less well-understood, despite their obvious importance to a global perspective of greenhouse climate influence. The lacustrine Wilkins Peak Member (WPM) of the of the Green River Formation in Wyoming represents an ideal location to examine continental sedimentary system responses to this period of global warmth, boasting a detailed and temporally well-constrained terrestrial EECO section. In this study, we use short eccentricity interference patterns present in a high-resolution, multi-proxy, radioisotopically calibrated XRF core scanner record from the WPM to establish the first direct model of astronomical phase derived from this important EECO-age interval. We find that lake lowstands and accompanying alluvial deposition in the WPM are exclusively associated with minima in short eccentricity, providing a new perspective on the interaction of astronomical forcing and terrestrial sedimentary system response during the EECO greenhouse climate. Based on this insight, we develop a tri-modal WPM lithofacies depositional model, identifying the phase of short eccentricity associated with lacustrine carbonate, bedded evaporite, and alluvial siliciclastic deposition. We compare this phase-adjusted WPM astronomical signal to the La04, La10d, La11, ZB17a, and ZB18a astronomical solutions for the EECO, finding some notable differences between these five models and the WPM astronomical signal.

Introduction

The Early Eocene Climatic Optimum (EECO; 53-50 Ma) represents the acme of a ~ 6 million year warming trend which started in the late Paleocene and continued into the early Eocene (**Figure 1**) (Zachos et al., 2001, 2008). In addition to a secular rise in temperatures, this greenhouse interval was punctuated by a series of abrupt, short-lived global warming events, termed 'hyperthermals' (Zachos et al., 2001, 2008; Lauretano et al., 2016; Westerhold et al., 2018). The Paleocene-Eocene Thermal Maximum (PETM)—which occurred prior to the EECO—is the most widely known of these hyperthermals, but deep marine geologic records suggest that these rapid warming events continued into the Early Eocene (**Figure 1**) (Zachos et al., 2001, 2008; Lauretano et al., 2016). They are thought to be related to the large-scale release of reduced carbon (Kirtland Turner et al., 2014) from one or more hypothesized reservoirs, including methane hydrates (Dickens et al., 1995; Katz et al., 1999; Zachos et al., 2010; Lunt et al., 2011), terrestrially derived organic carbon (Kurtz et al., 2003; DeConto et al., 2012), or marine organic carbon (Higgins and Schrag, 2006; Sexton et al., 2011).

In the deep marine record of the EECO, the largest compositional changes in lithofacies are hypothesized to result from these hyperthermal events. EECO hyperthermals are marked by punctuated carbonate dissolution horizons (which are expressed by enhanced clay content) and negative excursions in carbon and oxygen isotopes (Nicolo et al., 2007). Cyclostratigraphic analysis of deep marine sedimentary core records also suggests that these hyperthermal events are paced by short eccentricity (Lourens et al., 2005; Galeotti et al., 2010; Zachos et al., 2010; Lunt et al., 2011). Although hyperthermals have been hypothesized to be triggered by maxima in short eccentricity based on their coincidence in cyclostratigraphic models with dissolution horizons and negative carbon and oxygen isotope excursions (Lourens et al., 2005; Galeotti et

al., 2010; Zachos et al., 2010; Lunt et al., 2011), the temporal precision of current deep marine age models for the early Eocene leaves uncertainty in the exact phase relationship of these hyperthermal events (Smith et al., 2014a).

Terrestrial records of EECO climatic change are far less well-characterized than that of the deep marine record, but understanding their character is critical to reach a global perspective of greenhouse climate responses. The lacustrine Wilkins Peak Member (WPM) of the Green River Formation in Wyoming (**Figure 2**), represents one of the best locations from which to study continental sedimentary system responses to this period of global warmth due to its rich terrestrial archive of climate dynamics, tectonics, and geomorphology. Compared to contemporaneous deep marine records, the WPM includes an expanded record of the EECO, improved age control from radioisotopic geochronology, and the potential to record a high-fidelity depositional response to hyperthermal events due to an alkaline lake chemistry that can effectively buffer against acidification events.

Previous cyclostratigraphic assessments of the WPM have found evidence for astronomical influence on sedimentation (Fischer and Roberts, 1991; Machlus et al., 2008; Meyers, 2008; Aswasereelert et al., 2013), and particularly strong short-eccentricity forcing of alluvial deposition (Aswasereelert et al., 2013). Correlation of theoretical astronomical solutions into the WPM stratigraphy was completed by Smith et al. (2014a), which proposed that alluvial facies coincided with minima in short eccentricity and lacustrine facies coincided with maxima in short eccentricity. However, the temporal resolution of the Smith et al. (2014) tiered interpolation age model left uncertainty in the exact correlation of the theoretical astronomical solution and deep marine records into the WPM stratigraphy. The state-of-the-art theoretical astronomical solutions become less stable beyond ~50 Ma due to the chaotic behavior of the

solar system, further adding to the ambiguity of determining phase for astronomical cycles (Laskar et al., 2004, 2011a, 2011b; Westerhold et al., 2012; Laurin et al., 2016).

To constrain the phase and magnitude of eccentricity within the WPM, we apply a frequency modulation based approach for determination of eccentricity phase (Laurin et al., 2016) to a continuous, high-resolution, radioisotopically-calibrated, multi-proxy elemental dataset from the WPM. Through this evaluation of eccentricity phase and magnitude—extracted directly from the WPM rock record— we seek to constrain the relationship of eccentricity phase with lithofacies accumulation patterns in a radioisotopically anchored record that avoids astronomical tuning. This makes it is possible to rigorously test previous hypotheses for eccentricity phase driven lithofacies changes within the WPM. The independent timescale of the WPM record also allows us to evaluate the accuracy of key published theoretical orbital solutions for the EECO interval.

Geologic Setting

The Green River Formation was deposited over an approximately 8-million-year interval of the early Eocene (~ 54-43 Ma; Sheliga, 1980; Remy 1992; Smith et al. 2008), spanning the warmest stage of the early Eocene greenhouse climate (**Figure 1**). Deposition was centered around four main structural basins in the mid-latitude, mid-continental Laramide foreland of North America: the Greater Green River Basin (southwestern Wyoming), the Fossil Basin (southwestern Wyoming), the Uinta Basin (northeastern Utah), and the Piceance Creek Basin (northwestern Colorado) (**Figure 2**). These sedimentary basins are bounded by a series of basement-cored anticlinal uplifts, such as the Uinta and Wind River Mountains, produced by the late-Cretaceous to Eocene Laramide Orogeny east of the Sevier fold and thrust belt (**Figure 2**)

(Dickinson et al. 1988; Cashion 1995; Rhodes et al. 2002; Smith et al. 2008). This Laramide deformation is thought to be connected to the flat slab subduction of the Farallon plate under North America (Coney and Reynolds 1977; Dickinson and Snyder 1978; Smith et al. 2014b).

This study centers on the Bridger sub-basin, which composes the western half of the Greater Green River Basin in Wyoming (**Figure 2**). This sub-basin is bounded in the south by the Uinta Mountains, in the west by the Sevier fold and thrust belt, in the east by the Rock Springs Uplift, and in the north by the Wind River Mountains (**Figure 2**). Broad and low in relief in comparison to the other Green River Formation basins, the Bridger sub-basin contains a thick sequence of strata deposited by the paleo-Lake Gosiute lacustrine system. Paleo-Lake Gosiute experienced climatic, tectonic, and geomorphic shifts in chemistry and hydrologic balance during its existence, producing a diverse assemblage of sedimentary facies resulting from environmental changes to lake depth, water chemistry, and paleoecology (Smith et al., 2008; Smith and Carroll, 2015).

The Green River Formation in the Bridger sub-basin is divided into three primary depositional members: the Tipton Member, the Wilkins Peak Member, and the Laney Member (**Figure 3**). The Tipton Member, the lowermost member of the Green River Formation in the Bridger sub-basin (**Figure 3**) records several alternations between overfilled and balance-filled lake conditions (Carroll and Bohacs, 1999) in early Eocene Lake Gosiute, and ranges from 25.5 m to 51.5 m thick near the basin center. It is principally divided into two sub-units, the Scheggs Bed and the Rife Bed (Roehler, 1991; Graf et al., 2015).

This study primarily evaluates the Wilkins Peak Member, the middle member of the Green River Formation in the Bridger sub-basin (**Figure 3**). During deposition of the Wilkins Peak Member, the lake exhibited underfilled, evaporative conditions, leading to widespread

alkaline and saline conditions within the lake (Carroll and Bohacs, 1999). Deposition of this unit is also coincident with the Early Eocene Climatic Optimum (EECO; ~53-50 Ma), the peak of the early Cenozoic greenhouse climate interval (**Figure 1**) (Zachos et al. 2001, 2008; Smith et al., 2008). Relatively shallow lake levels, combined with the broad, low-relief morphology of the basin, appear to have made this unit particularly sensitive to environmental changes, including hypothesized astronomical climate forcing (Fischer and Roberts, 1991; Machlus et al., 2008; Meyers 2008; Aswassereelert et al., 2013).

Within the Wilkins Peak Member, which ranges from 200-325 m thick near the depocenter of the Bridger sub-basin, lithofacies can be broadly grouped into lacustrine carbonate, lacustrine bedded evaporite minerals, and alluvial siliciclastic deposits (**Figure 3**). Alluvial facies are principally green mudstones and siltstones at the basin center, with fine- to medium grained sandstones also occurring toward the basin margins. Alluvial facies are interpreted to be deposited during intervals of low lake level, during which low gradient alluvial plains grade into the basin (Smith and Carroll, 2015). Within the Wilkins Peak Member, nine of these alluvial units have been identified and correlated at the basin scale (Culbertson, 1961). Each of these key alluvial beds has been given a letter designation (A-bed through I-bed) by Culbertson (1961), starting at the base of the Wilkins Peak Member.

Lacustrine carbonate facies are primarily organic carbon-poor carbonate marlstone, interspersed with intervals of organic carbon-rich mudstone (oil shale) that are interpreted to reflect episodic deepening and expansion of paleo-Lake Gosiute. Lacustrine evaporite mineral beds, principally composed of trona, halite, and shortite, are present in the lower Wilkins Peak Member, principally below the C-bed in the region of the Bridger sub-basin depocenter (**Figure 3**). Above the C-bed, bedded evaporites are not as widely present in the central Bridger sub-

basin, and evaporite mineralization is primarily expressed as displacive crystals of shortite within carbonate marl facies. Within the Wilkins Peak Member, twenty-five evaporite beds have been identified, correlated throughout the basin, and assigned numerical designations (Trona Beds 1-25) (Wiig et al., 1995).

The Laney Member, which is not present in the study interval, lies above the Wilkins Peak Member and represents the uppermost unit of the Green River Formation in the Bridger sub-basin (**Figure 3**). This member records a shift in Lake Gosiute from an evaporitic, underfilled lake during Wilkins Peak Member deposition to a balance-fill and, eventually, overfilled lake, and is principally divided into the LaClede Bed and Sand Butte Bed within the Bridger sub-basin (Roehler, 1973; Rhodes et al., 2007; Smith et al., 2008; Rhodes and Carroll, 2015).

Methods

Solvay S-34-1 Core

This study is based on the Solvay S-34-1 core, which was drilled in 2016 and recovered approximately 642 m of 63.5 mm-diameter core from the Green River Formation and the overlying Bridger Formation (**Figure 3**). The core is positioned in the south-central Bridger sub-basin (41°24'51.23"N; 109°41'48.30"W), near the basin depocenter during deposition of the early Wilkins Peak Member (**Figure 2**).

This study examines the lowermost 257.29 m of core (Estimated recovery: 97%), which includes an 11.78-m interval of the upper Tipton member, a 238.22-m section of the overlying lower, middle, and upper Wilkins Peak Member, and a 7.29-m interval of deltaic sandstone and oil shale thought to be associated with the Desertion Point Tongue of the Wasatch Formation (Sullivan, 1980) (**Figure 4**). Within the lower and middle Wilkins Peak Member section

preserved in the core, dominant lithologies include organic carbon-poor carbonate marl, oil shale, green siltstone, green mudstone, and bedded evaporate, with minor intervals of volcanic tuff and very fine- to medium-grain sandstone. This interval of core includes 17 bedded evaporite units (TB 1-7, TB 9-18) and the A- through H-bed sequence of named alluvial beds (Culbertson, 1961) (**Figure 4**). Rock core from the interval of study was split, imaged, and logged at the LacCore facility at the University of Minnesota-Twin Cities.

XRF Core Scanning

Data Collection

X-ray fluorescence (XRF) core scanning was completed at the University of Wisconsin-Madison using a third-generation Avaatech X-ray fluorescence core scanner. Prior to scanning, split core samples were prepared slab face up in the scanner and cleaned of debris, leveled to horizontal, described, and covered in SPEX 3525 Ultralene foil. For each individual core section, a continuous down-core measurement path was selected to avoid anomalous intervals of core, which may include cracks, surface irregularities, or sedimentary clasts.

XRF core scanning was completed at a continuous 5 mm resolution (5 mm x 5 mm window size) to capture millimeter- to meter-scale variations in elemental intensity across the 257.29 m of core. To optimally measure a wide range of elements within the core, two different scans were completed at this resolution using different instrument settings. To measure Mg through Rh, an acceleration voltage of 10 kV (1200 uA source current, no filter, 20-second measurement time) was used. For elements Cu through U, an acceleration voltage of 30 kV (1600 uA source current, thin palladium filter, 20-second measurement time) was used. Deconvolution of X-ray fluorescence spectra was completed using a customized deconvolution model in the WinAxil (v. 4.5.2) X-ray analysis software.

We instituted a comprehensive approach to evaluate data quality and reproducibility. Standard samples were analyzed between each scan run of an individual core section (SARM-4) and before and after the complete analysis of each individual core section (JGb-1, JR-1) to evaluate instrument stability (Supplement B1). For each core section measured, sample replicate measurements were also taken at every fifth measurement for each of the two instrument settings to quantify instrument variation and evaluate reproducibility for each element (Supplement B2, B3). Through examination of mean coefficient of variation, standard deviation of the coefficient of variation, and cross plots of elemental intensities for all replicate measurements, we identify twenty elements (Mg, Al, Si, P, S, Cl, K, Ca, Ti, V, Mn, Fe, Cu, Zn, Br, Rb, Sr, Zr, Mo, Pb) with superior quality (Supplement B4).

Over the 14-month course of XRF scanning, long-term instrumental drift was observed in the XRF count values for standard samples (Supplement B1). To account for these artifacts and minimize the impact on subsequent data analysis and interpretations, we implemented data corrections on an element-by-element basis. This approach to evaluating and correcting for instrument drift is outlined in chapter 2.

Depth-Time Conversion

Spectral analysis was principally undertaken in the time domain, with time-depth conversion completed using a method designated the "time-equivalent surface" (TES) model. This method follows the approach used by Aswasereelert et al. (2013) to assign modeled ages to 51 time-equivalent surfaces within the Wilkins Peak Member. These time-equivalent surfaces are primarily widely correlatable tuffs, oil shale beds, and alluvial beds present within the Wilkins Peak Member. A second-order polynomial equation was fit to the weighted mean ages of Machlus et al. (2015) from their U-Pb analysis of the Firehole, Second, Grey, Main, Layered,

and Sixth tuffs (**Table 1**) and the cumulative depths associated with these tuffs in the White Mountain 1 (WM-1) core, a location approximately 28 km north east of the Solvay S-34-1 core (**Figure 2**). The WM-1 core was used for the polynomial fit because each of the WPM time-equivalent surfaces are physically present and unambiguous in this core, unlike the S-34-1 core (Aswasereelert et al., 2013).

Within the Solvay S-34-1 core, each of the 30 time-equivalent surfaces of the lower and middle WPM were identified (**Figure 4**), and their depths in the S-34-1 core were used to calculate a modeled age using this second-order polynomial time-depth model (**Table 2**). The goal of utilizing this number of time-depth control points is to produce a time-depth model that is sensitive to changes in sedimentation rate across the record, since unresolved sedimentation rate changes have the potential to cause "peak splitting" within power spectra by smearing the high frequency variance across a range of frequencies (Meyers et al., 2001; Aswasereelert et al., 2013). This can also lead to the creation of artifact "cycles" that look like harmonics of the fundamental cycle (Schiffelbein and Dorman, 1986; Aswasereelert et al., 2013).

Time Series Analysis

Spectral analysis in the time domain was conducted using Astrochron (Meyers, 2014), a package designed for astrochronologic analysis using the open-source R statistical program (R Core Team, 2014). For both depth and time domain, a range of statistical and spectral analysis techniques were applied to evaluate this high-resolution, multi-proxy XRF data. Multi-Taper Method (MTM) power spectral analysis (Thomson, 1982) was applied to the temporally calibrated, linearly interpolated (using piecewise linear interpolation) XRF dataset to provide information on oscillatory variability within the data series. This power spectral technique, which uses a specified series of prolate tapers for spectral estimation (Thomson, 1982), was

applied using the "mtm" function in Astrochron (Meyers, 2014). Additionally, Evolutive Harmonic Analysis (EHA), a method which applies MTM to a moving window, was applied using the "eha" function in Astrochron to identify cyclic variability and evaluate potential changes in sedimentation rate (Meyers et al. 2001; Meyers, 2014). Taner bandpass filtering (Taner et al., 1992) was applied to the time series record of different measured elements using the "taner" function in Astrochron (Meyers, 2014).

Eccentricity Phase Assessment

To determine eccentricity phase within the WPM record, this study applied the frequency modulation approach developed by Laurin et al. (2016), for assessment of the time-converted XRF core scanner record of Ca and Fe. The interaction of three fundamental frequencies, Venus (g2), mars (g4) and Jupiter (g5), create the three dominant eccentricity periodicities: E1 (~400 ky; g2-g5), E2 (~127 ky; g4-g2), and E3 (~96 ky; g4-g5) (Laskar, 2004; Hinnov, 2000; Laurin et al., 2016). The Laurin et al. (2016) technique examines the interference patterns of the two short eccentricity cycles (E2 and E3), which are modulated by the ~400 ky long eccentricity (E1) cycle.

This interference pattern is most easily observable in EHA plots of a time-series (**Figure 5**). Maxima in the phase of the E1 cycle show constructive interference of the E2 and E3 cycles; in an EHA plot, this is visually indicated by a 'junction' in the amplitude peaks of E2 and E3, where the two cycles come together to form a strong amplitude response at a single frequency halfway between the frequencies of E2 and E3 (Laurin et al., 2016) (**Figure 5**). Minima in the phase of the E1 cycle, on the other hand, show destructive interference of the E2 and E3 cycles; this is shown as a 'bifurcation' in the amplitude peaks of E2 and E3 within the EHA plot, where E2 and E3 split to form amplitudes at their associated frequencies (Laurin et al., 2016) (**Figure**

5). This constructive and destructive interference of E2 and E3 and its relationship to the phase of E1 can also be visualized through application of bandpass filters, such as a Taner filter (Taner et al., 1992) at the frequencies associated with the E1, E2, and E3 cycles (**Figure 5**). This bandpass filtering provides key information on cycle phase and magnitude, which can be used in combination with EHA plots to holistically evaluate patterns of constructive and destructive interference.

Results

Lithofacies Composition

High-resolution, continuous, multi-proxy XRF core scanning of the Solvay S-34-1 core provides unprecedented level of detail on variations in elemental intensity (in counts) within the WPM. Within the S-34-1 core, inferred carbonate (Mg, Ca, Cr, Sr), siliciclastic (Al, Si, K, Ti, Cu, Zn, and Rb), redox (S, Pb), and evaporite (Cl, Br) proxies show positive intercorrelation (**Table 3**). Fe appears to be positively correlated with both siliciclastic and redox proxy element groups, suggesting presence in both oxidized (siliciclastic) and reduced (redox) forms.

Examination of six key elemental records (Si, S, Ca, K, Fe, Br) within this proxy element framework permits the identification of key lithologic boundaries within the core (**Figure 6**). Near the base of the section (631 m depth), the Tipton Member bounds the overlying Wilkins Peak Member. Moving from the Tipton Member up into the Wilkins Peak Member, we observe a rapid decrease in counts of carbonate (Ca) and siliciclastic (Al, Si, K, Ti, Fe, Cu, Zn, and Rb) proxy elements (**Figure 6**). These changes in elemental intensity follow a lithologic shift from predominantly oil shale in the upper Tipton Member to bedded evaporite, carbonate marl, and oil shale in the lower WPM.

The lower and middle Wilkins Peak Member (392.78-631 m core depth), has observable internal lithologic variations in the S-34-1 core, principally alternations of lacustrine marl and bedded evaporite with alluvial siliciclastic facies. Alluvial beds A- through H- are present in the lower and middle WPM interval of this core section, and are identifiable as 1.5 m-16 m thick intervals of green mudstone, green siltstone, and fine-grained sandstone. These alluvial lithofacies are predominantly associated with increases in Fe counts (**Figure 6**), but can also be observed as increases in other siliciclastic proxy elements (Al, Si, K, Ti, Fe, Cu, Zn, and Rb). Alluvial beds also display consistently low counts for inferred carbonate proxy elements, such as Ca (**Figure 6**).

Lacustrine carbonate marlstone is characterized by high, but variable, counts in carbonate (Ca) and siliciclastic (Si, K) proxy elements (**Figure 6**). These XRF results are consistent with XRD-based mineralogical studies of Green River Formation carbonate marl and oil shale facies, which indicate that these facies typically contain calcite, dolomite, quartz, alkali feldspar, plagioclase, and illite and other clay minerals (Bradley and Eugster 1969; Hosterman and Dyni 1972; Picard and High 1972; Robb and Smith 1974; Dyni 1976; Mason, 1987). Bedded evaporite is principally concentrated in the lower Wilkins Peak Member between the base of the unit and the C-bed (**Figures 3, 4; Wiig et al., 1995**). These beds, which range from 0.25 m to 8 m in thickness, are associated with low XRF element counts for most non-evaporite proxy elements, including Si, S, K, Ca, and Fe (**Figure 6**). This unusual XRF response results from the trona- and halite-rich composition of these beds; these minerals are dominantly composed of H, C, O, Na, and Cl, of which only the latter can be measured on the Avaatech XRF core scanner. Bromine is also present, albeit in lower concentrations, within the evaporite beds. In the S-34-1 core, Br provides a more reliable, less noisy record of evaporite bed deposition than Cl, due to

interferences between the rhodium X-ray source scatter (Rayleigh scattering), and the primary (K-alpha) XRF peak associated with chlorine.

Near the top of the Solvay S-34-1 core study interval, the lacustrine and alluvial middle WPM is interrupted by the deposition of 7.29 m of deltaic sandstone and oil shale, which is thought to be the Desertion Point Tongue of the Wasatch Formation (Sullivan, 1980). This boundary is located above the H-bed of the WPM (385.49-392.78) and is marked by a major shift in elemental counts in Si, S, Ca, K, Ti, and Fe (**Figure 6**). Carbonate proxy element (Ca) counts decrease across this unit boundary, while siliciclastic (Si, K, Fe) and redox (S) element counts increase (**Figure 6**).

Power Spectral Analysis

MTM power spectral analysis was applied to the temporally calibrated records of Si, S, Ca, K, Fe, and Br to evaluate the frequency distribution of cyclic sedimentation within this WPM record (**Figure 7**). These six elements were selected because they represent the best measured elemental intensity records for the carbonate, siliciclastic, redox, and evaporite element proxy groups in the S-34-1 core. MTM spectral analysis of the temporally calibrated Si, S, K, Ca, and Fe shows that power is primarily concentrated between 0.0-0.03 cycles/ky (Period: > 33 ky) (**Figure 7**), with at least 55% of the power located within this frequency band for each of these elements. However, the frequency distribution of power peaks within this range varies widely with the proxy element.

MTM spectra for temporally calibrated Si and K show similarities in their power spectral results, with both displaying a prominent peak in power at approximately 0.02 cycles/ky (Period: 50 ky) as well as broader peaks in power between 0.0-0.015 cycles/ky (Period: > 66 ky), 0.030 cycles/ky (Period: 33 ky), 0.045 cycles/ky (Period: 22 ky), 0.055 cycles/ky (Period: 18 ky), and

0.065 cycles/ky (Period: 15 ky) (**Figure 7**). This similar power spectral character is consistent with a shared association with the siliciclastic proxy element group. MTM spectra for temporally calibrated S shows prominent power peaks between 0-0.015 cycles/ky (Period: > 66 ky) and 0.033 cycles/ky (Period: 30 ky), however this record appears noisier than the other key elements studied (**Figure 7**). MTM spectra for temporally calibrated Br show lower-magnitude peaks in power compared to the other key elements, with peaks concentrated at the frequencies lower than 0.0025 cycles/ky (Period: > 400 ky), around 0.01 cycle/ky (Period: 100 ky), and around 0.025 cycles/ky (Period: 40 ky) (**Figure 7**)

MTM spectra for temporally calibrated Fe shows a broad range of high-power peaks between 0.0-0.025 cycles/ky (Period: > 40 ky) (**Figure 7**), with approximately 75% of power concentrated within that frequency range. Similarly, MTM spectra for temporally calibrated Ca show that more than 60% of power is concentrated between 0.0-0.025 cycles/ky (Period: > 40 ky), with a series of smaller power peaks between 0.02-0.06 cycles/ky (Period: 16-50 ky) (**Figure 7**). Given the particularly strong power concentrated in the eccentricity frequency band of MTM power spectra of temporally calibrated Ca and Fe, these two elements serve as the basis of the WPM phase assessment using the frequency modulation phase analysis method.

Eccentricity Phase Assessment

Evolutive Harmonic Analysis

EHA plots of temporally calibrated Ca and Fe show strong power and amplitude peaks within the eccentricity band (0-0.11 cycles/ky) for much of the S-34-1 core record (**Figure 8**). Temporally calibrated Ca also shows a transition in spectral character at approximately 51.1 Ma (**Figure 8**). Below this point, power and amplitude are distributed across a broad range of frequencies, particularly between 0.0-0.06 cycles/ky (Period: > 16 ky); above this point, power is

strongly concentrated within the eccentricity band (0-0.11 cycles/ky) (**Figure 8**). This transition coincides with the abrupt discontinuation of bedded evaporite deposition; lithologies above this point are dominated by alternations in lacustrine carbonate and alluvial siliciclastic deposition.

Critically, EHA plots of temporally calibrated Ca and Fe show frequency modulation of the short eccentricity cycle in the WPM (**Figure 8**). This frequency modulation is visually distinguishable by junctions and bifurcations caused by the constructive and destructive interaction of the E2 and E3 short-eccentricity amplitude peaks (**Figure 8)**. While bifurcations can also result from hiatuses in the depositional record (Meyers and Sageman, 2004), the regular ~400 ky periodicity of these junction-bifurcation cycles supports a frequency modulation source for this pattern. Additionally, there is no clear sedimentological or stratigraphic evidence for hiatuses where these bifurcations occur. Both records—particularly Fe—also show a ~400-ky modulation of amplitude in the short eccentricity signal, distinguished by a periodic strengthening and weakening of amplitude throughout the record (**Figure 8)**. This appears most strongly associated with the junctions, which are inferred to result from constructive interference of E2 and E3, in the temporally calibrated Ca and Fe records.

Bandpass Filtering

Taner filters extract high-magnitude E1 (400 ky), E2 (127 ky), and E3 (96 ky) eccentricity cycles from the temporally calibrated Ca record (**Figure 9**). This bandpass analysis suggests that the Ca-derived E2 and E3 cycles constructively interfere at a Ca-derived E1 maximum (**Figure 9**). These intervals of constructive interference are associated with junctions in the EHA plot for temporally calibrated Ca (**Figure 9**). At Ca-derived E1 cycle minima, Ca-derived E2 and E3 cycles are anti-phased, resulting in destructive interference (**Figure 9**). These intervals of destructive interference are associated with bifurcations in the EHA plot for the

temporally calibrated Ca record (**Figure 9**). The consistency of the relationship of constructive Ca-derived E2 and E3 interference at Ca-derived E1 maxima and destructive Ca-derived E2 and E3 interference at Ca-derived E1 minima provides strong evidence that the phasing of the temporally calibrated Ca record has been properly extracted using the approach of Laurin et al. (2016). As a result, we conclude that the Ca-derived E1, E2, and E3 cycles are in phase with astronomical forcing (e.g. Ca E1 maximum=astronomical E1 maximum).

In the temporally calibrated record for Fe, Taner filters were also applied to extract E1, E2, and E3 cycles (**Figure 10**). Fe-derived E1, E2, and E3 cycles display a lower magnitude than comparable cycles derived from Ca, particularly for E1 (**Figures 9, 10**). This bandpass analysis suggests that Fe-derived E2 and E3 cycles destructively interfere at Fe-derived E1 maxima (**Figure 10**). These intervals of destructive interference are associated with bifurcations in the EHA plot of temporally calibrated Fe (**Figure 10**). At the Fe-derived E1 cycle minima, Fe-derived E2 and E3 cycles are in phase with one another, resulting in constructive interference (**Figure 10**). These intervals of constructive interference are associated with junctions in the temporally calibrated Fe record (**Figure 10**). This analysis indicates that the phase of the Fe-derived eccentricity signal is opposite to that derived from Ca and the astronomical forcing (e.g. Fe E1 maximum= Ca E1 minimum), displaying the expected constructive and destructive interference pattern.

Lithofacies Connections to Eccentricity Phase

Comparison of the occurrence of alluvial beds to the bandpass-filtered record for temporally calibrated Ca indicates that the alluvial beds coincide with periods of minima in the combined Ca E2+E3 short eccentricity cycles (**Figure 9**). Because the Ca-derived E1, E2, and E3 eccentricity cycles are recognized to be in phase with astronomical forcing based on our

frequency modulation analysis, this finding reveals that astronomical E2+E3 short eccentricity minima generate the environmental conditions necessary for alluvial deposition in the Bridger sub-basin during deposition of the WPM. These results are consistent with the interpretation of Smith et al. (2014a), which interpreted these intervals of alluvial deposition to be largely arid except for occasional high-precipitation events.

In the bandpass-filtered record of temporally calibrated Fe, these same alluvial beds are associated with maxima in the Fe-derived E2+E3 signal (**Figure 10**). Only one alluvial interval—the G-bed—shows a small offset between Fe E2+E3 maxima and alluvial deposition (**Figure 10**). We attribute this offset to a distortion of the bandpass-filtered signal resulting from a ~5 m interval of the G-bed where XRF data could not be reliably collected due to an uneven core surface, resulting in a blank interval in the XRF data. While the observation that alluvial bed deposition coincides with maxima in the Fe-derived E2+E3 signal appears contradictory to the Ca-derived results, the opposite phasing of the Fe record compared to Ca implies that this result remains consistent with short-eccentricity minima forcing of alluvial deposition in the WPM.

Comparisons to the Theoretical Orbital Solutions

Using the astronomical signal derived from the temporally calibrated Ca record, we make comparisons to the La04 (Laskar et al., 2004; La10d (Laskar et al., 2011a), La11 (Laskar et al., 2011b), ZB17a (Zeebe, 2017), and ZB18a (Zeebe and Lourens, 2019) solutions (**Figure 11**). Each of these models employ different assumptions for the planetary ephemeris, which impacts their predictions of solar system movement going back into deep time. Within the Laskar models, the La10d solution is thought to be the most reliable numerical model beyond 47 Ma (Westerhold et al., 2012), while La11 is the most recently published Laskar astronomical solution. The ZB17a and ZB18a models use a new solar system integration covering the last 100

myr, with the most current ZB18a models including a chaotic resonance transition at approximately 50 Ma (Zeebe and Lourens, 2019).

Comparisons of the inferred Ca-derived E1 cycle to the La04, La10d, La11, ZB17a, and ZB18a solutions for 50.25-51.75 Ma show similarities in the expression and magnitude of the E1 cycle, but also show an offset between the Ca-derived E1 maximum and La10d and La11 maxima (**Figure 11**). This offset is consistently ~100 ky for most of the study section, except in the time interval corresponding to pre-A-bed deposition, where it increases to ~200 ky (**Figure 11**). Comparing the Ca-derived E2+E3 record and the La10d, La11, ZB17a, and ZB18a solutions, it appears that the phase relationship of short eccentricity largely agrees between these models, with a ~50 ky offset occurring only within the A- and H-bed intervals.

Discussion

A frequency modulation-based analysis of radioisotopically calibrated lower- and middle-WPM Ca and Fe records show patterns of constructive and destructive interference in their eccentricity signal revealed the phase relationship of eccentricity across the study interval (**Figures 9, 10**). Using this cyclostratigraphic assessment, we propose a tri-modal model for eccentricity-forced lithofacies accumulation in the WPM and compare our WPM-based astrochronologic model to four published theoretical astronomical solutions for the EECO interval.

Model for Short Eccentricity Forced Lithofacies Accumulation

Based on a detailed sedimentologic and stratigraphic assessment of the WPM, Smith et al. (2014a) hypothesize that the lacustrine carbonate and bedded evaporite facies represent maxima in short eccentricity and that alluvial facies represent minima in short eccentricity.

Previous cyclostratigraphic assessments of the WPM, principally based on Fischer assay oil yield data, did not evaluate astronomical phase in the WPM, and so this component of the astronomical signal has remained unconstrained. Through the quantification of a WPM-derived eccentricity phase, we can more precisely evaluate the relationship between astronomical forcing and depositional environment within the WPM, allowing us to test the hypothesis of Smith et al. (2014a).

Spectral analysis of temporally calibrated Si, S, K, Ca, Fe, and Br show variance at frequencies consistent with astronomical cyclicity (**Figure 7**). These power spectral results from a broad suite of elements are consistent with previous cyclostratigraphic assessments of the Green River Formation (Fischer and Roberts, 1991; Machlus et al., 2008; Meyers, 2008; Aswasereelert et al., 2013; Walters et al., 2020) but also provide additional information on carbonate, siliciclastic, redox, and evaporite depositional responses. Temporally calibrated Ca and Fe, associated with lacustrine carbonates and alluvial siliciclastics, respectively, display particularly strong power concentrated at frequencies associated with short and long eccentricity. This finding is consistent with the results of Aswasereelert et al. (2013), which identified short-eccentricity pacing of carbonate and alluvial deposition in their macrostratigraphic analysis of the WPM in the Bridger sub-basin. Our frequency modulation-based evaluation of eccentricity phase in the WPM also establishes that alluvial facies were deposited at minima in the overall (E2+E3) short eccentricity beat (**Figures 9, 10**). This finding supports the lithofacies-phase hypothesis of Smith et al. (2014a), which proposed a short eccentricity minima trigger for alluvial deposition.

To explain this lithologic variation in the WPM of the Bridger sub-basin, we propose a tri-modal lithofacies accumulation model driven by short-eccentricity modulation of precession

(**Figure 12**), modified from the model of Smith et al. (2014a). During short-eccentricity maxima, precession-scale variations in insolation are at their greatest, resulting in the most extreme insolation-driven climate variation (**Figure 12**). During short-eccentricity minima, variations in insolation from the precession cycle are comparatively muted, resulting in less extreme variations in insolation-driven climate conditions (**Figure 12**).

During maxima in the E2+E3 short eccentricity cycle, when precessional insolation variation is maximized, we propose that precession-driven deposition shifts between lacustrine highstand and lacustrine lowstand facies in the WPM of the Bridger sub-basin (cf. Smith et al., 2014a) (**Figure 12**). At one extreme in precessional insolation variation, high annual precipitation and/or reduced evaporation processes lead to wetter conditions and a broadening and deepening of Lake Gosiute (Smith et al., 2014a). This expanded lake may have been able to support a chemocline and/or thermocline; this permitted the deposition of our interpreted lake highstand oil shale and bedded evaporite facies, which require stratification in order to be preserved in the rock record. At the opposing extreme of precessional insolation variation, low annual precipitation and/or enhanced evaporation led to drier conditions and a shallower, less expansive Lake Gosiute (Smith et al., 2014a). This shallower, more restricted lake may not have been able to support a chemocline and/or thermocline, leading to the deposition of organic-lean carbonate marl without bedded evaporite.

The placement of bedded evaporite within our precession-forced highstand is one essential modification of the depositional model of Smith et al. (2014a). In their model, bedded evaporite is interpreted to have formed during lacustrine lowstands, in a salt-pan style depositional environment (Smith et al., 2014a). Instead, we place bedded evaporite deposition at lacustrine highstands based on studies of comparative modern bedded evaporite formation

(**Figure 12**). For example, in the modern Dead Sea, bedded evaporite formation typically occurs below wave base and below the thermocline in a deep, stratified, perennial lake (Kiro et al., 2015; Sirota et al., 2016; Sirota et al., 2017; Demicco and Lowenstein, 2020). The close association of bedded evaporites with profundal mudstones in the Solvay S-34-1 core and other WPM core records supports a deep, stratified lake as a depositional environment for these bedded evaporite facies in the WPM (Jagniecki et al., 2015a).

During minima in the short eccentricity cycle, when precessional insolation variation is most muted, we propose that the alluvial siliciclastic facies are deposited in the WPM of the Bridger sub-basin (**Figure 12**), in agreement with Smith et al. (2014a). Without the extremes in precession-driven insolation inferred for intervals of short-eccentricity maxima, precipitation input and/or evaporation processes are thought to be more moderate and stable. These conditions permitted alluvial plains to expand down-dip into the lake basin. Precipitation delivery was sufficiently low as to not dramatically lower or raise Lake Gosiute, but it appears to have been efficient at transporting sediment into the lake basin (Smith et al., 2014a). Smith et al. (2014a) hypothesized that sediment transport in a relatively low-precipitation environment occurred during rare, but large magnitude, rain events which could overwhelm vegetative cover and distribute fine siliciclastic sediment in downstream alluvial stream networks. A similar association of lake lowstands with eccentricity minima is observed in several modern lakes; one of the best modern analogues to the WPM, Lake Titicaca of the Andes Mountains, is only able to capture significant hydrologic input to create a lake highstand during eccentricity maxima, when summer monsoons are enhanced (Fritz et al., 2012).

Overall, our tri-modal model, with a WPM-derived phase assessment and a revised depositional environment for bedded evaporite facies, provides a framework from which to

understand connections between eccentricity forcing and lithofacies stacking patterns in the GRF. As a result, our understanding of the influence of astronomical forcing on terrestrial landscape evolution has been further characterized, providing one of the most thoroughly constrained terrestrial perspectives on the interaction of climate and sedimentary deposition during the EECO greenhouse climate.

Comparisons to the Theoretical Orbital Solutions

Our phase-constrained WPM astronomical signal also permits comparisons to theoretical orbital solutions covering the same time interval of the EECO. Due to the chaotic behavior of the solar system, numerical astronomical solutions show reduced stability in their results beyond ~ 50 Ma, particularly for cycles of shorter period than the more stable ~400 ky long-eccentricity cycle (Laskar et al., 2004; Laskar et al., 2011a, 2011b; Westerhold et al., 2012; Laurin et al., 2016; Zeebe 2017; Zeebe and Lourens, 2019). Because of this instability, astronomical signals extracted from well-constrained ancient records play particularly useful roles in testing these theoretical models.

Through a comparison of the Ca-derived E1 cycle to the E1 cycle of the La04, La10d, La11, ZB17a, and ZB18a solutions, we identify a ~100 ky offset in their phase for much of the 50.25-51.75 Ma time interval studied (**Figure 11**). This offset could potentially result from uncertainties in the WPM age model, a lag between astronomical insolation forcing and terrestrial depositional response, or diminished accuracy of the astronomical solutions over this time interval due to accumulated error in the models.

Given that the uncertainties for the six U-Pb ages underpinning the temporal calibration range from between 60-75 ky (2σ total uncertainty, including analytical uncertainty, U-Pb tracer calibration error, and uranium decay constant errors) the uncertainties in the radioisotopic ages

underlying the TES time model do not appear to fully explain the observed offset between the Ca-derived and La10d/La11/ZB17a/Zb18a E1 cycles. Additionally, a ~100 ky lag between E1 insolation forcing and WPM E1 depositional response (**Figure 11**) appears incompatible with other cyclostratigraphic evidence for WPM sensitivity to Milankovitch and sub-Milankovitch climate forcings. Given the temporal constraints of the WPM record and the well-characterized instabilities in the astronomical solutions beyond 50 Ma (Laskar et al., 2004; Laskar et al., 2011a, 2011b; Westerhold et al., 2012; Ma et al., 2017), we suggest that the diminished accuracy of these astronomical solutions may explain at least part of this observed offset.

For the E2+E3 short eccentricity cycle, phase was well matched between the Ca-derived, La10d, and La11d models for much of the record, except the A- and H-bed intervals (**Figure 11**). Given the agreement in phase between the models for the remainder of the record, we do not anticipate that a lag of the terrestrial response is the root cause of this disagreement. Instead, we attribute the ~50 ky offset at the A- and H- beds to either WPM TES time model uncertainty or to a reduction in the accuracy of the theoretical astronomical solutions for this interval of the EECO.

Conclusions

Application of a frequency modulation assessment of a continuous, high-resolution, radioisotopically-constrained, broad elemental dataset from the WPM enhances our understanding of the connections between astronomical forcing and terrestrial sedimentary system response during the Early Eocene Climatic Optimum greenhouse climate and allows a rigorous independent test of published theoretical astronomical models. Our multi-proxy suite of temporally calibrated elemental records shows power spectral results consistent with previous

cyclostratigraphic assessments of the Green River Formation, including short-eccentricity forcing of lacustrine-alluvial deposition, while also revealing the differences in depositional response between carbonate, siliciclastic, redox, and evaporite proxy elements. Our evaluation of astronomical phase reveals that alluvial deposition is exclusively associated with short-eccentricity minima, supporting the depositional model of Smith et al. (2014).

Using this new constraint on short-eccentricity phase and depositional-system response, we develop a tri-modal lithofacies depositional model for the Wilkins Peak Member. According to this model, lacustrine deposition occurs during intervals of short-eccentricity maxima, when precessional insolation variation is strongest. Intense precession-scale insolation variation leads to large swings in hydrologic balance and/or evaporation that create lake highstands, which deposit oil shale and bedded evaporite, and lake lowstands, which deposit carbonate marlstone. On the other hand, alluvial deposition occurs during intervals of short-eccentricity minima, when insolation variation is comparatively muted. These moderate, stable conditions permit the formation of an alluvial plain in the Bridger sub-basin.

This detailed WPM-based cyclostratigraphy also provides the opportunity to evaluate published theoretical astronomical solutions for the EECO. We observe a ~100 ky offset in the long eccentricity cycle (E1) for much of the 50.25-51.75 Ma study interval, which we suggest may be attributed in part to the reduced stability of the La04, La10, La11, ZB17, and ZB18 numerical solutions past 50 Ma. The phase of the short eccentricity cycle (E2+E3) is generally consistent between the WPM-based astrochronology and the astronomical solutions, with a ~50 ky offset in phase at the top and bottom of the record, which we attribute to either WPM timescale uncertainty or the reduced stability of the theoretical orbital solutions during the EECO.

Acknowledgements

I thank Matteo Paperini and Solvay Chemicals, Inc. for the use of the Solvay S-34-1 core. I also thank Elizabeth Klonowski, Shlomo Honig, and Isaac Sageman for their contributions to the preparation, imaging, logging, and description of the core. Tim Lowenstein and Mike Smith provided valuable input that helped to shape this project. This study received financial support from the National Science Foundation Integrated Earth Systems Program (NSF-EAR 1813278) the National Science Foundation Early Career Development Program (NSF-EAR 1151438), the Geological Society of America Graduate Research Grant program, the American Association of Petroleum Geologists Foundation Grants-in-aid program, and the Department of Geoscience at the University of Wisconsin-Madison.

References Cited

Aswasereelert, W., Meyers, S.R., Carroll, A.R., Peters, S.E., Smith, M.E., and Feigl, K.L., 2013, Basin-scale cyclostratigraphy of the Green River Formation, Wyoming: GSA Bulletin, v. 125, p. 216-228.

Bradley, W.H., and Eugster, H.P.,1969, Geochemistry and paleolimnology of the trona deposits and associated authigenic minerals of the Green River Formation of Wyoming: U.S. Geological Survey Professional Paper 496-B.

Carroll, A.R., and Bohacs, K.M., 1999, Stratigraphic classification of ancient lakes: Balancing tectonic and climatic controls: Geology, v. 27, p. 99–102.

Cashion, W.B., 1995, Stratigraphy of the Green River Formation, eastern Uinta Basin, Utah and Colorado, *in* Averett, M.R., ed., The Green River Formation in Piceance Creek and

eastern Uinta Basins: Grand Junction Geological Society 1995 Field Trip Guidebook, p. 15–21.

Coney, P.J., and Reynolds, S.J., 1977, Cordilleran Benioff zones: Nature, v. 270, p. 403.

Culbertson, W.C., 1961, Stratigraphy of the Wilkins Peak member of the Green River Formation, Firehole Basin Quadrangle, Wyoming, Article 348: U. S. Geological Survey Professional Paper, p. D170–D173.

DeConto, R.M., Galeotti, S., Pagani, M., Tracy, D., Schaefer, K., Zhang, T., Pollard, D., and Beerling, D.J., 2012, Past extreme warming events linked to massive carbon release from thawing permafrost: Nature, v. 484, p. 87–91.

Demicco, R.V., and Lowenstein, T.K. When "evaporites" are not formed by evaporation: The role of temperature and pCO2 on saline deposits of the Eocene Green River Formation, Colorado, USA: GSA Bulletin, v. 132, p. 1365-1380.

Dickens, G.R., O'Neil, J.R., Rea, D.K., and Owen, R.M., 1995, Dissociation of oceanic methane hydrate as a cause of the carbon isotope excursion at the end of the Paleocene: Paleoceanography, v. 10, p. 965–971.

Dickinson, W.R., and Snyder, W.S., 1978, Plate tectonics of the Laramide orogeny: Geological Society of America Memoirs, Geological Society of America, v. 151, p. 355–366.

Dickinson, W.R., Klute, M.A., Hayes, M.J., Janecke, S.U., Lundin, E.R., McKittrick, M.A., and Olivares, M.D., 1988, Paleogeographic and paleotectonic setting of Laramide sedimentary basins in the central Rocky Mountain region: GSA Bulletin, v. 100, p. 1023–1039.

Dyni, J.R., 1976, Trioctahedral smectite in the Green River Formation, Duchesne County, Utah: U.S. Geological Survey Professional Paper, no. 967, 14 p.

Fritz, S.C., Baker, P.A., Tapia, P., Spanbauer, T., Westover, K., 2012. Evolution of the Lake Titicaca basin and its diatom flora over the last ~370 000years. Palaeogeography, Palaeoclimatology, Palaeoecology, v. 317–318, 93–103.

Fischer, A.G., and Roberts, L.T., 1991, Cyclicity in the Green River Formation (lacustrine Eocene) of Wyoming: Journal of Sedimentary Petrology, v. 61, p. 1146-1154.

Galeotti, S., Krishnan, S., Pagani, M., Lanci, L., Gaudio, A., Zachos, J.C., Monechi, S., Morelli, G., and Lourens, L., 2010, Orbital chronology of Early Eocene hyperthermals from the Contessa Road section, central Italy: Earth and Planetary Science Letters, v. 290, p. 192–200.

Graf, J.W., Carroll, A.R., and Smith, M.E., 2015, Lacustrine Sedimentology, Stratigraphy, and Stable Isotope Geochemistry of the Tipton Member of the Green River Formation, *in* Smith, M., and Carroll, A., eds., Stratigraphy and Paleolimnology of the Green River Formation, Western USA: Syntheses in Limnogeology, vol. 1: Springer, Dordrecht, p. 1-12.

Higgins, J.A., and Schrag, D.P., 2006, Beyond methane: Towards a theory for the Paleocene–Eocene Thermal Maximum: Earth and Planetary Science Letters, v. 245, p. 523–537.

Hinnov, L.A., 2000, New Perspectives on Orbitally Forced Stratigraphy: Annual Review of Earth and Planetary Sciences, v. 28, p. 419–475.

Hosterman, J.W., and Dyni, J.R., 1972, Clay mineralogy of the Green River Formation, Piceance Creek Basin-A preliminary study, in Geological Survey research 1972: U.S. Geol. Survey Prof. Paper 800-D, p. D159-D163.

Jagniecki, E.A., Lowenstein, T.K, 2015a, Evaporites of the Green River Formation, Bridger and Piceance Creek Basins: Deposition, Diagenesis, Paleobrine Chemistry, and Eocene

Atmospheric CO2, *in* Smith, M., and Carroll, A., eds., Stratigraphy and Paleolimnology of the Green River Formation, Western USA: Syntheses in Limnogeology, vol. 1: Springer, Dordrecht, p. 277-312.

Jagniecki, E.A., Lowenstein, T.K., Jenkins, D.M., and Demicco, R.V., 2015b, Eocene atmospheric CO_2 from the nahcolite proxy: Geology, p. G36886.1.

Katz, M.E., Pak, D.K., Dickens, G.R., and Miller, K.G., 1999, The Source and Fate of Massive Carbon Input During the Latest Paleocene Thermal Maximum: Science, v. 286, p. 1531–1533.

Kurtz, A.C., Kump, L.R., Arthur, M.A., Zachos, J.C., and Paytan, A., 2003, Early Cenozoic decoupling of the global carbon and sulfur cycles: Paleoceanography, v. 18, 1-14.

Kiro, Y., Goldstein, S.L., Lazar, B., and Stein, M., 2016, Environmental implications of salt facies in the Dead Sea: GSA Bulletin, v. 128, p. 824–841.

Kirtland Turner, S., Sexton, P.F., Charles, C.D., and Norris, R.D., 2014, Persistence of carbon release events through the peak of early Eocene global warmth: Nature Geoscience, v. 7, p. 748–751.

Laskar, J., Robutel, P., Joutel, F., Gastineau, M., Correia, A.C.M., and Levrard, B., 2004, A long-term numerical solution for the insolation quantities of the Earth: Astronomy and Astrophysics, v. 428, p. 261–285.

Laskar, J., Fienga, A., Gastineau, M., and Manche, H., 2011a, La2010: a new orbital solution for the long-term motion of the Earth: Astronomy & Astrophysics, v. 532, p. A89.

Laskar, J., Gastineau, M., Delisle, J.-B., Farrés, A., and Fienga, A., 2011b, Strong chaos induced by close encounters with Ceres and Vesta: Astronomy & Astrophysics, v. 532, L4.

Lauretano, V., Hilgen, F.J., Zachos, J.C., and Lourens, L.J., 2016, Astronomically tuned age model for the early Eocene carbon isotope events: A new high-resolution $d^{13}C_{benthic}$ record of ODP Site 1263 between ~ 49 and ~ 54 Ma: Newsletters on Stratigraphy, v. 49, p. 383–400.

Laurin, J., Meyers, S.R., Galeotti, S., and Lanci, L., 2016, Frequency modulation reveals the phasing of orbital eccentricity during Cretaceous Oceanic Anoxic Event II and the Eocene hyperthermals: Earth and Planetary Science Letters, v. 442, p. 143–156.

Lourens, L.J., Sluijs, A., Kroon, D., Zachos, J.C., Thomas, E., Röhl, U., Bowles, J., and Raffi, I., 2005, Astronomical pacing of late Palaeocene to early Eocene global warming events: Nature, v. 435, p. 1083–1087.

Lunt, D.J., Ridgwell, A., Sluijs, A., Zachos, J., Hunter, S., and Haywood, A., 2011, A model for orbital pacing of methane hydrate destabilization during the Palaeogene: Nature Geoscience, v. 4, p. 775–778.

Ma, C., Meyers, S.R., and Sageman, B.B., 2017, Theory of chaotic orbital variations confirmed by Cretaceous geological evidence: Nature, v. 542, p. 468–470.

Machlus, M.L, Olsen, P.E., Christie-Blick, N., Hemming, S.R., 2008, Spectral analysis of the lower Eocene Wilkins Peak Member, Green River Formation, Wyoming: Support for Milankovitch cyclicity: Earth and Planetary Science Letters, v. 268, p. 64-75.

Machlus, M.L., Ramezani, J., Bowring, S.A., Hemming, S.R., Tsukui, K., and Clyde, W.C., 2015, A strategy for cross-calibrating U–Pb chronology and astrochronology of sedimentary sequences: An example from the Green River Formation, Wyoming, USA: Earth and Planetary Science Letters, v. 413, p. 70–78.

Mason, G.M., 1987, Mineralogic aspects of stratigraphy and geochemisty of the Green River Formation, Wyoming [PhD Thesis]: Laramie, The University of Wyoming, 377 p.

Meyers, S.R, 2008, Resolving Milankovitchian controversies: the Triassic Latemar Limestone and the Eocene Green River Formation: Geology, v. 36, p. 319-322.

Meyers, S.R., 2014, Astrochron: An R Package for Astrochronology. https://cran.r-project.org/package=astrochron

Meyers, S.R., and Sageman, B.B., 2004, Detection, quantification, and significance of hiatuses in pelagic and hemipelagic strata: Earth and Planetary Science Letters, v. 224, p. 55-72.

Meyers, S.R., Sageman, B.B., and Hinnov, L.A., 2001, Integrated quantitative stratigraphy of the Cenomanian-Turonian Bridge Creek Limestone Member using evolutive harmonic analysis and stratigraphic modeling: Journal of Sedimentary Research, v. 71, p. 628–644.

Nicolo, M.J., Dickens, G.R., Hollis, C.J., and Zachos, J.C., 2007, Multiple early Eocene hyperthermals: Their sedimentary expression on the New Zealand continental margin and in the deep sea: Geology, v. 35, p. 699–702.

Picard, M.D. and High, L.R., 1972, Paleoenvironmental Reconstructions in an Area of Rapid Facies Change, Parachute Creek Member of Green River Formation (Eocene), Uinta Basin, Utah, *GSA Bulletin, v* 83, no. 9, p. 2689–2708.

R Core Team, 2014, R: A language and environment for statistical computing: R Foundation for Statistical Computing, Vienna, Austria.

Remy, R.R., 1992, Stratigraphy of the Eocene part of the Green River Formation in the south-central part of the Uinta Basin, Utah: Bulletin Report 1787-BB.

Rhodes, M.K., Carroll, A.R., Pietras, J.T., Beard, B.L., and Johnson, C.M., 2002, Strontium isotope record of paleohydrology and continental weathering, Eocene Green River Formation, Wyoming: Geology, v. 30, p. 167–170.

Rhodes, M.K., Malone, D.H., Carroll, A.R., and Smith, E.M., 2007, Sudden Desiccation of Lake Gosiute at ~49 Ma: A Downstream Record of Heart Mountain Faulting?: The Mountain Geologist, v. 44, p. 1–10.

Rhodes, M.K., and Carroll, A.R., 2015, Lake Type Transition from Balanced-Fill to Overfilled: Laney Member, Green River Formation, Washakie Basin, Wyoming, *in* Smith, M., and Carroll, A., eds., Stratigraphy and Paleolimnology of the Green River Formation, Western USA: Syntheses in Limnogeology, vol. 1: Springer, Dordrecht, p. 103-126

Robb, W.A., and Smith, J.W., 1974, Mineral profile of the oil shales in Colorado Core Hole No. 1, Piceance Creek Basin, Colorado: in D. Keith Murray, ed., Guidebook to the Energy Resources of the Piceance Creek Basin Colorado: Rocky Mountain Association of Geologists Twenty-Fifth Field Conference Guidebook, p. 91-100.

Roehler, H.W., 1973, Stratigraphic divisions and geological history of the Laney member of the Green River Formation in the Washakie Basin in southwestern Wyoming: US Geological Survey, Bulletin, v. 1372-E.

Roehler, H.W., 1991, Revised stratigraphic nomenclature for the Wasatch and Green River formations of Eocene age, Wyoming, Utah, and Colorado: US Geological Survey, Professional Paper, v. 1506-B.

Roehler, H.W., 1993, Eocene climates, depositional environments, and geography, greater Green River basin, Wyoming, Utah, and Colorado: US Geological Survey, Professional Paper Report 1506-F.

Schiffelbein, P., and Dorman, L., 1986, Spectral effects of time-depth nonlinearities in deep sea sediment records: A demodulation technique for realigning time and depth scales: Journal of Geophysical Research: Solid Earth, v. 91, p. 3821–3835.

Sexton, P.F., Norris, R.D., Wilson, P.A., Pälike, H., Westerhold, T., Röhl, U., Bolton, C.T., and Gibbs, S., 2011, Eocene global warming events driven by ventilation of oceanic dissolved organic carbon: Nature, v. 471, p. 349–352.

Sheliga, C.M., 1980, Sedimentation of the Eocene Green River Formation in Sevier and Sanpete Counties, Utah [M.S. Thesis]: Columbus, The Ohio State University, 166 p.

Sirota, I., Arnon, A., and Lensky, N.G., 2016, Seasonal variations of halite saturation in the Dead Sea: Water Resources Research, v. 52, p. 7151–7162.

Sirota, I., Enzel, Y., and Lensky, N.G., 2017, Temperature seasonality control on modern halite layers in the Dead Sea: In situ observations: GSA Bulletin, v. 129, p. 1181–1194.

Smith, M.E., Carroll, A.R., and Singer, B.S., 2008, Synoptic reconstruction of a major ancient lake system: Eocene Green River Formation, western United States: Geological Society of America Bulletin, v. 120, p. 54–84.

Smith, M.E., Carroll, A.R., Scott, J.J., and Singer, B.S., 2014a, Early Eocene carbon isotope excursions and landscape destabilization at eccentricity minima: Green River Formation of Wyoming: Earth and Planetary Science Letters, v. 403, p. 393–406.

Smith, M.E., Carroll, A.R., Jicha, B.R., Cassel, E.J., and Scott, J.J., 2014b, Paleogeographic record of Eocene Farallon slab rollback beneath western North America: Geology, v. 42, p. 1039–1042.

Smith, M.E., and Carroll, A.R., 2015, Introduction to the Green River Formation, *in* Smith, M., and Carroll, A., eds., Stratigraphy and Paleolimnology of the Green River Formation, Western USA: Syntheses in Limnogeology, vol. 1: Springer, Dordrecht, p. 1-12.

Smith, M.E., Carroll, A.R., and Scott, J.J., 2015, Stratigraphic Expression of Climate, Tectonism, and Geomorphic Forcing in an Underfilled Lake Basin: Wilkins Peak Member of the Green River Formation *in* Smith, M., and Carroll, A., eds., Stratigraphy and Paleolimnology of the Green River Formation, Western USA: Syntheses in Limnogeology, vol. 1: Springer, Dordrecht, p. 61–102.

Sullivan, R., 1980, A stratigraphic evaluation of the Eocene rocks of southwestern Wyoming: Reports of Investigations, The Geological Survey of Wyoming, no. 20, p. 1-50.

Taner, M.T., Schuelke, J.S., O'Doherty, R., and Baysal, E., 1994, Seismic attributes revisited *in* SEG Technical Program Expanded Abstracts 1994, Society of Exploration Geophysicists, SEG Technical Program Expanded Abstracts, p. 1104–1106

Thomson, D.J., 1982, Spectrum estimation and harmonic analysis: Proceedings of the IEEE, v.70, p. 1055–1096.

Walters, A.P., Meyers, S.R., Carroll, A.R., Hill, T.R., and Vanden Berg, M.D., 2020, Lacustrine cyclicity in the early Eocene Green River Formation, Uinta Basin, Utah: Evidence from X-ray fluorescence core scanning: Journal of Sedimentary Research, v. 90, p. 429–447

Westerhold, T., Röhl, U., and Laskar, J., 2012, Time scale controversy: Accurate orbital calibration of the early Paleogene: Geochemistry, Geophysics, Geosystems, v. 13.

Westerhold, T., Röhl, U., Donner, B., and Zachos, J.C., 2018, Global Extent of Early Eocene Hyperthermal Events: A New Pacific Benthic Foraminiferal Isotope Record from Shatsky Rise (ODP Site 1209): Paleoceanography and Paleoclimatology, v. 33, p. 626–642.

Wiig, S.V., Grundy, W.D., and Dyni, J.R., 1995, Trona resources in the Green River basin, southwest Wyoming: U.S. Geological Survey, Open-File Report USGS Numbered Series 95–476.

Zachos, J.C., 2001, Trends, Rhythms, and Aberrations in Global Climate 65 Ma to Present: Science, v. 292, p. 686-693.

Zachos, J.C., Dickens, G.R., and Zeebe, R.E., 2008, An early Cenozoic perspective on greenhouse warming and carbon-cycle dynamics: Nature, v. 451, p. 279–283.

Zachos, J.C., McCarren, H., Murphy, B., Röhl, U., and Westerhold, T., 2010, Tempo and scale of late Paleocene and early Eocene carbon isotope cycles: Implications for the origin of hyperthermals: Earth and Planetary Science Letters, v. 299, p. 242–249.

Zeebe, R. E., 2017 Numerical Solutions for the orbital motion of the Solar System over the Past 100 Myr: Limits and new results: The Astronomical Journal, v. 154, no. 5, 13p.

Zeebe, R. E. and Lourens, L. J., 2019, Solar system chaos and the Paleocene-Eocene boundary age constrained by geology and astronomy: Science, v. 30, p. 926-939.

Figures and Tables

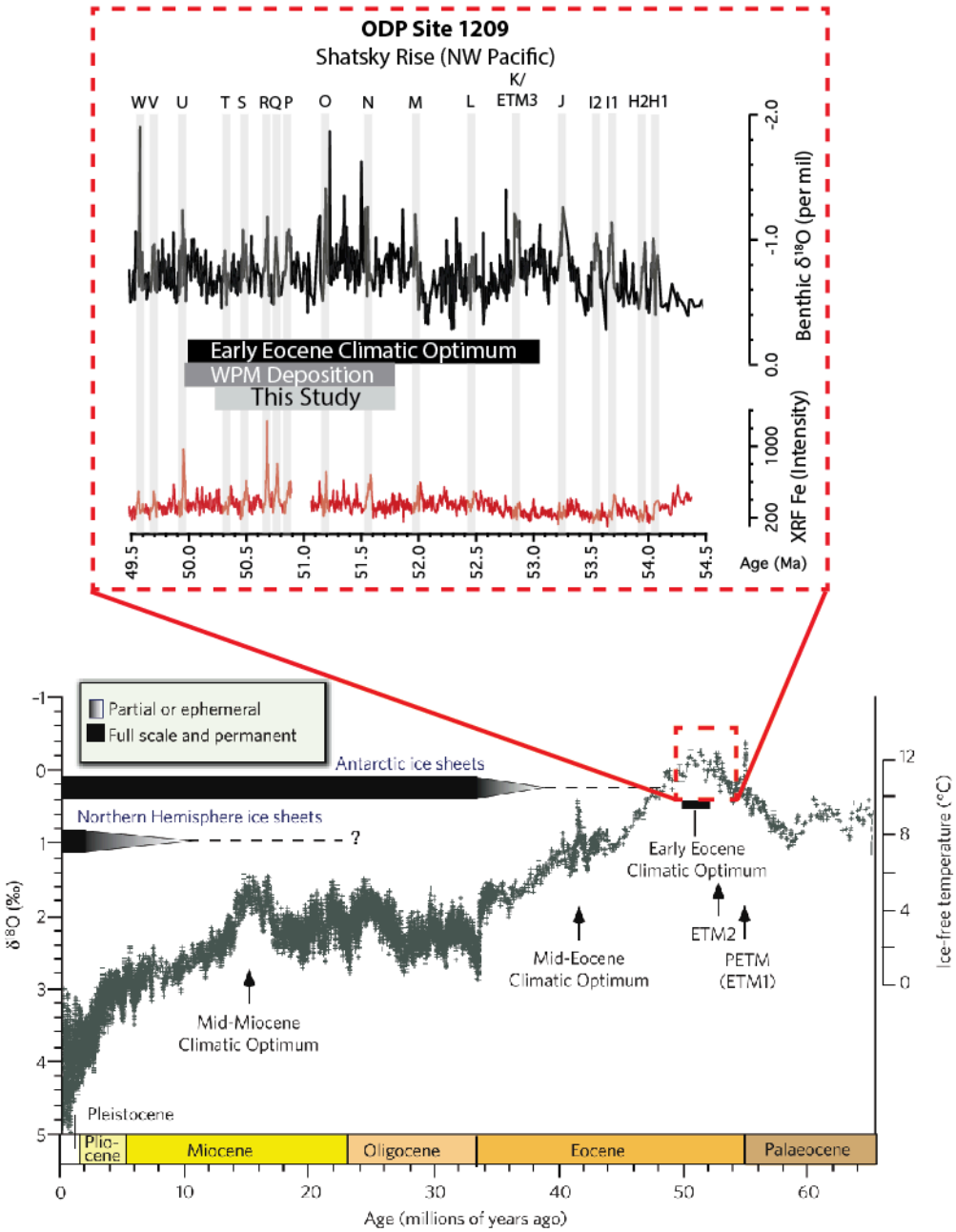

Figure 1: Climate context of the Early Eocene Climatic Optimum (EECO). Lowermost plot shows inferred deep marine paleo-temperature using the oxygen isotope record of Zachos et al. (2008). The upper inset shows an EECO oxygen isotope and Fe intensity record from ODP Site 1209 (Shatsky Rise), with hypothesized hyperthermal events highlighted in light grey. Vertical bars represent the duration of the EECO, overall WPM deposition, and the WPM interval covered in this study. Modified from Zachos et al. (2008) and Westerhold et al. (2018).

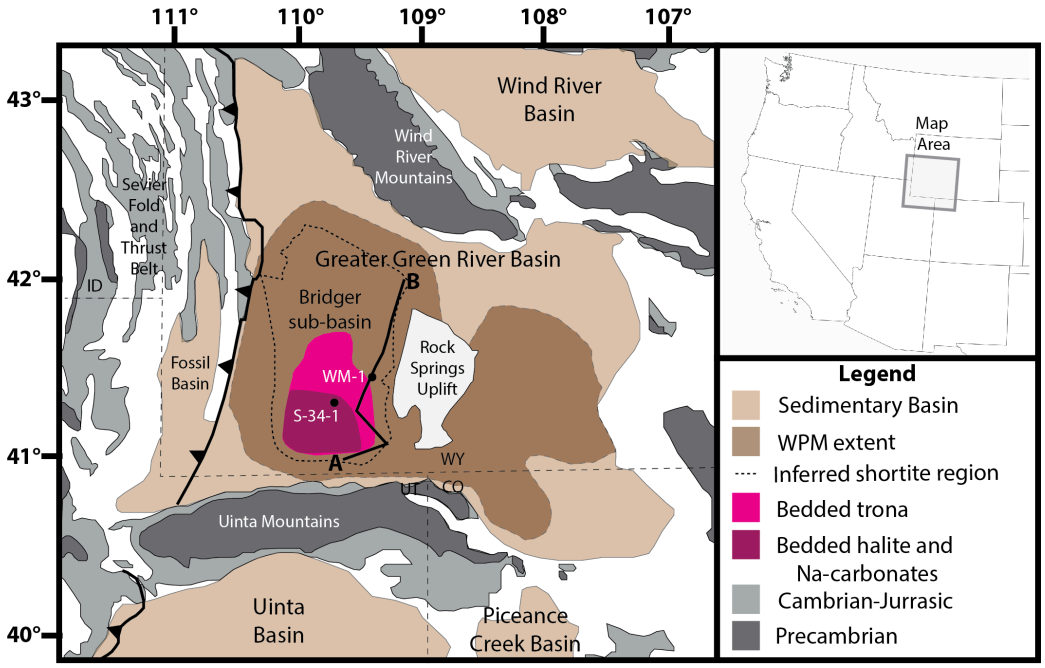

Figure 2: Location map for the Greater Green River Basin, Green River Formation. Modified from Smith et al. (2008) and Jagniecki et al. (2015).

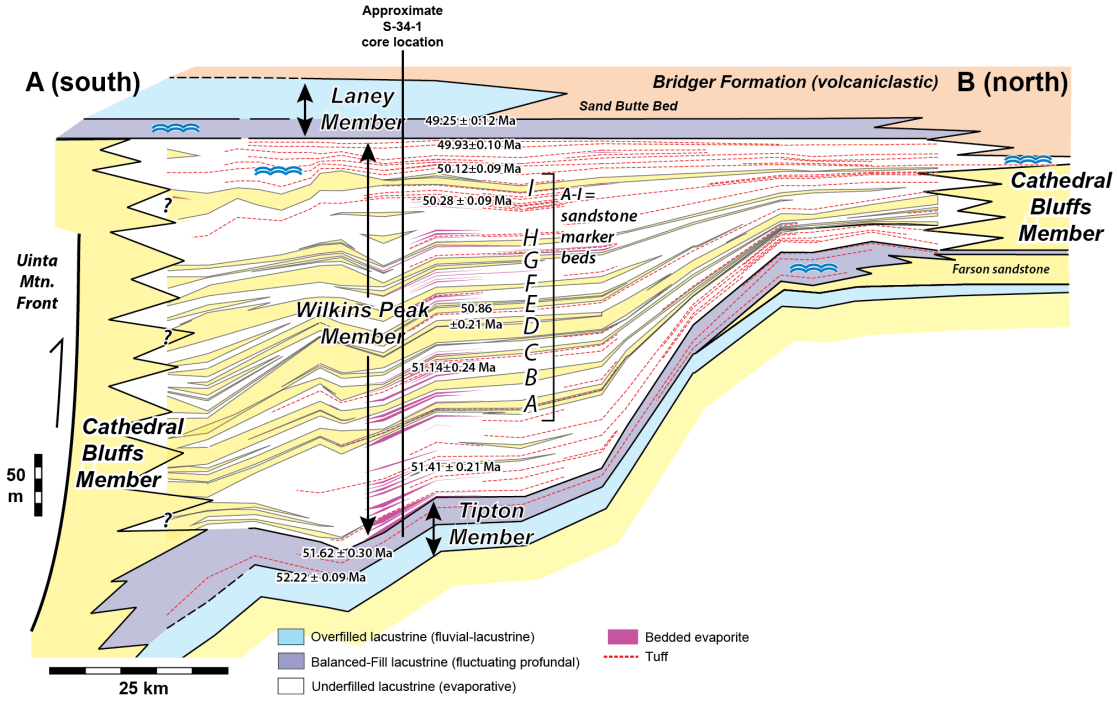

Figure 3: Cross section of the Bridger sub-basin, Greater Green River Basin across the A to B transect shown in Figure 2. Modified from Smith et al. (2015).

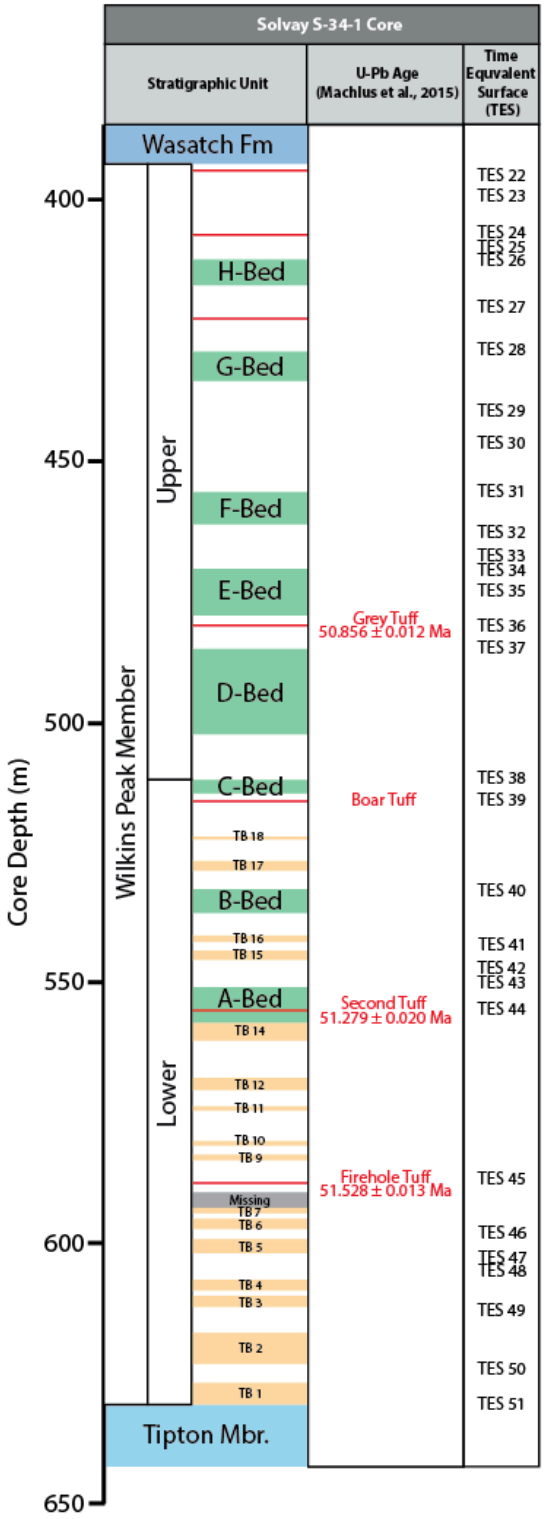

Figure 4: Generalized stratigraphy of the Solvay S-34-1 core, showing the depth distribution of time-equivalent surface (TES) points. Within the Wilkins Peak Member, green shading represents alluvial facies, orange shading represents bedded evaporite facies (TB=Trona Bed), and white represents carbonate marl facies. U-Pb ages are from Machlus et al. (2015) and the uncertainties shown are analytical uncertainties (2 sigma).

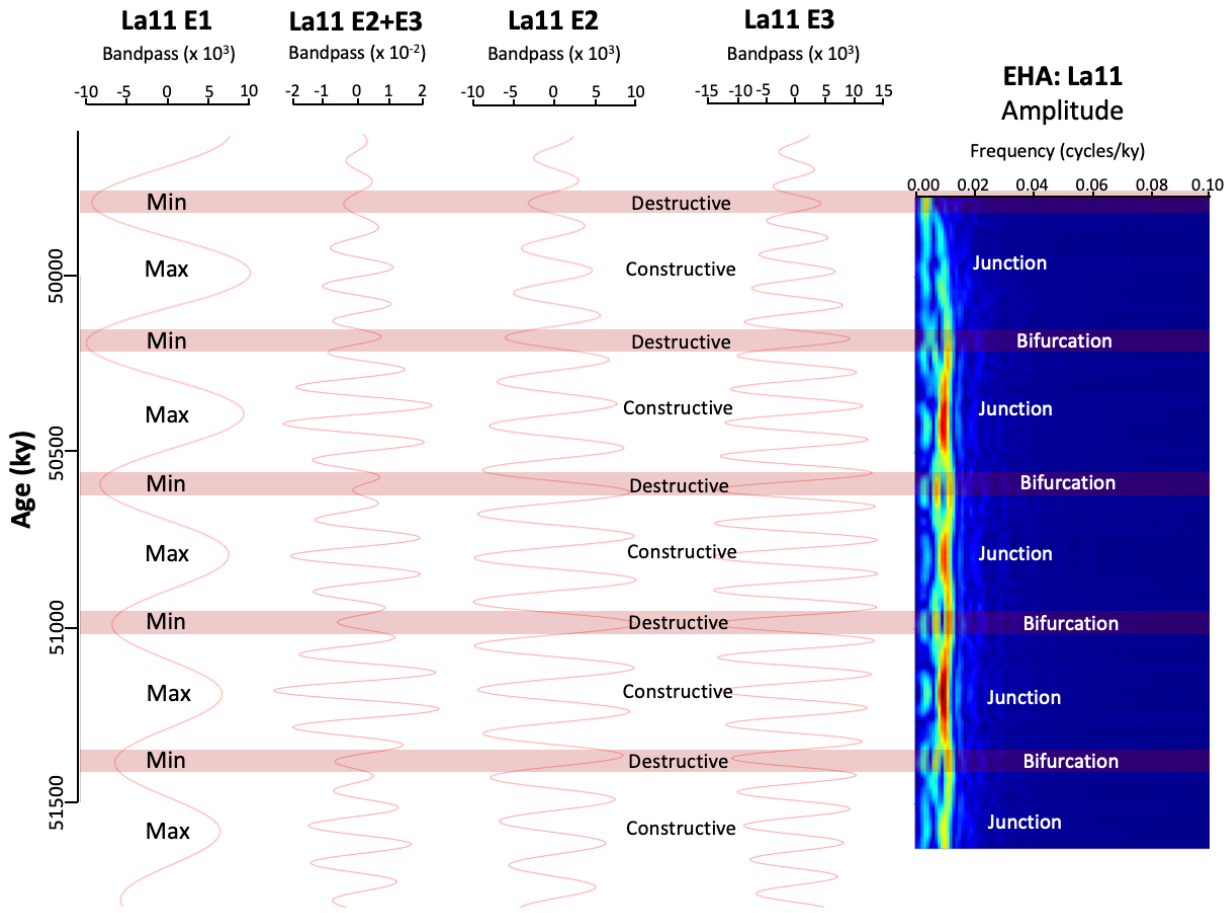

Figure 5: Example of the interference patterns between the E2 (~127 ky) and E3 (~96 ky) eccentricity cycles in the La11 Solution, which can be used to determine long eccentricity (E1) phase using the frequency modulation approach of Laurin et al. (2016).

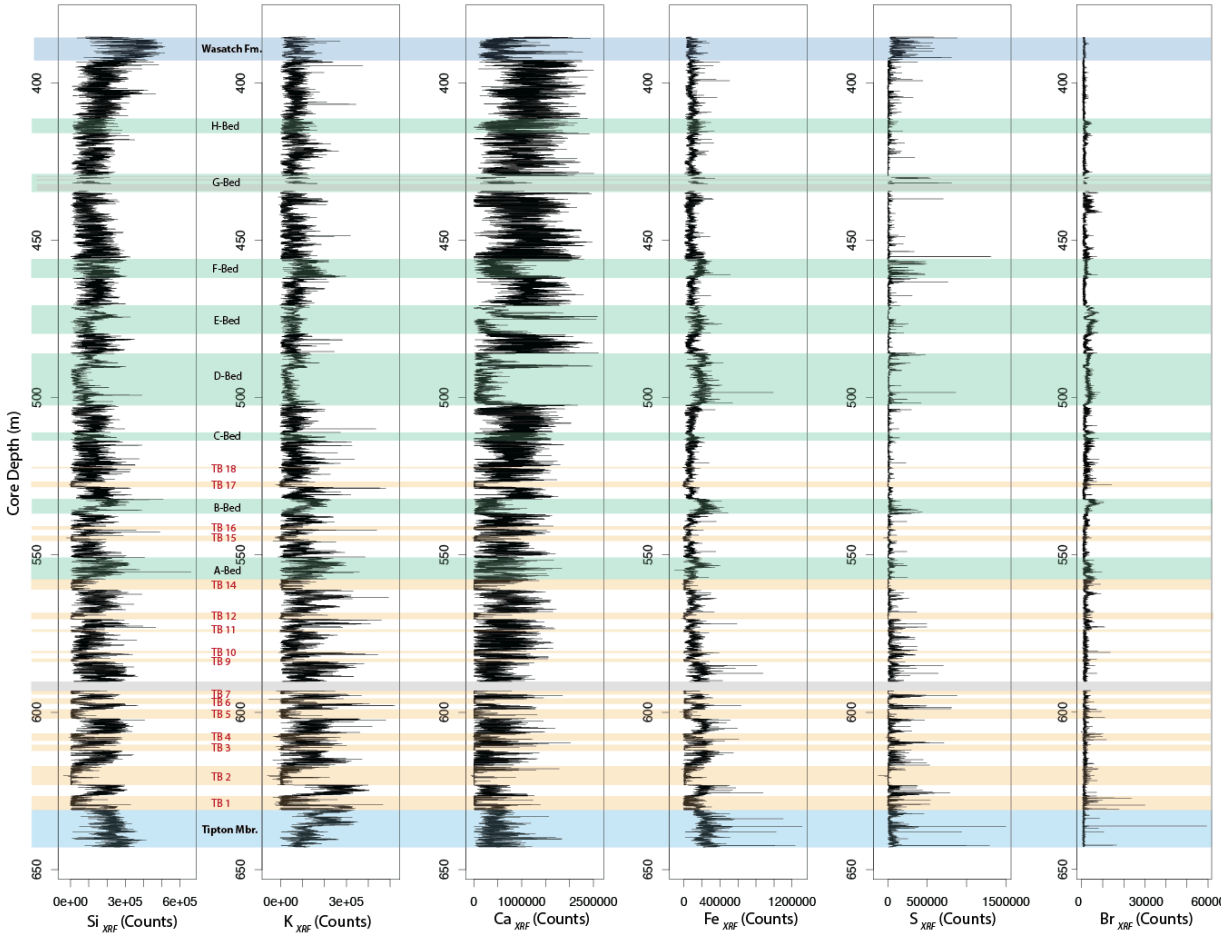

Figure 6: XRF core scanner results (in counts) for Si, K, Ca, Fe, S, and Br. Within the Wilkins Peak Member, green shading represents alluvial facies, orange shading represents bedded evaporite facies (TB=Trona Bed), and white represents carbonate marl facies.

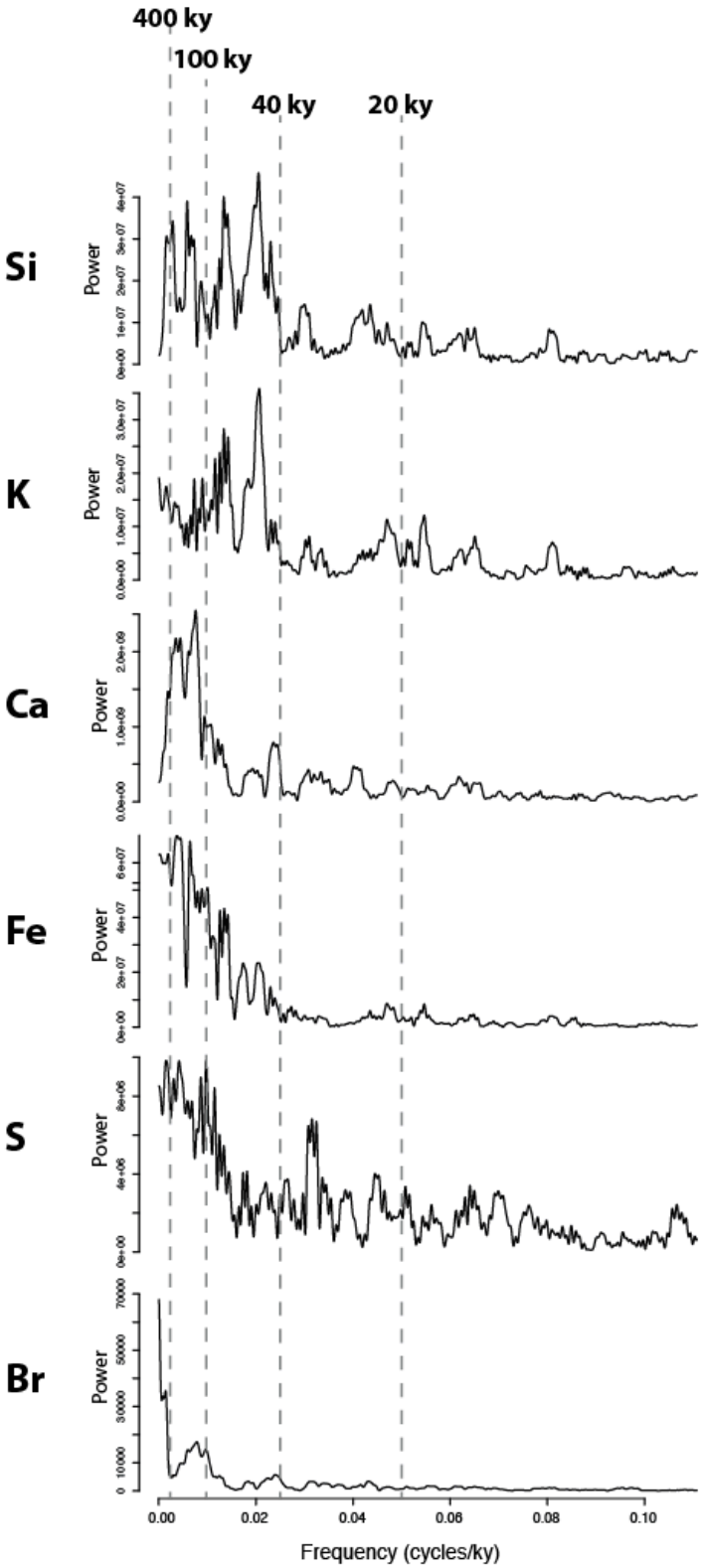

Figure 7: MTM power spectra (3-2 DPSS tapers) for TES calibrated Si, K, Ca, Fe, S, and Br elemental records. Dashed lines represent show the approximate frequency of long eccentricity (~ 400 ky), short eccentricity (~ 100 ky), obliquity (~ 40 ky), and precession (~ 20 ky).

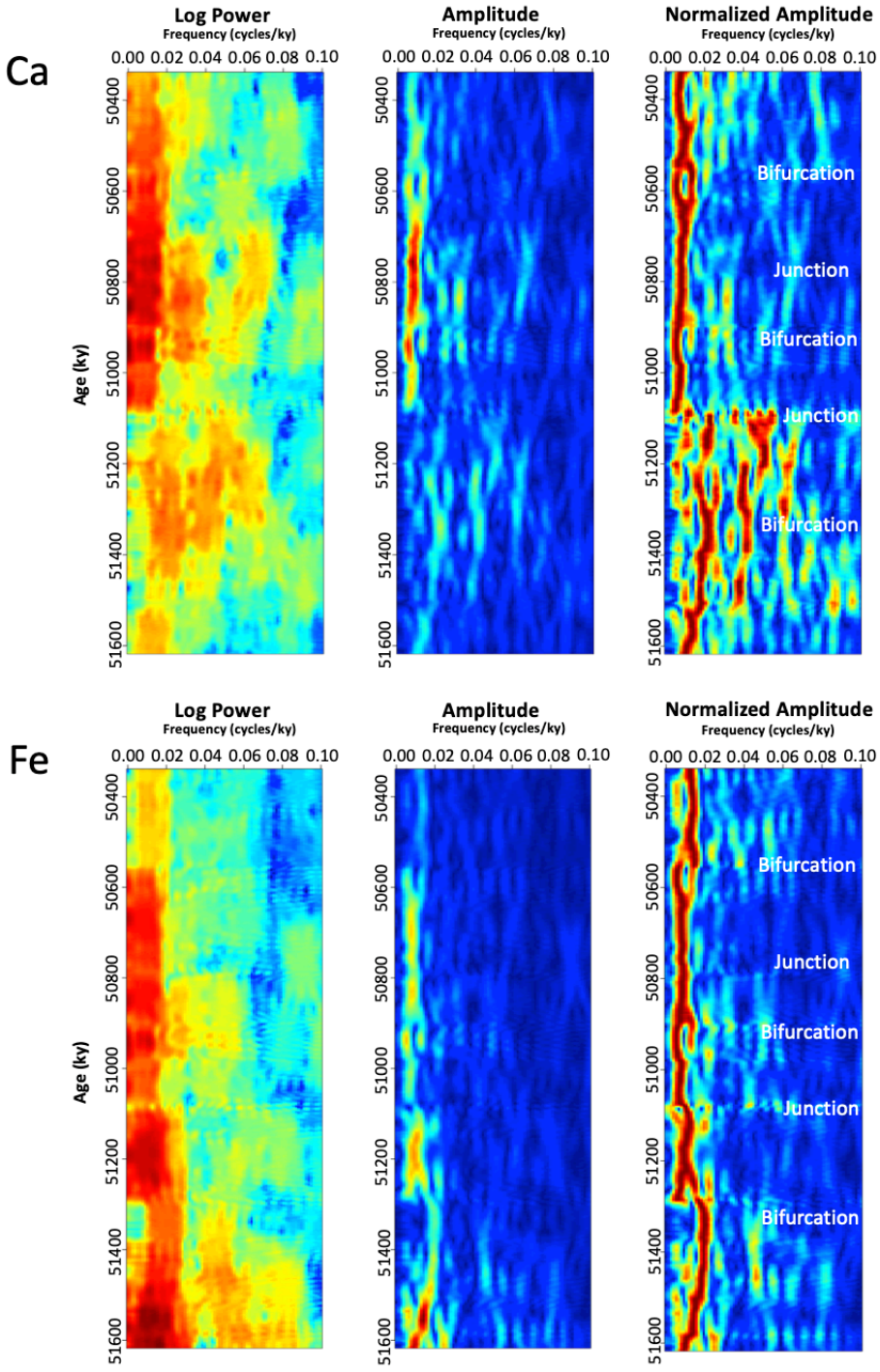

Figure 8: EHA (3-2 DPSS tapers, 200 ky window) plots for temporally calibrated Ca and Fe elemental records, showing log power, amplitude, and normalized amplitude. Text notes the approximate depth location of junctions and bifurcations in the eccentricity signal within the normalized amplitude EHA plot.

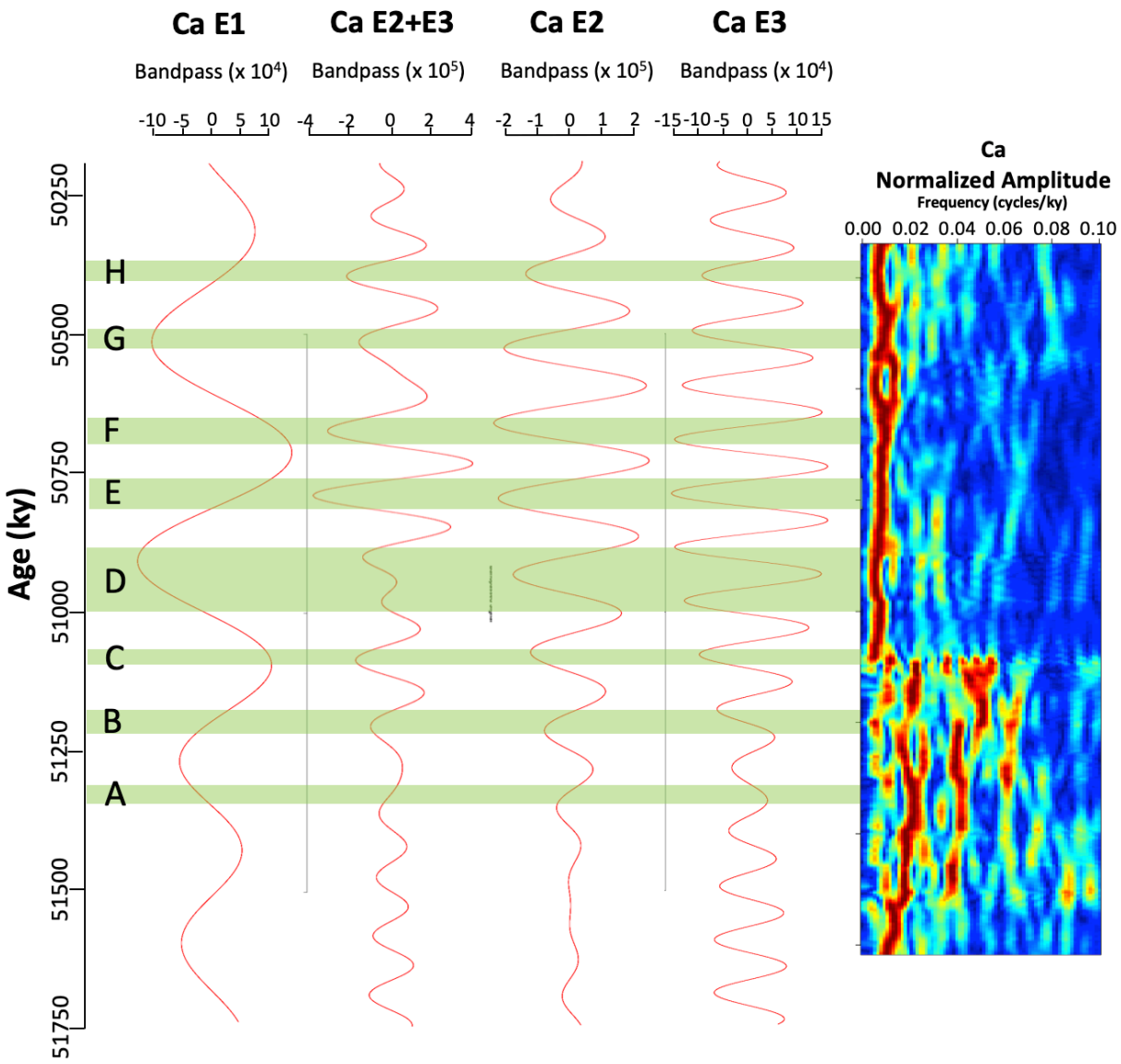

Figure 9: Taner bandpass filter results for the temporally calibrated Ca record, showing the filtered results for the E1, E2+E3, E2, and E3 eccentricity cycles in comparison to the EHA normalized amplitude plot for temporally calibrated Ca. The modeled temporal duration of alluvial bed deposition is highlighted using green bars.

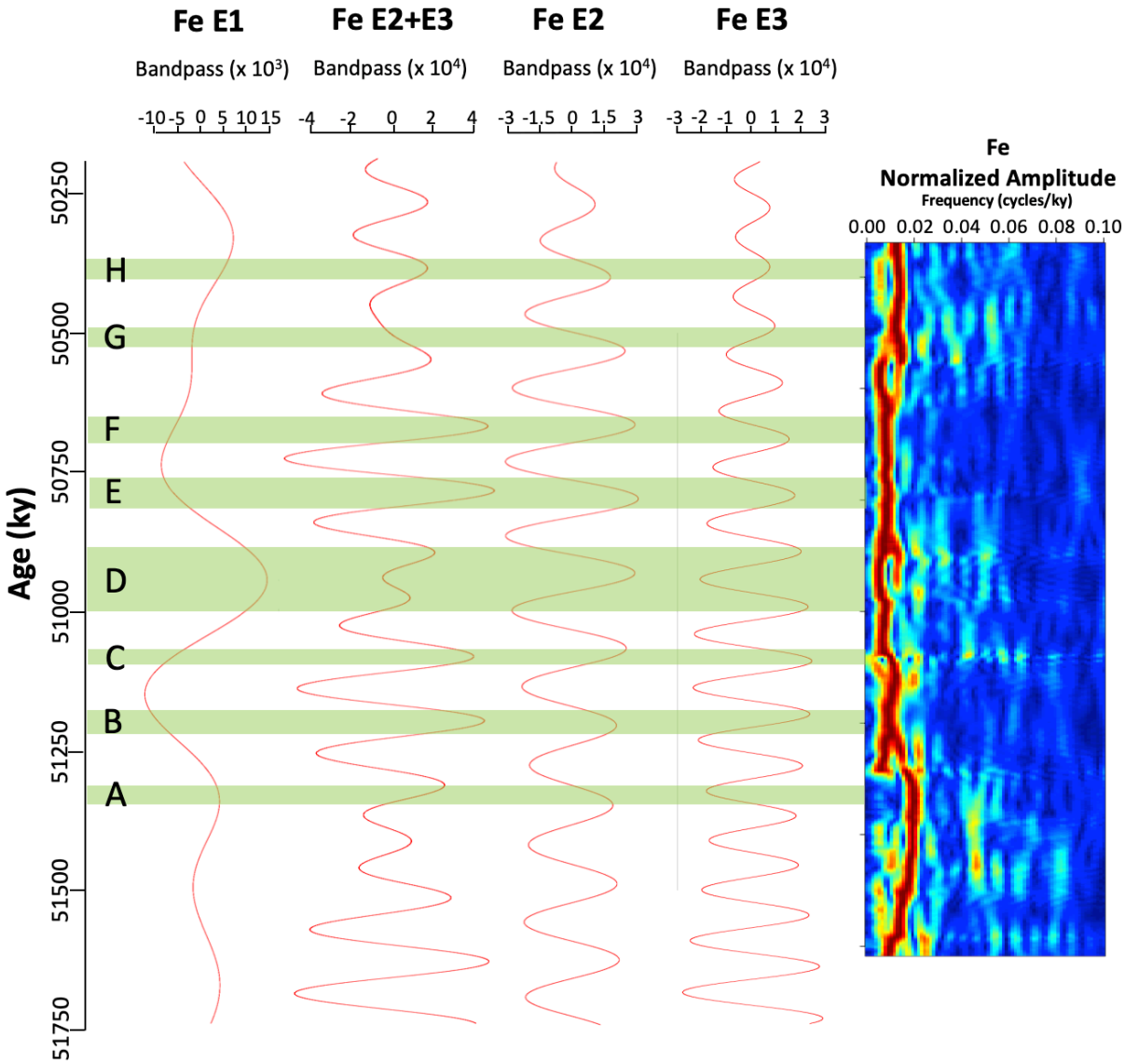

Figure 10: Taner bandpass filter results for the temporally calibrated Fe record, showing the filtered results for the E1, E2+E3, E2, and E3 eccentricity cycles in comparison to the EHA normalized amplitude plot for temporally calibrated Fe. The modeled temporal duration of alluvial bed deposition is highlighted using green bars.

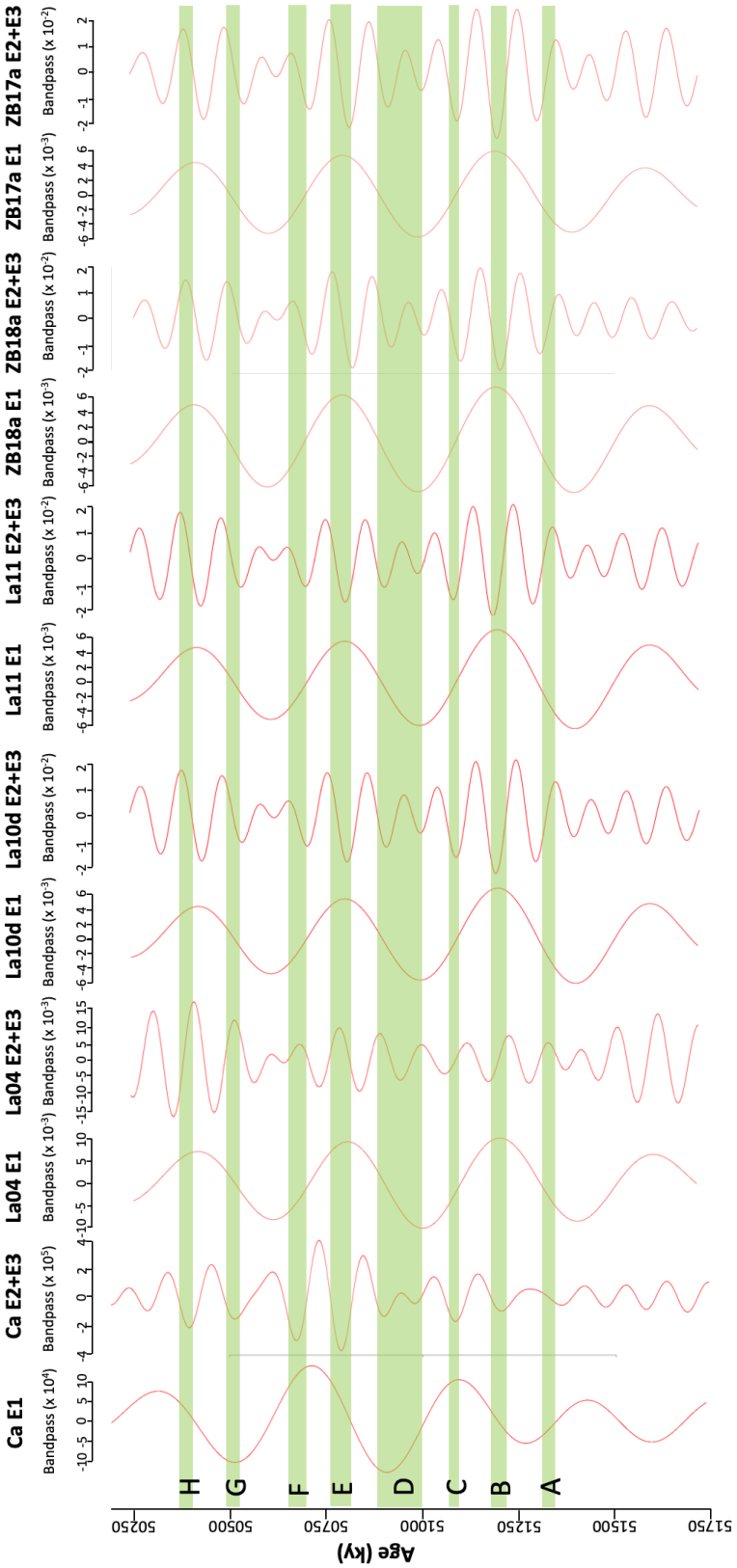

Figure 11: Taner bandpass filter comparison E1 and E2+E3 cycles of the WPM temporally calibrated Ca astrochronology and the La10d, La11, ZB17a, and ZB18a astronomical models, between 50.25-51.75 Ma. The modeled temporal duration of alluvial bed deposition is highlighted using green bars.

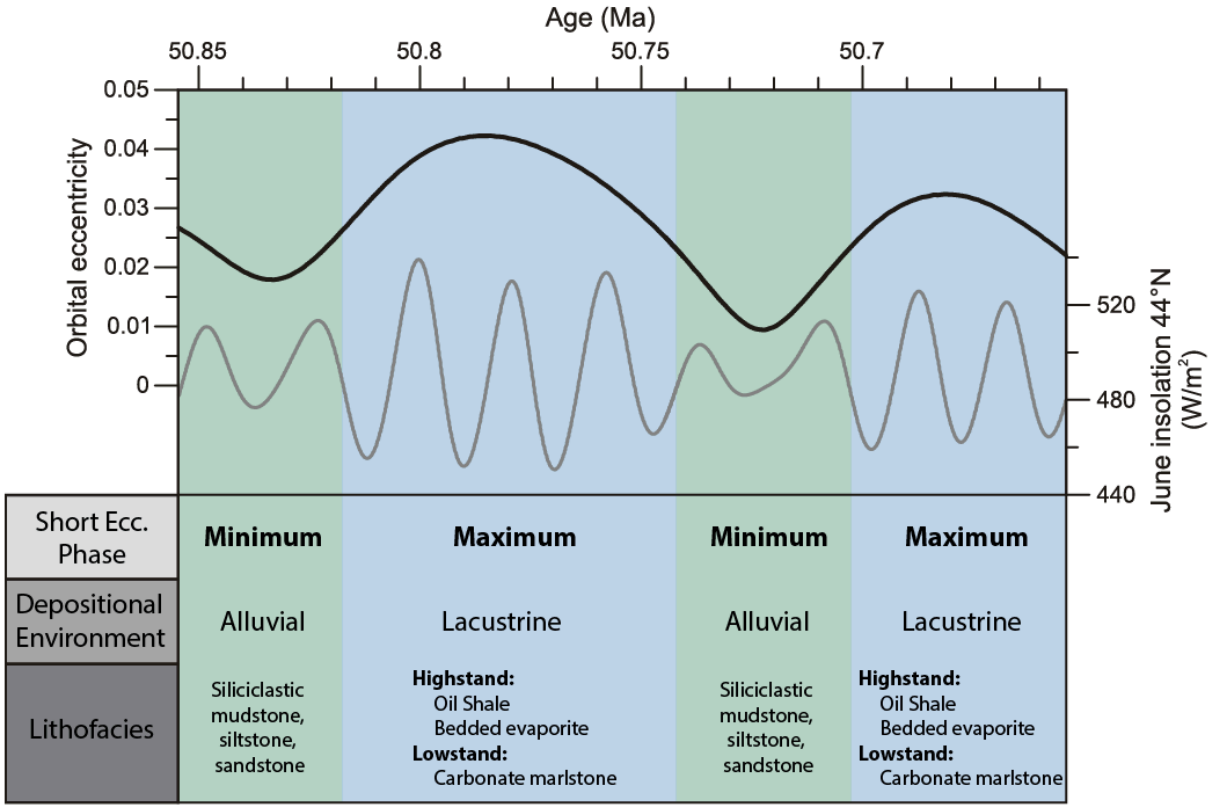

Figure 12: Tri-modal lithofacies deposition model for the Wilkins Peak Member of the Green River Formation. The short eccentricity cycle (black line) and precession cycle (grey line) are derived from the La04 astronomical solution (Laskar et al., 2004). Green bars highlight intervals of short eccentricity minima and blue bars highlight intervals of short eccentricity maxima. Modified from Smith et al. (2014a).

Table 1: Weighted mean U-Pb ages from Machlus et al. (2015) used in the tuff calibration model. U-Pb uncertainties are total uncertainties (2 sigma).

Tuff	Age (Ma)	Total Uncertainty (Ma)
Sixth	49.686	0.069
Layered	49.919	0.074
Main	50.104	0.067
Grey	50.856	0.060
Second	51.279	0.064
Firehole	51.528	0.061

Table 2: Modeled ages for the 30 time-equivalent surfaces identified in the S-34-1 core. These surfaces were calculated using the approach of Aswasereelert et al. (2013) and the weighted mean U-Pb ages of Machlus et al. (2015).

TES #	Modeled Age (Ma)	Surface Name
22	50.239	
23	50.256	
24	50.268	
25	50.327	
26	50.366	Top of H-Bed
27	50.409	
28	50.491	Top of G-Bed
29	50.554	
30	50.610	
31	50.650	Top of F-Bed
32	50.704	
33	50.735	
34	50.759	Top of E-Bed
35	50.784	
36	50.822	Grey Tuff
37	50.884	Top of D-Bed
38	51.056	Top of C-Bed
39	51.116	Boar/C-Bed Tuff
40	51.175	Top of B-Bed
41	51.241	
42	51.275	
43	51.331	Top of A-Bed
44	51.334	Second Tuff
45	51.488	Firehole Tuff
46	51.531	
47	51.610	
48	51.631	
49	51.657	
50	51.704	
51	51.718	Base of WPM

Table 3: Correlation coefficients between elements within the S-34-1 core XRF record.

Element	Mg	Al	Si	P	S	Cl	K	Ca	Ti	V	Cr	Mn	Fe	Rh	Cu	Zn	Br	Rb	Sr	Y	Zr	Mo	Pb
Mg	1.00	0.10	0.26	0.03	-0.15	-0.25	0.14	0.34	0.02	-0.12	0.17	0.31	0.05	0.02	0.04	-0.06	-0.18	-0.05	0.33	-0.30	-0.09	0.06	-0.03
Al	0.10	1.00	0.74	-0.04	0.15	-0.22	0.84	-0.14	0.71	-0.18	0.15	0.04	0.65	-0.04	0.65	0.62	-0.09	0.65	-0.19	-0.05	0.10	0.17	0.28
Si	0.26	0.74	1.00	-0.26	0.14	-0.29	0.62	0.12	0.47	-0.31	0.24	0.13	0.43	-0.03	0.40	0.48	-0.14	0.44	-0.01	-0.22	0.20	0.05	0.19
P	0.03	-0.04	-0.26	1.00	-0.10	0.06	0.03	-0.16	0.02	0.08	-0.03	0.08	0.06	-0.04	0.02	-0.07	0.10	0.00	0.02	0.09	-0.03	0.12	-0.02
S	-0.15	0.15	0.14	-0.10	1.00	0.05	0.17	-0.14	0.17	-0.08	0.04	-0.07	0.32	-0.06	0.13	0.19	0.06	0.19	-0.15	0.00	0.11	0.15	0.30
Cl	-0.25	-0.22	-0.29	0.06	0.05	1.00	-0.17	-0.30	-0.04	0.10	-0.15	0.07	0.17	-0.25	-0.02	0.26	0.50	0.35	-0.14	0.10	0.11	-0.13	0.01
K	0.14	0.84	0.62	0.03	0.17	-0.17	1.00	-0.12	0.58	-0.21	0.19	0.06	0.55	-0.07	0.57	0.56	-0.06	0.62	-0.12	-0.16	0.04	0.20	0.21
Ca	0.34	-0.14	0.12	-0.16	-0.14	-0.30	-0.12	1.00	-0.23	-0.30	0.41	0.19	-0.21	-0.06	-0.22	-0.25	-0.33	-0.36	0.85	-0.28	-0.03	-0.08	-0.11
Ti	0.02	0.71	0.47	0.02	0.17	-0.04	0.58	-0.23	1.00	-0.12	0.08	0.06	0.67	-0.03	0.57	0.62	0.05	0.67	-0.23	0.05	0.15	0.13	0.24
V	-0.12	-0.18	-0.31	0.08	-0.08	0.10	-0.21	-0.30	-0.12	1.00	-0.30	-0.14	-0.15	0.11	-0.08	-0.15	0.08	-0.12	-0.27	0.23	-0.07	0.00	-0.04
Cr	0.17	0.15	0.24	-0.03	0.04	-0.15	0.19	0.41	0.08	-0.30	1.00	0.07	0.15	-0.11	0.06	0.08	-0.10	0.06	0.40	-0.26	0.04	0.05	0.04
Mn	0.31	0.04	0.13	0.08	-0.07	0.07	0.06	0.19	0.06	-0.14	0.07	1.00	0.17	-0.08	0.02	0.06	0.07	0.07	0.24	-0.17	0.00	-0.04	-0.02
Fe	0.05	0.65	0.43	0.06	0.32	0.17	0.55	-0.21	0.67	-0.15	0.15	0.17	1.00	-0.12	0.55	0.66	0.21	0.75	-0.18	-0.02	0.11	0.14	0.34
Rh	0.02	-0.04	-0.03	-0.04	-0.06	-0.25	-0.07	-0.06	-0.03	0.11	-0.11	-0.08	-0.12	1.00	-0.03	-0.12	-0.13	-0.15	-0.10	0.08	-0.05	-0.02	-0.03
Cu	0.04	0.65	0.40	0.02	0.13	-0.02	0.57	-0.22	0.57	-0.08	0.06	0.02	0.55	-0.03	1.00	0.59	-0.07	0.57	-0.18	-0.03	0.06	0.17	0.34
Zn	-0.06	0.62	0.48	-0.07	0.19	0.26	0.56	-0.25	0.62	-0.15	0.08	0.06	0.66	-0.12	0.59	1.00	0.15	0.83	-0.27	-0.02	0.15	0.05	0.22
Br	-0.18	-0.09	-0.14	0.10	0.06	0.50	-0.06	-0.33	0.05	0.08	-0.10	0.07	0.21	-0.13	-0.07	0.15	1.00	0.30	-0.22	0.09	0.06	-0.04	0.18
Rb	-0.05	0.65	0.44	0.00	0.19	0.35	0.62	-0.36	0.67	-0.12	0.06	0.07	0.75	-0.15	0.57	0.83	0.30	1.00	-0.32	-0.03	0.15	0.10	0.21
Sr	0.33	-0.19	-0.01	0.02	-0.15	-0.14	-0.12	0.85	-0.23	-0.27	0.40	0.24	-0.18	-0.10	-0.18	-0.27	-0.22	-0.32	1.00	-0.30	-0.01	-0.04	-0.11
Y	-0.30	-0.05	-0.22	0.09	0.00	0.10	-0.16	-0.28	0.05	0.23	-0.26	-0.17	-0.02	0.08	-0.03	-0.02	0.09	-0.03	-0.30	1.00	0.11	-0.03	0.02
Zr	-0.09	0.10	0.20	-0.03	0.11	0.11	0.04	-0.03	0.15	-0.07	0.04	0.00	0.11	-0.05	0.06	0.15	0.06	0.15	-0.01	0.11	1.00	-0.01	0.05
Mo	0.06	0.17	0.05	0.12	0.15	-0.13	0.20	-0.08	0.13	0.00	0.05	-0.04	0.14	-0.02	0.17	0.05	-0.04	0.10	-0.04	-0.03	-0.01	1.00	0.11
Pb	-0.03	0.28	0.19	-0.02	0.30	0.01	0.21	-0.11	0.24	-0.04	0.04	-0.02	0.34	-0.03	0.34	0.22	0.18	0.21	-0.11	0.02	0.05	0.11	1.00

Supplemental Appendices

Supplement A: Chapter 1

Supplement A1.

Measurement of Ca counts in the SARM-4 standard, demonstrating the stability of the Avaatech XRF instrument over the period of study. This standard was measured before and after each core segment scan.

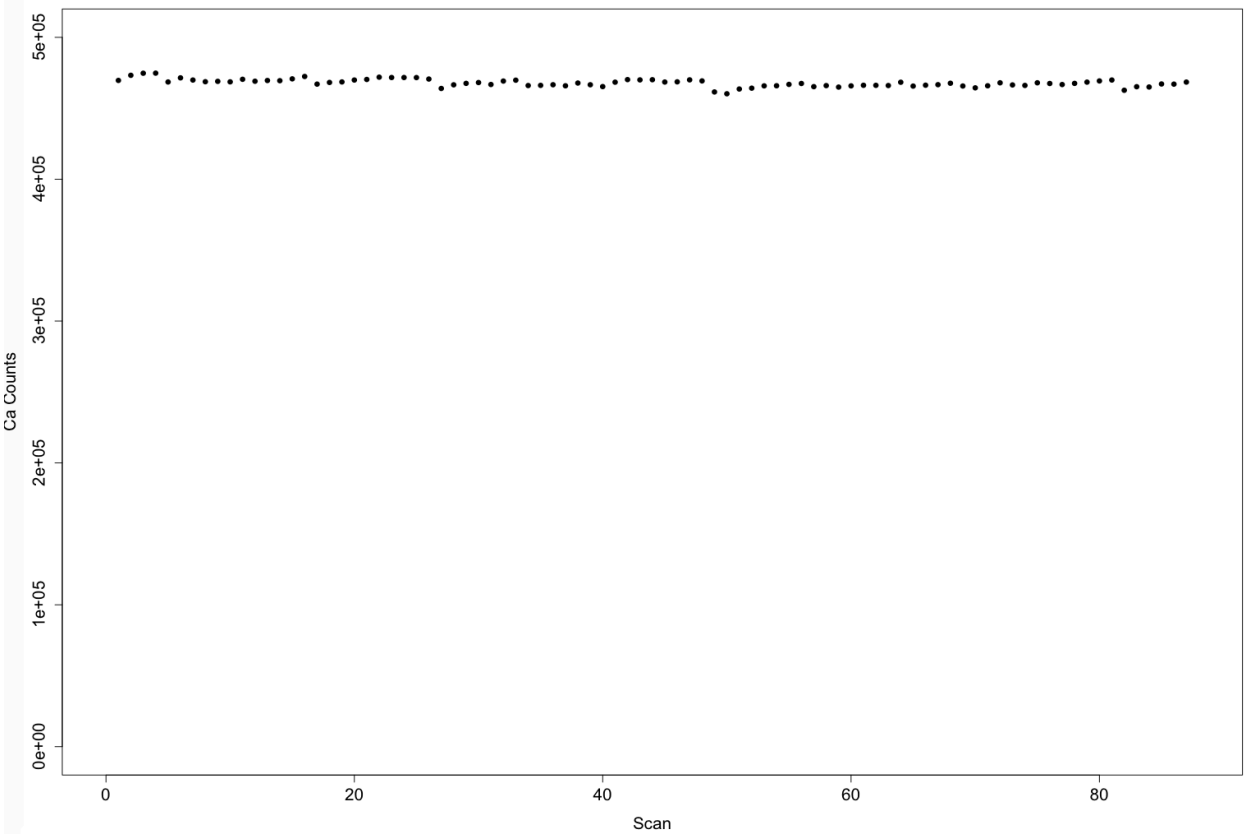

Supplement A2.

Coefficient of variation and the standard deviation of the coefficient of variation results for elements (in counts) at the 5 mm XRF scanning resolution.

Element	Mean Coefficient of Variation	Standard Deviation of Coefficient of Variation	Number of Duplicate Measurements
Mg	0.044	0.066	319
Al	0.018	0.028	326
Si	0.007	0.017	326
S	0.022	0.037	326
K	0.005	0.005	326
Ca	0.002	0.004	326
Ti	0.017	0.014	326
Mn	0.078	0.068	326
Fe	0.004	0.006	326
Cu	0.042	0.034	336
Zn	0.029	0.024	336
Rb	0.030	0.030	336
Sr	0.004	0.006	336
Zr	0.028	0.021	336
Mo	0.116	0.100	336
Pb	0.097	0.085	336

Supplement A3.

Coefficient of variation and the standard deviation of the coefficient of variation results for elements (in counts) at the 100 µm XRF scanning resolution. For elements Al, Si, S, K, Ca, and Fe, a correction has been applied to the duplicate XRF measurements before evaluation of uncertainty due to changes in the XRF counts after equipment maintenance. This correction varies from element to element and is equivalent to the mean average difference in counts between the original XRF measurement and the duplicate measurement.

Element	Mean Coefficient of Variation	Standard Deviation of Coefficient of Variation	Number of Duplicate Measurements
Al	0.082	0.076	1970
Si	0.063	0.038	1970
S	0.139	0.138	1970
K	0.077	0.110	1970
Ca	0.036	0.063	1970
Fe	0.062	0.051	1970
Sr	0.061	0.045	21

Supplement A4.

Cross plots of duplicate 5 mm resolution XRF analyses for the interval of the Skyline 16 core examined in this study. X- and y-axis units are in counts.

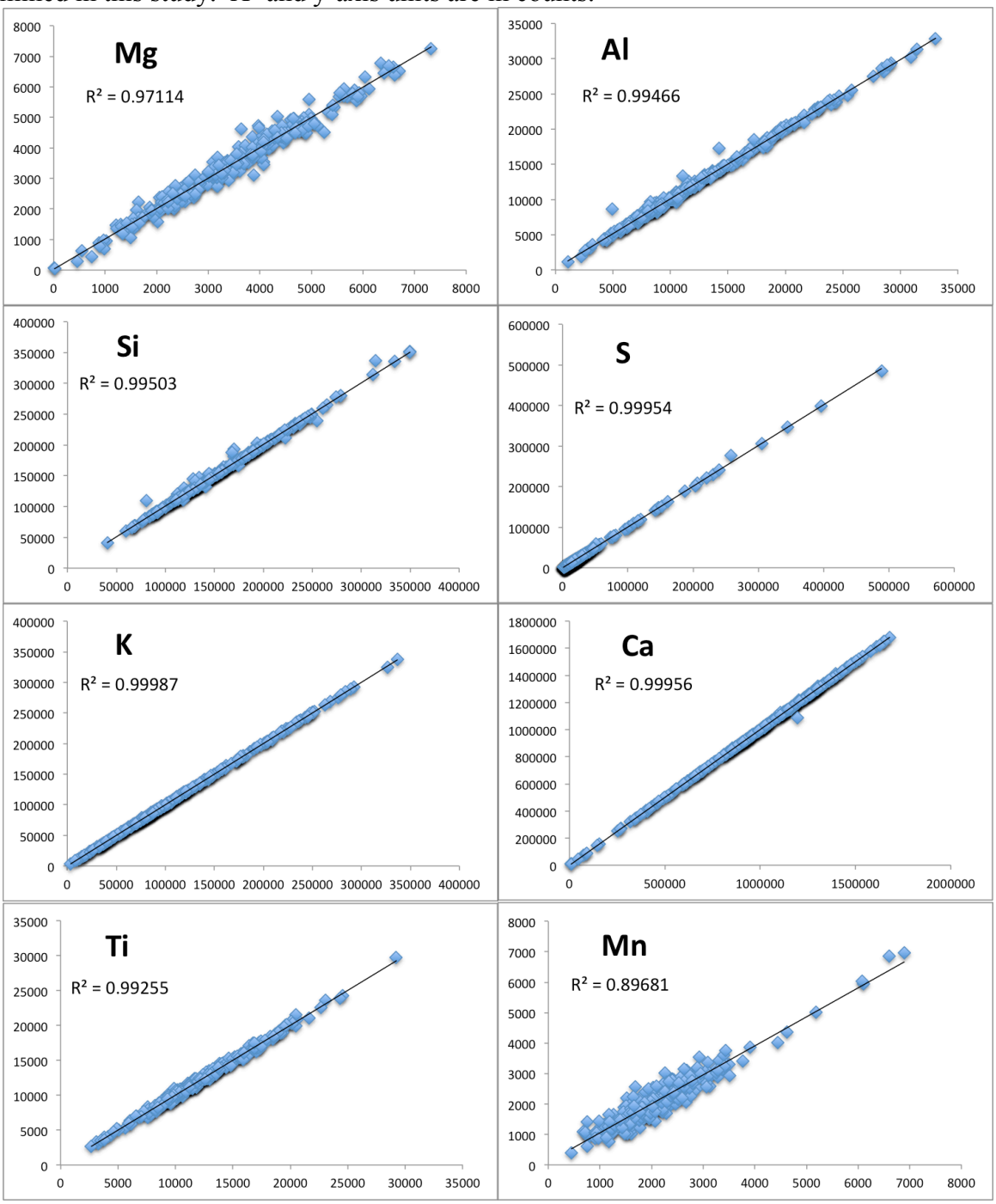

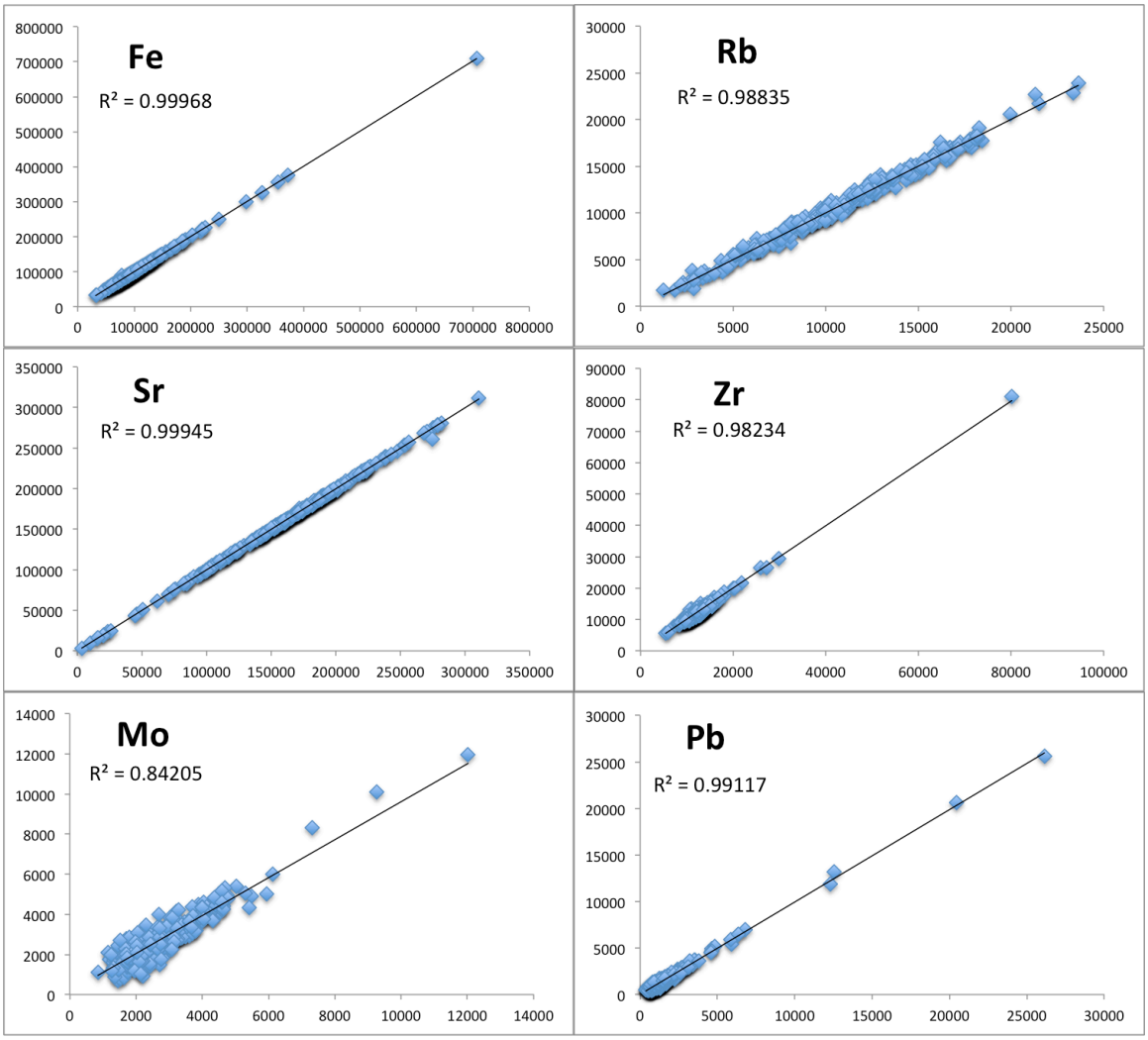
Fe
R² = 0.99968
Rb
R² = 0.98835
Sr
R² = 0.99945
Zr
R² = 0.98234
Mo
R² = 0.84205
Pb
R² = 0.99117

Supplement A5.

Cross plots of duplicate 100 µm resolution XRF analyses for the interval of the Skyline 16 core examined in this study. X- and y-axis units are in counts.

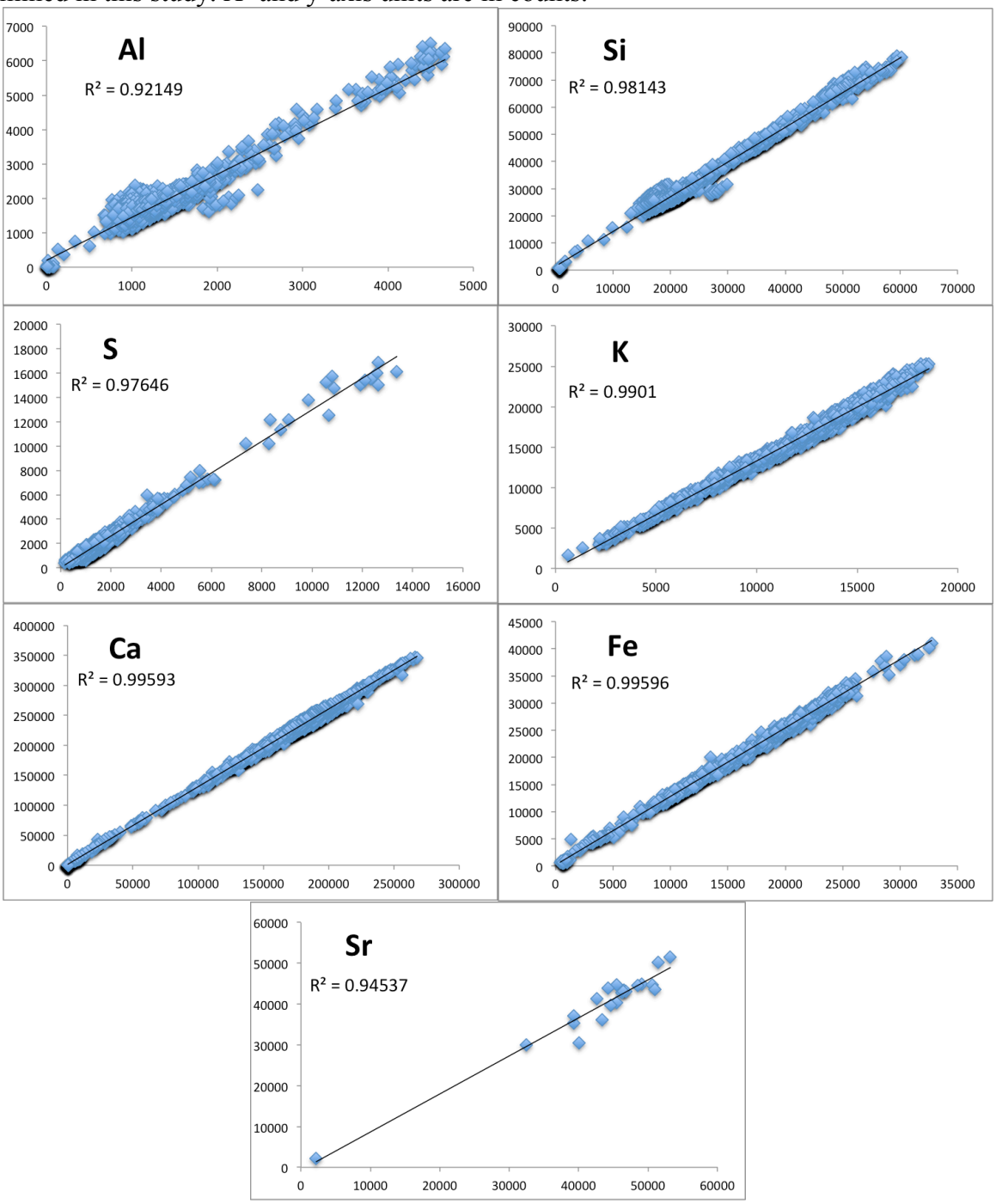

Supplement A6.

5-mm resolution ICP-XRF calibration curves using cross plotted XRF counts and ICP analyses from the interval of the Skyline 16 core studied.

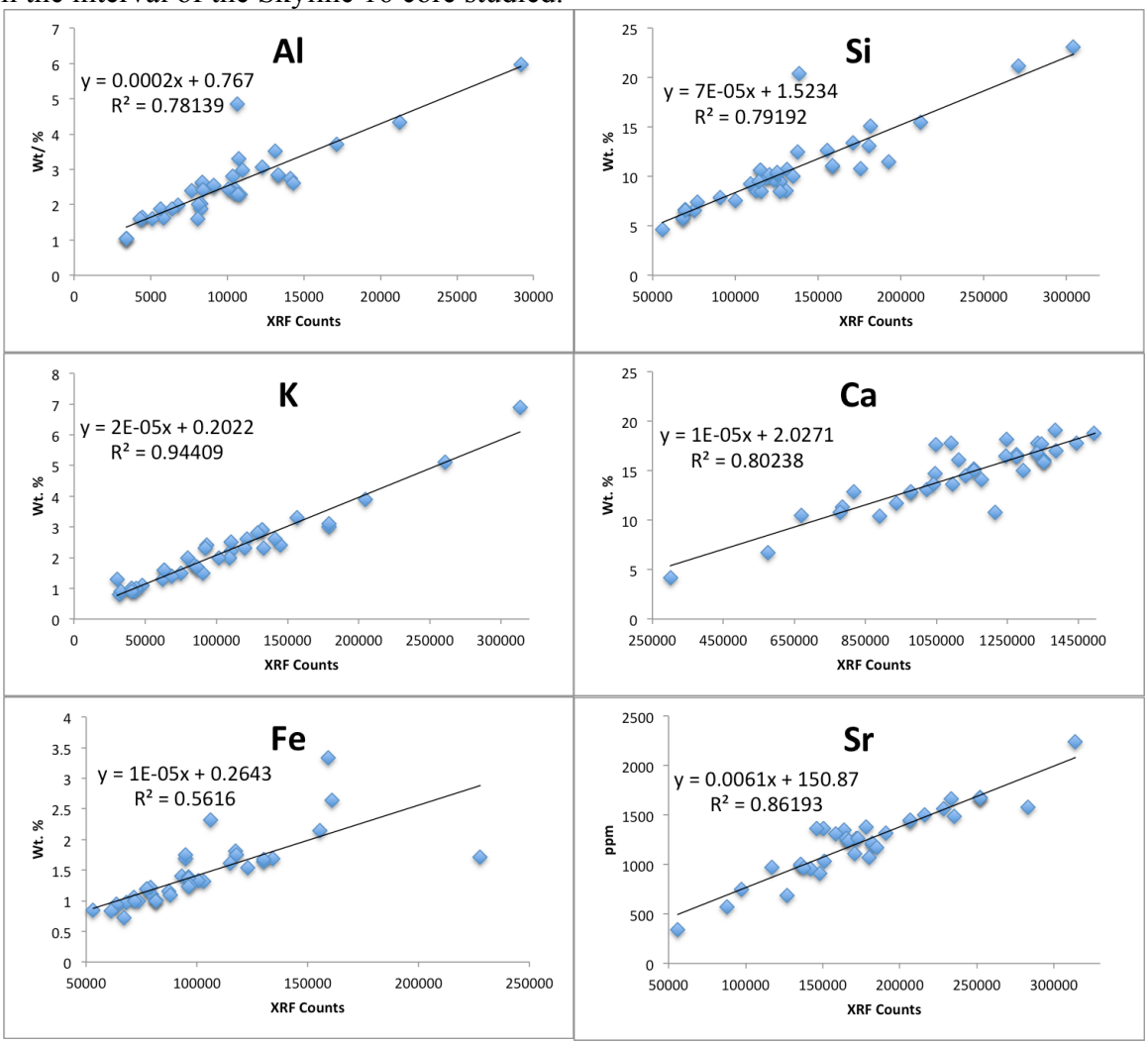

Supplement A7.

100-µm resolution ICP-XRF calibration curves for the Skyline 16 core high-resolution study interval. XRF counts and ICP analyses are cross plotted.

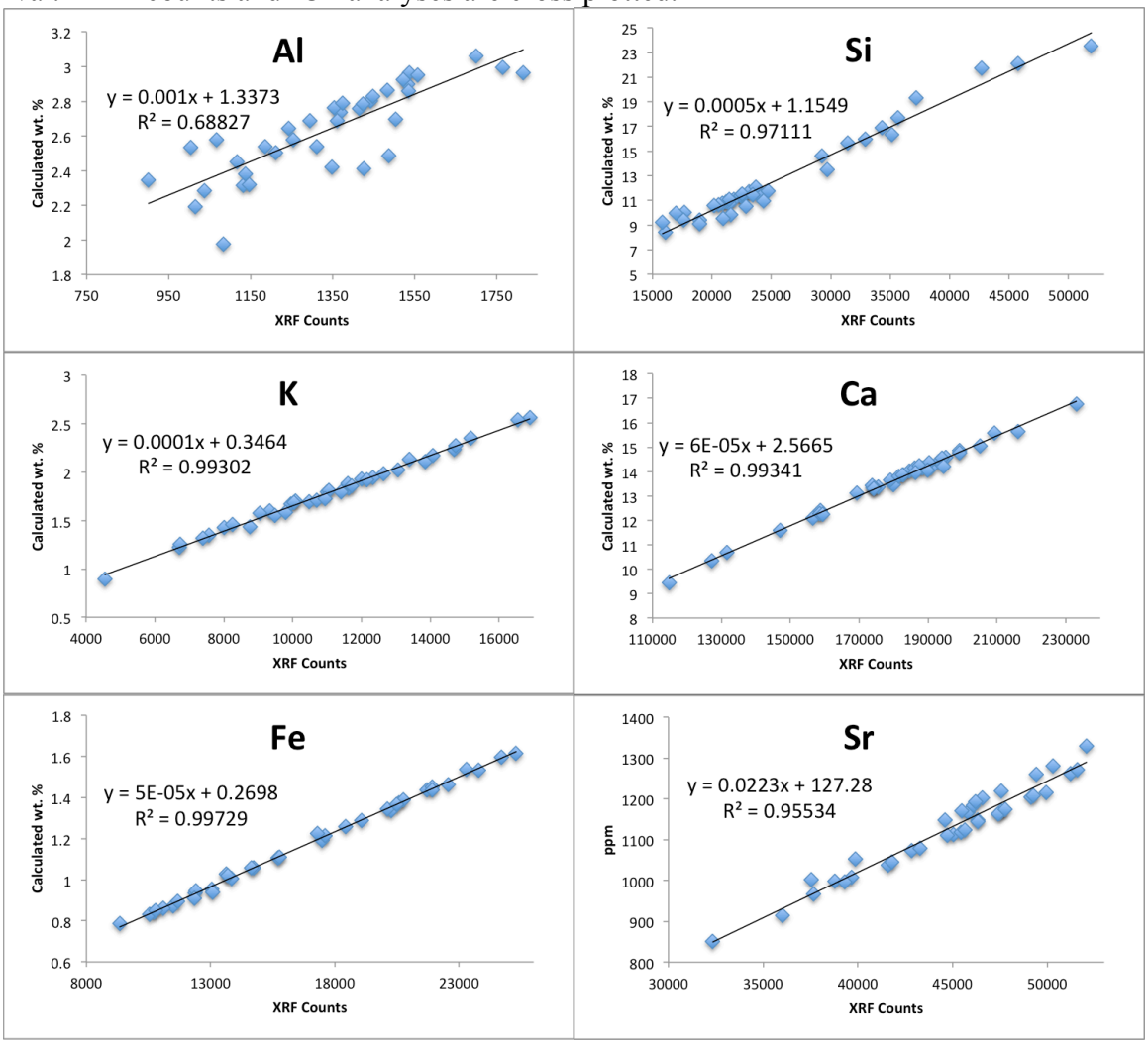

Supplement A8.

Cross plots of 100-µm resolution XRF (in counts) and grayscale data (in intensity) for Al, Si, S, K, Ca, Fe, and Sr within the Skyline 16 core. No points have been removed. See correlations in Table 3.

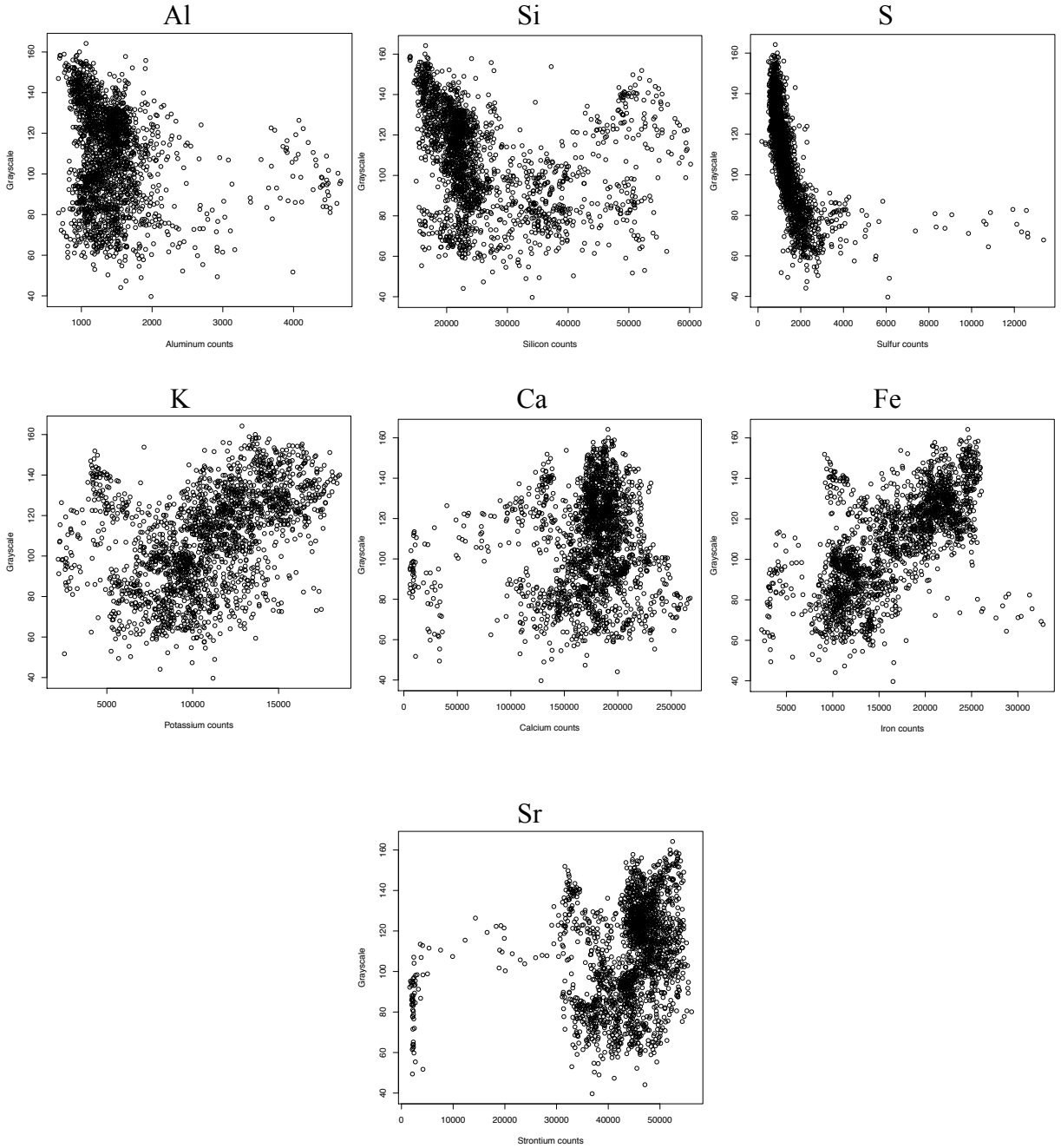

Supplement A9.

Cross plots of 100 µm resolution XRF (in counts) and grayscale (in intensity) data for Al, Si, S, K, Ca, Fe, and Sr within the Skyline 16 core following removal of outlying pyrite-rich laminae. See correlations in Table 3.

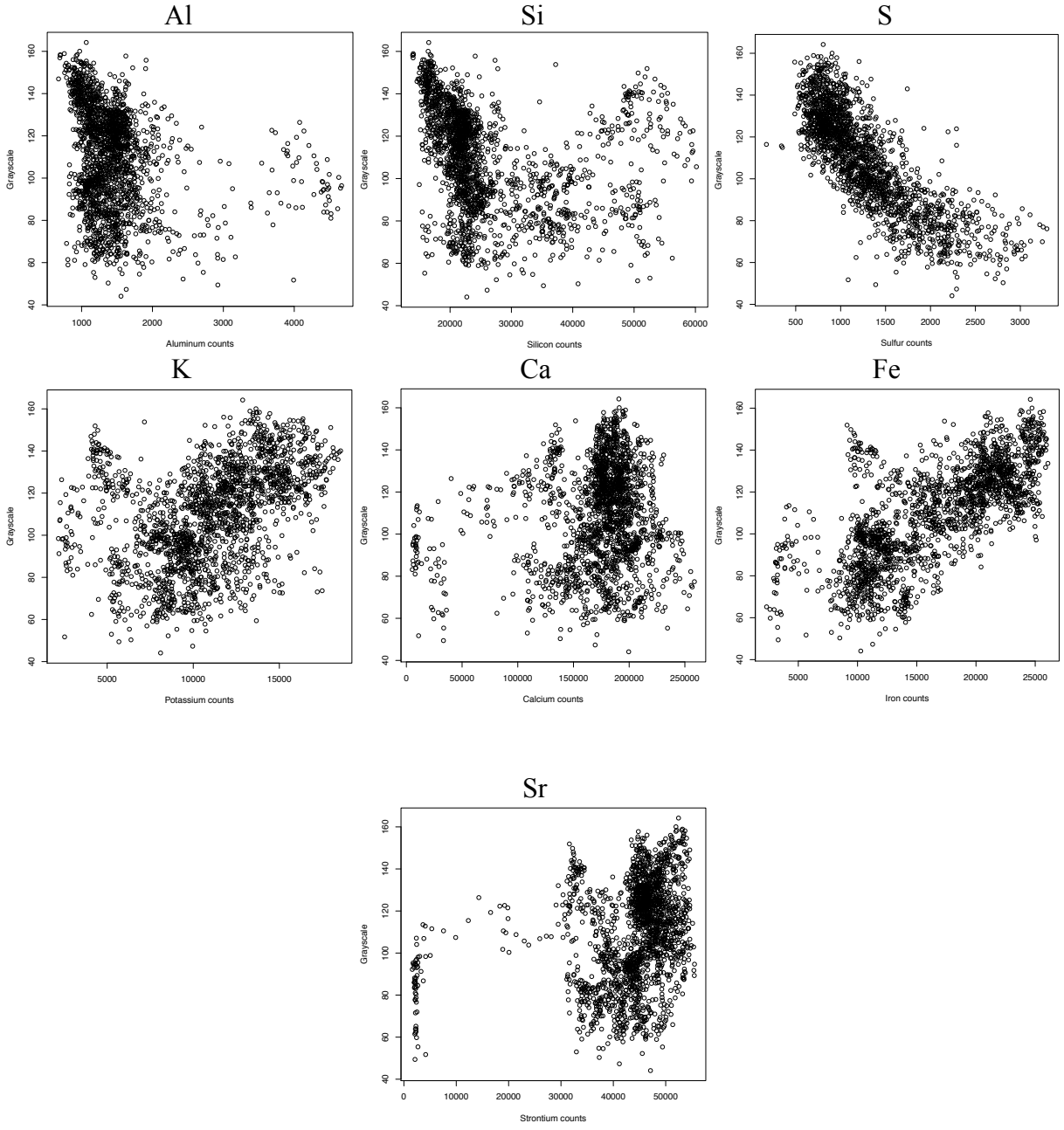

Supplement A10.

A comparison of Bruker M4 micro-XRF and Avaatech XRF core scanner results (in counts) for Ca, Fe, K, S, and Si across a 186.85-mm sub-section of the Skyline 16 core. Micro-XRF results are presented in color (Ca=Blue, Fe=Red, K=Orange, S=Yellow, Si=Grey), while XRF core-scanner results overlay the micro-XRF results in black.

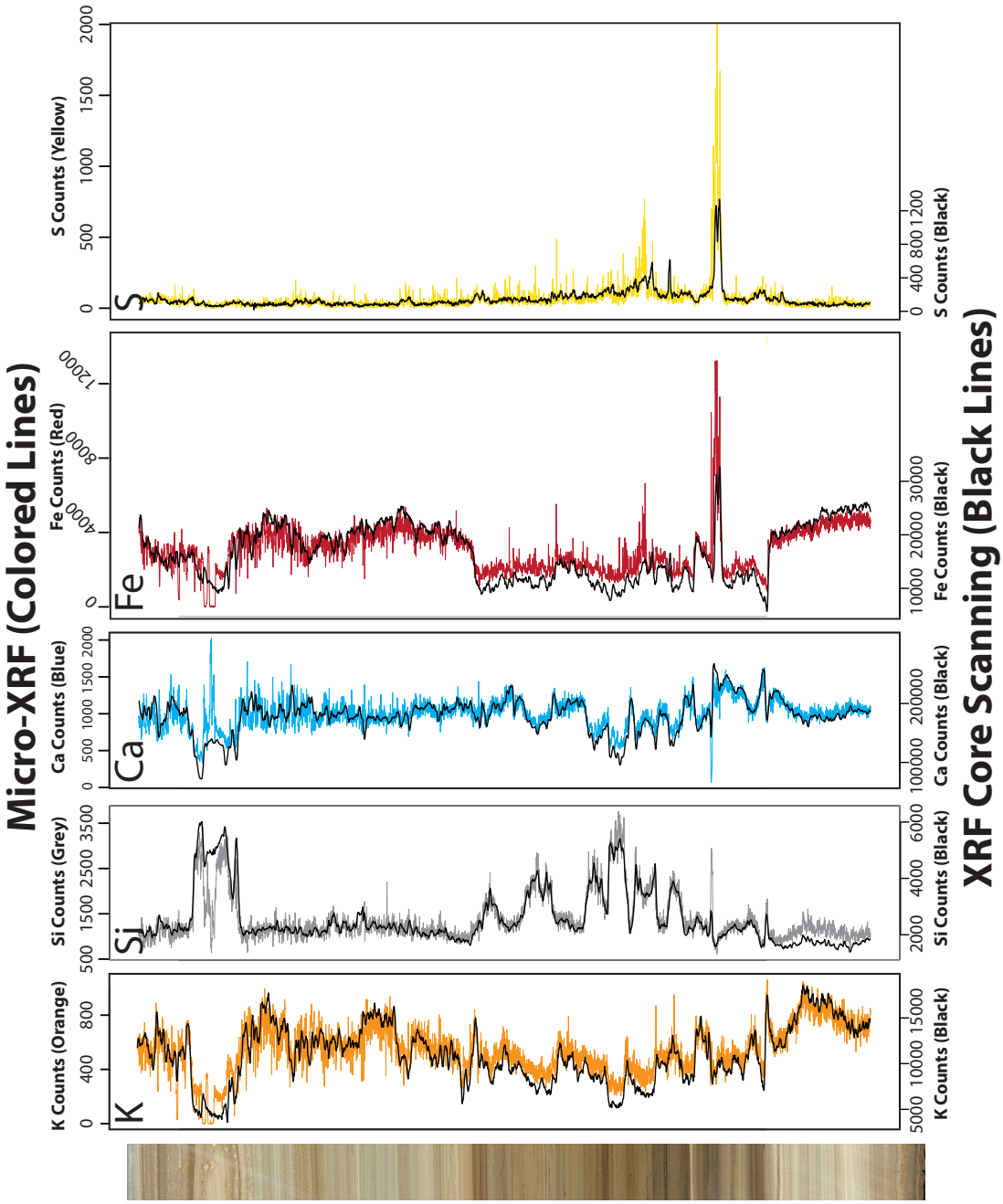

Supplement A11.

Power spectra from MTM analysis (3-2π DPSS tapers) of the micro-XRF K-Si moving-window cross-correlation results using 10 mm, 5mm, and 3 mm windows.

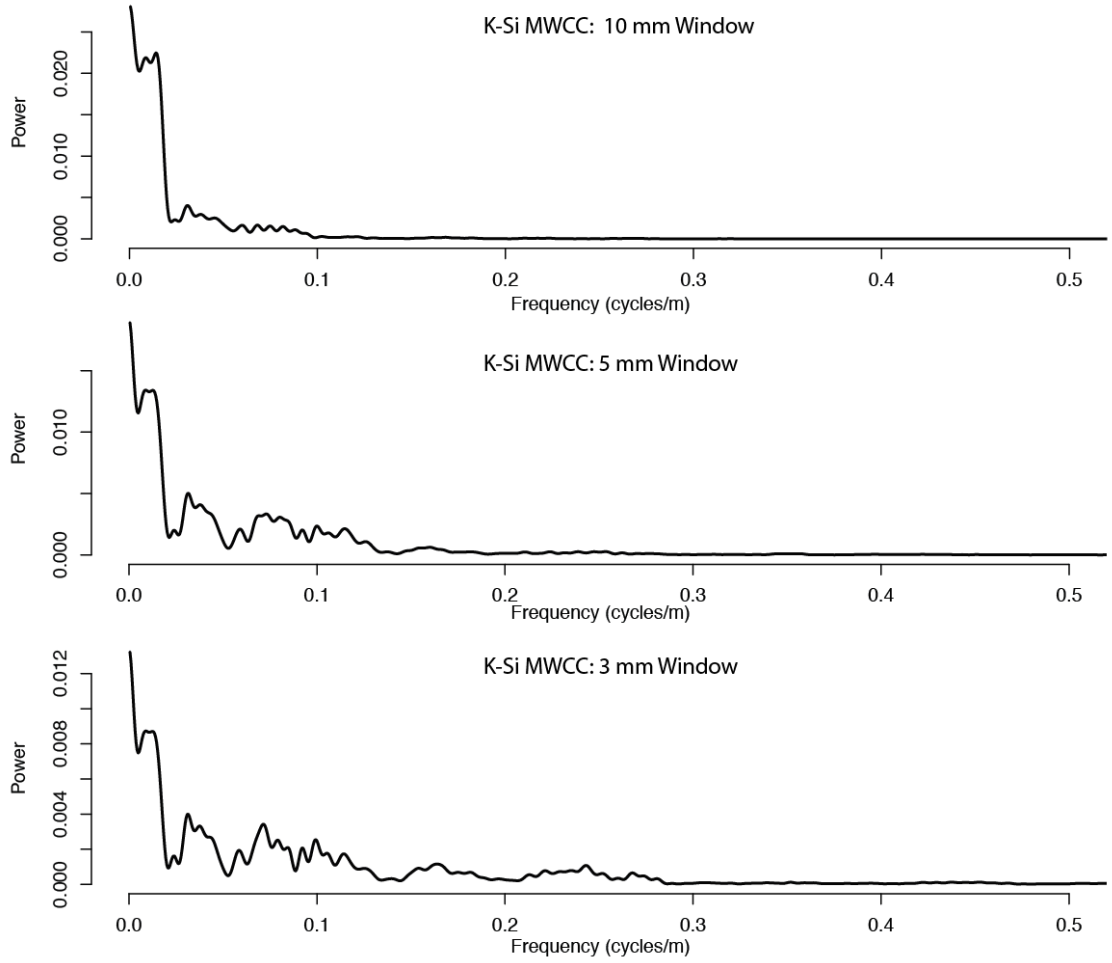

Supplement A12.

Comparison of the three constant-sedimentation method models for Si (100 micrometer resolution) over the 202.6-mm study sub-section using the A) minimum 120 μm/year rate B) nominal 168 μm/year rate and C) maximum 278 μm/year rate.

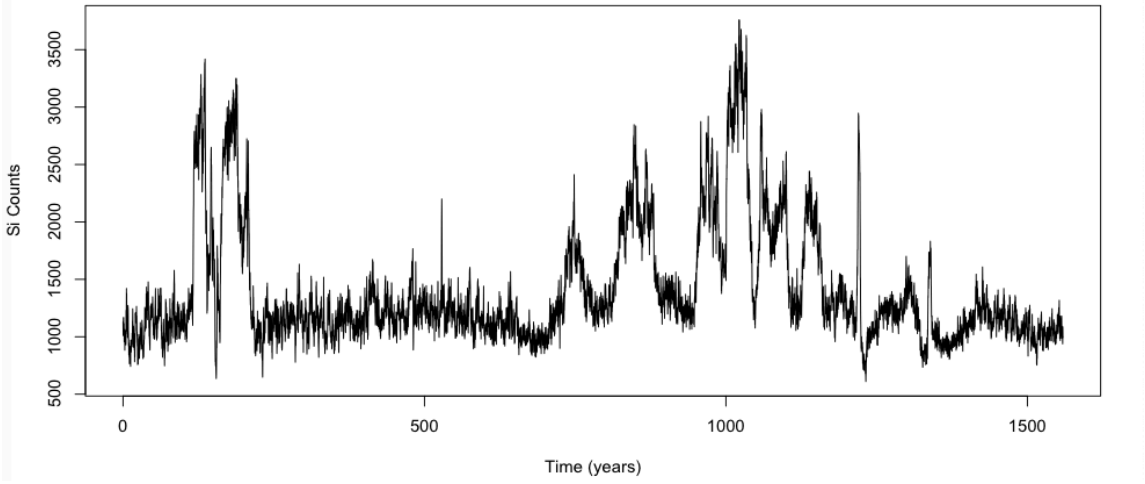

A)

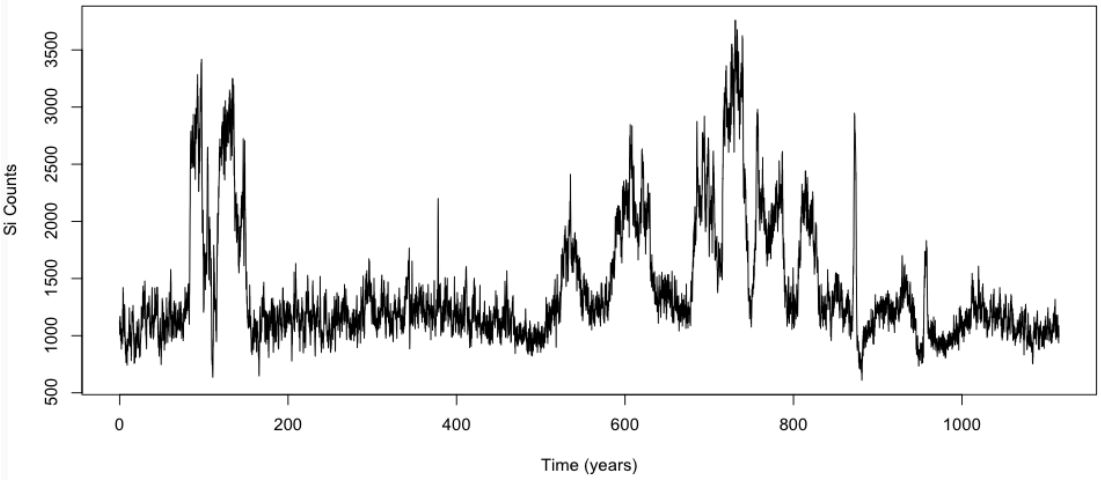

B)

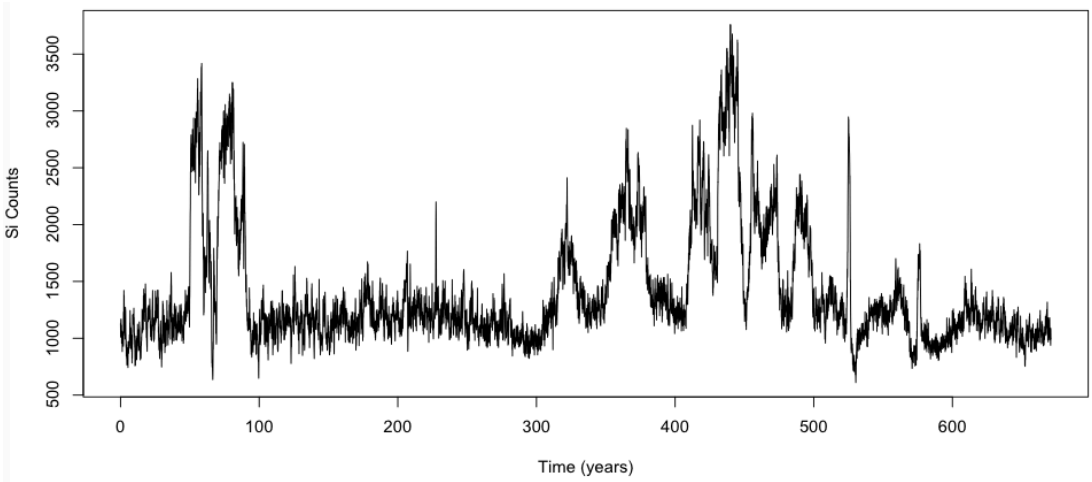

C)

Supplement A13.

Variance contained within the 0-0.09 cycle/yr band for Si, S, K, Ca, and Fe based time series models, which incorporate either the minimum (120 μm/yr), nominal (168 μm/yr), or maximum (278 μm/yr) net annual accumulation rate assumption.

Element	Time Series Model	Band Power	Total Power	Band/Total Power
Si	120 μm/yr	10567.28	24172.32	0.4371645
	168 μm/yr	3882.875	12173.9	0.3189508
	278 μm/yr	44783.63	55898.36	0.8011617
S	120 μm/yr	108.5578	282.788	0.383884
	168 μm/yr	59.80788	255.5285	0.2340556
	278 μm/yr	20.5495	97.46289	0.2108443
K	120 μm/yr	3498.014	11222.84	0.3116872
	168 μm/yr	2800.703	9242.092	0.3030378
	278 μm/yr	2681.54	5564.223	0.4819253
Ca	120 μm/yr	1095083	2794119	0.3919241
	168 μm/yr	534366	1541030	0.346759
	278 μm/yr	789300.9	1280232	0.6165295
Fe	120 μm/yr	85669.74	257662.1	0.3324888
	168 μm/yr	44348.9	212661.2	0.2085426
	278 μm/yr	44096.8	142596.7	0.3092414

Supplement A14.

MTM power spectra (3-2π DPSS tapers) for S, K, Ca, and Fe time models at the minimum, nominal, and maximum net accumulation rate values. Dashed lines mark approximate locations for 100-year, 15-year, and 10-year periodicities.

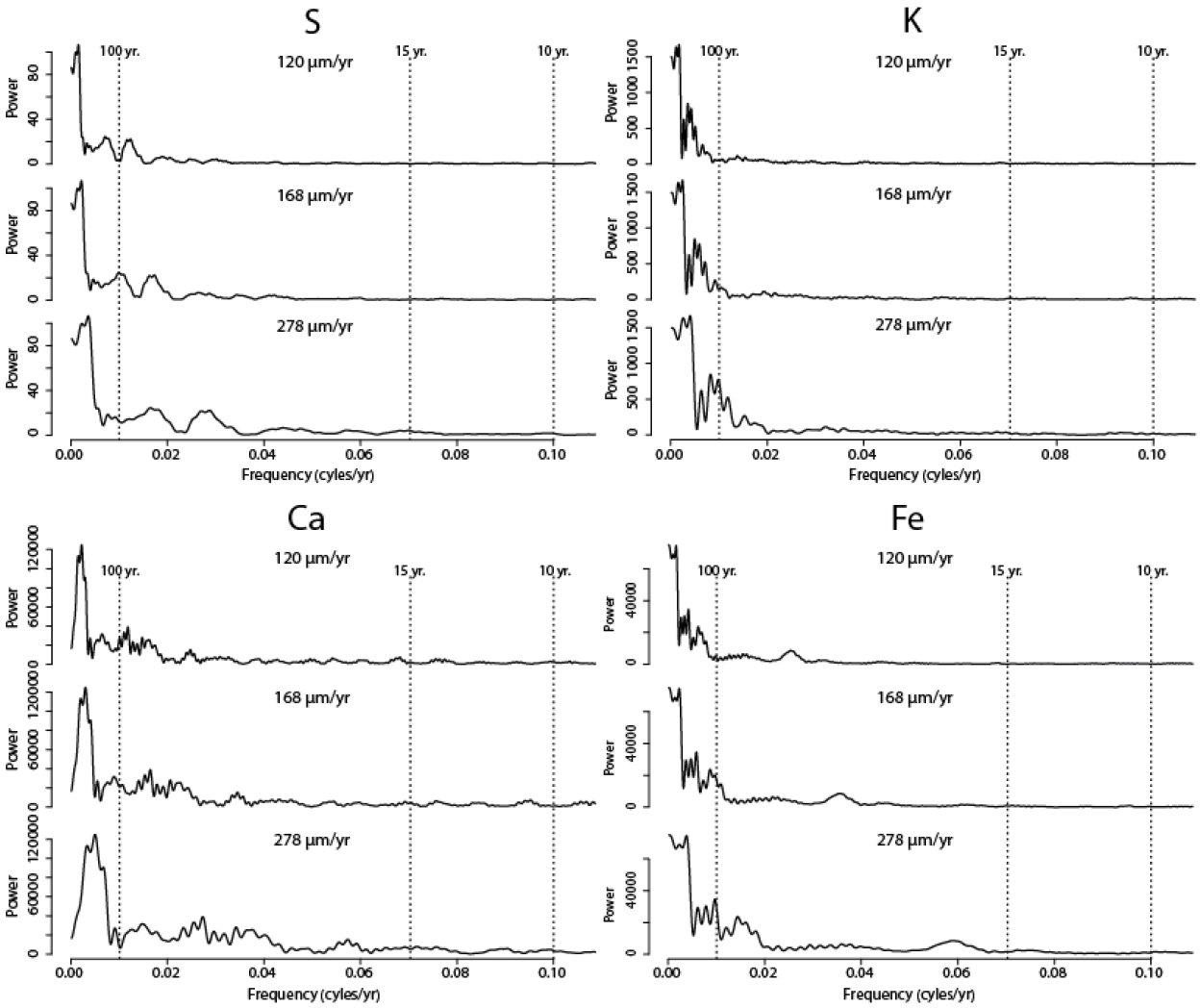

Supplement A15.

MTM power spectra (3-2π DPSS tapers) for pre-whitened S, K, Ca, and Fe time models at the minimum, nominal, and maximum net accumulation rate values. Pre-whitening was completed using a low-frequency LOESS smoother. Dashed lines mark approximate locations for 100-year, 15-year, and 10-year periodicities.

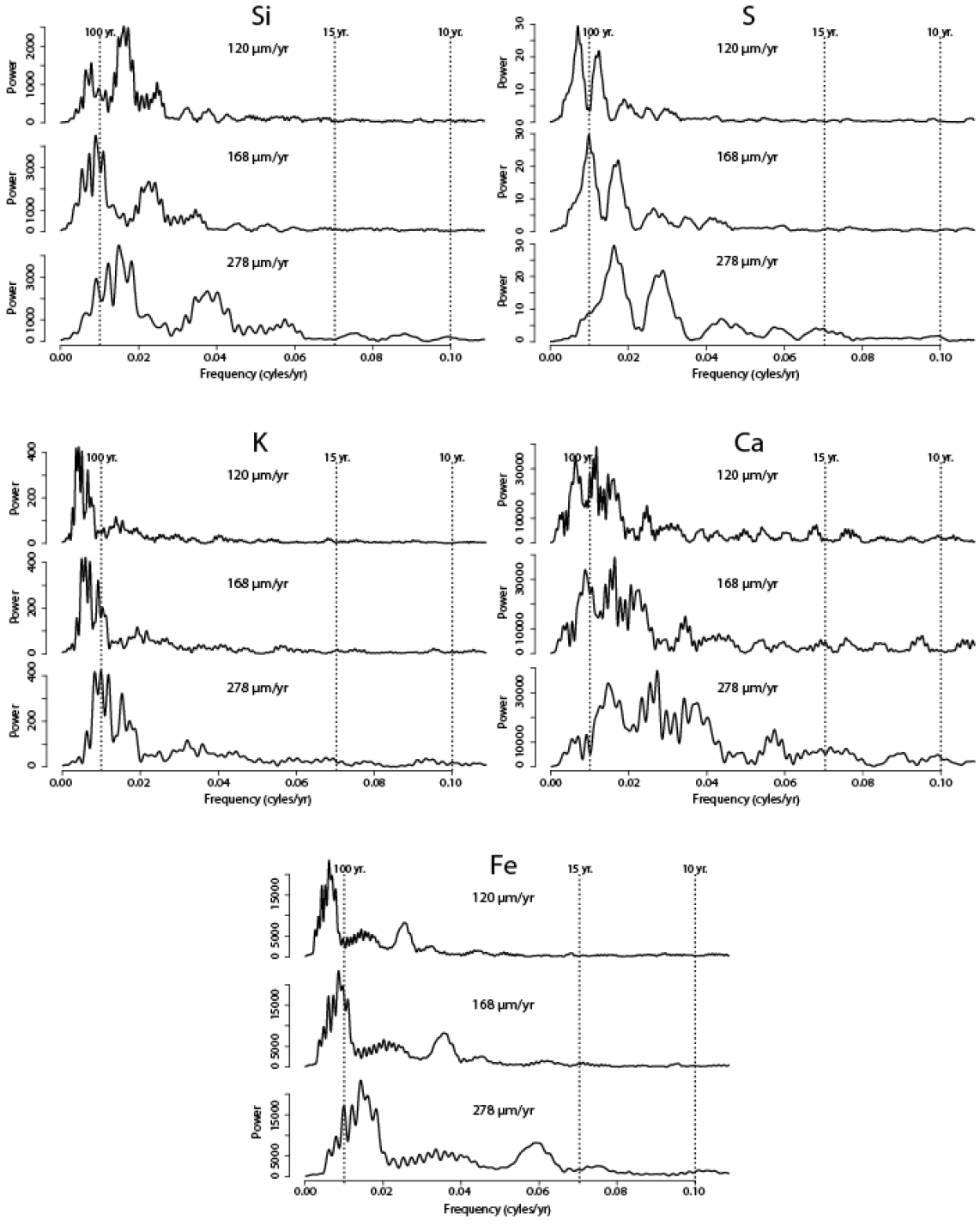

Supplement A16.

LOWSPEC power spectra results (3-2π DPSS tapers) for Si, S, K, Ca, and Fe time models at the minimum (120 µm/yr), nominal (168 µm/yr), and maximum (278 µm/yr) net accumulation rate values. The black line represents the MTM power spectra results, while the red line represents the LOWSPEC continuum estimate value. Dashed lines mark approximate locations for 100 year, 15 year, and 10 year periodicities.

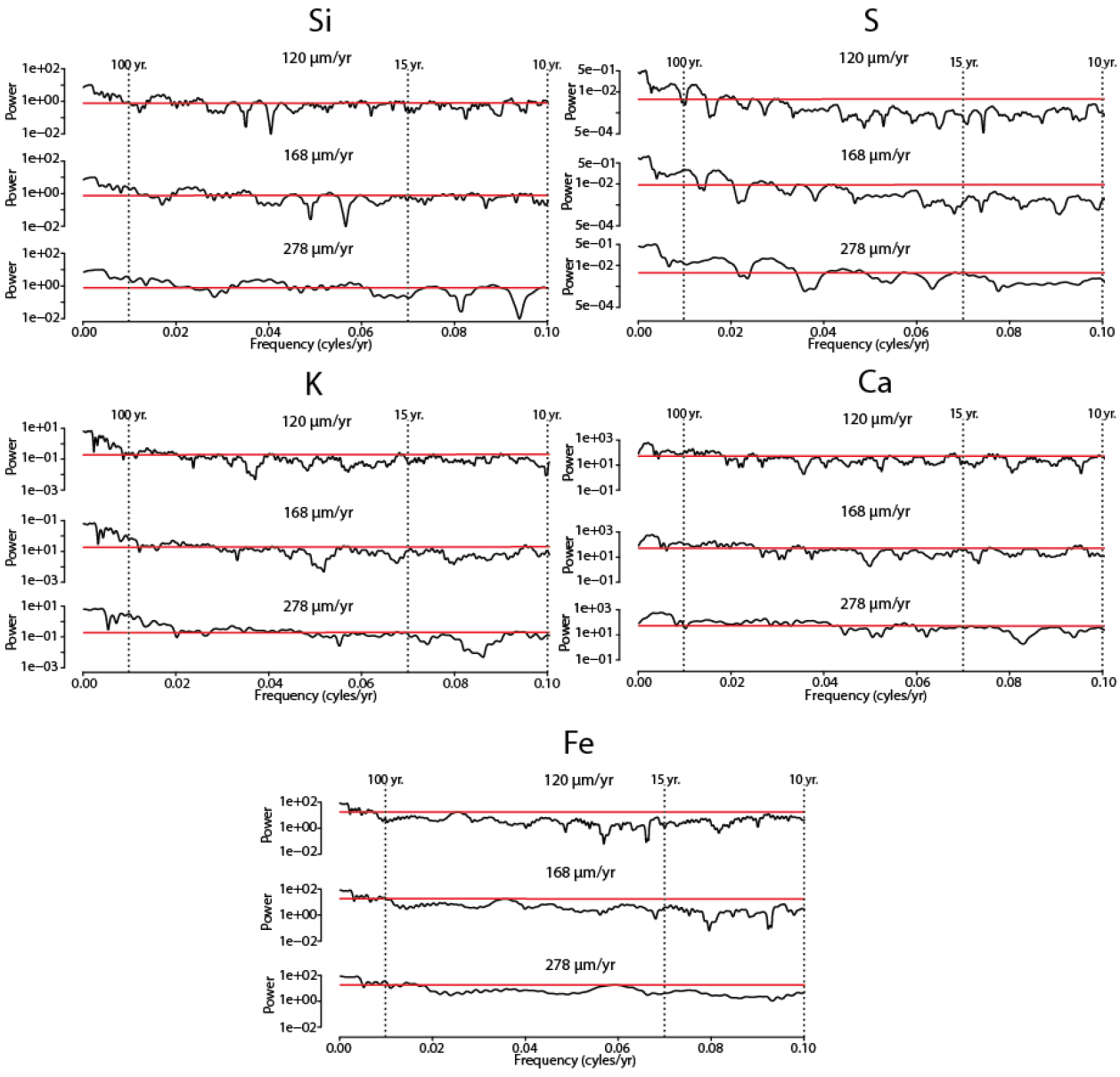

Supplement A17.

MTM log power spectra (3-2π DPSS tapers) for Si S, K, Ca, and Fe time models at the minimum, nominal, and maximum net accumulation rate values plotted out to a frequency of 1 cycle/year. Expected sunspot, ENSO, and annual varve periodicities are highlighted in gray.

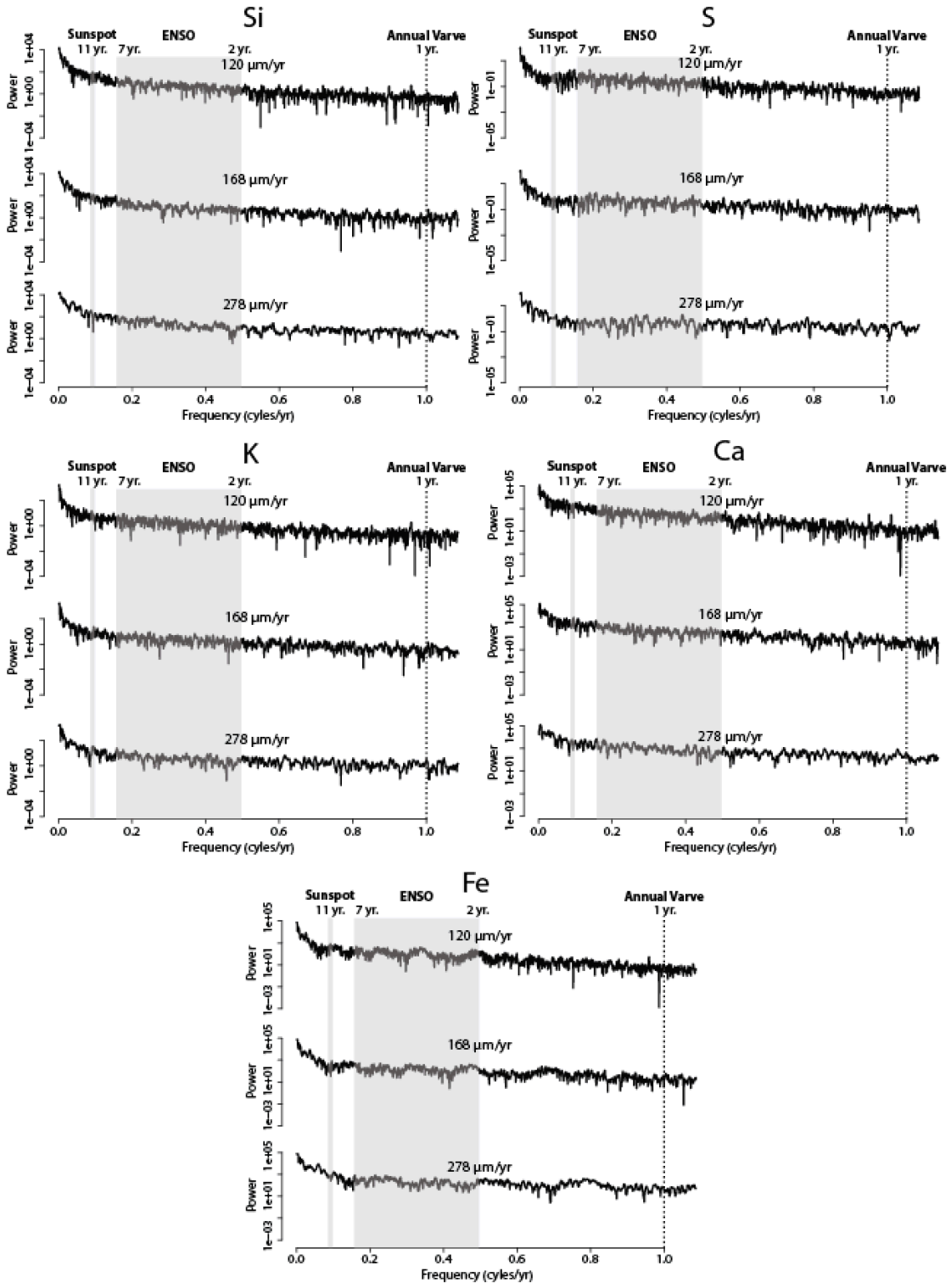

Supplement A18.

LOWSPEC power spectra results (3-2π DPSS tapers) for 5 mm resolution Si, S, K, and Ca data. The black line represents the MTM power spectra results, while the red line represents the LOWSPEC continuum estimate value. Dashed lines mark approximate locations for 20-ky, 1-ky, and 500-year periodicities.

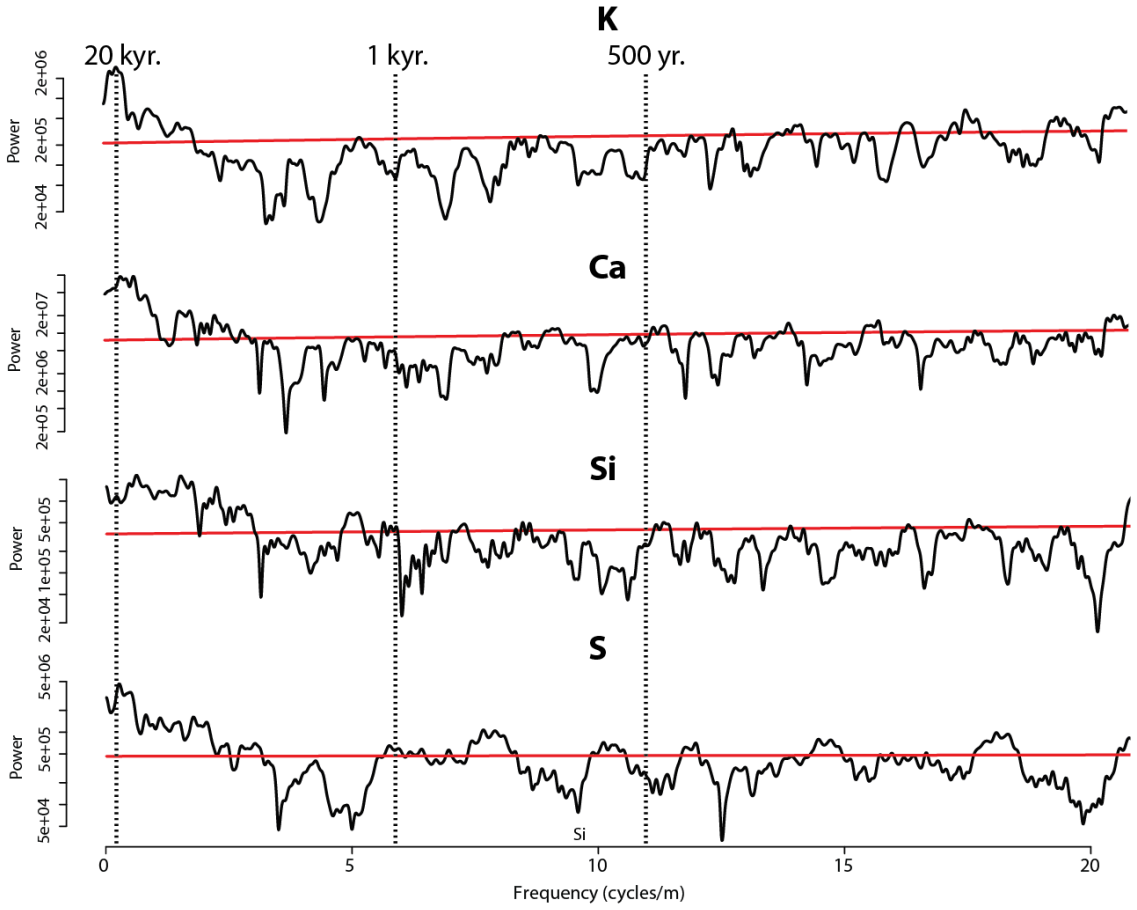

Supplement A19.

MTM power spectra (3-2π DPSS tapers) for pre-whitened 5-mm resolution K, Ca, Si, and S XRF data. Pre-whitening was completed using a low-frequency LOESS smoother. Dashed lines mark approximate locations for 20-ky, 1-ky, and 500-year periodicities.

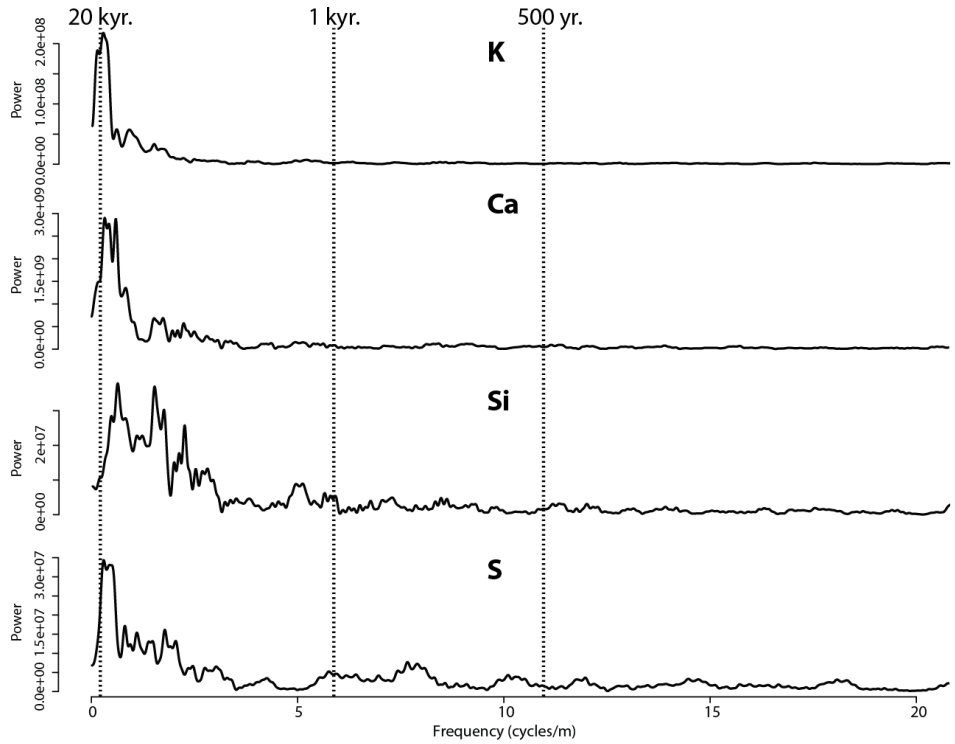

Supplement A20.

EHA plots of log power and amplitude based on gamma ray borehole logs from the "Upper R-6" zone of the Skyline 16 core (545.5-640.3 ft.). A window size of 15 ft. was used for this analysis.

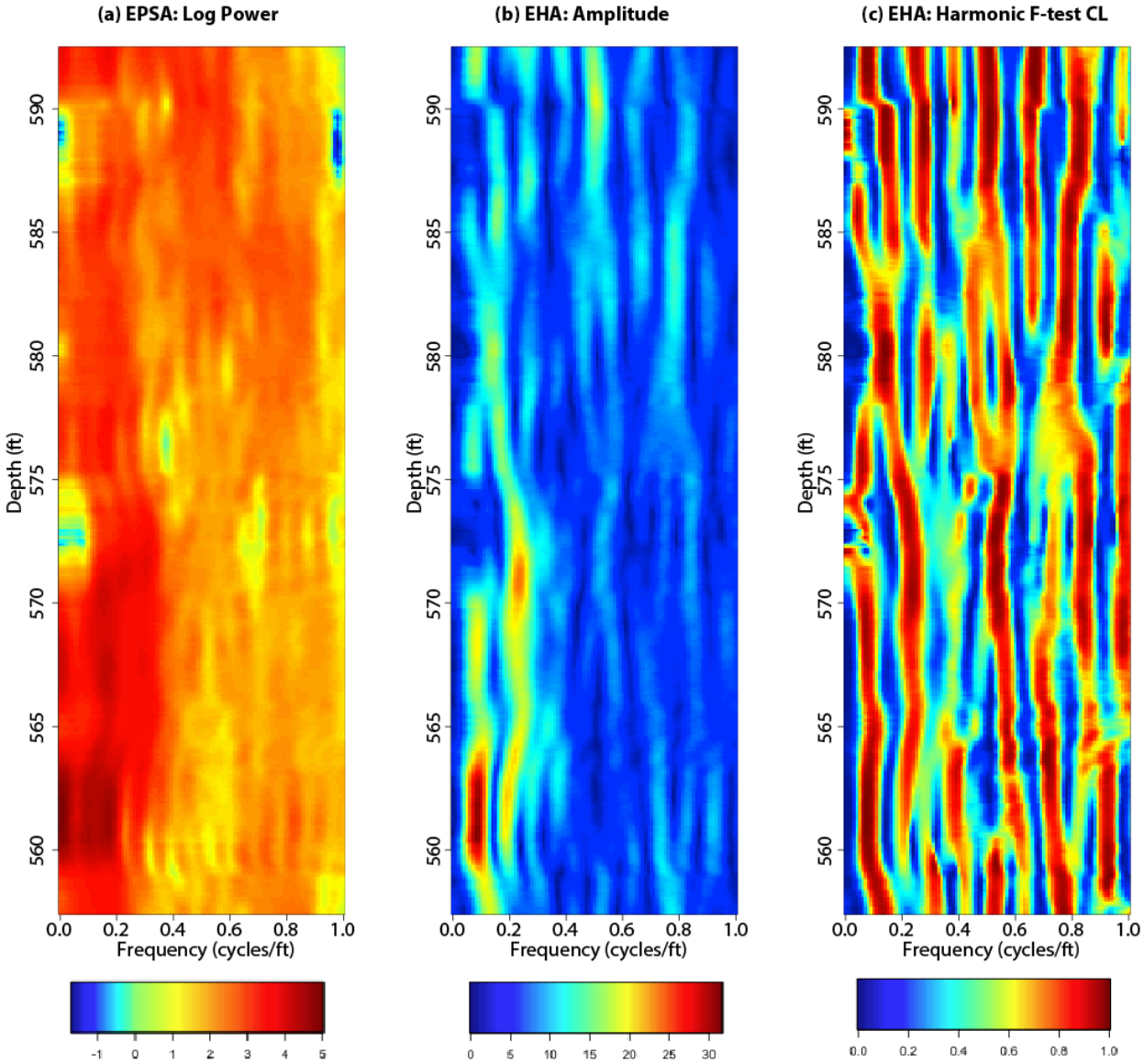

Supplement A21.

MTM power spectra (3-2π DPSS tapers) for K-Si moving-window cross-correlation results calculated using a range of window sizes (50 mm to 0.5 m).

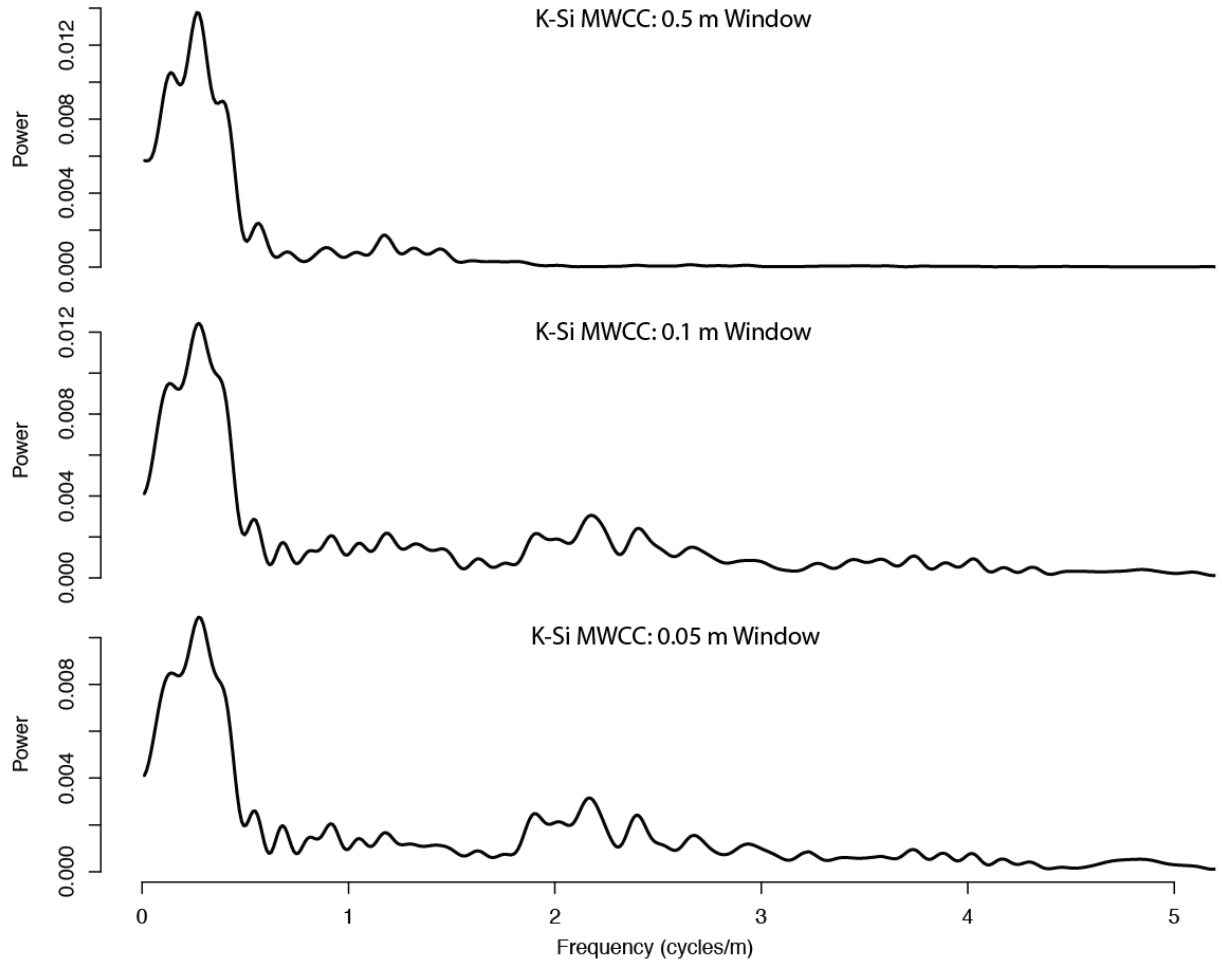

Supplement B: Chapters 2 and 3

Supplement B1.

Measurement of Ca counts in the JR-1 standard, demonstrating the stability of the Avaatech XRF instrument over the 14-month period of study. This standard was measured before the analysis of each core section. This standard (in addition to SARM-4 and JGb-1) was used to correct for instrument drift.

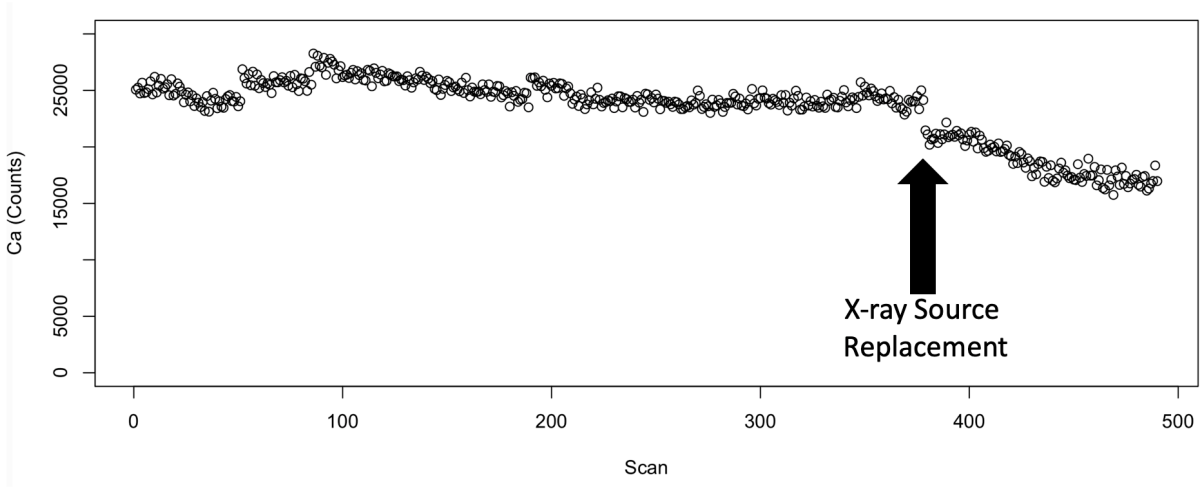

Supplement B2.

Cross plots of 5-mm resolution duplicate measurements of 10 kV elements from scanning of the Solvay S-34-1 core. X- and y-axis units are XRF counts.

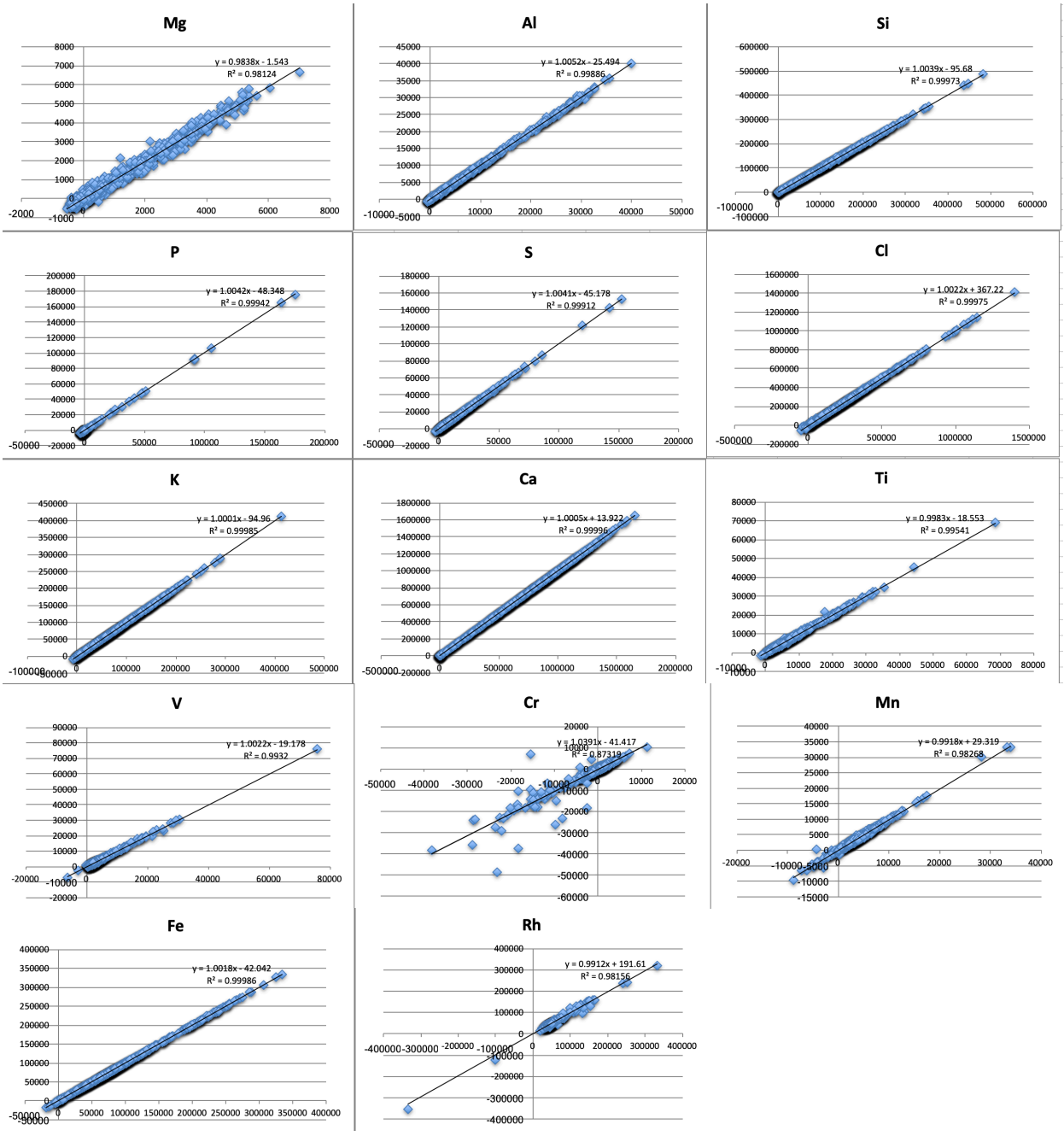

Supplement B3.

Cross plots of 5-mm resolution duplicate measurements of 30 kV elements from scanning of the Solvay S-34-1 core. X- and y-axis units are XRF counts.

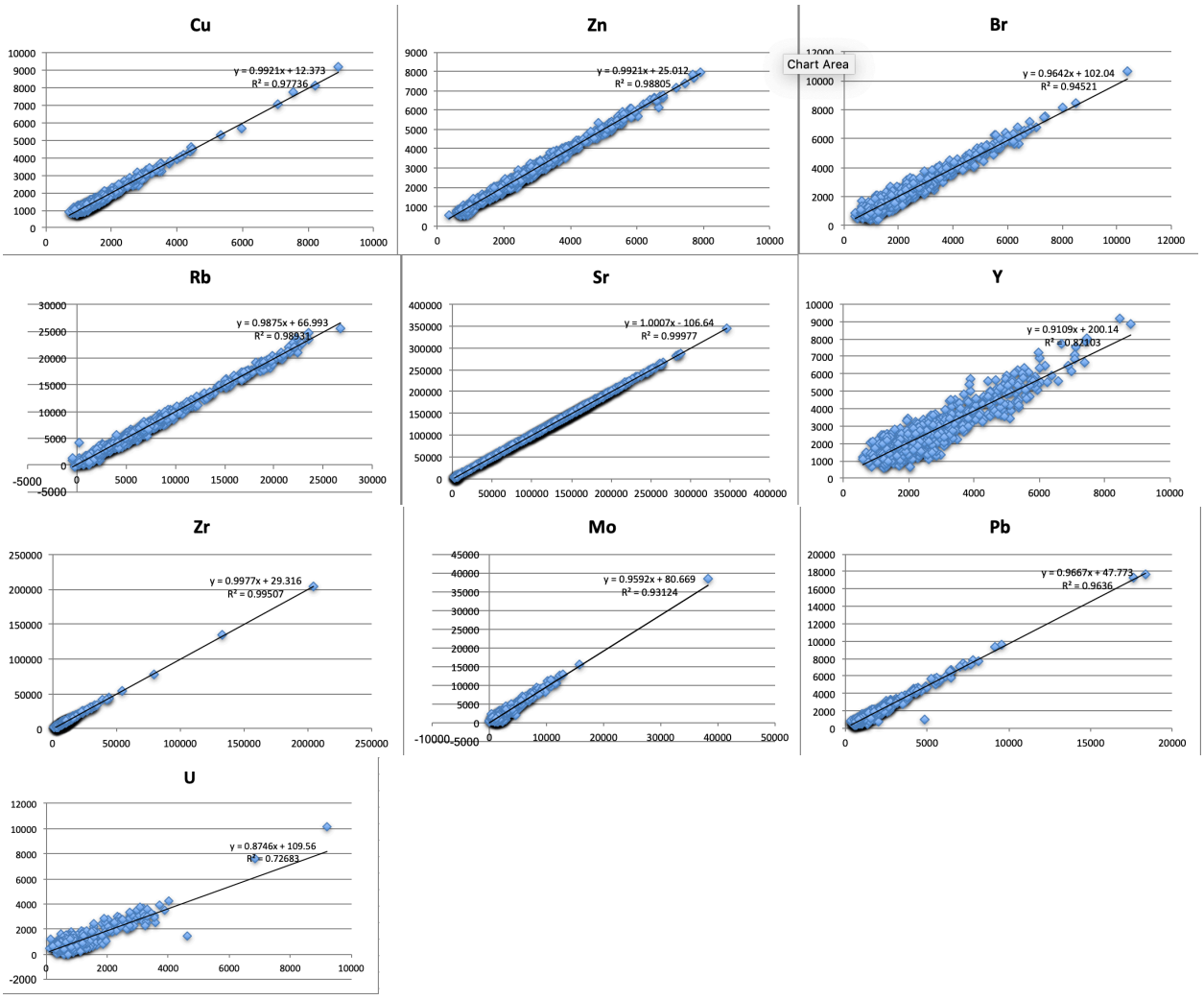

Supplement B4.

Coefficient of variation and the standard deviation of the coefficient of variation results for elements (in counts) at a 5-mm scanning resolution for the Solvay S-34-1 core project.

Element	Mean Coefficient of Variation	Standard Deviation of Coefficient of Variation	Number of Duplicate Measurements
Al	0.0608	0.9786	1077
Si	0.0073	0.0433	1077
S	0.0413	0.2109	1077
K	-0.0052	0.8492	1077
Ca	0.0061	0.0666	1077
Ti	0.0388	0.2955	1077
Mn	0.0421	0.5522	1077
Fe	0.0110	0.2135	1077
Cu	0.0399	0.0323	1077
Zn	0.0366	0.0368	1077
Br	0.1000	0.0924	1077
Rb	0.0795	0.1887	1077
Sr	0.0088	0.0215	1077
Zr	0.0419	0.0444	1077
Mo	0.1735	0.1917	1077
Pb	0.0948	0.0937	1077